UNIVERSITY OF SUSSEX

School of Engineering and Informatics

PhD dissertation

UNCERTAINTY AND SENSITIVITY ANALYSIS FOR BLADED DISKS WITH RANDOM BLADE ANISOTROPY ORIENTATIONS

---

by Rahul Rajasekharan Nair

Submitted in partial fulfilment of the requirements for the award of the degree Doctor of Philosophy

Supervisor: Dr. Evgeny Petrov

January 2019

To the memory of my parents, T. Rajasekharan Nair and C. Sreelatha.

DECLARATION

I hereby declare that I am responsible for the work submitted in this thesis, the original work is my own except as specified in acknowledgements or in footnotes, and the thesis has not been and will not be, submitted in whole or in part to another university for the award of any other degree.

Rahul Rajasekharan Nair

Acknowledgments

I am grateful to my supervisor, Dr Evgeny Petrov for giving the opportunity to work on this project. Without his guidance and support, this thesis would not have materialised.

I am grateful to MTU Aero Engines AG, Germany, for the financial and technical support provided for this study and for awarding MTU Scholarship to pursue my doctoral study at the University of Sussex.

Thanks to Prof. Julian Dunne and Dr Chang Wang for their critical comments on my progress at various stages of this study. Thanks to Dr Peter Cheng, the Director of doctoral studies, School of Engineering and Informatics for his useful guidance on the doctoral process.

Thanks to my colleagues at MTU Aero Engines AG, especially, Dr Andreas Hartung for his critical comments on my work during several project review meetings in the course of last three years. I am thankful to all my colleagues at the University of Sussex who have contributed to creating a pleasant working environment. Special thanks to Adam Koscso, Harri Koivisto and Hua Jun Li for their kind support.

I wish to thank Dr Jonathan Feinberg for creating the Python toolbox, Chaospy for uncertainty quantification. I also thank the team of Scikit-learn.

Special thanks to Mark Rahman for renting me a room in "The Old Rectory" in Falmer Village.

Thanks to all my friends and extended family members.

My gratitude for my grandparents cannot be put to words. They have made numerous sacrifices for the sake of my well-being since the time I was born.

All my accomplishments are nothing but humble tributes to my parents.

Abstract

Single crystal blades used in turbine bladed disks of modern gas turbine engines exhibit material anisotropy. The crystal orientations of blades in a bladed disk are usually different. The static and dynamic response of a mistuned bladed disk with a blade to blade variation in crystal orientations differs significantly from the tuned structure where all blades are identical. Based on detailed study of the available literature on mistuned bladed disk, a gap in knowledge on the effects of blade anisotropy orientation on static deformation and forced response of bladed disk was identified, since there are no studies for bladed disk mistuned by material anisotropy based on high-fidelity finite element models.

In the first part of this study, the effects of blade material anisotropy orientation on non-linear static deformation of the mistuned bladed disk are thoroughly investigated. Moreover, sensitivity and uncertainty analyses for non-linear static deformation are performed to quantify the effects of scattering in blade crystal orientation. A method based on Sobol indices, hitherto unused in the analysis of mistuned bladed disk, is introduced for global sensitivity analysis with respect to blade anisotropy angles.

The usefulness of polynomial chaos expansion as an efficient method for uncertainty analysis of mistuned blade disk is demonstrated. For mistuned bladed disk, with numerous design parameters in the form of blade anisotropy angles, the following two strategies are proposed to address the "curse of dimensionality" problem associated with uncertainty analysis: (i) reduce the dimension of the random space by screening the anisotropy angles based on their rank order of importance obtained from sensitivity analysis, (ii) by using gradient values, in addition to function evaluations, to calculate the coefficients in the polynomial chaos expansion.

Due to manufacturing errors, the contact geometry of blades at fir-tree root and shrouds will be different from the design geometry. The effects of variation in crystal orientation on non-linear static deformation of a tuned bladed disk is investigated for different variants of fir-tree root and shroud geometry.

In the second part of this study, the effects of blade material anisotropy orientation on the linear forced response of mistuned bladed disks are investigated. Considering blade anisotropy angles as random design parameters, uncertainty in forced response of mistuned bladed disk is quantified using gradient-based polynomial chaos expansion. Further, the crystal orientations of blades are optimised in order to achieve a reduction in the maximum forced response amplitude of a mistuned bladed disk.

Preface

This thesis study the static and dynamic response of gas turbine bladed disk considering uncertainty in the orientation of the single crystal blades. The work from this thesis has been published or is accepted for publication in the following papers:

i. Rajasekharan, R., Petrov, E. P., 2019. "Analysis of statistical characteristics and global sensitivity for forced response of bladed disks mistuned by material anisotropy". In *Proceedings of the ASME Turbo Expo*. GT2019-90632, Pheonix, Arizona, USA, 17-21 June 2019.

ii. Rajasekharan, R., Petrov, E. P., 2018. "Analysis of deformation of mistuned bladed disk with friction and random crystal anisotropy orientation using gradient-based polynomial chaos expansion". *Journal of Engineering for Gas Turbines and Power*, **141**, pp. 041016(1)-(10)

iii. Koscso, A., Rajasekharan, R., Petrov, E. P., 2018. "Sensitivity and uncertainty of modal characteristics and forced response of bladed disks mistuned by material anisotropy". In *Proceedings of the* 15^{th} *International Symposium on Unsteady Aerodynamics, Aeroacoustics & Aeroelasticity of Turbomachines.* ISUAAT15-092, University of Oxford, UK, 24-27 September 2018.

The following article has been prepared for journal publication:
Rajasekharan, R., Petrov, E. P., "Uncertainty and global sensitivity analysis of bladed disk with material anisotropy mistuning and root geometry variations".

Contents

Declaration ii

1 Introduction **1**

1.1 Uncertainty analysis 4

1.2 Sensitivity analysis 9

1.3 Survey of existing literature 12

1.3.1 Analysis of the deformation of fir–tree root joints 12

1.3.2 Effects of crystal orientation on mechanical properties of single crystal blades 13

1.3.3 Uncertainty and sensitivity analysis 16

1.3.4 Intentional mistuning of the bladed disk 24

1.4 Objectives and scope of the work 26

1.4.1 Project objectives 27

2 Methodology of analysis **29**

2.1 Modelling of anisotropy-mistuned bladed disks 29

2.1.1 Non-linear static analysis 29

2.1.2 Sensitivity of static displacement to anisotropy orientation . . 32

2.1.3 Sensitivity of stresses to anisotropy orientation 33

2.1.4 Sensitivity of forced response for anisotropy mistuned bladed disk 34

2.2 Uncertainty analysis 37

2.2.1 Random Forest 37

2.2.2 Polynomial chaos expansion. 41

2.2.3 Gradient-based polynomial chaos expansion. 44

2.3 Global sensitivity analysis 46

2.4 An analytical expression for the probability distribution of stochastic response of bladed disk 49

3 Finite element modelling 54

3.1 Finite element model of bladed disk 55

3.2 Finite element model constraints and boundary conditions 57

3.3 Integration of the FE solver with tools for uncertainty analysis and optimisation 60

3.3.1 The framework for uncertainty and global sensitivity analysis . 60

3.3.2 The framework for optimisation 61

4 Sensitivity of static deformation to blade anisotropy orientations 63

4.1 Deformation of a mistuned bladed disk 63

4.2 Local sensitivity analysis 68

4.3 Global sensitivity analysis 78

5 Analysis of static deformation considering variations in root geometry and anisotropy orientation 83

5.1 Effects of root geometry variations. 85

5.2 Effects of variation in material anisotropy orientation. 91

5.3 Statistical analysis using Random Forest based surrogate model . . . 102

6 Uncertainty analysis for static deformation of mistuned bladed disks 109

6.1 Scatter in deformation due to randomness in the crystal orientation of blades 109

6.2 Uncertainty analysis using polynomial chaos expansion 111

6.2.1 Analysis of the linear bladed disk. 113

6.2.2 Analysis of the non-linear bladed disk. 118

6.3 Analytically derived PDF using sensitivity-based linear approximation 122

7 Forced response analysis of mistuned bladed disks 129

7.1 Effects of scattering in anisotropy orientation on modal properties and forced response 131

7.1.1 Effect of blade anisotropy orientation on modal properties. . . 131

7.1.2 Effect of blade anisotropy orientation on the forced response. . 132
7.2 Uncertainty analysis using polynomial chaos expansion 142
7.3 Sensitivity of forced response to anisotropy angles 151
7.4 Optimisation of blade anisotropy angles 158

8 Concluding remarks **165**
8.1 Summary of methodology development 165
8.2 Summary of results from numerical studies 166
8.3 Further scope of research 169

List of Figures

1.1 Schematic diagram of (a) dovetail joint and (b) fir–tree root joint. . . 3
1.2 Crystal anisotropy angles for single crystal blades. 15

2.1 Regression tree: a piecewise constant regression model 38
2.2 Algorithm for constructing Random Forest model 42

3.1 Model of the full bladed disk 55
3.2 A section of the finite element model of the bladed disk. 56
3.3 Finite element model of the bladed disk sector having (a) 128071 nodes and (b) 6874 nodes. 57
3.4 Contact patches on right-hand side of (a) blade root and (b) disk slot. 58
3.5 Figure showing (a) nodes on the rim of the bladed disk where axial and tangential DOF are constrained, and (b) nodes where cyclic symmetry constraints are applied. 59
3.6 Schematic diagram showing the framework for (a) uncertainty and global sensitivity analysis, and for (b) optimisation of the blade anisotropy angles. 62

4.1 Distribution of the normalised anisotropy angles of all blades for an example mistuning pattern. 64
4.2 Displacements at blade tip node of all blades in (a) radial (b) circumferential and (c) axial direction in a mistuned bladed disk 65
4.3 Figure showing (a) axial, (b) circumferential and (c) radial displacement of a mistuned bladed disk. 67
4.4 Local sensitivity of axial displacement of a mistuned bladed disk w.r.t anisotropy angles (a) α, (b) β and (c) ζ of blade number 1. 69

4.5 Local sensitivity of tangential displacement of a mistuned bladed disk w.r.t anisotropy angles (a) α, (b) β and (c) ζ of blade number 1. . . . 70
4.6 Local sensitivity of radial displacement of a mistuned bladed disk w.r.t anisotropy angles (a) α, (b) β and (c) ζ of blade number 1. . . . 72
4.7 Sensitivity of displacements at blade tip of blade number 1 to anisotropy angles (a) α (b) β and (c) ζ for tuned linear bladed disk 73
4.8 Sensitivity of blade tip displacements of blade number 1 to anisotropy angle (a) α (b) β and (c) ζ for a mistuned linear bladed disk 74
4.9 Sensitivity of blade tip displacements of blade number 1 to anisotropy angle (a) α (b) β and (c) ζ of all blades in a mistuned non-linear bladed disk 75
4.10 Sensitivity of normal stresses at blade root of blade number 1 to anisotropy angle (a) α (b) β and (c) ζ of all blades in a mistuned non-linear bladed disk 76
4.11 Sensitivity of shear stresses at blade root of blade number 1 to angle (a) α (b) β and (c) ζ of all blades in a mistuned non-linear bladed disk 77
4.12 Sensitivity of von Mises stress at blade root of blade number 1 to anisotropy angles of all blades in a mistuned non-linear bladed disk . 77
4.13 A mistuned bladed disk showing the 30 blades for which the anisotropy angles are considered as random variables. 78
4.14 Sobol index for axial displacement w.r.t angle (a) α (b) β and ζ. . . . 80
4.15 Sobol index for tangential displacement w.r.t angle (a) α (b) β and ζ. 81
4.16 Sobol index for radial displacement w.r.t angle (a) α (b) β and ζ. . . 82

5.1 Schematic diagram of fir–tree root joint for (a) *Nominal*, (b) *Max-1* and *Max-2*, (c) *Min-1* and *Min-2*, (d) *Upper*, (e) *Lower*, (f) *Asym-A* and (g) *Asym-B* root geometry variants. 85
5.2 Radial displacement of blade sector for (a) *Nominal* and (b) *Asym-A* geometry variant. 87
5.3 Contact pressure for geometry *Nominal* on (a) lower-left and (b) lower-right fir-tree surfaces normalized w.r.t average contact pressure on upper-left surface. 88

5.4 Contact pressure for geometry *Max–1* on (a) upper-left, (b) upper-right, (c) lower-left, and (d) lower-right fir-tree surfaces normalized w.r.t average contact pressure on upper-left surface of *Nominal* geometry. 89
5.5 Contact pressure for geometry *Lower* on (a) lower-left and (b) lower-right fir-tree surfaces normalized w.r.t average contact pressure on upper-left surface of *Nominal* geometry. 90
5.6 Contact pressure on the lower fir–tree surface for (a) *Asym–A* and (b) *Asym–B* geometry variant normalized w.r.t average contact pressure on upper-left surface of *Nominal* geometry. 90
5.7 Variation in normalised blade tip displacement along (a) axial (b) tangential and (c) radial direction w.r.t orientation of the crystal defined by anisotropy angle α. 92
5.8 Variation in sensitivity to angle ζ for (a) axial, (b) tangential and (c) radial displacement w.r.t orientation of the crystal defined by anisotropy angle α. 93
5.9 Variation in sensitivity to angle β for (a) axial, (b) tangential and (c) radial displacement w.r.t orientation of the crystal defined by anisotropy angle α. 96
5.10 Variation in sensitivity to angle α (a) axial, (b) tangential and (c) radial displacement w.r.t orientation of the crystal defined by anisotropy angle α. 97
5.11 Normalised contact pressure on fir–tree upper right surface of *Asym–A* geometry variant for (a) $\alpha = X$, (b) $\alpha = 9 \times X$, where X is the reference value of α. In the coordinate system for bladed disk, X is the axial, Y is the tangential, and Z is the radial direction. 99
5.12 Residual error in RF model prediction of normalised average contact pressure on (a) left side and (b) right side of the fir–tree. 105
5.13 Residual error in prediction of normalised maximum contact pressure for (a) on left side and (b) on right side of the fir–tree. 106

5.14 Convergence of normalised mean and STD of (a) average contact pressure and (b) maximum contact pressure on left side of fir–tree joint for *Asym-B* variant. 107

6.1 Geometry of bladed disk showing the considered 9 blades with random anisotropy angles. 113
6.2 PCE and gradPCE approximations for (a) axial, (b) tangential and (c) radial displacement at blade tip of blade number one. 114
6.3 Normalised standard deviation of blade tip displacements for non-linear bladed disk. 119
6.4 Convergence of (a) mean and (b) standard deviation of von Mises stress. 121
6.5 Comparison of PDF obtained analytically to those obtained from a linear approximation when the anisotropy angles are distributed as defined for (a) case-2 and (b) case-1. 124
6.6 Comparison of PDFs obtained analytically to that obtained numerically based on FE model evaluations for (a) axial, (b) radial, and (c) tangential displacement when the anisotropy angles have distribution as defined for case–2. 126
6.7 Comparison of PDFs obtained analytically to that obtained numerically based on FE model evaluations for (a) axial, (b) radial, and (c) tangential displacement when the anisotropy angles have distribution as defined for case–1. 127
6.8 Comparison of analytically and numerically obtained PDFs for (a) axial, (b) radial, and (c) tangential displacement when the PDF of anisotropy angles are distributed as in case–2 but with reduced mean and standard deviation for angles α and β compared to the original distribution. 128

7.1 Finite element mesh of a section of the bladed disk model showing the location of the excitation load applied and the node for which blade response is obtained. 130

7.2 Variation in mean value and standard deviation of the frequency of tuned bladed disk with respect to the nodal diameter. 133
7.3 Envelope of forced response of bladed disk for 8EO excitation of frequencies in the range of (a) 1^{rst} mode family and (b) 2^{nd} mode family; 35EO excitation of frequencies in the range of (c) 1^{rst} mode family and (d) 2^{nd} mode family. 134
7.4 A mistuned bladed disk showing (a) 30 blades having random anisotropy angles, (b) 37 blades having random anisotropy angles, and (c) all 75 blades having random anisotropy angles. 135
7.5 Scatter in maximum amplitude of blades in mistuned bladed disks for excitation frequencies in the range of 1^{rst} mode family due to (a) 8EO and (b) 35EO, 2^{nd} mode family due to (c) 8EO and (d) 35EO considering 30 blade anisotropy angles as random variables. 137
7.6 Mean and STD of normalised maximum amplitude of blade for 8EO excitation of (a) 30 blades, (b) 37 blades and (b) all 75 blades having random anisotropy angles. 139
7.7 Mean and STD of normalised maximum amplitude of blade for 35EO excitation for the case (a) 30 blades (b) 37 blades chosen alternatively and (c) all 75 blades having random anisotropy angles. 140
7.8 Histogram for normalised maximum amplitude of bladed disk for 1^{rst} mode family due to (a) 8EO and (b) 35EO excitation, 2^{nd} mode family due to (c) 8EO and (d) 35EO excitation. 141
7.9 Convergence of STD of maximum forced response with number of FE model evaluations for 8EO excitation of frequencies in the range of (a) 1^{rst} mode family, (b) 2^{nd} mode family; and (c) 35EO excitation of 1^{rst} mode family for the case when weight coefficients w_1 and w_2 are different. 146
7.10 Convergence of STD of maximum forced response with number of FE model evaluations for 8EO excitation of frequencies in the range of (a) 1^{rst} mode family, (b) 2^{nd} mode family; and (c) 35EO excitation of 1^{rst} mode family for the case when weight coefficients w_1 and w_2 are equal. 147

7.11 Convergence of mean of maximum forced response with number of FE model evaluations for 8EO excitation of frequencies in the range of (a) 1^{rst} mode family, (b) 2^{nd} mode family; and (c) 35EO excitation of 1^{rst} mode family for the case when weight coefficients w_1 and w_2 are different. 148
7.12 Convergence of mean of maximum forced response with number of FE model evaluations for 8EO excitation of frequencies in the range of (a) 1^{rst} mode family, (b) 2^{nd} mode family; and (c) 35EO excitation of 1^{rst} mode family for the case when weight coefficients w_1 and w_2 are equal. 149
7.13 Convergence of STD of maximum forced response for 8EO excitation of frequencies in the range of (a) 1^{rst}, (b) 2^{nd} mode family, and (c) 35EO excitation of frequencies in the range of 1^{rst} mode family. . . . 154
7.14 (a) Normalised local sensitivity of maximum forced response amplitude of the bladed disk corresponding to 35EO excitation of frequencies in the range of (a) 1^{rst} mode family and (b) 2^{nd} mode family. . . 155
7.15 Sobol indices for maximum forced response amplitude of bladed disk corresponding to 35EO excitation of frequencies in the range of (a) 1^{rst} mode family and (b) 2^{nd} mode family. 156
7.16 Sobol indices for normalised maximum amplitude of bladed disk corresponding to 35EO excitation of frequencies in the range of (a) 1^{rst} mode and (b) 2^{nd} mode family. 157
7.17 Variation in maximum forced response amplitude of bladed disk with optimisation of blade anisotropy angles of the chosen 5 blades using (a) NELDER-MEAD and (b) COBYLA. 160
7.18 Variation in normalised maximum forced response amplitude of bladed disk with respect to optimisation of the blade anisotropy angles of the chosen (a) 5 blades and (b) 38 blades in the bladed disk. 161
7.19 Variation in normalised anisotropy angles (a) α, and (b) β of the chosen five blades with respect to optimisation step. 162

7.20 Variation in normalised maximum forced response amplitude of bladed disk with respect to the optimisation of blade anisotropy angles of the chosen one blade in the bladed disk. 163
7.21 Variation in normalised forced response amplitude of blades with respect to optimisation step number (a) one, (b) eleven, (c) thirteen, and (d) fifteen. 164

List of Tables

2.1 Choice of basis functions 43
2.2 Polynomial basis constituting a 3^{rd} order PCE of a bivariate function and its corresponding multi-index notation 48

5.1 Variation in normalised maximum blade displacements 86
5.2 Variation in maximum contact pressure w.r.t anisotropy angle α . . . 100
5.3 Variation in average contact pressure w.r.t anisotropy angle α 101
5.4 Error estimates for RF model 104
5.5 Statistics of normalised average contact pressure on fir–tree contact surfaces 108

6.1 Variation in normalised blade tip displacement in mistuned bladed disk 111
6.2 Statistics for blade tip displacements obtained from polynomial chaos expansion and MCS 116
6.3 Statistics for blade displacements of a linear mistuned bladed disk . . 117
6.4 Statistics for displacements of a mistuned non-linear bladed disk . . . 120
6.5 Probability distribution of anisotropy angles. 122

7.1 Statistics for amplification factor for response of a linear mistuned bladed disk. 150

List of Abbreviations

CS	Coordinate System
DOF	Degrees Of Freedom
EO	Engine Order
FE	Finite Element
gradPCE	gradient-based Polynomial Chaos Expansion
GSA	Global Sensitivity Analysis
IBR	Integrally Bladed Rotor
LCF	Low Cycle Fatigue
LCO	Limit Cycle Oscillation
LM	Large Mistuning
LSA	Local Sensitivity Analysis
MAE	Mean Absolute Error
MCS	Monte Carlo Simulation
MPC	Multi Point Constraint
MSE	Mean Square Error
ND	Nodal Diameter
NL-ROM	Non-linear Reduced Order Model
PCE	Polynomial Chaos Expansion
PDF	Probability Density Function
RANS	Reynolds Averaged Navier-Stokes
RF	Random Forest
ROM	Reduced Order Model
SI	Sobol Index
STD	Standard Deviation

Nomenclature

α, β, ζ	Crystal anisotropy angles
$\boldsymbol{\sigma}$	Cauchy stress tensor
$\boldsymbol{\epsilon}$	Strain tensor
$\mathbf{S}$	Material compliance matrix
$\mathbf{E}$	Material elasticity matrix
$\mathbf{T}$	Coordinate transformation matrix
$\mathbf{K}$	Global stiffness matrix
$\mathbf{k}^e$	Element stiffness matrix
$\mathbf{F}_{nln}$	Non-linear force vector
$\mathbf{P}$	Static force vector
ξ	Random variable
y	Stochastic function
n	Dimension of random space
p	Order of polynomial chaos expansion
ψ	Polynomial basis function
ρ	Probability density function
E	Young's modulus
ν	Poisson's ratio
G	Shear modulus
l, m, n	Direction cosines
N_{el}	Number of finite elements
N_B	Number of blades in bladed disk
$\mathbf{x}$	Displacement vector
J	Jacobian matrix
σ_V	von Mises matrix
$\mathbf{B}$	Strain-displacement matrix
λ	Eigen value
ϕ	Mode shape
F^S	Excitation load applied over one sector of bladed disk

$S_{i_1 \ldots i_s}$	Partial order Sobol index
S_{T_i}	Sobol total order index
μ	Mean of a probability distribution
σ	Standard of a probability distribution
c	Coefficients in PCE
$\mathbf{D}$	Damping matrix
$\mathbf{M}$	Mass matrix
$\mathbf{X}$	Forced response amplitude
M_t	Set of function evaluations associated with node t of a regression tree
n_t	Number of function evaluation associated with node t of a regression tree
$\mathbb{E}$	Expectation of a random variable
var	Variance of a random variable
w	Weight coefficient

Chapter 1

Introduction

Gas turbine engines used to propel modern aircraft are phenomenally complex machines. Thanks to innovations in the field of material science, fluid and solid mechanics and new capabilities in the field of manufacturing, design, and testing, the efficiency of the gas turbine engine has improved significantly. The three main factors that directly contribute to the overall efficiency of a gas turbine are the pressure rise achieved by the compressor, the temperature of the gas as it enters the turbine and the combustor efficiency [1].

The turbine entry temperature has risen from 1000^0C in the gas turbine engines operated in the 1940s to approximately 1700^0C in those that are currently in service. In addition to efficient cooling, the use of new materials that retain its mechanical properties at very high temperature has contributed to the significant increase in turbine entry temperature over the years. The essential properties required for a material to operate at very high temperature are creep resistance, thermal fatigue strength, and oxidation resistance. Single crystal nickel alloy blade with superior metallurgical properties in all directions was developed by Pratt and Whitney following their success in the development and implementation of directionally solidified blades in the 1960s [2]. These blades were first used in Pratt and Whitney F100 engines that propelled the F-15 and F-16 military aircraft and later in Pratt and Whitney JT-9D engine that powered Boeing 767 and Airbus A310. Today single crystal blades are widely used by all gas turbine engine manufacturers including Rolls Royce and General Electric.

The casting process of single crystal blades is based on directional solidification of the molten metal. Due to certain randomness in the solidification process, it is impossible to manufacture blades with identical crystal orientation. The crystal anisotropy orientation of the blade influences its mechanical properties, and therefore, in a bladed disk the variation in anisotropy orientation between blades results in mistuning of the bladed disk. Due to mistuning, each blade in the bladed disk will deform differently to centrifugal and gas pressure loads acting on the bladed disk.

For a mistuned bladed disk, a significant difference in displacements and stresses between individual blades in a bladed disk is possible. In order to improve the efficiency of gas turbine engines, the clearance between the blades and the turbine casing must be minimised to reduce blade tip leakage. Modern gas-turbine engines use an abradable material seal or honeycomb structure in the outer lining which facilitates the formation of a groove by allowing the blade tip to rub into the material during the initial running of the engine. Even though this technique has proved to be effective in minimizing the radial gap, there are two main concerns associated with it: (i) the possibility of the abradable material sticking to the blades, thereby, inducing turbulence in gas flow, and (ii) the phenomenon of blade wear due to friction between blades and abradable material [3]. However, for a mistuned bladed disk with significant scatter in blade mechanical properties, each blade will have marginally different radial displacement which then precludes the possibility of creating an optimal gap. In this case, the blade with the largest radial displacement will determine the amount of abradable material removed, thereby, creating a suboptimal tip-casing gap for other blades in the bladed disk. To minimise the amount of abradable material removed and to maintain an optimal tip-casing gap for all blades, there is a need to quantify the scatter in static deformation of the mistuned bladed disk due to scattering in the crystal orientation of the blades.

Dovetail root joints (Fig. 1.1a) are commonly used to secure compressor blades to disk, and fir–tree root joints (Fig. 1.1b) are widely used for turbine blades in gas turbines. These joints form a critical region from the point of service life of the bladed disk as higher stress gradients near the edges of the contact could initiate crack growth when the structure is subjected to high frequency-small amplitude

aerodynamic loads. Random errors in manufacturing process introduce variability in the geometry of the blade root and the disk slots. Due to the variability in blade and disk geometry within the tolerance limits, the contact areas at root could be higher or lower than that of the design geometry. This variation in contact area affects the magnitude of contact pressure, and therefore, the contact stresses at the bladed disk root joint. The analysis of bladed disk joints is essential to understand the failure mechanisms involved and to ensure that the life of the joint does not limit the life of the bladed disk. For single crystal blades, the variation in contact pressure at fir–tree roots due to the combined effect of scattering in material anisotropy orientation and variation in root geometry is investigated.

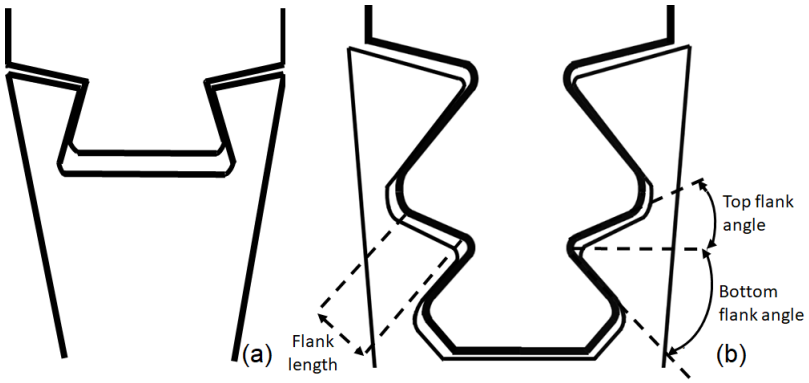

Figure 1.1: Schematic diagram of (a) dovetail joint and (b) fir–tree root joint.

It is well known that a mistuned bladed disk can have drastically higher forced response levels compared to the corresponding tuned bladed disk. The stress levels and vibration amplitude of mistuned bladed disk can be highly sensitive to even small variations in the material properties of the blades within the manufacturing tolerance limits. In order to avoid premature failure of the blades due to higher stress levels resulting from the amplified response of the mistuned structure, it is essential to study the forced response of the bladed disks considering the scattering in anisotropy orientation of the blades.

The overall aim of this research is to perform efficient uncertainty and sensitivity analysis of static and dynamic response of bladed disk structures used in gas-turbine engines considering the crystal orientation of the single crystal blades as random design parameters. Further, the effects of manufacturing variations in the geometry of the bladed disk joints on static deformation of the structure are also investigated.

Finally, the possibility of optimising the blade anisotropy angles in order to minimise the amplification of forced response arising from blade-to-blade variations in crystal orientation is investigated.

1.1 Uncertainty analysis

The uncertainty associated with dynamics of structures is classified into two categories:

(i) *Aleatory uncertainties* - they are due to random variations in material properties and boundary conditions, inaccuracies associated with manufacturing and assembly techniques. In modelling and simulation, this could transfer into parameter uncertainties which require some of the input parameters to be treated as stochastic variables. Random variations in the mechanical properties of dynamic systems can also be due to gradual wear and tear or due to inherent scatter in material properties [4]. For example, blades in a bladed disk are not identical due to random errors in manufacturing and due to uneven wear and tear of blades while in operation. This class of uncertainties can be defined in the probabilistic framework as the associated randomness is often unbiased. Therefore, with the help of numerous experiments, it is possible to obtain the statistical and probability measures for aleatory uncertainties [5].

(ii) *Epistemic uncertainties or systematic uncertainties* - they are due to inaccuracies and simplifying assumptions in modelling. Numerical errors, model errors and model discrepancies are some of the factors that contribute to epistemic uncertainties. The uncertainties in this class are not readily amenable to probabilistic analysis as they are often biased [5].

Parameter uncertainty results in uncertainty in static and forced response of bladed disks. In order to ensure system safety, it is essential that the uncertainty in the response of bladed disks to centrifugal and gas pressure loads experienced at all operating conditions within the flight envelope is accounted in the design. Traditionally, uncertainty analysis using computational models has relied on repeated analysis of the model based on random sampling of the input parameter space, the

Monte Carlo Simulation (MCS) technique. While this is the most straightforward approach for uncertainty analysis and provide accurate estimates of the variation in system response, the convergence obtained using this method is a function of the square root of the number of model evaluations. Therefore, for realistic high–fidelity finite element (FE) models of the bladed disk, cost of uncertainty analysis using the MCS is often prohibitive. The prime mover of research on more sophisticated and efficient approaches for uncertainty has been the computational cost incurred due to slow convergence of the MCS.

Surrogate modelling

Surrogate models provide a close approximation to FE model and are inexpensive to evaluate. Surrogate models are used as an approach to address the high computational cost of uncertainty analysis based on the MCS of high-fidelity computational models. Following are some of the approaches used to construct surrogate models: (i) polynomial regression (ii) polynomial chaos (iii) kriging and (iv) supervised learning methods such as Random Forest (RF), support vector machines and artificial neural networks. Two of the above approaches for surrogate modelling namely polynomial chaos and random forest algorithm will be discussed in detail in this section.

Random Forest

The structure of the input parameter space is one of the deciding factors in the choice of surrogate models. When the input parameter space is n dimensional real space, the choice of polynomial chaos or kriging is recommended. For situations when the input parameter set includes both categorical[‡] and continuous variables RF[6] is a viable option. RF is a predictive model constituted by an ensemble of binary regression trees. A regression tree divides the input parameter space into distinct and non-overlapping regions where the dependent variable is approximated by a constant value. The input-output data obtained from FE model realisations are randomly partitioned into a training set and test set. In order to train the RF

[‡]Categorical variable takes one of a limited number of possible values assigning each observation to a particular category.

model, each regression tree in the ensemble is trained on a random subset of the training data where the subset is obtained by random sampling with replacement. The predictions from individual regression trees are then aggregated by averaging. This so–called bagging* procedure significantly reduces the variance in prediction associated with individual regression trees. The performance of the RF model is validated using data in the test set. RF methods have been applied with varying degree of success to regression and classification problems arising in different fields ranging from turbulence modelling [7] to medical prognosis [8].

Polynomial chaos expansion

Polynomial chaos expansion allows representing an arbitrary random variable as a function of another random variable or a set of random variables, for which the distribution is known, in the form of a polynomial expansion [9]. Therefore, the main feature of polynomial chaos expansion, introduced by Wiener [10], is the decomposition of the stochastic response of a system into a linear combination of deterministic and stochastic components:

$$y = \mathcal{M}(\mathbf{X}) = \sum_{j=0}^{\infty} c_j \psi_j(\boldsymbol{\xi}) \tag{1.1}$$

where y is the model output such as displacements at a node on a FE model, $\mathcal{M}$ is the computational model and $\boldsymbol{X}$ is a vector of input parameters, some of which are stochastic variables and others are deterministic. The stochastic component in the PCE is constituted by the orthogonal polynomial basis, $\psi_j(\boldsymbol{\xi}) : j = \{0, \ldots, \infty\}$, that are functions of random variables, $\boldsymbol{\xi} \subset \{\xi_1, \ldots, \xi_n\}$, with known probability distribution and the deterministic components are the coefficients, c_j, in the expansion. The polynomial bases are orthogonal with respect to the joint probability density function of the random variables. The original polynomial chaos proposed by Weiner is based on Hermite polynomials in terms of Gaussian random variables. Cameron and Martin [11] proved that Weiner's Hermite polynomial chaos approximation of any function that is square integrable has convergence in the $\mathbf{L}^{2\dagger}$ sense.

*Bagging or bootstrap aggregating is based on random sampling with replacement which allows generating new training sets of size s' from the original training set of size s. The model is fitted for each of the new training set and are combined by averaging the output of each model.

†$\mathbf{L}^2$ norm of a function $f(x)$ is defined as $|f(x)|^2 \equiv \int |f(x)|^2 \mathrm{d}x$

This result implies that a second order random process, meaning that the variance of the process is bounded, can be expanded as a Hermite polynomial chaos[12]. The computational cost associated with constructing a PCE is associated with the calculation of coefficients in the expansion. The different approaches used to calculate coefficients in the PCE are classified into two: (i) *intrusive* and (ii) *non-intrusive*.

(i) *Intrusive* - The approach uses Galerkin projection of PCE on the governing equations which in most cases are differential equation describing the response of the structure under load to obtain a system of equations of the form[9]

$$\langle \mathcal{M}(y(t), x), \psi_k \rangle = 0 \text{ for } k = 0, \ldots, P \tag{1.2}$$

where $\mathcal{M}(y(t), x)$ is the simulation model that solves the governing differential equation to obtain the response y as a function of space and/or time. When the governing equations are not complicated, it is possible to derive the expression for the inner product in Eqn. (1.2) analytically after approximating y as a polynomial chaos expansion of order p, i.e. $y = \sum_{j=0}^{P} c_j \psi_j$. Thus $P + 1$ differential equations can be obtained which must be solved for $P + 1$ unknown expansion coefficients in PCE where $P = (n + p)!/n!p!$, n being the number of random variables and p the order of the polynomial basis. The solution of the modified set of equations requires modification of existing solver or a new program that solves the new set of $p + 1$ differential equations. The practical difficulty associated with modifying FE solvers has limited the use of intrusive methods.

(ii) *Non-intrusive* - Contrary to intrusive method, non-intrusive methods treat the solver as a black-box. The different non-intrusive methods used to calculate the unknown coefficients in PCE are:

(1) Method of least squares: The idea behind the method of least squares, as used in model parameter estimation, is to minimise the sum of squares of the deviation of the approximation from results obtained by numerical or physical experiments. Applying this method to calculate the coefficients in PCE requires N evaluations of the computational model based on the sampling of the input parameter space. This provides us a set of data points of random input parameters, $\{\boldsymbol{\xi}_i\}_{i=0}^{N}$ and corresponding model output, $\{y_i\}_{i=0}^{N}$ where the coefficients in expansion can then

be obtained:

$$\min_{\boldsymbol{c}\in\mathbf{R}^{(P+1)}} \|\boldsymbol{\Psi}(\boldsymbol{\xi})\boldsymbol{c}-\mathbf{y}\|_2 \tag{1.3}$$

where, $\boldsymbol{\Psi}=\{\psi_0,\ldots,\psi_P\}$ is the orthogonal polynomial basis set, $P+1$ is the number of unknown coefficients in the expansion; $\boldsymbol{c}=\{c_0,\ldots,c_P\}^{\mathrm{T}}$ and $\mathbf{y}=\{y_0,\ldots,y_N\}^{\mathrm{T}}$ are the vector of unknown coefficients and of function values obtained from N number of FE model evaluations respectively. The optimal solution for the problem is obtained as $c^*=(\Phi^{\mathrm{T}}\Phi)^{-1}\Phi^{\mathrm{T}}\boldsymbol{y}$, provided $(\Phi^{\mathrm{T}}\Phi)^{-1}$ is invertible. The number of terms in a PCE of order p that approximates a multivariate function of n random parameters is given by the formula $(n+p)!/n!p!$. As the dimension of the random space increases, the number of terms in PCE increases at a rate faster than that of exponential growth, and therefore, results in the so-called *curse of dimensionality* problem. One approach to address this issue is to use the gradient of the multivariate function w.r.t input parameters in creating the approximation[13]. This approach will be discussed at length in the following chapter. For the problem of creating PCE to approximate a multivariate function with many random variables, special sampling approaches can also be used to reduce the computational cost [14].

(2) Stochastic collocation: The coefficients for PCE are calculated such that the approximation error is reduced to zero at sample points chosen based on the sampling of the input parameter space. The approximation at chosen points in the input parameter space can be reduced to zero by equating the predicted value of the dependent variable to its value at those points in the stochastic space obtained from FE evaluations. A set of N linear algebraic equations are obtained from N FE evaluations which can be solved to obtain the unknown coefficients, $\boldsymbol{c}$ in the PCE:

$$[\Psi(\boldsymbol{\xi})]_{N\times(P+1)}\{\boldsymbol{c}\}_{(P+1)}-\{\mathbf{y}\}_N=0 \tag{1.4}$$

where, $P+1$ is the number of unknown coefficients in the expansion, $\Psi(\boldsymbol{\xi}_i)$ is the orthogonal polynomial basis, and $\boldsymbol{\xi}_i\in\{\boldsymbol{\xi}_1,\ldots,\boldsymbol{\xi}_N\}$ is the vector of design parameters obtained by sampling the input parameter space.

(3) Spectral projection: This method calculates the expansion coefficients in PCE approximation by imposing the requirement that the approximation error, $(y-\sum_{j=0}^{p} c_j\psi_j)$ is orthogonal to the span of polynomial basis [15, 16]. Since the polynomial basis in the expansion are orthogonal, the coefficients in the expansion can be

obtained from the expression below:

$$\left\langle (y - \sum_{j=0}^{p} c_j \psi_j), \psi_k \right\rangle = 0 \Rightarrow c_j = \langle y, \psi_j \rangle = \int_{\Omega} y \psi_j \rho(\boldsymbol{\xi}) dx \tag{1.5}$$

The integrals in Eqn. (1.5) can be evaluated using Monte Carlo method or using quadrature rules.

1.2 Sensitivity analysis

There are several reasons for performing sensitivity analysis one of which is to identify factors or groups of factors that contribute to uncertainty in model output [17]. Sensitivity analysis is not a replacement for uncertainty analysis but rather complements it and is often used to reduce the computational cost associated with the latter by reducing the dimensionality of the problem. The methods available for sensitivity analysis are broadly classified into two (i) Local Sensitivity Analysis (LSA) and (ii) Global Sensitivity Analysis (GSA).

(i) **Local Sensitivity Analysis (LSA)** - Local sensitivity analysis essentially involves the computation of the derivatives of the model response function w.r.t the input parameters. For a structural component constituting a machine, the derivative of its response under loading with respect to a design parameter gives information on how design changes affect the static and vibration response of the structure about the design point at which the derivative is evaluated. Consider the governing equation of motion for a m degrees of freedom (D.O.F) linear system in the descretized form:

$$\mathbf{K}(\mathbf{r},\mathbf{x})\mathbf{u}=\mathbf{P} \tag{1.6}$$

where $\mathbf{K}$ is the global stiffness matrix, $\mathbf{u}$ and $\mathbf{P}$ are the m-dimensional displacement and load vector respectively, $\mathbf{r}$ is the vector of stochastic input parameters and $\mathbf{x}$ is the vector of deterministic variables that defines the system in the m dimensional state-space. The above finite element (FE) equation can be solved to obtain the state variable $\mathbf{u}$. The system response function $V(\mathbf{r},\mathbf{x})$ is defined as a function of $\mathbf{u}$:

$$V(\mathbf{r},\mathbf{x}) = F(\mathbf{u}(\mathbf{r},\mathbf{x}),\mathbf{x}) \tag{1.7}$$

The objective of LSA is to obtain the derivative, or sensitivity, of V w.r.t the stochastic input parameters as below,

$$\frac{dV}{d\mathbf{r}} = \frac{dF}{d\mathbf{u}}\frac{d\mathbf{u}}{d\mathbf{r}} \tag{1.8}$$

To evaluate the sensitivity of response function from Eqn. (1.8), when $\mathbf{u}$ is not defined explicitly as a function of $\mathbf{r}$, following methods can be used [18]:

(1.) *Finite difference method*: This method is based on Taylor series expansion of the output function. It is comparatively easy to implement but often results in high computational cost and low accuracy of the sensitivity values. Based on the forward–difference method, the sensitivity of system response V w.r.t design parameter r_i is:

$$\nabla_i V(\mathbf{r},\mathbf{x}) = \frac{(V(\mathbf{r}+\Delta\mathbf{r},\mathbf{x}) - V(\mathbf{r},\mathbf{x}))}{\Delta r_i} + O(\Delta r_i) \tag{1.9}$$

where $V(\mathbf{r}+\Delta\mathbf{r},\mathbf{x}) = F(\mathbf{u}(\mathbf{r}+\Delta\mathbf{r},\mathbf{x}),\mathbf{x})$, $\Delta\mathbf{r} = \{0,\ldots,\Delta r_i,\ldots,0\}$ and the truncation error is of the order $O(\Delta r_i)$. Here the displacement vector, $\mathbf{u}(\mathbf{r}+\Delta\mathbf{r},\mathbf{x})$ can be obtained by solving the following descritized equation using an FE solver:

$$\mathbf{K}(\mathbf{r}+\Delta\mathbf{r},\mathbf{x})\mathbf{u}(\mathbf{r}+\Delta\boldsymbol{r}) = \mathbf{P} \tag{1.10}$$

Therefore, for each parameter in $\mathbf{r}$, the sensitivity analysis using finite difference requires one FE model evaluation. For n dimensional random space of design parameters, the total number of FE evaluations is $n+1$ which makes the method computationally expensive.

(2.) *Direct differentiation method*: To calculate sensitivity using the direct differentiation method, the first step is to evaluate the derivative $\frac{d\mathbf{u}}{d\mathbf{r}}$, for which we differentiate Eqn. (1.6) with respect to each parameter in the input parameter set:

$$\frac{d\mathbf{K}}{dr_i}\mathbf{u} + \mathbf{K}\frac{d\mathbf{u}}{dr_i} = \frac{d\mathbf{P}}{dr_i} \tag{1.11}$$

which can be rearranged to the form

$$\mathbf{K}\frac{d\mathbf{u}}{dr_i} = \frac{d\mathbf{P}}{dr_i} - \frac{d\mathbf{K}}{dr_i}\mathbf{u} \quad \text{for } i = 1,2,\ldots,n \tag{1.12}$$

where n is the number of random parameters in the input parameter set w.r.t which the sensitivities are calculated. Note that the above equation is of the similar form as Eqn. (1.6), and therefore, solved for $\frac{d\mathbf{u}}{dr_i}$ with little additional cost once the $\mathbf{K}^{-1}$ matrix is obtained as a by–product of solving Eqn. (1.6). This process must be repeated for each of the n random parameters. Once all the components in the vector $\frac{d\mathbf{u}}{d\mathbf{r}}$ are obtained, the sensitivities for the response function V can be calculated from Eqn. (1.8).

(3.) *Semi-analytical method*: The semi-analytical method combines the finite difference method and the direct differentiation method in an attempt to find a trade-off between the ease of implementation of the former and the accuracy and efficiency of the latter. In this method, the derivatives, $\frac{dK}{d\mathbf{r}}$ and $\frac{dP}{d\mathbf{r}}$ are calculated using the finite difference method and the sensitivities are calculated using the direct differentiation method.

(ii) **Global sensitivity analysis (GSA)** - A sensitivity analysis method must preferably be able to take into account the interaction effects among input uncertainties and provide an estimate for the influence of input parameters irrespective of the linearity or additivity properties of the model [17]. LSA does not account for interaction effects of input parameters and is performed at a chosen design point in the domain of variation of the input parameter. Therefore, in many cases, LSA does not provide sufficient information regarding the effect of variations in design parameters on system response over the whole domain of possible design parameter variations. GSA can be classified into following two groups [19, 20]: (i) regression based methods such as Pearson or Spearman correlation coefficient which is suitable for linear (Pearson) or monotonic (Spearman) models and, (ii) variance based techniques such as Fourier Amplitude Sensitivity Analysis (FAST) [21] and Sobol' indices [22]. Among the two classes of methods, variance–based methods have both the attributes mentioned above required of an ideal sensitivity analysis method. The idea of variance decomposition methods is to partition the output variance into contributions from each of the input parameters. Variance decomposition based methods are useful to identify the subset of the input parameters that

contribute significantly to output variance [23]. This information can also be used to reduce the dimensionality of the input parameter space, and therefore, the computational cost of uncertainty analysis.

1.3 Survey of existing literature

A considerable amount of research exists that investigates the deformation of bladed disk structures under static and dynamic loading conditions. It is almost impossible to mention all the works that have been done to date though every effort has been taken to include those relevant to the present study.

In this section an attempt is made to collect and review relevant works that can be found in the open literature on the following four topics:

i. Analysis of the deformation of the fir–tree root joints and the effects of variations in fir–tree geometry on deformation of bladed disks.

ii. Effects of crystal orientation on mechanical properties of single crystal blades.

iii. Uncertainty and sensitivity analysis of mechanical systems focussing on gas turbine engines.

iv. Intentional mistuning of the bladed disk.

1.3.1 Analysis of the deformation of fir–tree root joints

In a bladed disk assembly, the blade–disk joint constitutes the most critical load path, and therefore, a detailed analysis of the stresses in the region close to disk slot is necessary for the lifetime certification of gas turbine disk [24]. Several studies that investigate the deformation and stresses at blade–disk joints are available in the literature for both dovetail and fir–tree joints [25–31]. There are also several studies investigating the effects of fir–tree geometry on stresses developed in the turbine disk. Meguid et al. [24] studied the effect of variation in certain key geometric features of the fir–tree, such as the number of teeth, flank angle and flank length, on von Mises stresses at disk slot. Different studies exist in the literature that optimises the fir-tree joint geometry in order to reduce the stresses developed in the

joint [8, 32–35].

Due to the inherent randomness in the manufacturing process, it is impossible to eliminate the variability in the geometry of the blade root and the disk slots. While the geometry of fir-tree root joint in the design geometry of bladed disks is often optimised for minimum stresses in the vicinity of the joint, the deviations from design geometry result in a suboptimal contact area between blade and disk. This variation in contact area affects the magnitude of contact pressure, and therefore, the contact stresses at the bladed disk root joint. Zboinski [36], while investigating the effects of deviation in fir–tree root joints of bladed disks under static load, found that manufacturing deviations can significantly change the contact stresses and concluded that neglecting the deviations in geometry can result in erroneous estimation of the contact stresses on fir–tree joints. Deshpande et al. [37] addressed the issue of variation in geometry of fir–tree tooth by parametrising the geometry using parametric CAD models. Qin et al.[38] studied the effect of geometry mismatch in fir–tree joints on the natural frequency of blade by varying the surfaces where contact or gap exists. From the survey of existing literature, it is evident that small manufacturing variations in the fir–tree geometry can have significant influence on the static deformation and stresses of bladed disk.

1.3.2 Effects of crystal orientation on mechanical properties of single crystal blades

The nickel–based alloy blades in high–pressure turbine stages of modern gas turbine engines are often monocrystalline, and the crystallographic orientation of the monocrystal relative to the blade geometry influences the mechanical properties of the blades [39–42]. The scatter in crystal orientations due to inaccuracies in the casting process of single crystal blades results in the scatter in material properties of the blades. For designing a robust bladed disk, it is vital to quantify the effects of uncertainty in crystal orientations on deformation of the structure under different operational loads. For a mistuned bladed disk, with scattering in blade properties due to unavoidable inaccuracies in casting, a significant difference in displacements and stresses between individual blades in a bladed disk is possible.

McKay and Maier [42] studied the influence of crystal orientation on the stress rupture properties of nickel-based superalloy single crystals. They reported that crystals oriented in a region just a few degrees off the crystal lattice direction [001]† exhibited inferior stress rupture properties compared to those of crystals aligned approximately with [001] axis (see Fig.1.2). The influence of anisotropy orientation on stress rupture life was found to be higher at elevated temperature. Arakere and Swanson [39] developed a fatigue failure criteria for single crystal blades and proposed a fatigue life equation for turbine blades subjected to low cycle fatigue (LCF). Further, using FE stress analysis and the fatigue life equation, they studied the effects of variation in the primary and secondary orientation on fatigue life at critical locations of the blade. More investigations on the influence of crystal orientation on thermomechanical and fatigue behaviour of single-crystal alloys are available in the literature [43–50]. Weiss et al.[51] investigated the effects of crystal orientation on LCF and creep damage based lifetime of monocrystal blades using probabilistic finite element analysis based on Monte-Carlo-Simulation (MCS) techniques.

Few investigations on the effects of blade material anisotropy orientations on the static and dynamic response of the blades are available in the literature. Kaneko [52], Manetti et al.[53], and Wen et al.[54] investigated the effects of variation in crystal orientation on natural frequencies of blades. In his study, Kaneko [52] used a simplified geometry to model the blade, and the results indicated that the variations in three orientation angles, defining the crystal orientation, has different effects on natural frequencies of the blade. He observed that an increase in primary angle, α (Fig. 1.2), results in (i) an increase in natural frequency in the lower vibration modes and for bending modes along the blade height and (ii) a decrease in natural frequency for torsion modes. Further, he reported that the variation in secondary angle, ζ, does not affect natural frequency of lower vibration modes and is significant only for bending modes along the blade chord. Wen et al. [54], while investigating the influence of crystal orientation on vibration characteristics of turbine blades observed similar behaviour. They observed that the effect of the secondary angle on lower mode frequencies is negligible when the primary axis is aligned with the blade

†Miller indices for a direction in the cubic lattice is represented as [u v w] where u, v, w are projections of the direction vector on the cell edges represented as [100], [010] and [001] respectively.

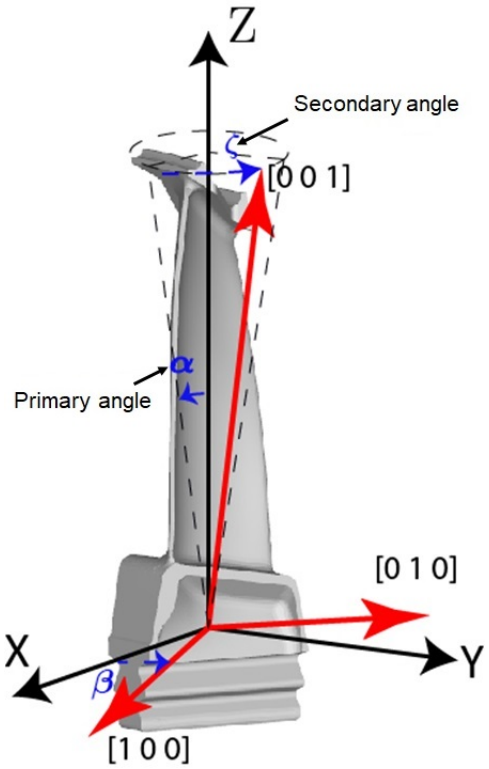

Courtesy: MTU Aero Engines AG

Figure 1.2: Crystal anisotropy angles for single crystal blades.

geometry axis. Also, the primary angle was found to have a significant influence on lower mode frequencies whereas the secondary angle influenced the higher mode frequencies. Kaneko et al. [55] studied the sensitivity of frequency response of mistuned bladed disk with respect to anisotropy axis orientation. Sensitivity derivatives of the blade alone natural frequency with respect to elastic constants and crystal angles were obtained through finite element analysis and response surface for blade natural frequency was generated using sensitivity derivatives. Monte Carlo simulation using the surrogate model was used for frequency response analysis to obtain statistical characteristics of vibration response with respect to variation of material constant and crystal angles. Using the same methodology, Kaneko et al. [56] studied the effect of mistuning due to scattering in material constants and crystal angle on resonant response and random response of bladed disk. Savage [57] investigated the effects of crystal orientation on elastic stresses in single crystal blades. He observed that for a primary angle of 10°, depending on the location of the primary axis in the plane normal to that axis, the stress at turbine blade root was found to vary between 9.7% and -19%. Fang and Li [58] studied the dynamic response properties

of single crystal blades for two different orientation of crystal axis under different rotor speeds. Zhang et al. [59] investigated the effect of crystal orientation on the mechanical response of turbine blades using a non-linear FE model. Further, they created a surrogate model with which they optimised the crystal orientation of the blade with respect to shear stress and displacement at critical blade locations.

1.3.3 Uncertainty and sensitivity analysis

Uncertainty analysis (UA) often requires numerous evaluations of computational models based on the sampling of input parameter space. The computational cost of UA using conventional Monte Carlo methods are prohibitive when using high–fidelity FE models. Therefore, in order to perform UA, the use of computationally inexpensive surrogate models that can closely approximate the FE model is imperative. The structure of the input parameter space is one of the deciding factors in the choice of surrogate models. For situations when the input parameter set includes both categorical and continuous variables, random forest (RF)[6] is a viable option. RF is constituted by an ensemble of regression trees which are peace-wise continuous models. Regression trees partition the input parameter space into smaller regions where the output function can be approximated by simple models. The approximate value of the function in the input parameter space is obtained by combining the output of individual regression trees by averaging. Ling and Templeton [60] investigated the use of three different data-driven algorithms including RF and support vector machines [61] to identify regions in a fluid flow where the inaccuracy of Reynolds Averaged Navier Stokes (RANS) models are high. They concluded that data–driven algorithms provided a substantial improvement over conventional error detection methods and showed the performance of RF based model to be superior in detecting flow regions of high RANS simulation error compared to the other algorithms used. Trehan et al. [62] used RF–based regression to model the error introduced by reduced order models of parametrised dynamical systems. The possibility of using data-driven algorithms such as RF for uncertainty analysis to avoid MCS and using high-fidelity FE models has not been explored rigorously in the existing literature.

Polynomial chaos expansion (PCE) based surrogate models have been studied extensively because of its usefulness in quantifying uncertainty in dynamic systems

[63, 64]. The main feature of PCE is the decomposition of stochastic function into a linear combination of deterministic and stochastic components. The computational effort in obtaining PCE is associated with the calculation of coefficients in the expansion based on numerous evaluations of the deterministic computational model. Panunzio et al. [65] used PCE to study the effects of uncertainty in the tip-casing gap on non-linear normal modes of turbine blades. Considering the modal stiffness of blades as random variables, Sinha [66] obtained the statistics of forced response for mistuned bladed disks using PCE.

Local sensitivity analysis cannot efficiently capture the higher order interaction between different input parameters if it exists in the model. Therefore, for sensitivity analysis of non-linear, non-additive models global sensitivity analysis (GSA) is recommended [67]. The objective of GSA is to quantify the variation in system output with respect to variations in input parameters over the entire domain of variation. There is a subclass of GSA methods known as variance decomposition. The idea behind variance decomposition methods is to partition the output variance into contributions from each of the input parameters. The variance decomposition method includes methods such as Fourier Amplitude Sensitivity Analysis and Sobol' indices [22]. Kala and Vales [67] used Sobol indices to study the influence of initial geometric imperfections and residual stresses on lateral-torsional buckling resistance of I-beams. To reduce the computational cost involved in calculating Sobol indices using conventional Monte Carlo Simulation (MCS), they used a polynomial approximation of the output. Hesse et al. [19] used Sobol indices to identify important design parameters that influence the maximum deformation of an automotive structure in order to reduce the complexity involved in designing the structure for crashworthiness. They used a response surface approximation based on support vector machines to reduce the computational cost involved in calculating Sobol indices using MCS. Sudret [68] derived expressions for calculation of Sobol indices analytically from the expansion coefficients of PCE. While performing uncertainty analysis of a coupled flow-thermo-mechanical model of a low–pressure turbine rotor of gas turbine engines, Antinori et al. [69] used Sobol indices to reduce the dimensionality of the input parameter space by identifying most influential design parameters in the secondary air system of the aircraft engine.

The uncertainty and sensitivity analysis of bladed disk structures can be grouped into the following three categories: (i) uncertainty and sensitivity analysis of the linear mistuned bladed disks, (ii) uncertainty and sensitivity analysis of the non-linear mistuned bladed disks, and (iii) uncertainty and sensitivity analysis of the non-linear tuned bladed disks. A literature review for each of the three categories of uncertainty and sensitivity analysis of bladed disk is presented here.

(i.) *Uncertainty and sensitivity analysis of linear mistuned bladed disks*: One of the first investigations focussing on the statistics of forced response for the mistuned bladed disk is by Griffin and Hoosac [70]. Wei and Pierre [71] studied the response of nearly cyclically symmetric assemblies of mono-coupled single-mode blades. The effects of random mistuning on the forced response of bladed disk was investigated using a statistical study of the forced response considering the modal properties of blades as random variables. The investigation on the parameter sensitivity of the forced response of bladed disk showed that, while for tuned systems the maximum amplitude across the assembly steadily decreases as the coupling between blades increases, for mistuned systems, the amplitude peaks in weak coupling zone before reducing as the coupling strength increases.

Statistical analysis using FE based reduced order models (ROM) of the mistuned bladed disk is a popular approach. Avalos and Mignolet [72] studied the effect of variability in blade–disk interface properties on the forced response of bladed disks using Monte Carlo simulation. A blade-interface-disk model was developed by combining substructuring with local modelling of the interface. They randomised interface mass and stiffness matrices using non-parametric stochastic modelling. It was observed that the combination of mistuning resulting from scattering in blade–disk interface characteristics and blade natural frequencies gives higher amplitude factors compared to that obtained due to scatter in blade natural frequency alone. Beck et al. [73] studied statistics of the mistuned response of Integrally Bladed Rotor (IBR). A reduced order model using component mode synthesis was used in Monte Carlo simulation to obtain the distribution of mistuning response. Two different methods namely nominal method and geometric method were used to

simulate mistuning. While the nominal method alters the modal stiffness but not mode shapes, the geometric method perturbs both frequency and mode shapes. Statistics of mistuned forced response was obtained at three different frequency ranges using 1000 IBRs, each investigated using the nominal and geometric method. They concluded that the accuracy of the nominal method decreases for higher frequencies. Myhre et al. [74] investigated the effect of blade–to–blade coupling and rotation speed on maximum amplitude of a mistuned bladed disk. He obtained statistics for maximum amplitude using Monte Carlo simualtion of a ROM.

Joshi and Epureanu [75] studied statistical effects of damping variability on the steady–state response of an IBR. A generalized component mode mistuning method was developed to capture damping variability. Mistuning due to damping was simulated as scatter in structural damping coefficients amongst the blades. Scattering in blade amplification factor was computed using MCS of numerous random damping patterns. D'Souza and Epureanu [76] used component mode mistuning model to study uncertainty in forced response of multi–stage bladed disks. Mistuning was simulated as scatter in stiffness among each sector of a stage with each stage mistuned differently from the adjacent stage. To investigate the effects of mistuning a reduced order model of the two–stage rotor with a different number of blades was analysed for numerous mistuning patterns of each stage. It was found that an increase in mistuning level increased the amplification factor of the multi–stage system. Laxalde and Pierre [77] proposed a stochastic reduced order modelling technique for the uncertainty analysis of multi–stage mistuned bladed disk. Vishwakarma and Sinha [78] used a high–fidelity reduced order model to obtain the statistics for normalised maximum amplitude of the forced response of bladed disk with geometric mistuning. Peiyi and Li [79] investigated the effect of design parameters defining blade–to–blade coupling and strength of mistuning on natural frequency of bladed disk using a lumped parameter model. They concluded that the vibration amplification can be reduced by choosing an optimum coupling strength and mistuning strength.

Sinha [66] estimated forced response statistics of the bladed disk correspond-

ing to random scatter in blade stiffness using PCE. He introduced mistuning in the model using random deviations in blade stiffness. The amplitude of steady–state response was expanded using PCE. A set of linear algebraic equations was formed using a non-intrusive method which was then solved for deterministic PCE coefficients. Tan et al. [80] studied forced response sensitivity to mistuning introduced by perturbing mass matrix. Sine and cosine functions of different harmonics were used as shape functions to generate a response surface for maximum blade amplitude as a function of blade mistuning using known values of response amplitudes and their first and second order sensitivities.

Hohl et al. [81] used reduced order modelling which combines component mode synthesis and wave–based sub-structuring in Monte Carlo simulations. Mistuning was introduced by varying fixed interface blade frequencies. Wave–based sub-structuring reduces the number of coupling degrees of freedom of the substructures. An optimisation procedure based on maximum amplitude was developed to find the best and the worst case blade patterns. Bah et al. [82] used a stochastic reduced basis method, which approximates the response of bladed disk using stochastic basis vectors, for statistical analysis of the forced response of mistuned bladed disks. They introduced mistuning as variation in the stiffness matrix. Liao et al. [83] determined maximum amplitude with respect to different mistuning patterns by formulating an optimisation problem. Two lumped parameter models of the bladed disk with 2 DOF and 3 DOF per sector with mass and stiffness mistuning was studied. A hybrid approach using Genetic Algorithm and Sequential Quadratic Programming algorithm was used to solve the optimisation problem. Raeisi and Ziaei-Rad [84] obtained the worst mistuning pattern in terms of forced response amplification by combining artificial neural network and genetic algorithm.

Bhartiya and Sinha [85] used a reduced order model based on modified modal domain analysis which relies on proper orthogonal decomposition and allows modelling of the mistuned bladed disk in the presence of simultaneous variations in mass and stiffness matrices. Mistuning patterns were generated from random permutations of blades in an integrally bladed disk. Using the reduced

order model, they investigated the effect of mistuning due to variation in blade frequencies alone and due to simultaneous variation in blade frequency and mode shapes on forced response of the bladed disk. Rahimi and Ziaei-Rad [86] studied uncertainty in forced response of the mistuned bladed disk by representing it based on a relationship between the tuned and mistuned system. Genetic Algorithm was used to solve an optimisation problem to find the worst-case response of bladed-disk assembly. A lumped mass model of the bladed disk with 2 DOF per sector was used to study the effect of intentional mistuning and rearrangement of blades on maximum amplitude response.

Yuan et al. [87] proposed a computationally efficient stochastic analysis of bladed disk. The method addressed the limitation of the MCS that it cannot yield small failure probabilities with a reasonable number of sample evaluations. Subset simulation technique was used to reduce the number of evaluations required to compute small failure probabilities using MCS. A stochastic analysis was performed on the lumped parameter model of the bladed disk to obtain the probability density function of maximum amplitude due to stiffness mistuning. Bhartiya and Sinha [88] studied the statistics of forced response amplitude and natural frequency of multi–stage rotor with geometric mistuning. A reduced order model (ROM) using tuned modes from finite element sector analysis was developed for a multi–stage rotor. The thickness of the blade was varied to introduce geometric mistuning. Monte Carlo simulation using ROM was performed to obtain the statistics of natural frequency and forced response with respect to numerous random permutations of the mistuning pattern.

Yuan et al. [89] proposed a novel hybrid Neumann expansion method for stochastic analysis of the bladed disk. The Neumann expansion coupled with matrix factorization was used to circumvent the requirement for direct inversion of uncertain dynamic stiffness matrix in stochastic finite element method which incurs a high computational cost. The stochastic analysis was performed to model uncertainty in frequency response due to perturbation in the mass or stiffness matrix. Nikolic, Petrov and Ewins [90] studied the effectiveness of large mistuning (LM) concept in reducing the forced response of the

bladed disk. Statistics of forced response for mistuned patterns, drawn randomly from a uniform distribution, was obtained using MCS. Several carefully chosen mistuning patterns based on LM concept was studied for their sensitivity to small unavoidable random mistuning. An improvement in maximum forced response robustness was obtained using LM patterns.

Chan and Ewins [91] proposed a procedure to estimate the probability of extreme vibration levels, i.e. rare probability events, due to mistuning. Optimisation based on the conjugate gradient method was used to find the maximum response and associated worst mistuning pattern. The probability of encountering forced response beyond a threshold value was evaluated using importance sampling. The number of experiments required to evaluate extreme vibrations levels was reduced to a fraction of that used by direct MCS. Cazenove et al. [92] used the one-step-at-a-time method, i.e., for each numerical experiment only one input parameter is perturbed to study the forced response of mistuned bladed disk. The sensitivity of forced response to Young's modulus, modal damping ratio and aeroelastic coefficients were investigated. To introduce geometry mistuning a fringe projection 3D scanner was used to scan the geometry of an industrial bladed disk. In order to reduce a large number of response computations needed for sensitivity analysis a ROM was used.

(ii.) *Uncertainty and sensitivity analysis of non-linear mistuned bladed disks*: Cha and Sinha [93] studied the statistical characteristics of a frictionally damped, mistuned bladed disk when subjected to white noise and narrowband excitations. They proposed an analytical method to calculate the variance in the response of friction damped bladed disk subjected to random excitation. Equivalent linearization method which is an approximation to replace nonlinear terms by linear ones that minimise the error between the two methods was used. Random scatter in blade stiffness was used to introduce mistuning in the model. Two types of friction dampers were modelled; (a) due to the blade to ground contact and (b) due to the blade to blade contact. For white noise excitation, it was observed that mistuning does not affect the response significantly for the blade to blade damper models compared to the blade to ground

damper models. Capiez-Lernout et al. [94] developed a mean computational model of the tuned bladed disk using FEM accounting for nonlinearity due to large displacements. Non-linear reduced order model (NL-ROM) of the tuned structure was obtained using proper orthogonal decomposition method. Mistuning was introduced by replacing operators of mean NL-ROM with random operators whose probability distribution is obtained using the maximum entropy principle. The modified model was used to perform MCS and to obtain uncertainty in the response of the integrally bladed disk.

(iii.) *Uncertainty and sensitivity analysis of non-linear tuned bladed disks*: Petrov [95] derived expressions for first and second order sensitivity coefficients of forced response, of strongly nonlinear structures, from the nonlinear multi–harmonic equation of motion. For the forced response, a set of coupled nonlinear equations was solved simultaneously using Newton-Raphson iteration. General expressions for sensitivity with respect to parameters of nonlinear interaction forces at contact interfaces, such as friction coefficient, interference and clearance values and stiffness coefficients were derived. Also, expressions for sensitivity with respect to variation in linear components in the structure such as mass, stiffness and damping values were derived in addition to those for variation with respect to excitation frequency and excitation forces.

The analytically derived expression allowed the efficient computation of sensitivity coefficients. Further reduction in the computational cost was achieved because the Jacobian matrices required for the calculation of sensitivity coefficients could be obtained as a by-product of the Newton Raphson iteration procedure. The study on the sensitivity of forced response of bladed disk with friction interface at shroud contact showed that forced response become sensitive to interference value and friction coefficient in the vicinity of resonance peak with sensitivity coefficients with respect to interference value being significantly higher. A similar study to elucidate the effect of under-platform damper parameters, such as damper mass, friction coefficient and damper location on forced response vibration showed that the sensitivity to these parameters is most evident near resonance peak. Also, the sensitivity of forced response with respect to damper mass was found to be higher than for damper

radius and friction coefficient.

In Ref.[96], Petrov studied the sensitivity of the steady–state limit cycle oscillations (LCO), the flutter of the bladed disk, with respect to friction interface parameters such as friction coefficient, tangential stiffness and static normal load. Reduced order modelling using condensation of the degree of freedom was used to reduce the size of the LCO model. Analytical expressions for the sensitivity of limit cycle amplitude and frequency were obtained, thereby allowing sensitivity coefficients to be obtained without significant additional computational cost. It was found that the LCO amplitude and frequency of a tuned bladed disk are sensitive to variation in fluttering mode damping factor and friction coefficient at contact interfaces. In Ref. [97], he obtained statistical characteristics of forced response of bladed disk with friction damping. First and second–order Taylor series approximations of response, in terms of local sensitivity values, were used to obtain the response statistics. The method allows estimation of the mean and standard deviation of response when these statistical characteristics are available for input parameters whereas when probability density function of input parameters are available, the method allows calculation of response PDF.

1.3.4 Intentional mistuning of the bladed disk

A turbine bladed disk will experience travelling wave excitation due to a finite number of flow distortions occurring upstream or downstream of the bladed disk. If there is P number of flow distortions, then the rotating bladed disk will experience a travelling wave excitation with wave number or spatial frequency of P times the rotational speed of the turbine which is referred as P engine order (EO) excitation. For a tuned bladed disk, in the absence of any non-linear effects, the forced response to these excitations are also a travelling wave with the same spatial frequency as that of the forcing wave. Therefore, all blades follow the same vibration cycle under travelling wave excitation but with a constant phase difference between adjacent blades, determined by the EO, resulting in nodal diameters (NDs) with zero modal deflections across the diameter of the disk. Hence a travelling wave excitation of P EO will result in a P nodal diameter structural mode shape with a maximum

number of nodal diameter equal to half the number of blades in the bladed disk.

In a mistuned bladed disk, due to distortion of the mode shapes and splitting of the natural frequency, the response of the bladed disk to travelling wave excitations are no longer a single travelling wave but can be represented as a superposition of travelling waves with different EOs. Mistuning produces coupling between tuned modes that are in the vicinity of the tuned mode that is directly excited. The higher the number of modes that participate in the mistuned response, the higher the amplification of the response can be. Therefore, intentional mistuning aims to reduce the possibility of blade-to-blade interaction, by moving the frequency of adjacent blades apart, in order to reduce the amplification due to random mistuning [98].

Griffin and Hoosac [70] investigated a scheme of blade mistuning where identical high–frequency blades and identical low–frequency blades were arranged alternatively in slots around the disk. They found that the scatter in vibration amplitude reduced while using the proposed scheme compared to randomly mistuned bladed disk. Castanier and Pierre [99] investigated the combined effects of intentional and random mistuning on forced response vibration of the bladed disk. They introduced intentional mistuning in the bladed disk by varying blade stiffness in harmonic patterns. It was concluded that for certain intentional mistuning patterns the maximum forced response obtained is significantly smaller than that of tuned bladed disk. Considering the forced response of the bladed disk, Petrov et al. [100] formulated the problem of finding the best and worst mistuning pattern as a combinatorial optimisation problem. In order to reduce the computational cost involved in optimisation using a genetic algorithm, a gradient–based polynomial response surface for maximum displacement was used. Several studies have reported the tendency of the forced response amplitude to exhibit a peak at a small value of mistuning as the mistuning strength is increased. Based on this idea, Nikolic et al. [90] investigated the idea of intentional mistuning using blades with larger mistuning strength to limit the amplification of forced response due to mistuning. For an axial turbine IBR, Beirow et al. [101] investigated the potential of intentional mistuning for reducing the forced response due to low engine order excitations. Martel et al. [98] investigated the beneficial effects of using intentional mistuning on the forced response of

IBR when the damping is predominantly due to aerodynamic effects.

1.4 Objectives and scope of the work

The present study focuses on the static and dynamic response of bladed disks structures considering the effects of random variations in the design due to deviations resulting from inherent randomness in the manufacturing processes. The effects of variations in the design of bladed disks with single crystal blades due to the following two aspects are investigated:

(1.) The variations in design geometry of fir–tree root joints due to deviations within the manufacturing tolerance.

(2.) The variations in material anisotropy orientation of single crystal blades due to inherent randomness in the casting process of such blades.

A thorough review of the existing literature reveals that, while there are few published results that provide an account of the effects of variations in material anisotropy orientation on the static and dynamic response of individual blades, no effort has been made to understand the effects of crystal anisotropy orientation on the response of mistuned bladed disks. For the case of tuned bladed disks, as it is clear from the literature review, there is a gap in knowledge on the effects of variations in material anisotropy on static response of bladed disks when the deviations in fir–tree root joint geometry are also accounted.

As far as the analysis of any engineering structure is concerned the uncertainty in the response of the structure might result from the uncertainty in design parameters or due to lack of sufficient knowledge about the operational conditions. In this study uncertainty and sensitivity analysis is performed to quantify the effects of uncertainty in design parameters on the response of bladed disks and to obtain a rank order of importance of the design parameters in terms of their influence on the response of the structure.

Uncertainty analysis for realistic high–fidelity FE models of the bladed disk using conventional Monte Carlo method is computationally intensive. Therefore, the usefulness of carefully chosen, computationally inexpensive surrogates of FE models for

uncertainty quantification is investigated. The structure of the parameter space is an important factor that concerns the choice of the surrogate model. In this study two different surrogate models are used:

(i.) Random forest - when the input parameter set is a combination of continuous and categorical variables.

(ii.) Polynomial chaos expansion - when all the input parameters are continuous variables.

Local and global sensitivity analysis for deformation of bladed disks w.r.t material anisotropy orientation of single crystal blades is performed. In order to calculate the local sensitivity of static deformation of bladed disk with respect to blade anisotropy angles, the sensitivity function implemented in *CalculiX* [102] FE solver is used. The global sensitivity, namely Sobol indices, are calculated efficiently after obtaining PCE for blade deformation using *ChaosPy* [103], which is a Python module for uncertainty analysis.

1.4.1 Project objectives

The following objectives define the scope of the present study:

i. Sensitivity and uncertainty analysis for static deformation of tuned bladed disks with friction joints and randomness in blade material anisotropy orientation with due account for some possible variations in fir–tree root joint geometry.

ii. Sensitivity and uncertainty analysis for static deformation of mistuned bladed disks with random material anisotropy orientations for the following two cases: (i) linear bladed disk and (ii) non-linear bladed disks with friction joints between blades and disk.

iii. Sensitivity and uncertainty analysis for the forced response of mistuned linear bladed disks with bonded contacts at shroud and blade–disk interface.

The forced response analysis of the bladed disk and the related local sensitivity analysis with respect to blade anisotropy angles is performed using an in-house code, named *ContaDyn*. For uncertainty and sensitivity analysis of anisotropy mistuned bladed disk, a code, named *ChaoStat*, was developed to integrate different

tools including the FE solver *CalculiX*, the Python module for uncertainty analysis *ChaosPy*, and the in-house code for forced response analysis *ContaDyn*.

The methods and tools developed in this study can be used in an industrial setting to determine the most influential angles defining the crystal orientation of a single crystal blade. From the manufacturing point of view, this information can be used to set tighter tolerance values for the most influential crystal anisotropy angles identified. This will result in subsequent reduction in uncertainty of static and dynamic response of the bladed disk under operating conditions.

Chapter 2

Methodology of analysis

The mathematical formulation for static and dynamic analysis of bladed disk structures and calculation of the sensitivities of blade deformation w.r.t material anisotropy orientations are presented in this chapter. For computationally efficient uncertainty and global sensitivity analysis using high–fidelity FE simulation models of bladed disks, surrogate models are used. The mathematical formulation for (i) random forest and (ii) polynomial chaos expansion based surrogate models are presented. A theoretical formulation for a sensitivity based method for estimation of the probability density function of the stochastic response of a bladed disk is also presented in this chapter.

2.1 Modelling of anisotropy-mistuned bladed disks

A single crystal blade made of nickel alloy has a face-centred cubic crystal structure, and due to the symmetry of the crystal structure, the elastic constants are constant along three principal crystallographic directions namely [100], [010] and [001] shown in Fig. 1.2. Therefore, in this study, the single crystal blades in the bladed disk are modelled as orthotropic materials.

2.1.1 Non-linear static analysis

Fig. 3.1 shows a realistic bladed disk model with 75 blades. The orientation of the crystal coordinate system is defined with respect to the blade geometry coordinate

system by three Euler angles, α, β and ζ as shown in Fig.1.2. These angles are obtained from the manufacturer of the blades and are defined as below:

- α - The angle between crystallographic direction [001] and Z–axis. Its is also called the primary angle and is always positive.
- β - The angle between crystallographic direction [100] and X–axis or angle between crystallographic direction [010] and X–axis depending on whichever is smaller. It is also called the secondary angle and is always positive.
- ζ - The angle of rotation defining the orientation of crystallographic direction [001] with respect to the Z–axis.

The elastic stress–strain relationship for orthotropic materials is given by Eq.(2.1)

$$\{\boldsymbol{\epsilon}\} = [\mathbf{S}]\{\boldsymbol{\sigma}\} \tag{2.1}$$

where, $\boldsymbol{\sigma}$ and $\boldsymbol{\epsilon}$ are stress tensor and strain tensor in the crystal coordinate system, and the material compliance matrix $[\mathbf{S}]$, expressed in the crystal coordinate system as:

$$[\mathbf{S}] = \begin{bmatrix} S_{11} & S_{12} & S_{13} & 0 & 0 & 0 \\ S_{12} & S_{22} & S_{23} & 0 & 0 & 0 \\ S_{13} & S_{23} & S_{33} & 0 & 0 & 0 \\ 0 & 0 & 0 & S_{44} & 0 & 0 \\ 0 & 0 & 0 & 0 & S_{55} & 0 \\ 0 & 0 & 0 & 0 & 0 & S_{66} \end{bmatrix} \tag{2.2}$$

where, S_{ij} is the element of the compliance matrix in the crystal coordinate system. For orthotropic material, $S_{11} = S_{22} = S_{33} = 1/E$, $S_{12} = S_{12} = S_{23} = -\nu/E$, and $S_{44} = S_{55} = S_{66} = 1/G$, where ν is Poisson's ratio, E is Young's modulus and G is shear modulus. The compliance matrix for orthotropic material with cubic symmetric is identical to that for isotropic material except that, for orthotropic material, the ratio $E/(2\mu(1+\nu)) \neq 1$.

In order to perform FE analysis of a bladed disk, the stress-strain relationship (Eq.2.1) has to be transformed to a global CS. The coordinate transformation for

stress and strain tensor in crystal coordinate system to stress and strain tensor in global CS is given by Eq.(2.3) and Eq.(2.4) respectively

$$\{\boldsymbol{\sigma}'\} = [\mathbf{T}]\{\boldsymbol{\sigma}\}[\mathbf{T}]^T = [\bar{\mathbf{T}}]\{\boldsymbol{\sigma}\} \tag{2.3}$$

$$\{\boldsymbol{\epsilon}'\} = [\mathbf{T}]\{\boldsymbol{\epsilon}\}[\mathbf{T}]^T = [\bar{\mathbf{T}}]\{\boldsymbol{\epsilon}\} \tag{2.4}$$

where, $\boldsymbol{\sigma}'$, $\boldsymbol{\epsilon}'$ are stress and strain tensors in global CS, and

$$[\mathbf{T}] = \begin{bmatrix} l_1 & l_2 & l_3 \\ m_1 & m_2 & m_3 \\ n_1 & n_2 & n_3 \end{bmatrix} \tag{2.5}$$

and

$$[\bar{\mathbf{T}}] = \begin{bmatrix} l_1^2 & l_2^2 & l_3^2 & 2l_2l_3 & 2l_1l_3 & 2l_1l_2 \\ m_1^2 & m_2^2 & m_3^2 & 2m_2m_3 & 2m_1m_3 & 2m_1m_2 \\ n_1^2 & n_2^2 & n_3^2 & 2n_2n_3 & 2n_1n_3 & 2n_1n_2 \\ m_1n_1 & m_2n_2 & m_3n_3 & m_2n_3+n_2m_3 & m_1n_3+m_3n_1 & m_1n_2+n_3m_1 \\ l_1m_1 & l_2m_2 & l_3m_3 & l_2n_3+n_2l_3 & l_1n_3+n_1l_3 & l_1n_2+n_1l_2 \\ l_1n_1 & l_2n_2 & l_3m_3 & l_2m_3+l_3m_2 & l_1m_3+l_3m_1 & l_1m_2+m_1l_2 \end{bmatrix} \tag{2.6}$$

are transformation matrices formed from direction cosines, l_i, m_i and n_i, between blade anisotropy CS and global CS, while allowing for orientation of blade stacking axis in the bladed disk. From Eqs.(2.1), (2.3) and (2.4), the compliance matrix in global CS could be written as in Eq.(2.7)

$$[\mathbf{S}'] = [\bar{\mathbf{T}}][\mathbf{S}][\bar{\mathbf{T}}]^{-1} \tag{2.7}$$

Similarly, the elasticity matrix in global CS is given by Eq.(2.8)

$$[\mathbf{E}'] = [\bar{\mathbf{T}}][\mathbf{E}][\bar{\mathbf{T}}]^{-1} \tag{2.8}$$

where, $\mathbf{E}$ is the elasticity matrix in crystal CS. For non-linear static problem, the solution is obtained by solving the governing equation of the bladed disk:

$$\mathbf{K}(\boldsymbol{\xi}_j)\mathbf{x} + \mathbf{F}_{nln}(\mathbf{x}) = \mathbf{P},\ j = 1, \ldots, N_B \tag{2.9}$$

where, $\boldsymbol{\xi}_j = \{\alpha_j, \beta_j, \zeta_j\}$ is the vector of anisotropy angles defining the orientation of the crystallographic axis of j^{th} blade in the bladed disk, N_B is the number of blades

in the bladed disk, $\mathbf{F}_{nln}(\boldsymbol{x})$ is the vector of non-linear internal forces due to the non-linear contact interactions and the geometric non-linearity, $\mathbf{P}$ is the vector of static external forces and the global stiffness matrix, $\mathbb{K}$ of the bladed disk is obtained by assembling the element stiffness matrices $\mathbf{k}^e$:

$$\mathbf{k}^e = \int_{V^e} \mathbf{B}^T \mathbf{E}'(\boldsymbol{\xi}_j) \mathbf{B} \, \mathrm{d}V^e, \; e = 1, \ldots, N_{el}, \; j = 1, \ldots, N_B \tag{2.10}$$

where, $\mathbf{B}$ is the strain-displacement matrix , V^e is the element volume and N_{el} is the total number of elements and N_B is the number of blades in the bladed disk.

Eqn. (2.9) is solved using Newton-Raphson iteration method:

$$\mathbf{x}_{k+1} = \mathbf{x}_k + \mathbf{J} \left(\mathbf{K}\mathbf{x}_k + \mathbf{F}_{nln}(\mathbf{x}_k) - \mathbf{P} \right) \tag{2.11}$$

where $\mathbf{J} = \left(\mathbf{K} + \frac{\partial \mathbf{F}_{nln}}{\partial \mathbf{x}} \right)$ is the Jacobian of Eq.(2.9) and $\mathbf{x}_k$, $\mathbf{x}_{k+1}$ are the approximate solutions obtained at k^{th} and $(k+1)^{\text{th}}$ iteration respectively. The iterative process terminates when the solution reaches sufficient accuracy, ϵ; for example, when $||\mathbf{x}_{k+1} - \mathbf{x}_k|| < \epsilon$.

2.1.2 Sensitivity of static displacement to anisotropy orientation

The equation for displacement sensitivity corresponding to j^{th} blade anisotropy is obtained by differentiating Eq.(2.9) with respect to vector of anisotropy angles, $\boldsymbol{\xi}_j$:

$$\frac{\partial \mathbb{K}}{\partial \boldsymbol{\xi}_j}\mathbf{x} + \mathbf{K}\frac{\partial \mathbf{x}}{\partial \boldsymbol{\xi}_j} + \frac{\partial \mathbf{F}_{nln}}{\partial \mathbf{x}}\frac{\partial \mathbf{x}}{\partial \boldsymbol{\xi}_j} = 0 \tag{2.12}$$

rearranging terms in Eq.(2.12):

$$\left(\mathbf{K} + \frac{\partial \mathbf{F}_{nln}}{\partial \mathbf{x}} \right) \frac{\partial \mathbf{x}}{\partial \boldsymbol{\xi}_j} = \mathbf{J}\frac{\partial \mathbf{x}}{\partial \boldsymbol{\xi}_j} = -\frac{\partial \mathbf{K}}{\partial \boldsymbol{\xi}_j}\mathbf{x}^*, \; j = 1, \ldots, N_B \tag{2.13}$$

where $\mathbf{x}^*$ is solution vector obtained by solving Eq.(2.9), $\partial \mathbf{x}/\partial \boldsymbol{\xi}_j$ is the required sensitivities and N_B is the total number of blades in the bladed disk.

The sensitivities of the element stiffness matrix w.r.t crystal orientation is calculated by differentiating Eq.(2.10)

$$\frac{\partial \mathbf{k}^e}{\partial \boldsymbol{\xi}_j} = \int_{V^e} \mathbf{B}^T \frac{\partial \mathbf{E}'}{\partial \boldsymbol{\xi}_j} \mathbf{B} \, \mathrm{d}V^e \tag{2.14}$$

where $\partial\mathbf{E}'/\partial\boldsymbol{\xi}_j$, the derivative of the elasticity matrix with respect to anisotropy angles of j^{th} blade is obtained as:

$$\frac{\partial\mathbf{E}'}{\partial\boldsymbol{\xi}_j} = \frac{\partial\bar{\mathbf{T}}}{\partial\boldsymbol{\xi}_j}\mathbf{E}\bar{\mathbf{T}}^T + \bar{\mathbf{T}}\mathbf{E}\frac{\partial\bar{\mathbf{T}}^T}{\partial\boldsymbol{\xi}_j} \tag{2.15}$$

The sensitivities of element stiffness matrix, $\mathbf{k}^e$, is assembled using standard FE assembling procedure to obtain the sensitivities of global stiffness matrix, $\partial\mathbf{K}/\partial\boldsymbol{\xi}_j$, in the right hand side of Eq.(2.13).

The Jacobian matrix, $\mathbf{J}$ in Eq.(2.13) is evaluated while solving Eq.(2.9), and hence, the computational cost involved in calculation of sensitivities is kept to minimum.

2.1.3 Sensitivity of stresses to anisotropy orientation

In order to obtain the sensitivity of stresses with respect to blade anisotropy angles of a mistuned bladed disk, we begin by calculating the sensitivity of strain from the expression:

$$\frac{\partial\boldsymbol{\epsilon}}{\partial\boldsymbol{\xi}_j} = \mathbf{B}\frac{\partial\mathbf{x}}{\partial\boldsymbol{\xi}_j} \tag{2.16}$$

where, $\boldsymbol{\epsilon}$ is the vector of strain components, $\boldsymbol{\xi}_j$ is the vector of anisotropy angles of j^{th} blade, $\mathbf{B}$ is the strain-displacement matrix and $\partial\mathbf{x}/\partial\boldsymbol{\xi}_j$ is the sensitivity of displacements which is obtained by solving Eqn. (2.13).

From constitutive law, we have the expression for stresses as:

$$\boldsymbol{\sigma} = \mathbf{E}'\boldsymbol{\epsilon} \tag{2.17}$$

where, $\boldsymbol{\sigma} = \{\sigma_{xx}, \sigma_{yy}, \sigma_{zz}, \tau_{xy}, \tau_{yz}, \tau_{zx}\}^T$ is the vector of stress components and $\mathbf{E}'$ is the elasticity matrix in the global CS.

Differentiating Eqn. (2.17) and substituting Eqn. (2.16) for the sensitivity of strain components, we obtain the expression for the sensitivity of stresses:

$$\frac{\partial\boldsymbol{\sigma}}{\partial\boldsymbol{\xi}_j} = \mathbf{E}'\mathbf{B}\frac{\partial\mathbf{x}}{\partial\boldsymbol{\xi}_j} \tag{2.18}$$

When the stress components are known, von Mises stress can be calculated from the expression:

$$\sigma_V = \sqrt{\frac{(\sigma_{xx}-\sigma_{yy})^2 + (\sigma_{yy}-\sigma_{zz})^2 + (\sigma_{zz}-\sigma_{xx})^2 + 6(\tau_{xy}^2+\tau_{yz}^2+\tau_{zx}^2)}{2}} \tag{2.19}$$

The sensitivity of von Mises stresses with respect to j^{th} blade anisotropy angles is obtained by differentiating Eqn. (2.19):

$$\begin{aligned} 2\sigma_V \frac{\partial \sigma_V}{\partial \boldsymbol{\xi}_j} = (\sigma_{xx} - \sigma_{yy})(\frac{\partial \sigma_{xx}}{\partial \boldsymbol{\xi}_j} - \frac{\partial \sigma_{yy}}{\partial \boldsymbol{\xi}_j}) + (\sigma_{yy} - \sigma_{zz})(\frac{\partial \sigma_{yy}}{\partial \boldsymbol{\xi}_j} - \frac{\partial \sigma_{zz}}{\partial \boldsymbol{\xi}_j}) + \\ (\sigma_{zz} - \sigma_{xx})(\frac{\partial \sigma_{zz}}{\partial \boldsymbol{\xi}_j} - \frac{\partial \sigma_{xx}}{\partial \boldsymbol{\xi}_j}) + 6(\tau_{xy}\frac{\partial \tau_{xy}}{\partial \boldsymbol{\xi}_j} + \tau_{yz}\frac{\partial \tau_{yz}}{\partial \boldsymbol{\xi}_j} + \tau_{zx}\frac{\partial \tau_{zx}}{\partial \boldsymbol{\xi}_j}) \end{aligned} \tag{2.20}$$

2.1.4 Sensitivity of forced response for anisotropy mistuned bladed disk

The mathematical formulation for forced response analysis and its sensitivity to blade anisotropy angles of a mistuned bladed disk with linear bonded contacts is presented in this section. In order to investigate the effects of blade material anisotropy orientation on the forced response of mistuned bladed disk, the analysis is restricted to bladed disks with linear bonded contacts at fir–tree roots and shrouds. For uncertainty and sensitivity analysis of forced response, the choice of bladed disks with linear bonded contacts is justified for the following two reasons:

1. The bladed disk with bonded contacts at joints has higher stiffness compared to the case when the joints are modelled using friction contact elements. For such a system, due to the absence of additional damping provided by friction joints, the effects of variation in the crystal orientation of blades on the forced response will be higher compared to that of the non-linear bladed disk. Therefore the analysis of linear bladed disk provides a conservative estimate of the effects of anisotropy mistuning on the forced response.

2. The computational cost associated with forced response analysis of bladed disk with linear bonded contacts at fir–tree root and shrouds is comparatively low while considering the corresponding cost for a bladed disk with non-linear friction contacts.

In order to calculate the local sensitivity of the forced response of a multi-degree-of-freedom system, the derivatives of eigenvalues and mode shapes with respect to the anisotropy angles have to be calculated. The eigenvalue problem of the multi-degree-of-freedom dynamic systems is formed for the whole anisotropy mistuned

bladed disk in the form:

$$\mathbf{K}\boldsymbol{\phi}_j = \lambda_j \mathbf{M}\boldsymbol{\phi}_j \tag{2.21}$$

where j denotes the mode number, and the stiffness matrix denoted as $\mathbf{K}$, the eigenvalue λ_j and the mode shape $\boldsymbol{\phi}_j$, are dependent on the anisotropy axis orientation, but the mass matrix $\mathbf{M}$ is not. By differentiating Eqn. (2.21) with respect to the vector of anisotropy angles of a blade, $\boldsymbol{\xi}$, and considering mass normalised mode shapes, the sensitivity of the eigenvalues for a multi-degree-of-freedom dynamic system results in [104]:

$$\frac{\partial \lambda_j}{\partial \boldsymbol{\xi}} = \boldsymbol{\phi}_j^T \frac{\partial \mathbf{K}}{\partial \boldsymbol{\xi}} \boldsymbol{\phi}_j \tag{2.22}$$

The derivative of the stiffness matrix in Eqn. (2.22) is calculated by the numerical scheme of finite differences described in detail in [105].

The calculation of the sensitivity of mode shapes with respect to the anisotropy parameters is carried out using an enhanced method presented in [105]. The derivative of the eigenvectors are expressed by a series expansion formula that accounts for the terms that are not included in the expansion:

$$\frac{\partial \boldsymbol{\phi}_j}{\partial \boldsymbol{\xi}} = \sum_{k=1}^{m} d_{jk} \boldsymbol{\phi}_k + \mathbf{r}_j \tag{2.23}$$

where d_{jk} are the coefficients of the series expansion and can be expressed as;

$$d_{jk} = \begin{cases} \frac{\lambda_j - \lambda_0}{(\lambda_k - \lambda_j)(\lambda_k - \lambda_0)} \boldsymbol{\phi}_k^T \mathbf{f}_j & \text{if } k \neq j \\ -\frac{\boldsymbol{\phi}_k^T \mathbf{f}_j}{\lambda_k - \lambda_0} & \text{if } k = j \end{cases} \tag{2.24}$$

and the residual term, $\mathbf{r}_j$, can be calculated by solving the system of linear equations:

$$(\mathbf{K} - \lambda_0 \mathbf{M})\mathbf{r}_j = \mathbf{f}_j \tag{2.25}$$

The term $\mathbf{f}_j$ introduced in Eqns. (2.24) and (2.25) can be calculated as:

$$\mathbf{f}_j = -\left(\frac{\partial \mathbf{K}}{\partial \boldsymbol{\xi}} - \frac{\partial \lambda_j}{\partial \boldsymbol{\xi}} \mathbf{M}\right) \boldsymbol{\phi}_j \tag{2.26}$$

The reference frequency, λ_0, used in Eqns. 2.25 and 2.24 is obtained for each mode shape as:

$$\lambda_0 = \frac{\lambda_j + \lambda_{j-1}}{2} \tag{2.27}$$

The equation of motion for a mistuned structure under harmonic excitation, $\mathbf{f}(t) = \mathbf{F}e^{i\omega t}$, when the forced response, $\mathbf{x}(t) = \mathbf{X}e^{i\omega t}$, is also harmonic takes the form:

$$\left[\mathbf{K} + i\omega\mathbf{D} - \omega^2\mathbf{M}\right]\mathbf{X} = \mathbf{F} \tag{2.28}$$

For the engine order excitation by k-th excitation harmonic, the phase shift between neighbouring sectors is equal to $e^{i\delta k}$, where $\delta = 2\pi/N_B$ and N_B is the total number of blades in the bladed disk, and the force vector for the whole structure takes the following form:

$$\mathbf{F} = \left\{\mathbf{F}^S, e^{i\delta k}\mathbf{F}^S, \ldots, e^{i\delta k(N_B-1)}\mathbf{F}^S\right\}^T \tag{2.29}$$

where $\mathbf{F}^S$ is the distribution of the complex amplitude of excitation load over one sector of the bladed disk. The amplitude, $\mathbf{X}$, of forced response of the structure can be calculated when the modal characteristics are known:

$$\boldsymbol{X} = \sum_{j=1}^{r} \frac{\phi_j^T \boldsymbol{F}}{(1 + i\eta_j)\omega_j^2 - \omega^2}\phi_j = \sum_{j=1}^{r} a_j\phi_j \tag{2.30}$$

where r is the number of mode shapes retained for the forced response analysis, η_j is the modal damping factor for j^{th} mode, ω_j is the j^{th} natural frequency and ϕ_j is the corresponding mode shape of the mistuned bladed disk. Using Eqn. (2.30), the blade amplitudes can be calculated for any set of nodes selected from the whole structure, thereby significantly reducing the computational time by selection of set nodes of interest from the whole finite element model of the bladed disk. This set of selected nodes usually contains several hundred or thousand degrees of freedom (DOF) while the whole FE model can contain millions of DOF.

Differentiating Eqn. (2.30) with respect to anisotropy angles we obtain the expression for the sensitivity of the amplitude of forced response:

$$\boldsymbol{X'} = \sum_{j=1}^{r} a_j'\phi_j + a_j\phi_j' \tag{2.31}$$

where the prime symbol indicates the derivative, $\partial/\partial\boldsymbol{\xi}$, and the derivative of the modal expansion coefficient can be obtained from the expression below:

$$a_j' = \frac{\mathbf{F}^T\phi_j'}{(1 + i\eta_j)\omega_j^2 - \omega^2} - \frac{\mathbf{F}^T\phi_j\left[(1 + i\eta_j')\omega_j^2 + 2(1 + i\eta_j)\omega_j\omega_j'\right]}{\left[(1 + i\eta_j)\omega_j^2 - \omega^2\right]^2} \tag{2.32}$$

where $\phi_j' = \partial\phi_j/\partial\boldsymbol{\xi}$ is the derivative of mode shape ϕ_j with respect to the vector of anisotropy angle $\boldsymbol{\xi}$.

2.2 Uncertainty analysis

As an alternative for computationally inefficient uncertainty analysis using Monte Carlo simulations of high–fidelity FE models of bladed disks, effective surrogates for FE models are used in this study. The following two surrogate models are used to obtain the statistical characteristics for bladed disks: (i) Random Forest and (ii) Polynomial Chaos Expansion.

2.2.1 Random Forest

The computational cost associated with uncertainty analysis of bladed disks could be significantly reduced by using computationally inexpensive surrogate models that can closely approximate the FE model. In this section, the idea behind random forest based surrogate model is explained. A random forest is a collection of randomised regression trees. Each regression tree consists of a series of criteria, about the input parameters, that split the input parameter space into subregions. The function analysed is then approximated by a constant value within each sub-domain. Therefore, the regression tree could be thought of as a piecewise constant regression model.

Splitting the domain into sub-domains

The idea of regression tree approximation can be illustrated using a simple example. Let us consider a function of two variables, $y(x_1, x_2)$. In order to approximate this function in the domain $0 \leq x_1 \leq 6$, $0 \leq x_2 \leq 4$, we need to know the the criteria for splitting the domain into sub-domains (also referred as "nodes" of a decision tree) and also the constant value of approximation (node constant) for each sub-domain. In each sub-domain, the value of approximation is equal to the mean or median of the function evaluations within the considered domain depending on the chosen criteria of splitting the domain. For an example case, when the sub-domains and the function approximation within each sub-domain is given by Eqn. (2.33), the

regression tree approximation of the function y can be visualised as in Fig. 2.1.

$$y(x_1, x_2) \approx \begin{cases} 28 & x_1 \leq 4, x_2 \leq 2 \\ 55 & x_1 \leq 4, x_2 > 2 \\ 18 & 4 < x_1 \leq 5 \\ 12 & x_1 > 5 \end{cases} \tag{2.33}$$

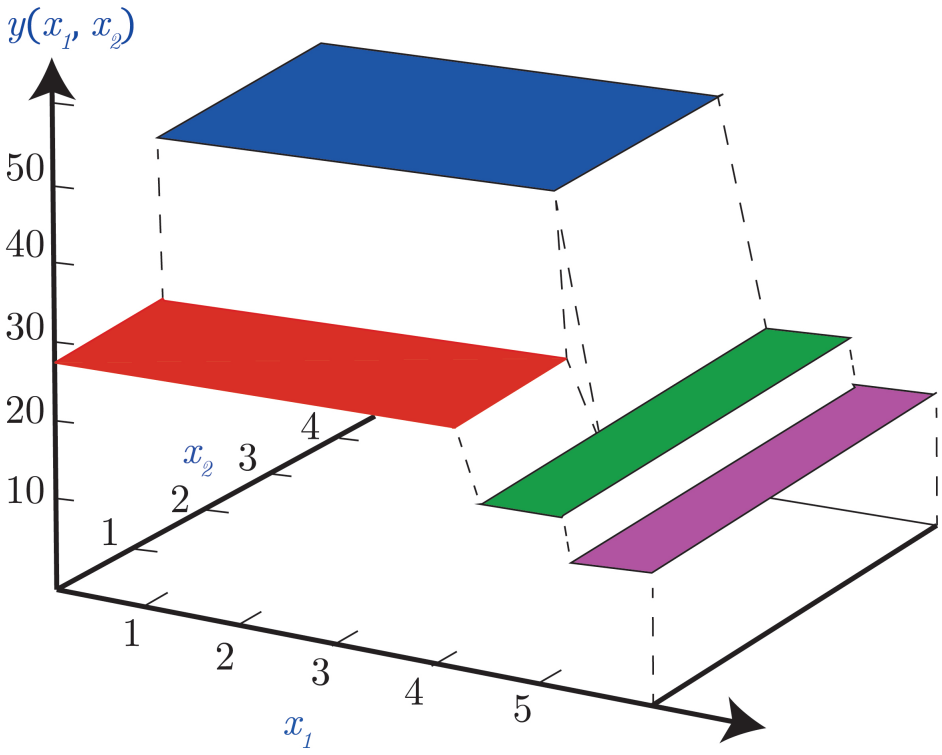

Figure 2.1: Regression tree: a piecewise constant regression model

Note that each of the four sub-domains, shown in Fig. 2.1, can be further split by specifying additional splitting criteria depending on the number of function evaluations, for example, FE model realisations, available within a particular sub-domain. The minimum number of function evaluations required for further splitting a sub-domain is two. By increasing the minimum number of function evaluations required for further splitting, the number of splits in a regression tree, and therefore the number of sub-domains, can be reduced.

The two popular splitting criteria used to build regression trees are minimising the mean square error (MSE) and minimising the mean absolute error (MAE). Based on the MSE criterion the error of approximation associated with a sub-domain in

the decision tree is the average of the squared differences between the function evaluations within the node and the node constant. The node constant in this case is the mean of the function evaluations associated with the node. If $\{\mathbf{x}_i, y_i\} : i \in M_t$ represent the set of values of independent variables and the corresponding value of function evaluations associated with node t, the mean square error of the node is [106]:

$$mse(t) = \frac{1}{n_t} \sum_{i \in M_t} (y_i - \bar{y})^2 \tag{2.34}$$

where, M_t is the set of function evaluations within the considered node or sub-domain, n_t is the number of function evaluations at node t, y_i is the value of function corresponding to i^{th} values of the independent variables represented by vector $\mathbf{x}_i$, $\bar{y}$ is the mean of all values obtained from the function evaluation for node t. To split a node in the regression tree into two daughter nodes, splitting rule is chosen such that the weighted average of the error in the resulting nodes is minimum. In other words, the splitting rule that minimises the error $mse(s,t)$ of the split s is chosen, where

$$mse(s,t) = \frac{n_{t_L}}{n_t} mse(t_L) + \frac{n_{t_R}}{n_t} mse(t_R) \tag{2.35}$$

where n_{t_L} and n_{t_R} are the number of model realisations that are associated to the left and right daughter nodes respectively. This is equivalent to maximising the reduction in error, $\Delta mse(s,t)$, in the tree after the splitting, where

$$\Delta mse(s,t) = mse(t) - mse(s,t) \tag{2.36}$$

Building a regression tree based on MAE criterion requires that the mean absolute deviation at all nodes be reduced to the minimum. The value of the node constant that minimises the mean absolute error of the node, for the set of function evaluations $\{\mathbf{x}_i, y_i\}$ within the node, is given by the median of the response variables in the set. Given the set of function evaluations, $\{\mathbf{x}_i, y_i\} : i \in M_t$ within node t, the mean absolute deviation of the node is:

$$mae(t) = \frac{1}{n_t} \sum_{i \in M_t} |(y_i - \hat{y})| \tag{2.37}$$

where, M_t is the set of function evaluations within the considered node or sub-domain, n_t is the number of function evaluations at node t, y_i is the value of function corresponding to i^{th} values of the independent variables represented by vector $\mathbf{x}_i$, $\hat{y}$

is the median of the function evaluations in the set M_t. The mean absolute error (mae) of a split s is:

$$mae(s,t) = \frac{n_{t_L}}{n_t} mae(t_L) + \frac{n_{t_R}}{n_t} mae(t_R) \tag{2.38}$$

For the case of MAE criterion, the best split at a node is the one among the set of all possible splits which maximises the reduction in the mean absolute error in the tree after the split obtained as:

$$\Delta mae(s,t) = mae(t) - mae(s,t) \tag{2.39}$$

Training and test sets

In order to build the regression tree model and to test the accuracy of the model obtained, the function evaluations represented by the set, $\{\mathbf{x}_i, y_i\} : i \in M$, are divided into the following two subsets: (i) training set represented as $\{\mathbf{x}_i, y_i\} : i \in M_{tr}$ and (ii) test set represented as $\{\mathbf{x}_i, y_i\} : i \in M_{te}$, where the vector $\mathbf{x}_i$ is the i^{th} values of independent variables, y_i is the value of function corresponding to $\mathbf{x}_i$, M is the complete set of function evaluations available, M_{tr} is the set of function evaluations to which the regression tree model is fitted, and M_{te} is the set of function evaluations on which accuracy of prediction of the regression tree model is tested.

The application of a regression tree model is limited because these models often suffer from high variance[107] and overfitting*. The primary reason for the high variance is the hierarchical nature of the process where an error in the higher nodes of the tree affects all the nodes below it. By averaging the regression estimate of an ensemble of regression trees, RF algorithm mitigates high variance and overfitting associated with the individual regression trees, and thereby, improve the predictive accuracy of the surrogate model. For the present study we use *scikit-learn* [108] which is a Python library that integrates several state-of-the-art machine learning algorithms. The main steps involved in the RF algorithm is shown in Fig.2.2. The user defines the number of regression trees in the ensemble and the minimum number of function evaluations, associated with a particular node, required to split that

*The regression model is considered to be an overfit when it corresponds closely to a particular training data, and therefore to the noise associated with that set of data, thereby failing to model the underlying variation. Thus overfitting reduces the accuracy of prediction of the model for new data sets and therefore affects the generality of the model.

node. Each regression tree in the RF model is trained using a bootstrap sample of the FE evaluations. In order to further randomise the regression trees, the best split is obtained, using MSE or MAE criteria, by considering a random subset of the design variables. The binary split of a node results in two daughter nodes which are further split until the minimum number of sample evaluations at the node is less than the value specified by the user.

2.2.2 Polynomial chaos expansion.

The idea behind PCE is to project the stochastic output $y(\boldsymbol{\xi})$ in the n-dimensional random space spanned by orthogonal polynomial basis $\psi_i(\boldsymbol{\xi})$ which are functions of the n-dimensional random variable $\boldsymbol{\xi} = \{\xi_1, \xi_2, \ldots, \xi_n\}$. The output function, which can be displacement, stress or modal characteristics like natural frequency, could be expanded using PCE as shown in Eq.(2.40)

$$y(\boldsymbol{\xi}) = \sum_{i=0}^{\infty} c_i \psi_i(\boldsymbol{\xi}) \tag{2.40}$$

where c_i are unknown coefficients in the expansion that need to be evaluated. For practical reasons, the series in Eq.(2.40) could be truncated by limiting the order of polynomials in the basis terms to m, resulting in a truncated PCE given by Eq.(2.41)

$$y(\boldsymbol{\xi}) \approx y^{PCE}(\boldsymbol{\xi}) = \sum_{i=0}^{P} c_i \psi_i(\boldsymbol{\xi}) \tag{2.41}$$

where, $P + 1 = (n + m)!/n!m!$, n being the number of random variables, and m the order of the PCE. The orthogonality of the basis function with respect to the probability distribution of the random variables is imposed by requiring the inner product of the basis functions to satisfy Eq.(2.42):

$$\langle \psi_r(\boldsymbol{\xi}), \psi_s(\boldsymbol{\xi}) \rangle = \int_{\Omega} \psi_r(\boldsymbol{\xi}) \psi_s(\boldsymbol{\xi}) d\mu(\boldsymbol{\xi}) = \gamma \delta_{rs} \tag{2.42}$$

where, $\gamma = 1$ for orthonormal basis functions and a constant for orthogonal basis functions, δ_{rs} is the Kronecker delta, and $d\mu(\boldsymbol{\xi})$ is the probability measure in the n-dimensional random space. It is given by Eq.(2.43) for statistically independent random variables

$$d\mu(\boldsymbol{\xi}) = \rho_1(\xi_1)\rho_2(\xi_2) \ldots \rho_n(\xi_n) d\xi_1 d\xi_2 \ldots d\xi_n \tag{2.43}$$

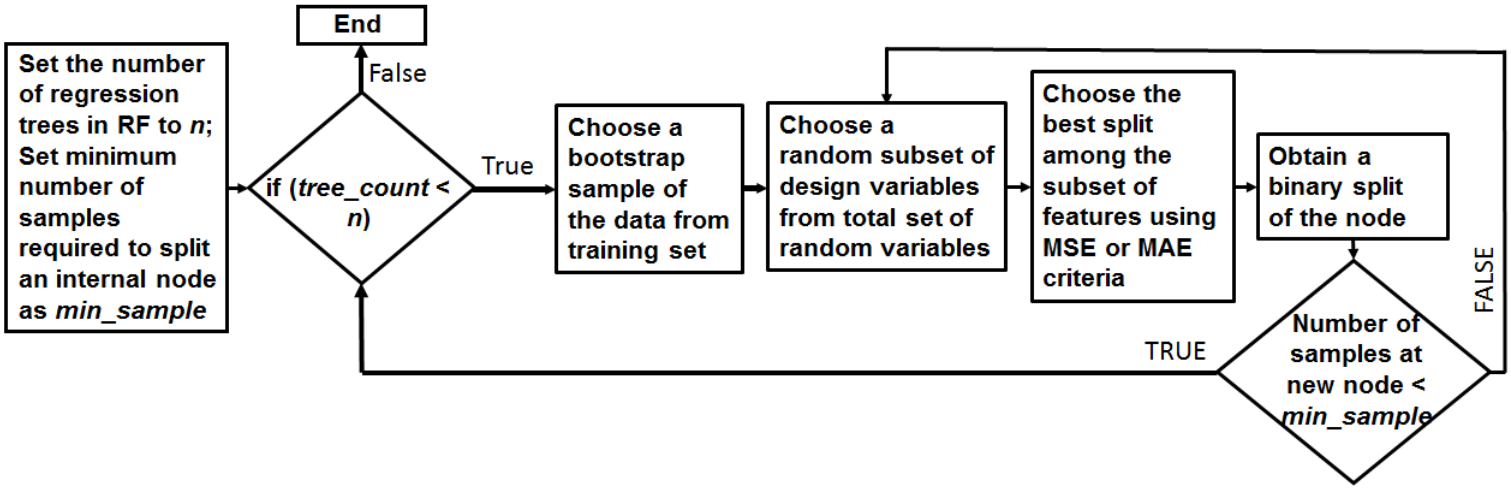

Figure 2.2: Algorithm for constructing Random Forest model

where, ρ_n is the probability density function of ξ_n. The choice of basis functions in Eq.(2.40) is based on the probability distribution of the random variables. Table 2.1 provides the choice of polynomial basis for some commonly used probability distributions of the random variables. For one dimensional problem, the orthogonal basis polynomials can be calculated easily using a method known as discretized Stieltjes' method which uses a three terms recurrence formula [109]. For a multivariate output function, the polynomial basis functions are obtained as tensor products of corresponding univariate cases. For example, if $\mathbf{\Psi}_1 = \{1, \xi_1, \xi_1^2 - 1\}$ are first three orthogonal basis terms in the PCE of a univariate function of random variable ξ_1 having normal distribution and $\mathbf{\Psi}_2 = \{1, \xi_2, \xi_2^2 - 0.3333\}$ are the corresponding orthogonal polynomials in PCE of a univariate function of random variable ξ_2 with uniform distribution, then the tensor product of $\mathbf{\Psi_1}$ and $\mathbf{\Psi_2}$ is obtained as:

$$\mathbf{\Psi_1} \otimes \mathbf{\Psi_2} = \begin{bmatrix} 1 & \xi_2 & \xi_2^2 - 0.3333 \\ \xi_1 & \xi_1\xi_2 & \xi_1(\xi_2^2 - 0.3333) \\ (\xi_1^2 - 1) & (\xi_1^2 - 1)\xi_2 & (\xi_1^2 - 1)(\xi_2^2 - 0.3333) \end{bmatrix} \tag{2.44}$$

Table 2.1: Choice of basis functions

Distribution	Polynomial	Basis terms
Normal $\mathcal{N}(0,1)$	Hermite	$\psi_0 = 1, \psi_1 = \xi, \psi_2 = \xi^2 - 1,$ $\psi_3 = \xi^3 - 3\xi,$ $\psi_4 = \xi^4 - 6\xi^2 + 3$
Uniform $\mathcal{U}(-1,1)$	Legendre	$\psi_0 = 1, \psi_1 = \xi,$ $\psi_2 = \xi^2 - 0.3333,$ $\psi_3 = \xi^3 - 0.6\xi,$ $\psi_4 = \xi^4 - 0.8571\xi^2 + 0.08571,$
Exponential	Laguerre	$\psi_0 = 1, \psi_1 = \xi - 1,$ $\psi_2 = \xi^2 - 4\xi + 2,$ $\psi_3 = \xi^3 - 9\xi^2 + 18\xi - 6,$ $\psi_4 = \xi^4 - 16\xi^3 + 72\xi^2 - 96\xi + 24$

There are different methods available for calculating the unknown coefficients in PCE, such as the point collocation method and the least square regression method.

Point collocation method is based on reducing the error in approximation of stochastic to zero at selected points, called collocation points, in the n-dimensional random space. The condition that the residual vanishes at the set of sample points of random variables, $\boldsymbol{\xi}_1, \ldots, \boldsymbol{\xi}_N$, provides a set of N linear algebraic equations in c_i, $i \in \{0, 1 \ldots, P\}$. When the number of realisations of the exact model is greater than the number of coefficients in Eq.(2.40), then the system of linear equations is overdetermined and is solved using the least squares approach.

2.2.3 Gradient-based polynomial chaos expansion.

The number of terms in PCE increases factorially as the dimension of random space increases, increasing the computational cost. This problem is often referred to in the literature as the "curse of dimensionality". In order to address this problem, gradient values can be used for evaluating the unknown coefficients in polynomial chaos expansion [13]. For an n-dimensional random space, the number of linearly independent equations obtained by including gradient values is $(1 + n)$ times the number of FE evaluations where n is the number of random variables. Therefore, the minimum number of model realisations required to obtain the coefficients in a polynomial approximation is reduced by a factor of $(1 + n)^{-1}$. The gradient values of output function evaluated at sample points are used to determine the coefficients:

$$\begin{bmatrix} \psi_0(\boldsymbol{\xi}_1) & \psi_1(\boldsymbol{\xi}_1) \ldots \psi_P(\boldsymbol{\xi}_1) \\ w_1 \frac{\partial \psi_0(\boldsymbol{\xi}_1)}{\partial \xi_1} & w_1 \frac{\partial \psi_1(\boldsymbol{\xi}_1)}{\partial \xi_1} \ldots w_1 \frac{\partial \psi_P(\boldsymbol{\xi}_1)}{\partial \xi_1} \\ \vdots & \\ w_1 \frac{\partial \psi_0(\boldsymbol{\xi}_1)}{\partial \xi_n} & w_1 \frac{\partial \psi_1(\boldsymbol{\xi}_1)}{\partial \xi_n} \ldots w_1 \frac{\partial \psi_P(\boldsymbol{\xi}_1)}{\partial \xi_n} \\ \psi_0(\boldsymbol{\xi}_2) & \psi_1(\boldsymbol{\xi}_2) \ldots \psi_P(\boldsymbol{\xi}_2) \\ w_1 \frac{\partial \psi_0(\boldsymbol{\xi}_2)}{\partial \xi_1} & w_1 \frac{\partial \psi_1(\boldsymbol{\xi}_2)}{\partial \xi_1} \ldots w_1 \frac{\partial \psi_P(\boldsymbol{\xi}_2)}{\partial \xi_1} \\ \vdots & \\ \psi_0(\boldsymbol{\xi}_N) & \psi_1(\boldsymbol{\xi}_N) \ldots \psi_P(\boldsymbol{\xi}_N) \\ \vdots & \\ w_1 \frac{\partial \psi_0(\boldsymbol{\xi}_N)}{\partial \xi_n} & w_1 \frac{\partial \psi_1(\boldsymbol{\xi}_N)}{\partial \xi_n} \ldots w_1 \frac{\partial \psi_P(\boldsymbol{\xi}_N)}{\partial \xi_n} \end{bmatrix} \cdot \begin{Bmatrix} c_0 \\ c_1 \\ \vdots \\ c_P \end{Bmatrix} = \begin{Bmatrix} y(\boldsymbol{\xi}_1) \\ w_2 \frac{\partial y(\boldsymbol{\xi}_1)}{\partial \xi_1} \\ \vdots \\ w_2 \frac{\partial y(\boldsymbol{\xi}_1)}{\partial \xi_n} \\ y(\boldsymbol{\xi}_2) \\ w_2 \frac{\partial y(\boldsymbol{\xi}_2)}{\partial \xi_1} \\ \vdots \\ y(\boldsymbol{\xi}_N) \\ \vdots \\ w_2 \frac{\partial y(\boldsymbol{\xi}_N)}{\partial \xi_n} \end{Bmatrix} \tag{2.45}$$

where, $\psi_0(\boldsymbol{\xi}_1)$, $\psi_1(\boldsymbol{\xi}_1)$, ..., $\psi_P(\boldsymbol{\xi}_1)$ are basis functions evaluated at first set of sample values of the random variables $\boldsymbol{\xi}_1$; w_1 and w_2 are weight coefficient which allows setting the relative importance between function evaluations and its gradients in building the PCE approximation; c_0, c_1, ..., c_P are deterministic coefficients in the polynomial expansion, and $y(\boldsymbol{\xi}_1)$, ..., $y(\boldsymbol{\xi}_N)$ are function evaluations obtained at sample points $\boldsymbol{\xi}_1, \ldots, \boldsymbol{\xi}_n$. $\partial y(\boldsymbol{\xi}_i)/\partial \xi_j$ represents the derivative of the function w.r.t j^{th} random variable evaluated for i^{th} set of sample values of the random variables. The weight coefficients, w_1 and w_2, are used to weight the importance of the information about the function and its derivatives. They can be chosen to obtain faster convergence of PCE-based statistical characteristics. When the value of weight coefficients are equal, i.e. $w_1 = w_2$, the system of linear algebraic equations remain unmodified and can be solved for unknown coefficients in the expansion as in the conventional least squares minimization approach. It is also possible to choose the value of the two weight coefficients such that $w_1 \neq w_2$.

Statistical characteristics from polynomial chaos expansion.

Due to the orthogonality of shape functions $\psi_j(\boldsymbol{\xi})$ in PCE as defined by Eqn. 2.42, the first and second order moments of multivariate orthonormal polynomials are

$$\mathbb{E}\left[\psi_j(\boldsymbol{\xi})\right] = \begin{cases} 1 & j = 0 \\ 0 & j \neq 0 \end{cases} \tag{2.46}$$

and

$$\mathbb{E}\left[\psi_j(\boldsymbol{\xi})\psi_k(\boldsymbol{\xi})\right] = \begin{cases} 1 & j = k \\ 0 & j \neq k \end{cases} \tag{2.47}$$

respectively.

From polynomial chaos expansion approximation for the function $y(\boldsymbol{\xi})$, the statistical characteristics of the function, i.e. the first and second moment, can be obtained analytically. From the definitions:

$$\mathbb{E}\left[y^{PCE}(\boldsymbol{\xi})\right] = \mathbb{E}\left[\sum_{i=0}^{P} c_i \psi_i(\boldsymbol{\xi})\right] \tag{2.48}$$

and

$$\mathrm{Var}\left[y^{PCE}(\boldsymbol{\xi})\right] = \mathrm{Var}\left[\sum_{i=0}^{P} c_i\psi_i(\boldsymbol{\xi})\right] = \mathbb{E}\left[\left(\sum_{i=0}^{P} c_i\psi_i(\boldsymbol{\xi}) - \mathbb{E}\left[\sum_{i=0}^{P} c_i\psi_i(\boldsymbol{\xi})\right]\right)^2\right] \quad (2.49)$$

Substituting Eqn.2.46 in Eqn.2.48, we get the expression for the mean value of the function as

$$\mathbb{E}\left[y^{PCE}(\boldsymbol{\xi})\right] = c_0 \quad (2.50)$$

Substituting Eqn.2.50 and Eqn.2.47 in Eqn.2.49, the expression for variance of the function can be obtained as

$$\mathrm{Var}\left[y^{PCE}(\boldsymbol{\xi})\right] = \mathbb{E}\left[\left(\sum_{i=0}^{P} c_i\psi_i(\boldsymbol{\xi}) - c_0\right)^2\right] = \mathbb{E}\left[\sum_{i=1}^{P} c_i^2\psi_i^2(\boldsymbol{\xi})\right] = \sum_{i=1}^{P} c_i^2\mathbb{E}\left[\psi_i(\boldsymbol{\xi})^2\right] = \sum_{i=1}^{P} c_i^2 \quad (2.51)$$

The m^{th} order PCE approximation of the variance of $y(\boldsymbol{\xi})$, approaches $\mathrm{Var}\left[y(\boldsymbol{\xi})\right]$ as $m \to \infty$.

2.3 Global sensitivity analysis

The analysis of variance representation allows decomposition of stochastic output $f(\boldsymbol{\xi})$ into summands of increasing dimensions[22]:

$$y = f(\boldsymbol{\xi}) = f_0 + \sum_{i=1}^{n} f_i(\xi_i) + \sum_{1\le i<j\le n} f_{i,j}(\xi_i,\xi_j) \quad + \cdots + f_{1,\ldots,n}(\xi_1,\ldots,\xi_n) \quad (2.52)$$

where n is the total number of random input parameters.

Such decomposition of the function allows the decomposition of the variance of y in the form:

$$D = \sum_{i=1}^{n} D_i + \sum_{1\le i<j\le n} D_{ij} + \cdots + \sum_{1\le i<\cdots<i_s\le n} D_{i_1,\ldots,i_s} + \cdots + D_{1,2,\ldots,n} \quad (2.53)$$

where,

$$D_{i_1,\ldots,i_s} = \int_{\Omega_{\xi_k}} f^2_{i_1,\ldots,i_s}(\xi_k) \prod_{k=i_1,\ldots,i_s} \rho_{\xi_k}(\xi_k)\mathrm{d}\xi_k \text{ for } \mathrm{k} = \mathrm{i}_1,\ldots,\mathrm{i}_\mathrm{s} \quad (2.54)$$

where ρ_{ξ_k} is the probability density function of ξ_k and Ω_{ξ_k} is the support of ξ_k. The support of a continuous random variable is the interval in which its probability density function is positive. Here, $D_i = \mathrm{var}(\mathbb{E}[y|\xi_i])$ is the first order partial variance

and $D_{ij} = \text{var}(\mathbb{E}[y|\xi_i, \xi_j]) - D_i - D_j$ is the second order partial variance and so on. The first order partial variance D_i can be understood as the reduction in variance of y when the random variable ξ_i is assigned a fixed value. Therefore, first order partial variance w.r.t an input parameter gives the individual contribution of that parameter to output variance. The second order partial variance D_{ij} measures the contribution to output variance due to interaction between ξ_i and ξ_j. The Sobol' sensitivity indices [22] are obtained by normalizing the partial variance by total variance D:

$$S_{i_1,\ldots,i_s} = \frac{D_{i_1,\ldots,i_s}}{D} \tag{2.55}$$

$S_{i_1,\ldots,i_s}$ is a measure of the contribution to the total variance due to the uncertainty in value of the set of design parameters $\{\xi_{i_1}, \ldots, \xi_{i_s}\}$. From eqn. (2.53) and eqn. (2.55), the sensitivity indices satisfy the condition

$$\sum_{i=1}^{n} S_i + \sum_{1 \le i < j \le n} S_{ij} + \cdots + S_{1,2,\ldots,n} = 1 \tag{2.56}$$

The total order Sobol' indices S_{T_i} are defined as the sum of all Sobol' indices, starting from first order to the maximum order, that involves the input parameter i. For example for $n = 3$, the total order Sobol' index for the first parameter is given by

$$S_{T_1} = S_1 + S_{12} + S_{13} + S_{123} = 1 - S_2 - S_3 \tag{2.57}$$

The total order Sobol' indices can be used to rank the parameters in the order of their importance. Considering the extreme cases: (i) when $S_{T_i} = 0$: it means that the uncertainty in parameter i does not contribute to the uncertainty in system response and (ii) when $S_{T_i} = 1$: it implies that the uncertainty in output is solely due to the uncertainty in parameter i.

The Sobol' indices are traditionally calculated using MCS which is computationally intensive. PC-based method for calculation of Sobol' indices was proposed [68] as an alternative to using MCS. Consider the stochastic function $f(\boldsymbol{\xi})$ is approximated by a PCE:

$$f(\boldsymbol{\xi}) \approx f_{PCE}(\boldsymbol{\xi}) = \sum_{j=0}^{P-1} c_j \psi_j(\boldsymbol{\xi}) = \sum_{\boldsymbol{\eta} \in \mathbb{N}^m} c_{\boldsymbol{\eta}} \psi_{\boldsymbol{\eta}}(\boldsymbol{\xi}) \tag{2.58}$$

Table 2.2: Polynomial basis constituting a 3^{rd} order PCE of a bivariate function and its corresponding multi-index notation

j	$\boldsymbol{\eta}$	$\psi_j \equiv \psi_{\boldsymbol{\eta}}$
0	[0, 0]	$\psi_0 = 1$
1	[1, 0]	$\psi_1 = \xi_1$
2	[0, 1]	$\psi_2 = \xi_2$
3	[2, 0]	$\psi_3 = (\xi_1^2 - 1)/\sqrt{2}$
4	[1, 1]	$\psi_4 = \xi_1\xi_2$
5	[0, 2]	$\psi_5 = (\xi_2^2 - 1)/\sqrt{2}$
6	[3, 0]	$\psi_6 = (\xi_1^3 - 3\xi_1)/\sqrt{6}$
7	[2, 1]	$\psi_7 = (\xi_1^2 - 1)\xi_2/\sqrt{2}$
8	[1, 2]	$\psi_8 = (\xi_2^2 - 1)\xi_1/\sqrt{2}$
9	[0, 3]	$\psi_9 = (\xi_2^3 - 3\xi_2)/\sqrt{6}$

where, $\boldsymbol{\eta} = \{\eta_1, \ldots, \eta_n\} : \eta_1 \geq 0, \sum_{i=1}^{M} \eta_i \leq p$ is multi-indices defining the multivariate basis polynomial as product of univariate polynomials:

$$\psi_j \equiv \psi_{\boldsymbol{\eta}}(\boldsymbol{\xi}) = \prod_{i=1}^{n} P_{\eta_i}(\xi_i) \tag{2.59}$$

where, P_{η_i} is a univariate polynomial.

The indicial representation of multivariate polynomials is illustrated with an example. Consider a 3^{rd} order PCE of a stochastic function of two random variables ξ_1 and ξ_2 having normal distribution. The basis functions of the PCE for this case, obtained as a product of univariate Hermite polynomials are given in Table 2.2 along with its corresponding multi-index notation η.

For PCE approximation of $f(\boldsymbol{\xi})$ given by eqn. (2.58), the PC-based Sobol' indices are defined as [68]:

$$S^{PCE}_{i_1,\ldots,i_s} = \sum_{\boldsymbol{\eta} \in \mathcal{L}_{i_1,\ldots,i_s}} c^2_{\boldsymbol{\eta}} \mathbb{E}\left[\psi^2_{\boldsymbol{\eta}}\right] / D_{PCE} \tag{2.60}$$

where $\mathcal{L}_{i_1,\ldots,i_s} = \{\boldsymbol{\eta} \in \mathbb{N}^n : \eta_k \neq 0 \iff k \in (i_1, \ldots, i_s)\}$ is the set of multi-indices depending exactly on the subset of variables $\{i_1, \ldots, i_s\}$ and D_{PCE} is the variance of the stochastic function calculated from PCE:

$$D_{PCE} = \sum_{j=1}^{P-1} c_j^2 \mathbb{E}\left[\psi_{\boldsymbol{\eta}}^2\right] \tag{2.61}$$

Therefore, once the PCE approximation is obtained, the sensitivity indices can be calculated analytically by selecting the coefficients in the expansion based on the dependency of each basis polynomial which is then square-summed and normalised as shown in Eqn. (2.60).

2.4 An analytical expression for the probability distribution of stochastic response of bladed disk

In Sections 2.2.1 and 2.2.2, methodologies for two different surrogate models that can approximate the deformation of bladed disk with respect to variation in blade anisotropy angles were presented. The use of polynomial chaos expansion based surrogate models allows fast and efficient estimation of the statistical characteristics of the probability distribution of blade deformation for the known probability distribution of the design parameters. However, the full description of the stochastic response of bladed disk can only be provided by the probability density functions. In this section, a methodology for determination of the probability density function for the deformation of bladed disk in terms of the sensitivity and known statistical characteristics of the design parameters is developed.

The strategy employed here to obtain the probability distribution functions of the stochastic response of blades in the bladed disk with respect to a known probability distribution of blade anisotropy angles can be described in the following three steps [100]:

1 A sensitivity based approximation for the response of the bladed disk to variation in blade anisotropy angles is obtained.

2 Based on the approximated response, a constraint for the anisotropy angle is derived such that the response of the structure does not exceed a pre-defined value.

3 The probability distribution functions for the blade response level is derived analytically based on known PDFs of the blade anisotropy angles after imposing the constraints for the anisotropy angle obtained from the previous step.

Let us now consider the approach in detail. The stochastic response of bladed disk can be approximated in many cases as a linear combination of the blade anisotropy angles and the corresponding sensitivity value for bladed response with respect to those angles:

$$a(\boldsymbol{\xi}) \approx a_0 + \sum_{j=1}^{N} s_{\alpha_j}(\alpha_j - \mu_\alpha) + s_{\beta_j}(\beta_j - \mu_\beta) + s_{\zeta_j}(\zeta_j - \mu_\zeta) \tag{2.62}$$

where, $a(\boldsymbol{\xi})$ is the stochastic response of a blade as a function of $\boldsymbol{\xi}$, which the vector of blade anisotropy angles of N blades in the bladed disk; a_0 is the blade response corresponding to mean value of anisotropy angles obtained from finite element analysis of the bladed disk; s_{α_j}, s_{β_j} and s_{ζ_j} are the sensitivities of blade response to angles α, β and ζ respectively of the j^{th} blade; μ_α, μ_β and μ_ζ are the mean values of anisotropy angles α, β and ζ respectively.

From Eqn. (2.62), the expression for anisotropy angle α_1 of the first blade such that the response of the blade does not exceed a specified value, ϵ takes the form:

$$\alpha_1(\epsilon) = \mu_\alpha + \left(\epsilon - a_0 - \sum_{j=2}^{N} s_{\alpha_j}(\alpha_j - \mu_\alpha) - \sum_{j=1}^{N} s_{\beta_j}(\beta_j - \mu_\beta) - \sum_{j=1}^{N} s_{\zeta_j}(\zeta_j - \mu_\zeta) \right) / s_{\alpha_1} \tag{2.63}$$

For the case of blade anisotropy angles, it is assumed that each blade anisotropy angle is stochastically independent. Therefore, the probability that the stochastic response of bladed disk does not exceed the value ϵ can be written as:

$$P(a(\boldsymbol{\xi}) < \epsilon) = \int_{-\infty, a<\epsilon}^{\infty} p_\alpha(\alpha_1) \ldots p_\beta(\beta_1) \ldots p_\zeta(\zeta_1) \ldots p_\zeta(\zeta_N) \mathrm{d}\alpha_1 \ldots \mathrm{d}\beta_1 \ldots \mathrm{d}\zeta_1 \ldots \mathrm{d}\zeta_N \tag{2.64}$$

where, p_α, p_β and p_ζ are the known probability distribution functions of anisotropy angles α, β and ζ respectively.

Based on the above restriction for α_1, Eqn. (2.64), defining the probability of

stochastic response not exceeding ϵ can be written in the following form:

$$\begin{aligned} P(\epsilon) &= \int_{-\infty}^{\infty} p_\zeta(\zeta_N) \cdots \int_{-\infty}^{\alpha_1(\epsilon,\alpha_2,\ldots,\zeta_N)} p_\alpha(\alpha_1) \mathrm{d}\alpha_1 \ldots \mathrm{d}\zeta_N \text{ for } s_{\alpha_1} > 0 \\ P(\epsilon) &= \int_{-\infty}^{\infty} p_\zeta(\zeta_N) \cdots \int_{\alpha_1(\epsilon,\alpha_2,\ldots,\zeta_N)}^{\infty} p_\alpha(\alpha_1) \mathrm{d}\alpha_1 \ldots \mathrm{d}\zeta_N \text{ for } s_{\alpha_1} < 0 \end{aligned} \tag{2.65}$$

The probability distribution functions for the stochastic response can be obtained from Eqn. (2.65) as

$$p(\epsilon) = |s_{\alpha_1}|^{-1} \int_{-\infty}^{\infty} p_\zeta(\zeta_N) \cdots \int_{-\infty}^{\infty} p_\alpha(\alpha_1(\epsilon, \alpha_2, \ldots, \zeta_N)) \mathrm{d}\alpha_2 \ldots \mathrm{d}\zeta_N \tag{2.66}$$

where, s_{α_1} is the value of sensitivity of the considered static displacement or forced response amplitude of the bladed disk with respect to the anisotropy angle α of the first blade. For a given bladed disk model, the value of s_{α_1} will vary depending on the considered stochastic response of the bladed disk.

For the case of tuned bladed disk, the number of blade anisotropy angles which are random is limited to three, and therefore, the expression for pdf of stochastic response, given by Eqn. (2.66), can be evaluated analytically depending on the choice of the probability distribution of the anisotropy angles.

For example, assuming the following distribution of anisotropy angles:

$$\begin{aligned} \alpha &\sim \text{Normal}(\mu_1, \sigma_1) \\ \beta &\sim \text{Uniform}(\mu_2 - \sqrt{3}\sigma_2, \mu_2 + \sqrt{3}\sigma_2) \\ \zeta &\sim \text{Weibull}(\eta, \theta, \tau) \end{aligned}$$

For a tuned bladed disk with three random anisotropy angles, the expression for anisotropy angle α_1, such that the blade response does not exceed ϵ can be obtained from Eqn. (2.63):

$$\alpha_1(\epsilon, \beta_1, \zeta_1) = \mu_1 + \left(\epsilon - a_0 - s_2(\beta - \mu_2) - s_3(\zeta - \mu_3)\right) / s_1 \tag{2.67}$$

where μ_1, μ_2 and μ_3 are the mean values of the distribution of anisotropy angles α, β and ζ respectively and s_1, s_2 and s_3 are sensitivities of blade response to those anisotropy angles. The expression for probability density function (PDF) of blade

response can be obtained by evaluating the following integral:

$$
\begin{aligned}
p(\epsilon) =& |s_1|^{-1} \int_{-\infty}^{-\infty} p_\zeta(\zeta_1) \int_{\mu_2-\sqrt{3}\sigma_2}^{\mu_2+\sqrt{3}\sigma_2} p_\beta(\beta_1) p_\alpha(\alpha_1(\epsilon, \beta_1, \zeta_1)) \mathrm{d}\beta_1 \mathrm{d}\zeta_1 \\
=& \frac{1}{|s_1|} \int_{-\infty}^{\infty} \left[\begin{cases} 0 & \zeta < \tau \\ \frac{\eta(\zeta-\tau)^{\eta-1} e^{-\left(\frac{\zeta-\tau}{\theta}\right)^\eta}}{\theta^\eta} & \text{else} \end{cases} \right] \left[\frac{\sqrt{3}s_1}{12\tilde{\sigma_2}} \left(\mathrm{erf}\left(\frac{a_0 - \epsilon + \sqrt{3}\tilde{\sigma_2} + s_3(\zeta - \mu_3)}{\sqrt{2}\sigma_1 s_1} \right) \right. \right. \\
& \left. \left. -\mathrm{erf}\left(\frac{a_0 - \epsilon - \sqrt{3}\tilde{\sigma_2} + s_3(\zeta - \mu_3)}{\sqrt{2}\sigma_1 s_1} \right) \right) \right] \mathrm{d}\zeta
\end{aligned}
\tag{2.68}
$$

where $\tilde{\sigma_2} = \sigma_2 s_2$. The integral in Eqn.2.68 must be evaluated numerically to obtain the required PDF for blade response with respect to the assumed probability distribution of the three anisotropy angles of the tuned bladed disk. Note that depending on the probability distribution of anisotropy angles, the required probability distribution of the blade response can be obtained analytically or semi-analytically. For example, consider the following distribution of anisotropy angles:

$$
\begin{aligned}
\alpha &\sim \text{Normal}(\mu_1, \sigma_1) \\
\beta &\sim \text{Uniform}(\mu_2 - \sqrt{3}\sigma_2, \mu_2 + \sqrt{3}\sigma_2) \\
\zeta &\sim \text{Uniform}(\mu_3 - \sqrt{3}\sigma_3, \mu_3 + \sqrt{3}\sigma_3)
\end{aligned}
$$

The expression for PDF can be obtained completely analytically:

$$
\begin{aligned}
p(\epsilon) =& |s_1|^{-1} \int_{\mu_3-\sqrt{3}\sigma_3}^{\mu_3+\sqrt{3}\sigma_3} p_\zeta(\zeta_1) \int_{\mu_2-\sqrt{3}\sigma_2}^{\mu_2+\sqrt{3}\sigma_2} p_\beta(\beta_1) p_\alpha(\alpha_1(\epsilon, \beta_1, \zeta_1)) \mathrm{d}\beta_1 \mathrm{d}\zeta_1 \\
=& \frac{1}{|s_1|} \int_{l_1}^{l_2} \left[\begin{cases} 0 & \zeta < \mu_3 - \sqrt{3}\sigma_3 \\ \sqrt{3}/6\sigma_3 & \zeta < \mu_3 + \sqrt{3}\sigma_3 \\ 0 & \text{else} \end{cases} \right] \left[\frac{\sqrt{3}s_1}{12\tilde{\sigma_2}} \left(\mathrm{erf}\left(\frac{a_0 - \epsilon + \sqrt{3}\tilde{\sigma_2} + s_3(\zeta - \mu_3)}{\sqrt{2}\sigma_1 s_1} \right) \right. \right. \\
& \left. \left. -\mathrm{erf}\left(\frac{a_0 - \epsilon - \sqrt{3}\tilde{\sigma_2} + s_3(\zeta - \mu_3)}{\sqrt{2}\sigma_1 s_1} \right) \right) \right] \mathrm{d}\zeta
\end{aligned}
\tag{2.69}
$$

where, $\tilde{\sigma_2} = \sigma_2 s_2$, $l_1 = \mu_3 - \sqrt{3}\sigma_3$, and $l_2 = \mu_3 + \sqrt{3}\sigma_3$. The integral in Eqn.(2.69) can be evaluated analytically which is not shown here for brevity. The expressions for PDF given by Eqn. (2.68) and (2.69) are obtained by integrating the normal distribution defining the angle α, over $-\infty$ to ∞. In reality the range of variation of the anisotropy angles is restricted within the limits specified by the manufacturer of the blades. Such restriction of the angle can introduce some error in the analytical

PDF, the magnitude of which will depend on the value of mean and standard deviation of the normal distribution. For the present study, the area under the normal distribution that lies outside the range of variation of the anisotropy angle α is less than 5% of the total area under the normal distribution. Therefore, for the present study, the error introduced due to specifying finite range for the variation of angle α is neglected.

Chapter 3

Finite element modelling

Single crystal blades exhibit material anisotropy and the orientation of the crystal anisotropy axis influence the response of the bladed disk to mechanical loads. Due to manufacturing tolerances, each blade in a bladed disk will differ from another in terms of the crystal orientation, and therefore, induce mistuning in the bladed disks.

In order to investigate the effects of scatter in crystal anisotropy orientation of single crystal blades on static and dynamic response of bladed disks, realistic high–fidelity finite element models of the bladed disk are used. All finite element models used in the present study are provided by MTU Aero Engines AG. Using finite element models, sensitivity and uncertainty analysis are performed to quantify the effect of variation in blade anisotropy orientation on static and dynamic response of the bladed disk.

Finite tolerance in manufacturing results in small variations in fir–tree root and shroud geometry of blades. Depending on the manufacturing tolerance condition of blade root and disk slot, the area and position of contact between blade and disk could vary. Similarly depending on the manufacturing tolerance of shroud, the shroud-to-shroud contact region between adjacent blades could also vary from blade to blade. To investigate the effects of root and shroud geometry variations on non-linear static deformation, finite element models of bladed disk sector geometry with different fir–tree root and shroud contact regions are analysed.

In this chapter, detailed descriptions of various finite element models of bladed disks

used to study the current set of problems are presented. This chapter is laid out in the following fashion. Firstly, different finite element models of bladed disk used for computation are presented. Further, the details of the finite element boundary conditions used are described.

3.1 Finite element model of bladed disk

Considering blade material anisotropy angles as stochastic design parameters, uncertainty and sensitivity analysis for the response of the bladed disk has been performed using finite element models of a realistic bladed disk. The full model of the bladed disk with 75 blades attached to the disk is shown in Fig. 3.1. The blades are attached to disk using fir–tree root joints and are connected through shrouds. The disk is modelled as an isotropic material, and the blades are modelled as an orthotropic material.

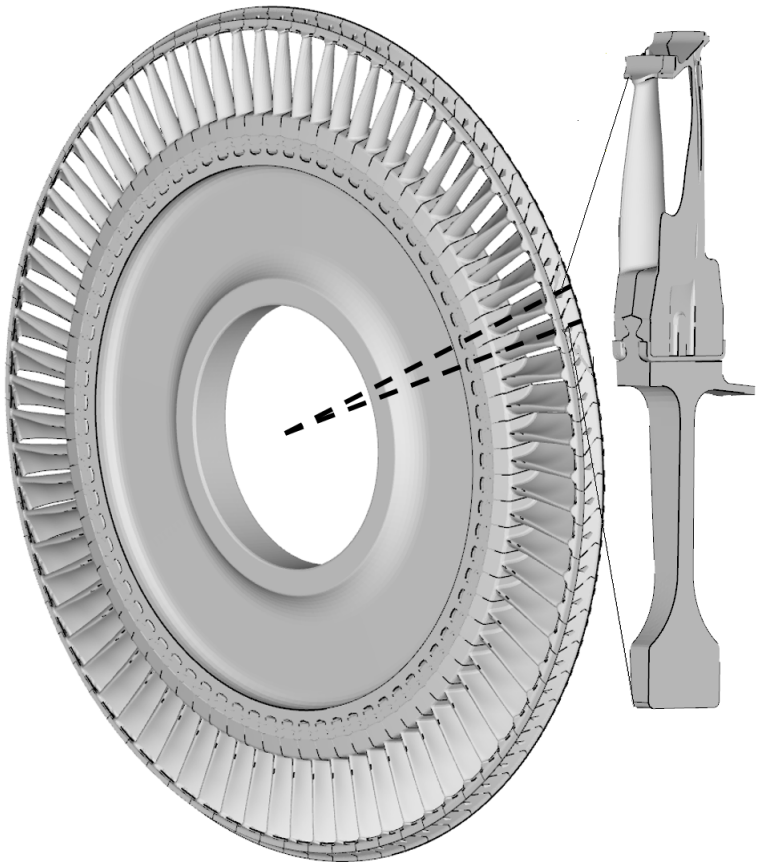

Figure 3.1: Model of the full bladed disk

The finite element model of the full bladed disk with 0.5 million nodes is shown in

the Fig.3.2. Ten-node tetrahedral elements are used in the finite element model. The total number of contact elements used to model the blade to disk fir–tree root contacts are 17475 and to model blade to blade shroud contacts are 3075.

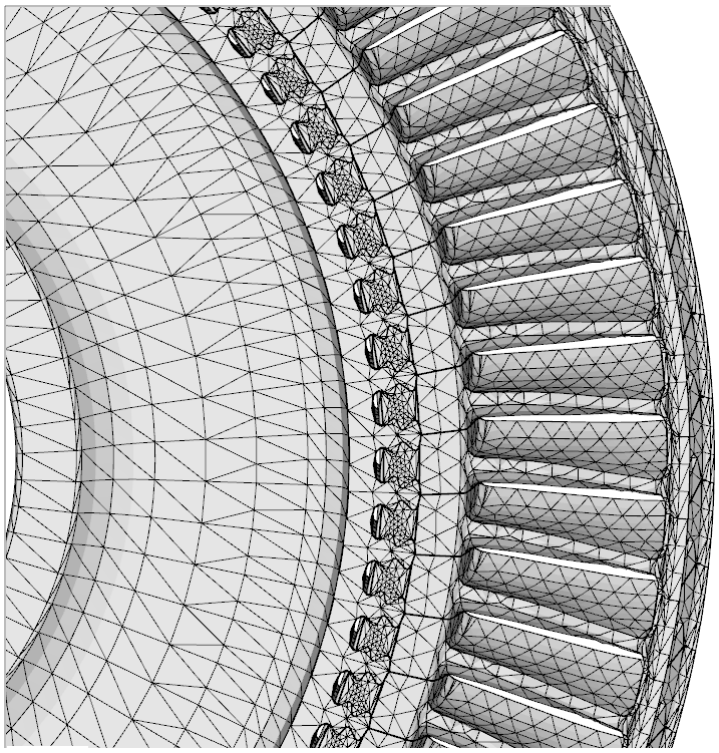

Figure 3.2: A section of the finite element model of the bladed disk.

Sector models of bladed disks are used to study the effects of variations in fir–tree root and shroud geometry on static deformation of the tuned bladed disk. By using sector models with cyclic symmetry constraints applied, the computational cost involved in finite element analysis can be significantly reduced when tuned bladed disk is analysed. Two different sector geometries of the bladed disk are used. Fig.3.3(a) shows the finite element mesh of blade sector model used to investigate the effect of fir–tree root and shroud geometry variations. The finite element model of the bladed disk sector has 128071 nodes. The number of friction contact elements used to model the root joints, and shroud joints are 2160 and 141 respectively. A coarser finite element model of the bladed disk sector geometry with only 6874 nodes is used to study the influence of blade material anisotropy orientation on the natural frequency of the tuned bladed disk. This model is shown in Fig. 3.3(b).

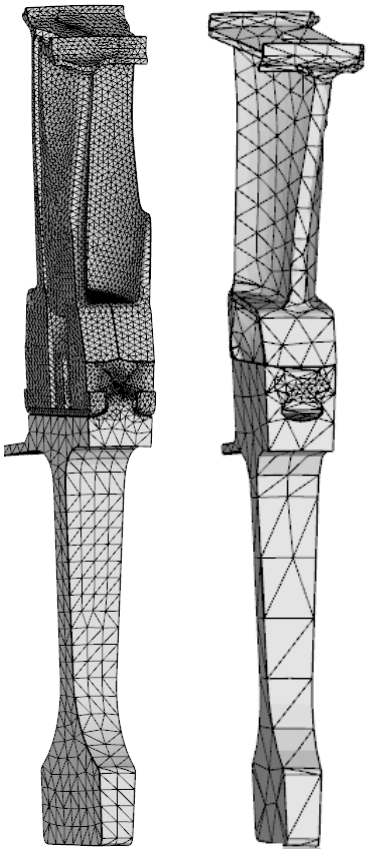

(a) (b)

Figure 3.3: Finite element model of the bladed disk sector having (a) 128071 nodes and (b) 6874 nodes.

3.2 Finite element model constraints and boundary conditions

The blade-to-disk fir–tree root joints and blade-to-blade shroud joints are modelled as either linear bonded contacts or as non-linear friction contacts. The bonded contacts are defined based on multipoint constraints (MPCs), and friction contacts are defined as surface-to-surface penalty contacts. For fir–tree root the patches of contact elements on blade root and disk slot are shown in Fig. 3.4(a) and (b) respectively.

In order, to investigate the effect of crystal anisotropy mistuning, full bladed disk model is used. The degrees of freedom of nodes on the rim of the bladed disk, shown in Fig.3.5(a), is constrained in the axial and tangential direction in order to model

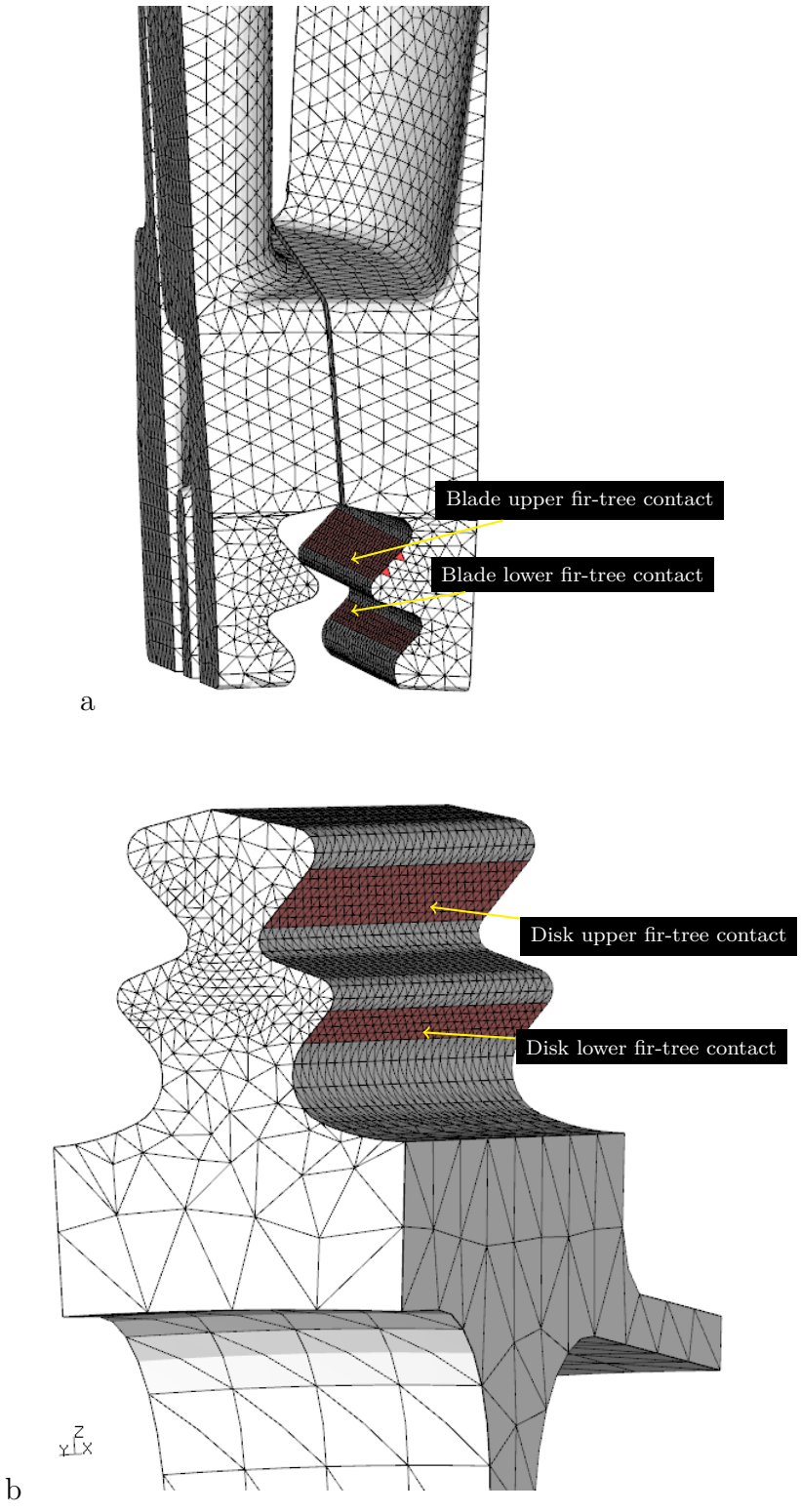

Figure 3.4: Contact patches on right-hand side of (a) blade root and (b) disk slot.

the effect of neighbouring bladed disks. For analysis of tuned bladed disk, the sector models of bladed disk are used, and cyclic symmetric constraints are applied on all nodes on either side of the bladed disk sector model shown in Fig.3.5(b).

Finite element analysis is performed using CalculiX [102] which is an open source finite element analysis package used in both academic and industrial settings.

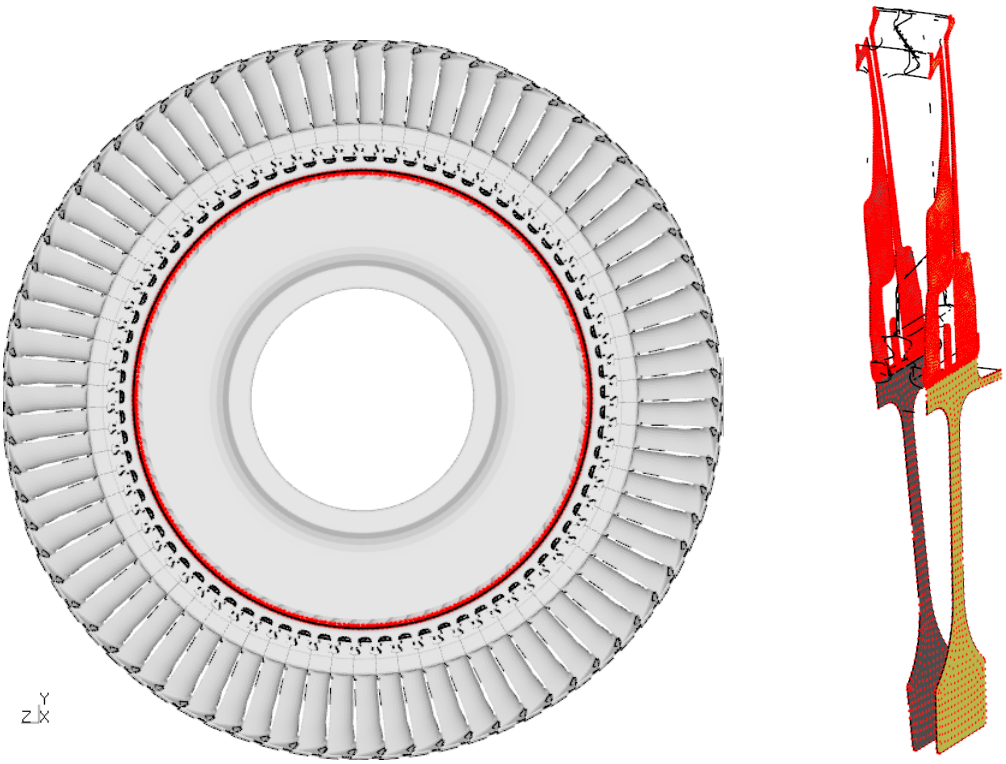

(a) (b)

Figure 3.5: Figure showing (a) nodes on the rim of the bladed disk where axial and tangential DOF are constrained, and (b) nodes where cyclic symmetry constraints are applied.

3.3 Integration of the FE solver with tools for uncertainty analysis and optimisation

3.3.1 The framework for uncertainty and global sensitivity analysis

The uncertainty in the crystal orientation of the blades will result in uncertainty in the static and dynamic response of a bladed disk. When the probability density function of anisotropy angles, defining the crystal orientation of blades are available, uncertainty and sensitivity analysis can be performed to quantify the scattering in the response of the bladed disk. In order to perform uncertainty and sensitivity analysis, a Python code namely *ChaoStat* was developed the author. The code allows seamless integration of different tools used for FE analysis, forced response analysis, and for building polynomial chaos approximation.

A schematic diagram illustrating different tools used by *ChaoStat*, the specific function of each of those tools, and the flow of control within *ChaoStat* is shown in Fig. 3.6(a). A brief description of the different tools used in *ChaoStat* is given below:

1. *ChaosPy* [103] – An open source tool used for designing methods for uncertainty analysis using polynomial chaos expansion and Monte Carlo methods. The tool is available as a Python module for installation. Within *ChaoStat* code, the tool is used for sampling the input parameter space based on the user-defined probability distribution of individual blade anisotropy angles, for generating orthogonal basis functions for PCE, and to calculate the statistical characteristics of blade response as well as the global sensitivity indices of blade anisotropy angles. As part of this work, the capability to use gradient values of functions for calculating the coefficients in polynomial chaos approximation was developed using the standard *ChaosPy* module.

2. *CalculiX* [102] – An open source FE package used for building, solving and post–processing finite element models. *CalculiX* package includes the FE solver, *CalculiX CrunchiX*, and the graphical interface *CalculiX GraphiX*. Within *ChaoStat*, CalculiX is used for linear and non-linear static analysis,

modal analysis, and local sensitivity analysis of static deformation and modal properties of the bladed disk with respect to blade anisotropy angles [105].

3. *ContaDyn* – An in–house code developed as part of the current project [110]. The code is used for forced response analysis of complex structures with contact non-linearities using harmonic balance method and a novel approach for condensation of DOF for high-fidelity FE models [111]. Within *ChaoStat*, *ContaDyn* is used for forced response analysis and to obtain the local sensitivity of forced response amplitude [95] of the bladed disk with respect to the crystal orientation of blades.

4. *SciPy* – SciPy is a collection of mathematical algorithms, arranged as different sub–packages, available to a Python programmer [112]. Within *ChaoStat*, the *SciPy* package for linear algebra named *scipy-linalg* is used for solving a system of linear equations.

3.3.2 The framework for optimisation

The amplification of forced response of a mistuned bladed disk, in comparison to that of a tuned bladed disk with same blade crystal orientations, can be reduced by optimising the crystal orientation of blades in the bladed disk. In order to perform the optimisation of the blade anisotropy angles, a Python code was developed to integrate an open source optimisation framework namely OpenMDAO [113] to the FE solver *CalculiX* and the forced response analysis tool *ContaDyn*. In order to convert the modal analysis results of *CalculiX* to the input format of *ContaDyn*, a code developed by Adam Koscso [105] was used. A schematic diagram illustrating different tools used in the code for optimisation of blade anisotropy angles, the specific function of each of those tools, and the flow of control within the code is shown in Fig. 3.6(b).

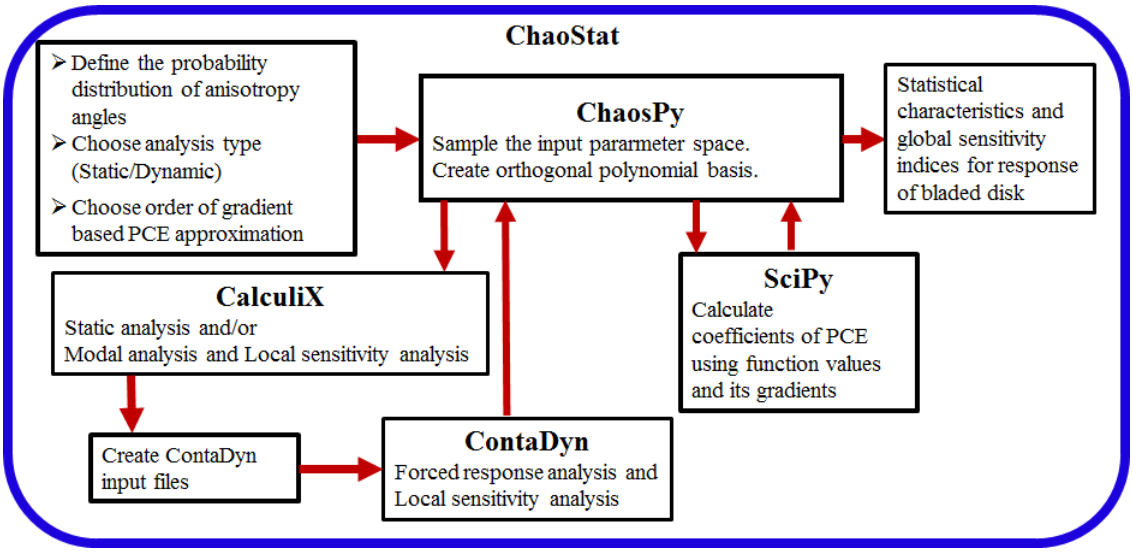

(a)

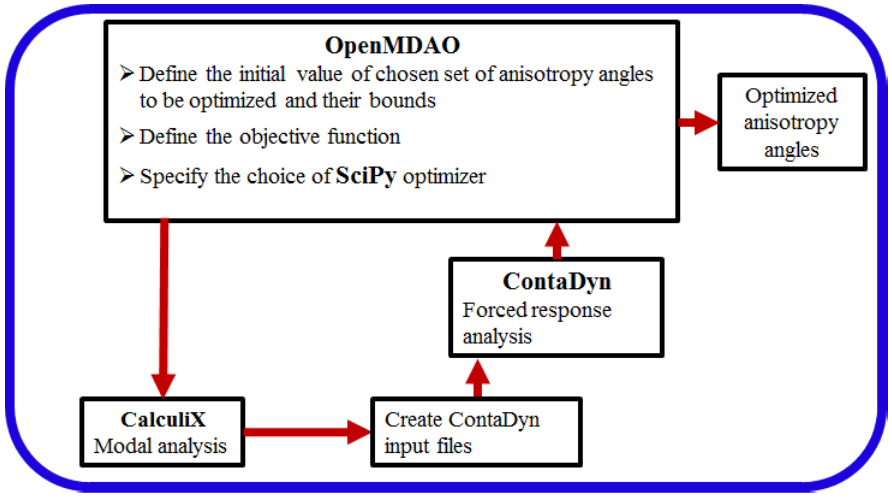

(b)

Figure 3.6: Schematic diagram showing the framework for (a) uncertainty and global sensitivity analysis, and for (b) optimisation of the blade anisotropy angles.

Chapter 4

Sensitivity of static deformation to blade anisotropy orientations

In this chapter, the methods discussed in Chapter 2 for obtaining local sensitivity of displacements (Eqn. 2.13) and stresses (Eqn. 2.18, 2.20) and for global sensitivity (Eqn. 2.55) are applied to static deformation of anisotropy mistuned bladed disk under centrifugal loading. To study the effects of blade material anisotropy mistuning on static displacements and stresses, bladed disk with linear and non-linear contacts at fir–tree root and shroud interfaces are analysed. Mistuning is introduced by sampling the material anisotropy angles, α, β and ζ, of each blade of the bladed disk randomly from the realistic statistical distribution for these angles provided by the manufacturer. An example of the realistic distribution of blade anisotropy angles for all blades in the mistuned bladed disk is shown in Fig. 4.1. In the figure, the angles for α, β and ζ are normalized by the maximum value of those angles in the considered pattern.

4.1 Deformation of a mistuned bladed disk

In order to investigate the effects of blade anisotropy mistuning on static deformation of the bladed disk under centrifugal loading, corresponding to a realistic rotational speed specified by the manufacturer, both linear and non–linear models are analysed. While non–linear model has friction contacts at fir–tree root and

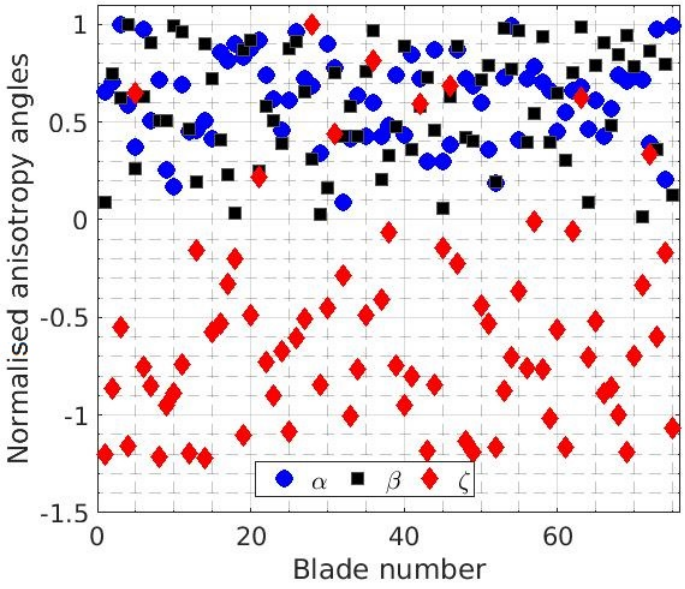

Figure 4.1: Distribution of the normalised anisotropy angles of all blades for an example mistuning pattern.

shroud interfaces, for a linear model these interfaces are modelled as bonded contact. For the mistuning pattern shown in Fig. 4.1 the variation in normalised axial, circumferential and radial displacements at blade tip node of all blades in the bladed disk is shown in Fig. 4.2(a), (b) and (c) respectively for linear and non-linear bladed disk. The value of displacement and the local sensitivity of displacement presented in this chapter are normalised with respect to the maximum radial displacement value for the non-linear tuned bladed disk with crystal orientation aligned with blade geometry. For the mistuning pattern studied, the variation in displacements along axial, circumferential and radial direction are 12%, 14% and 2.5%. In comparison with the variation of displacement for non-linear bladed disk, it is observed that the scatter in displacement for the linear bladed disk is larger with respective values for axial, circumferential and radial displacement being 18%, 33% and 5%. Note that for the linear bladed disk model, each blade is connected to its adjacent blade through bonded contact at shroud and therefore, results in a stiffer connection between blades. Therefore, in the case of linear bladed disk, the structure is comparatively more sensitive to variation in blade anisotropy orientation of blades. The magnitude of blade displacements for the non-linear bladed disk is higher compared to that of the linear bladed disk given the same mistuning pattern which substan-

tiates the argument that bonded contacts at interfaces increases the stiffness of the structure. In the case of a bladed disk with friction contact interfaces at shrouds, the friction interface reduces the effect of variation in anisotropy angles of a blade on the deformation of other blades.

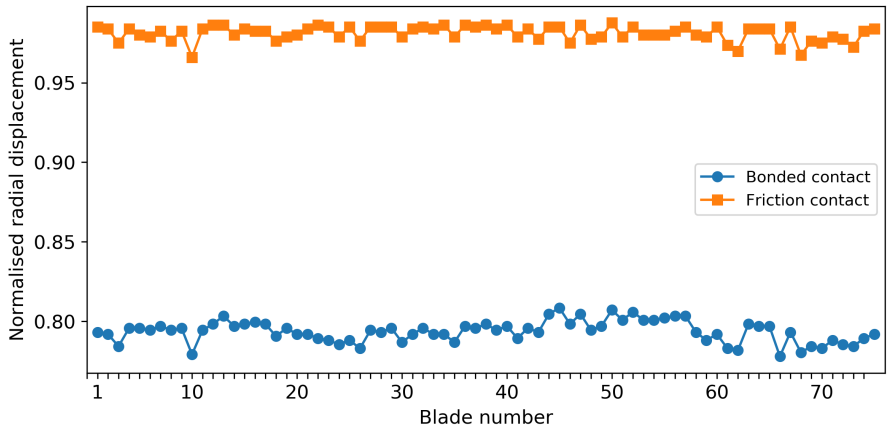

(a)

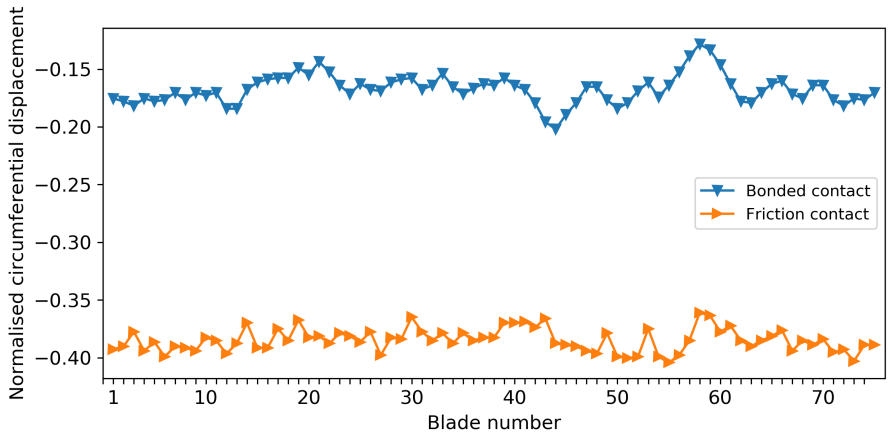

(b)

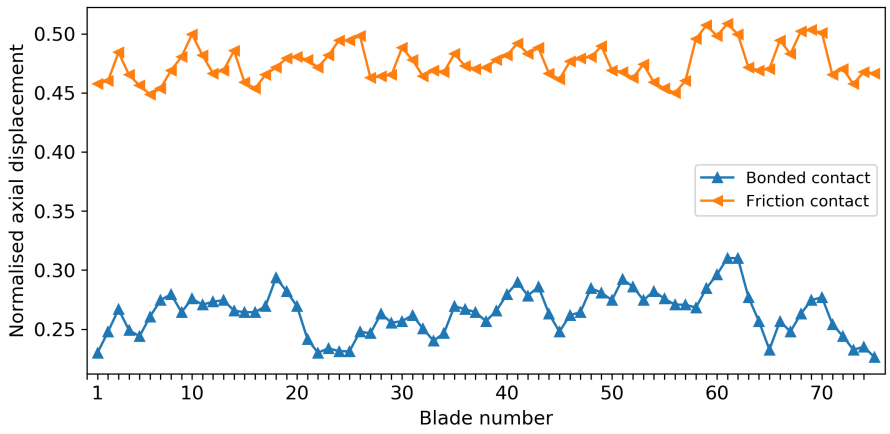

(c)

Figure 4.2: Displacements at blade tip node of all blades in (a) radial (b) circumferential and (c) axial direction in a mistuned bladed disk

For a sample mistuning pattern, the normalized displacements of the bladed disk along axial, tangential and radial directions are shown in Figs. 4.3(a), (b) and (c) respectively for a blade tip node. The displacement values are normalized with respect to the value of radial displacement at the considered node for the case of a tuned bladed disk with the blade anisotropy axis aligned with the blade geometry axis. By comparing the axial displacement of different blades, it can be observed that, due to mistuning, there is a difference in displacements from blade to blade. In order to highlight the small variation in axial displacements between blades, a zoomed view of several blades in the bladed disk is shown in the inset in Fig. 4.3(a). Compared to the differences in blade displacements along the axial direction between different blades in the bladed disk, the difference in displacements along the tangential direction and radial direction is not easily discernible from Fig. 4.3(b) and (c).

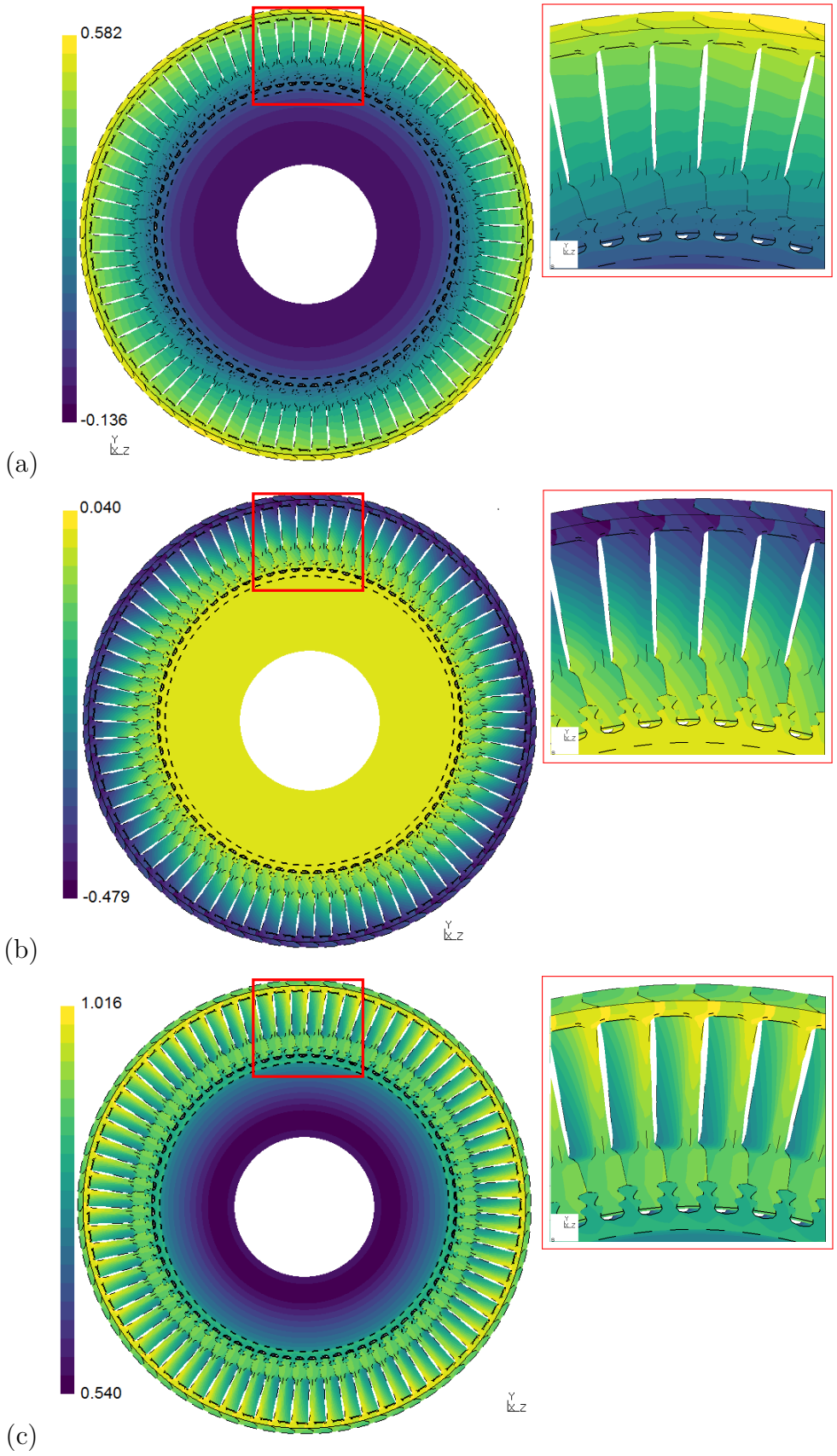

Figure 4.3: Figure showing (a) axial, (b) circumferential and (c) radial displacement of a mistuned bladed disk.

4.2 Local sensitivity analysis

In this section, based on local sensitivity analysis, the influence of crystal orientation of blades on displacements and stresses in a mistuned bladed disk with (i) linear bonded contacts and (ii) non-linear friction contacts at blade roots and shrouds are investigated.

Local sensitivity analysis is used to quantify the effect of small variations in blade anisotropy angles on deformation of the bladed disk. Therefore, based on local sensitivity analysis, it is possible to identify the most important anisotropy angles concerning their influence on the deformation of the structure. Further, while performing the uncertainty analysis, this information can be used to reduce the dimensionality of the problem by ignoring the anisotropy angles that are less influential. Depending on the method used for uncertainty analysis, such a reduction in dimensionality of the problem will allow us to reduce the computational cost significantly. For non-linear mistuned bladed disk, Fig. 4.4(a), (b) and (c) shows the sensitivity of the axial component of displacements due to anisotropy angles α, β and ζ of blade number 1 respectively. The value of displacement sensitivities presented in this section is normalised with respect to the maximum radial displacement value for the non-linear tuned bladed disk. While a small variation in material anisotropy angles of blade number 1 influences the displacements of adjacent blades apart from blade 1 itself, it has no significant influence on the displacement of blades located farther from blade 1 and also on displacements of the disk. While a positive value of displacement sensitivity indicates that the displacement increases with a small change in the anisotropy angle, a negative value indicates that the displacement decreases with a small change in anisotropy angle.

The location of maximum sensitivity of displacement, with respect to blade anisotropy angles, along the blade will vary depending on the considered anisotropy angle. For example, the sensitivity of axial displacement to anisotropy angle α is maximum at the leading edge around mid-span. Note that the maximum sensitivity with respect to anisotropy angle β is at blade root and shrouds. Fig. 4.5(a), (b) and (c) shows the sensitivity of tangential displacement with respect to blade anisotropy angles α, β and ζ of blade number 1. The negative values for sensitivity indicate that

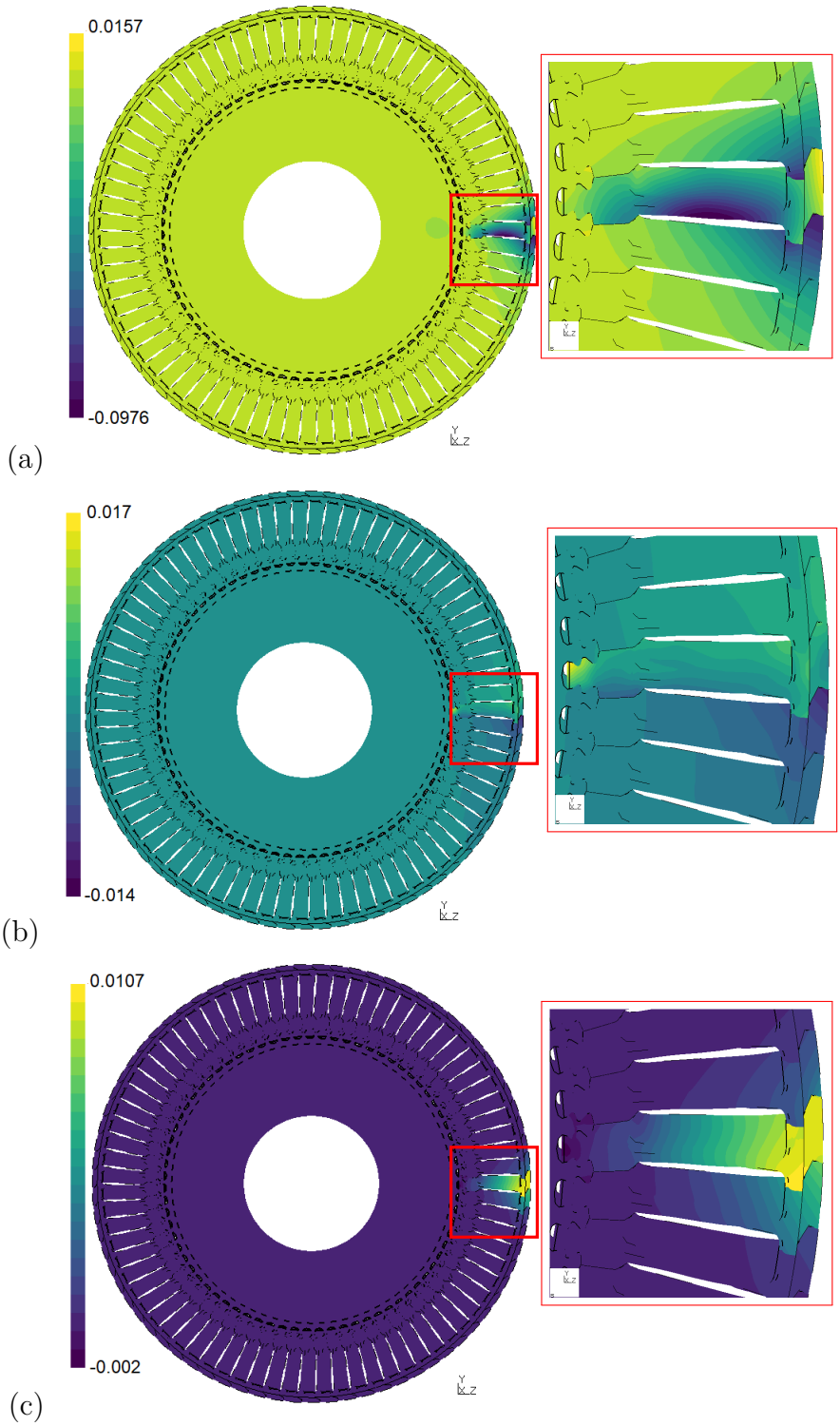

Figure 4.4: Local sensitivity of axial displacement of a mistuned bladed disk w.r.t anisotropy angles (a) α, (b) β and (c) ζ of blade number 1.

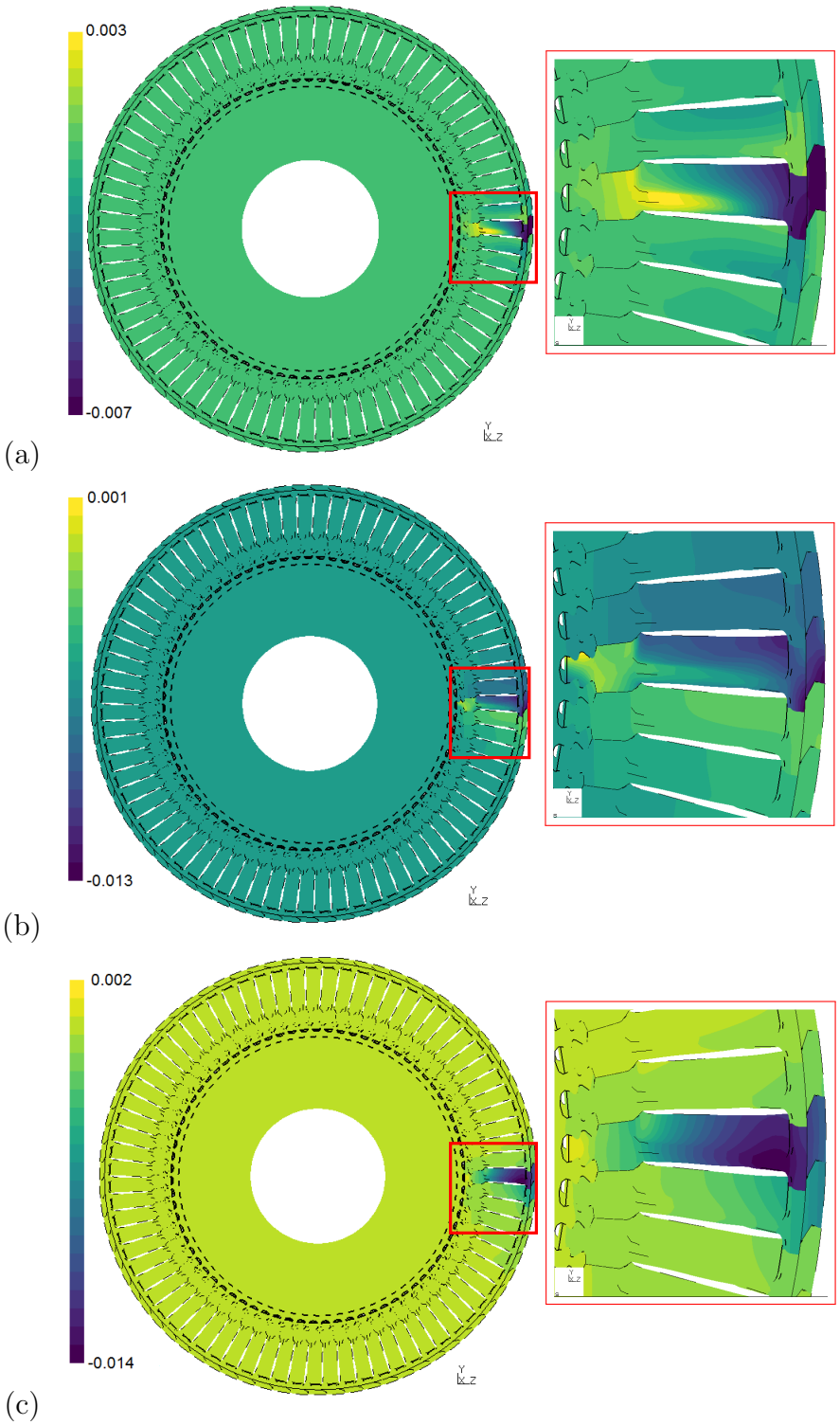

Figure 4.5: Local sensitivity of tangential displacement of a mistuned bladed disk w.r.t anisotropy angles (a) α, (b) β and (c) ζ of blade number 1.

the tangential displacement towards the shroud region of the blade decreases for a small change in anisotropy angles. Fig. 4.6(a), (b) and (c) shows the sensitivity of radial displacement to the three blade anisotropy angles of blade number 1. For the considered mistuning pattern, and in general, the displacements along the radial direction, is most sensitive to anisotropy angle α. By analysing many mistuning patterns, it was inferred that the magnitude of sensitivity for radial displacement with respect to anisotropy angle α is an order of magnitude higher than that with respect to angle ζ.

A comparison of the sensitivity analysis of bladed disk with linear bonded contact and non–linear friction contacts at fir–tree root and shrouds gives valuable information on how the presence of friction joints affects the uncertainty in blade deformation due to scattering in crystal orientation. For tuned linear bladed disk, with anisotropy axis aligned with blade geometry axis, Fig. 4.7(a), (b) and (c) shows the sensitivity of displacements at blade tip of blade number 1 with respect to anisotropy angles α, β, and ζ of all blades in the bladed disk. A similar plot for the mistuned bladed disk with linear bonded contacts at blade-to-disk and blade-to-blade interface is shown in Fig. 4.8. Even though mistuning has significantly changed the influence of individual blade anisotropy angles, especially of those blades positioned close to the considered blade, the maximum value of displacement sensitivity is comparable to that of the tuned case. This is particularly noticeable for the case of sensitivity to anisotropy angle β and ζ. For a non-linear mistuned bladed disk, Fig. 4.9(a), (b), and (c) shows the normalised sensitivity of blade displacements at a selected node on blade number 1 to anisotropy angles α, β, and ζ of all blades. It was already mentioned in Section 4.1 that in the presence of friction joints, the effect of anisotropy angle of a specified blade on displacements of adjacent blades decreases. A comparison of Fig. 4.8(b) and Fig. 4.9(b), for the case of anisotropy angle β, and Fig. 4.8(c) and Fig. 4.9(c), for angle ζ, shows that the number of blade anisotropy angles with a high value of sensitivity has considerably reduced for the non-linear mistuned bladed disk. In comparison with that of linear mistuned bladed disk, the sensitivity of axial and tangential displacement to ζ has increased significantly. On the contrary, there is noticeable decrease in sensitivity of displacements with respect to *beta* for non-linear bladed disk compared to the linear bladed disk.

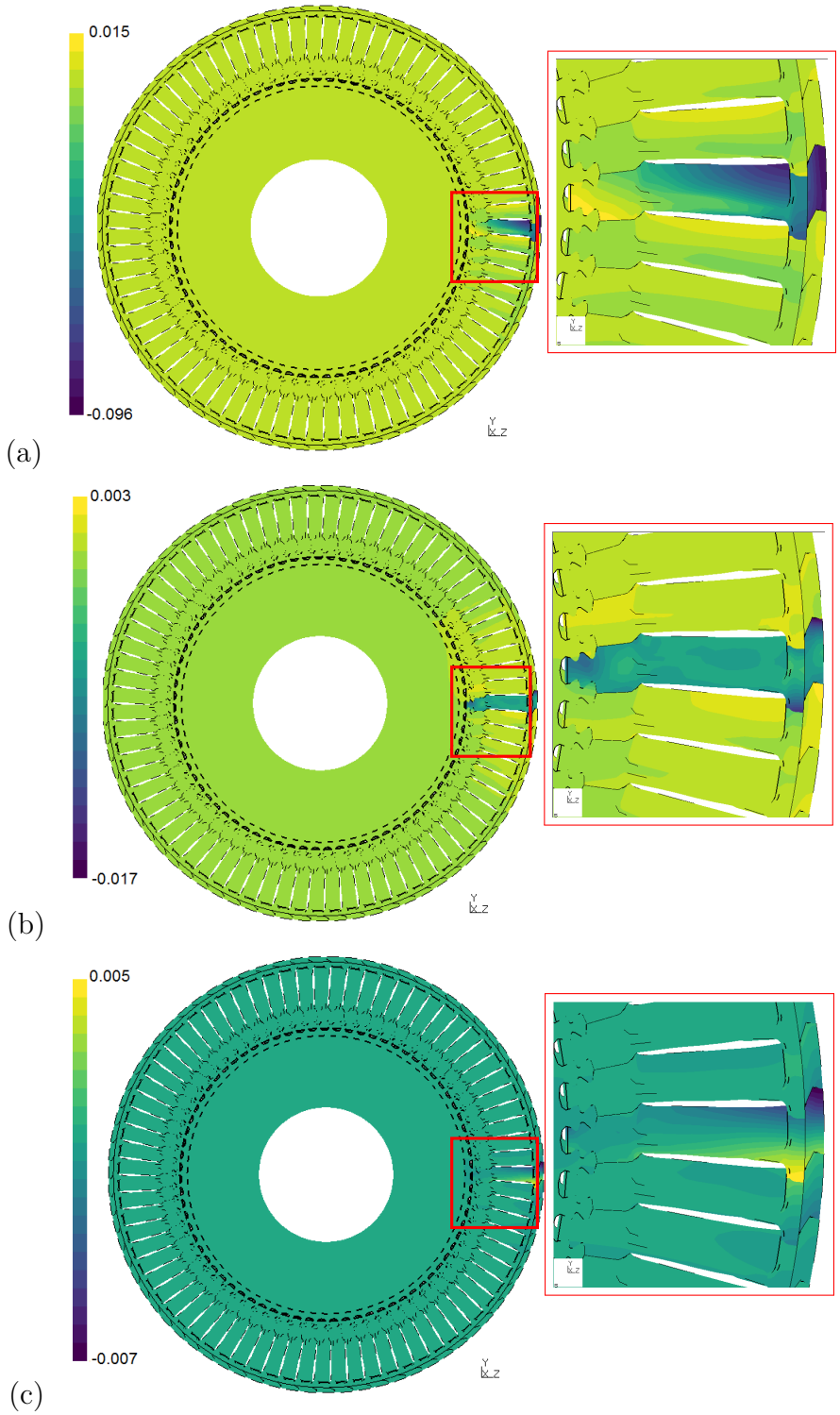

Figure 4.6: Local sensitivity of radial displacement of a mistuned bladed disk w.r.t anisotropy angles (a) α, (b) β and (c) ζ of blade number 1.

It should be borne in mind that the local sensitivity results indicate the magnitude of variation in displacements that would result from a small change in the anisotropy angles about the considered point in the domain of variation. Therefore, the sensitivity values can vary slightly for different mistuning patterns of blade anisotropy angles analysed. For an example case of anisotropy mistuning, Fig. 4.10 (a), (b), and (c) shows the sensitivity of normal stresses σ_{XX}, σ_{YY}, and σ_{ZZ} at a chosen node on fir–tree root of blade number 1 with respect to angle α, β, and ζ respectively. Similarly, the sensitivity of shear stresses is shown in Fig. 4.11(a), (b) and (c). The value of sensitivity for stresses is normalised with respect to maximum normal stress along the radial direction, σ_{ZZ}, for non-linear tuned bladed disk. It is evident from

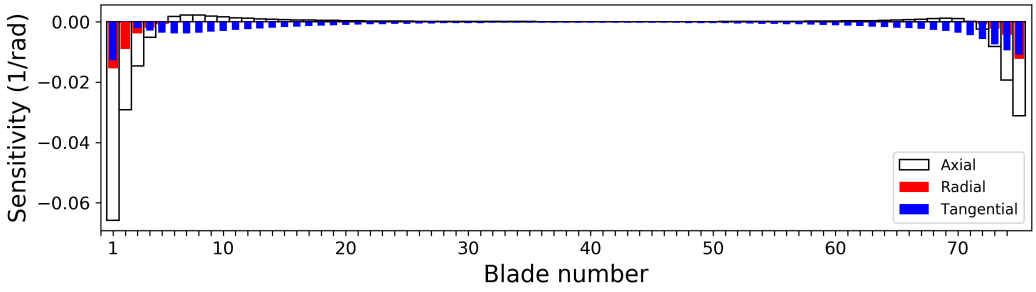

(a)

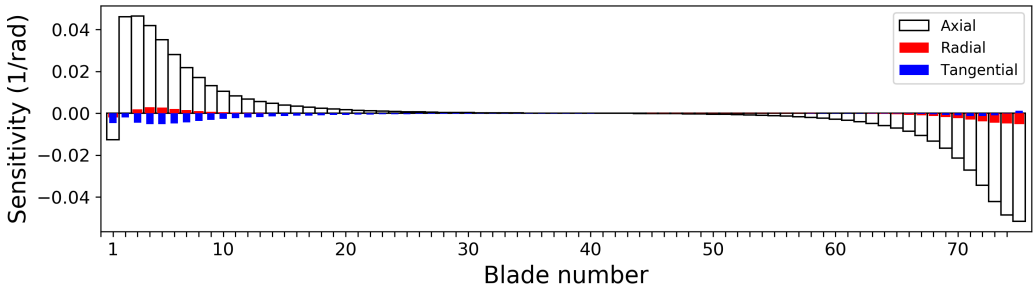

(b)

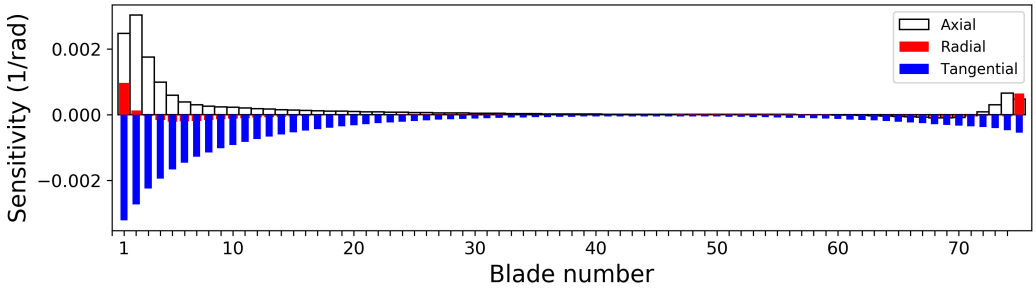

(c)

Figure 4.7: Sensitivity of displacements at blade tip of blade number 1 to anisotropy angles (a) α (b) β and (c) ζ for tuned linear bladed disk

the plots that, unlike the case for displacements, the stresses on a particular blade is significantly influenced by the anisotropy angles of that blade alone. Similar to that observed for radial displacement, the influence of anisotropy angle ζ on stresses is significantly small compared to the influence of α and β. When the sensitivity of normal and shear stress components at any location of the bladed disk is known, the sensitivity of von Mises stress at that location can be evaluated. For the considered node on the fir-tree root of blade 1, the sensitivity of von Mises stress to anisotropy angle is shown in Fig. 4.12.

From the analysis of several mistuning patterns, it was inferred that, while consid-

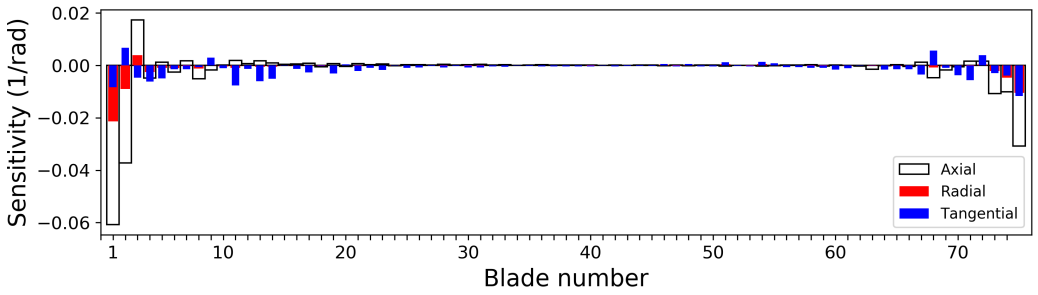

(a)

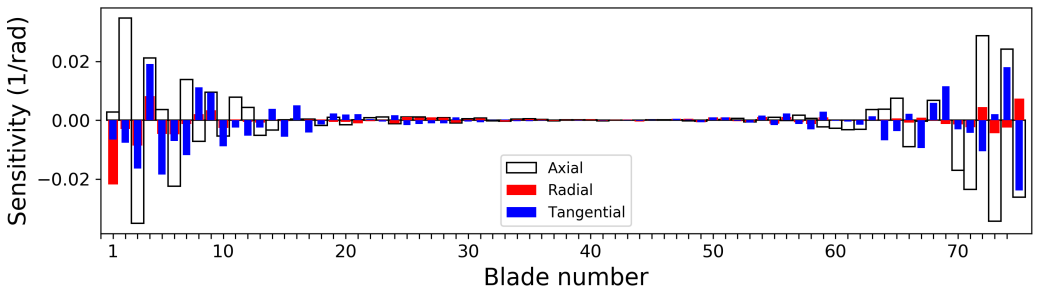

(b)

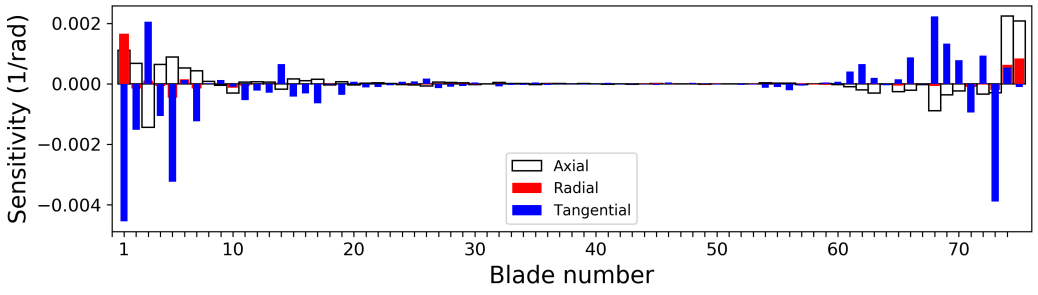

(c)

Figure 4.8: Sensitivity of blade tip displacements of blade number 1 to anisotropy angle (a) α (b) β and (c) ζ for a mistuned linear bladed disk

ering the displacement of a blade in the bladed disk, the influence of anisotropy angles of that blade and other blades adjacent to it is predominant. Based on local sensitivity analysis, it can be inferred that the variation in blade displacement along radial direction with respect to the anisotropy angles α and β are higher as compared to anisotropy angle ζ. While considering static deformation, the variation in radial displacement is of primary concern as it dictates the blade tip-casing gap, and therefore, directly influence the efficiency of the gas-turbine.

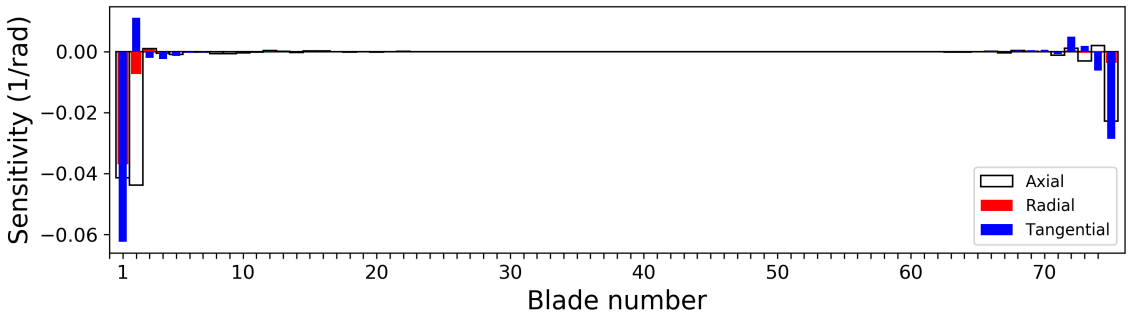

(a)

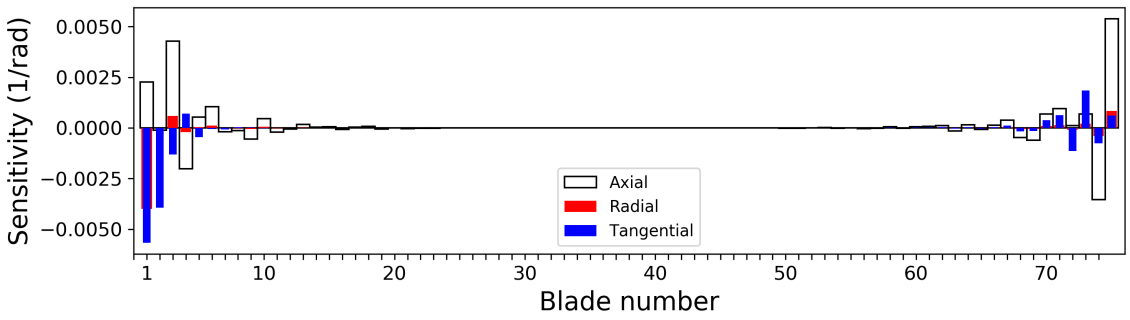

(b)

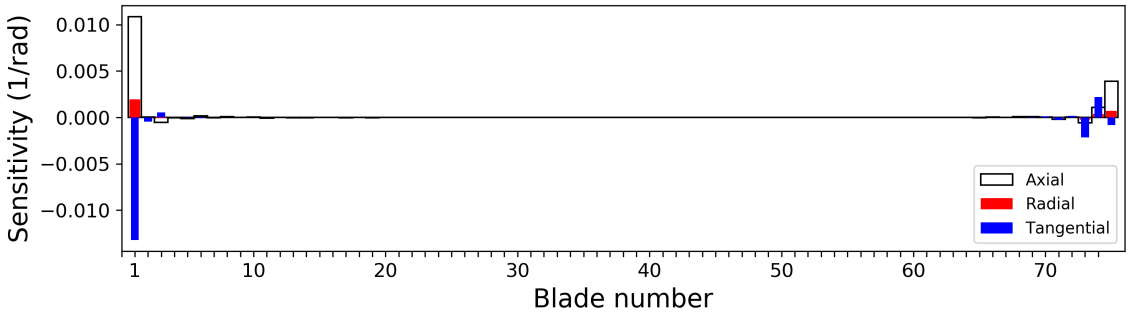

(c)

Figure 4.9: Sensitivity of blade tip displacements of blade number 1 to anisotropy angle (a) α (b) β and (c) ζ of all blades in a mistuned non-linear bladed disk

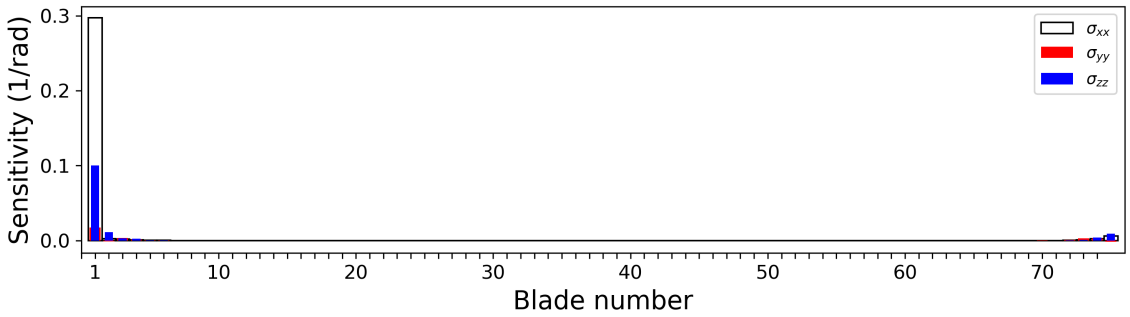

(a)

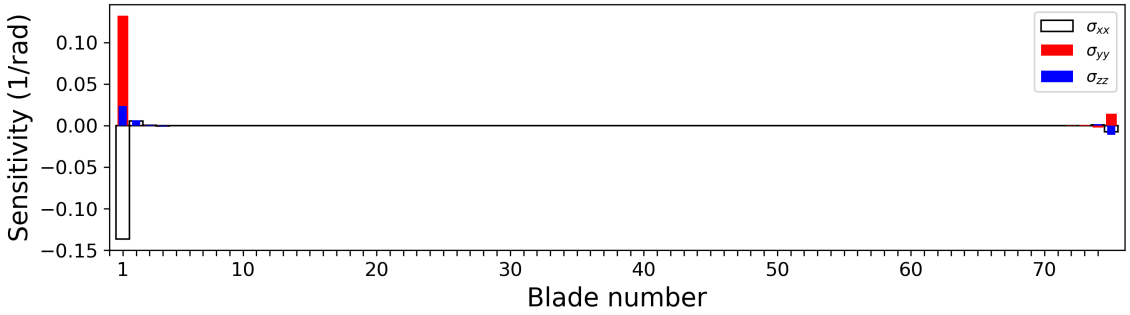

(b)

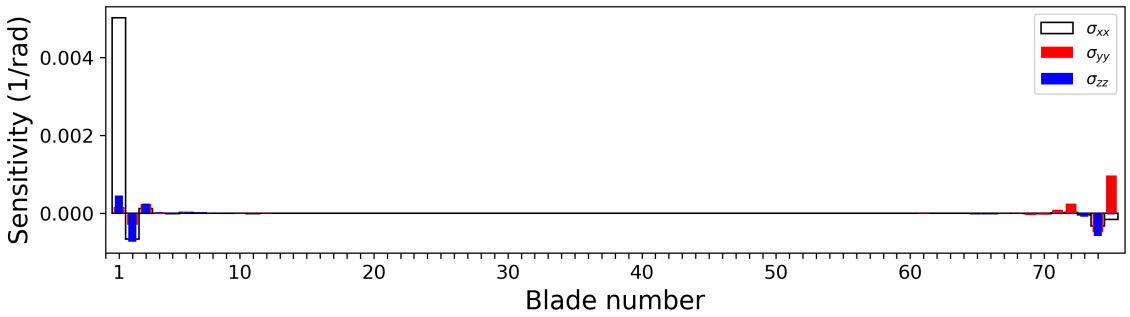

(c)

Figure 4.10: Sensitivity of normal stresses at blade root of blade number 1 to anisotropy angle (a) α (b) β and (c) ζ of all blades in a mistuned non-linear bladed disk

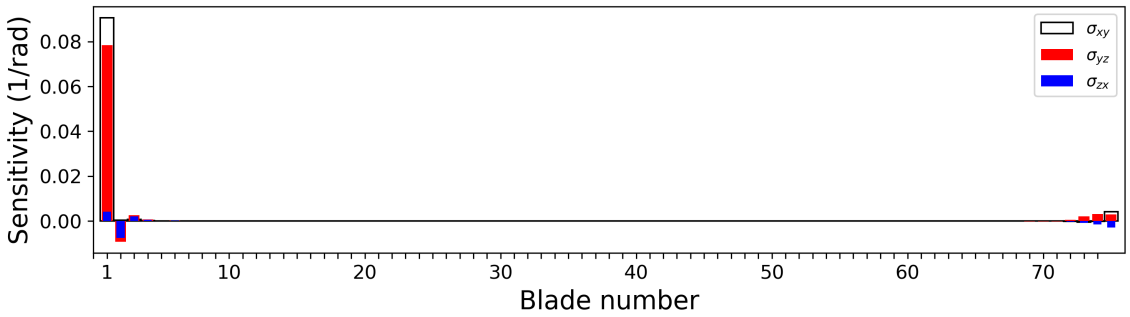

(a)

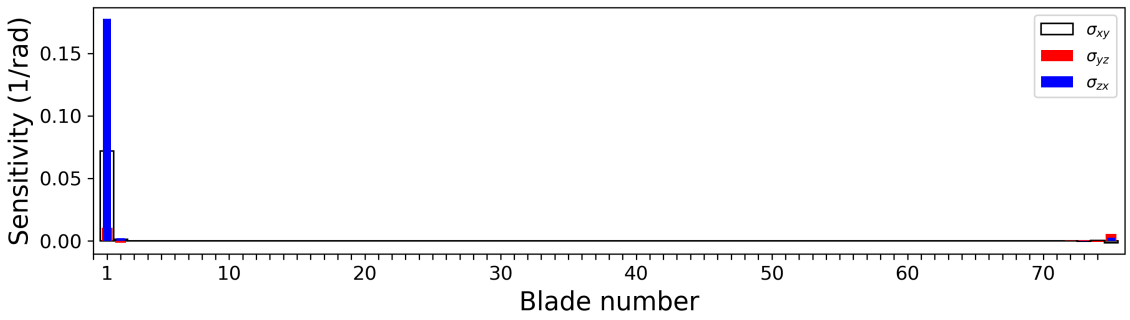

(b)

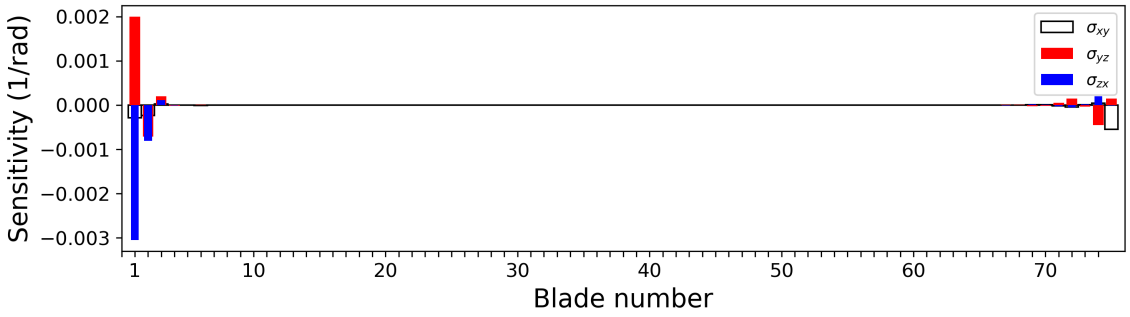

(c)

Figure 4.11: Sensitivity of shear stresses at blade root of blade number 1 to angle (a) α (b) β and (c) ζ of all blades in a mistuned non-linear bladed disk

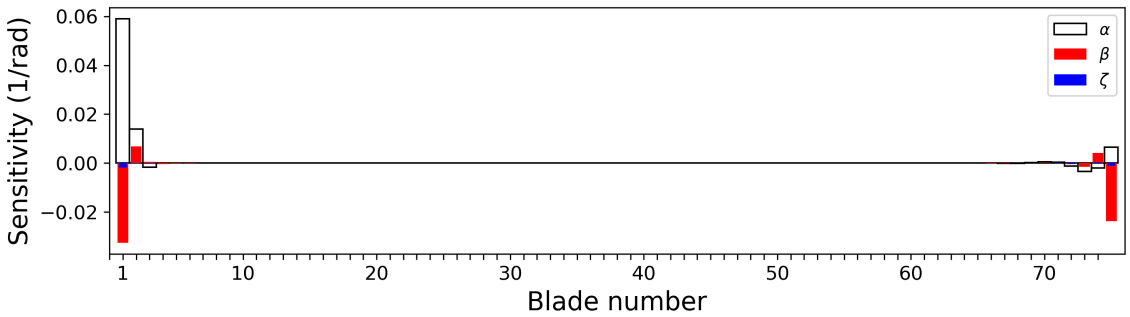

Figure 4.12: Sensitivity of von Mises stress at blade root of blade number 1 to anisotropy angles of all blades in a mistuned non-linear bladed disk

4.3 Global sensitivity analysis

One of the main aims of sensitivity analysis is to obtain a rank order of importance of the design parameters in terms of their influence on the response of the structure. Local sensitivity analysis results presented in Section 4.2 is based on the evaluation of gradient of blade displacements and stresses at chosen points in the domain of variation of the blade anisotropy angles. Therefore, the relative importance of the three anisotropy angles cannot be confirmed based on the results obtained from local sensitivity analysis. In this section, global sensitivity analysis based on Sobol indices is presented for blade anisotropy angles. While studying the displacements or stresses of a mistuned bladed disk, considering blade material anisotropy angles as random design parameters, Sobol index for a blade anisotropy angle indicates the contribution of that anisotropy angle to the variance of the displacements or stresses. As discussed in detail in Chapter 2, Sobol indices are obtained from coefficients of polynomial chaos approximation from Eqn. 2.60 and 2.61. A detailed discussion

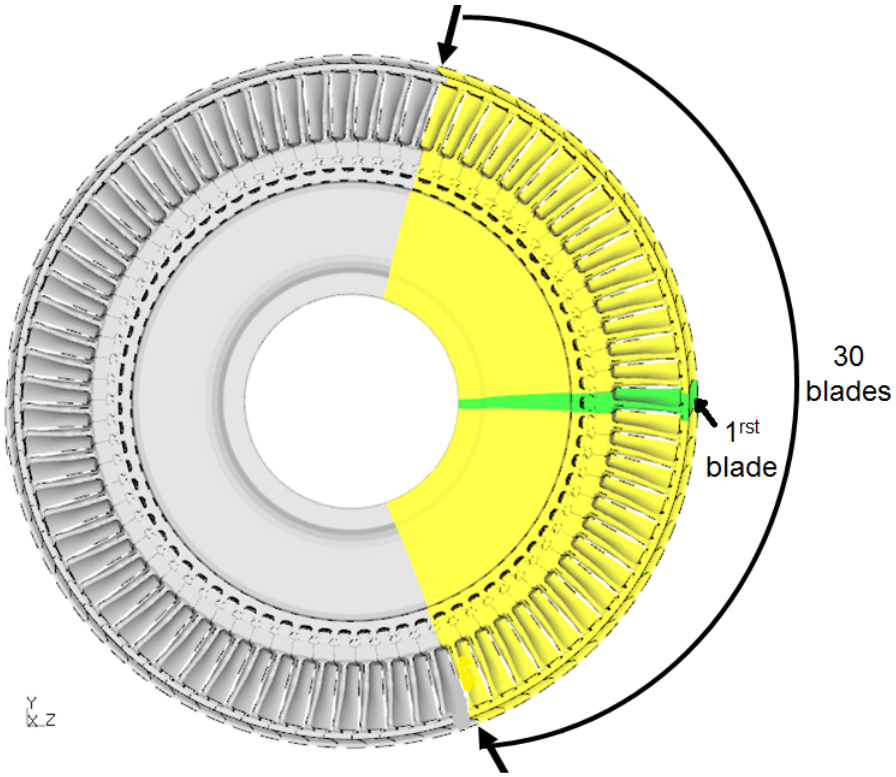

Figure 4.13: A mistuned bladed disk showing the 30 blades for which the anisotropy angles are considered as random variables.

of the accuracy of polynomial chaos approximation obtained for static deformation of the mistuned bladed disk is presented in Chapter 6. Since Sobol indices are calculated using the polynomial chaos approximation, most of the computational effort involved is spent on constructing the approximate model.

As an example, the influence of blade anisotropy angles on variation in displacements at tip node of blade number 1 is investigated. Sobol indices are calculated from polynomial chaos approximation of the blade displacements for the considered node in the mistuned non-linear bladed disk. In the previous section, based on local sensitivity analysis, it was inferred that the effect of anisotropy angles of blades located farther from the considered blade has negligible influence on the blade displacements. Therefore, to build polynomial chaos approximation, the dimensionality of the design space is reduced by including anisotropy angles of only 30 blades, adjacent to and including blade number one as shown in Fig. 4.13, are considered as random variables.

Fig. 4.14(a), (b) and (c) show the first order and total Sobol indices, for anisotropy angles α, β and ζ respectively of thirty adjacent blades, affecting the axial displacement of the considered node. While first order index is a measure of the contribution, to variance of displacement, of individual blade anisotropy angles considered alone, the total order index accounts for the interaction of the considered blade anisotropy angles in the bladed disk. Therefore, the total order index of a blade anisotropy angle is always higher than its first order index. For a given anisotropy angle, the difference between total order index and first order index is a measure of the contribution to variance of blade displacement resulting from the interaction between the angle with other anisotropy angles. It is evident from Figure 4.14(c), that about 50% of the variance in axial displacement of the considered node on blade one is due to anisotropy angle ζ. In the same figure, the small difference in magnitude of first order index from total order index for blade number one suggests that the uncertainty in anisotropy angle ζ of blade at position one has a predominant effect on the uncertainty of axial displacement on that blade. Note that this is in contradiction to the results obtained from local sensitivity analysis (see Fig. 4.9) which indicates that the axial displacement is significantly more sensitive to anisotropy angle α of blade number 1 and 75 compared to angle ζ of those blades . Figure 4.14(a) shows

that the contribution to axial displacement variance of the considered node on blade 1 from anisotropy angle α of that blade is mostly due to the interaction of the angle with other anisotropy angles. This is evident from the significant difference in the first order and total order Sobol indices for that angle of blade one. The contribution of anisotropy angle β of the considered 30 blades to variance in axial displacement of the considered node amounts to less than 5% of the total variance.

For the case of tangential displacement at blade tip of blade at position one, Fig. 4.15(a), (b) and (c) shows the Sobol indices for the anisotropy angles of the 30 adjacent blades to blade 1. The contribution of blade anisotropy angles α and ζ

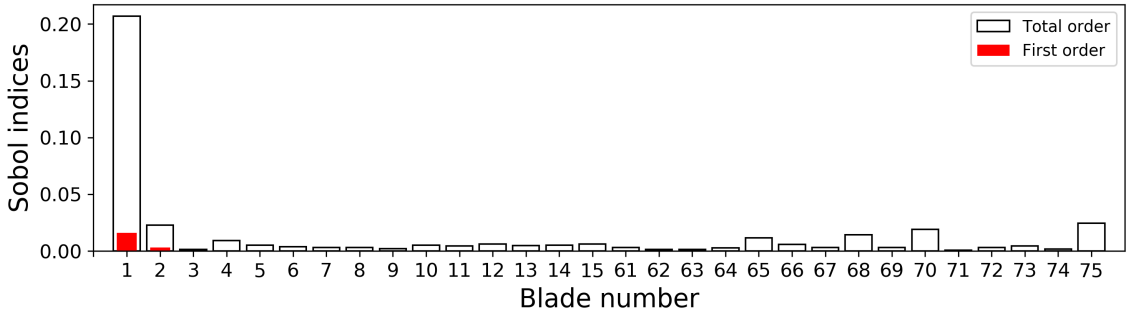

(a)

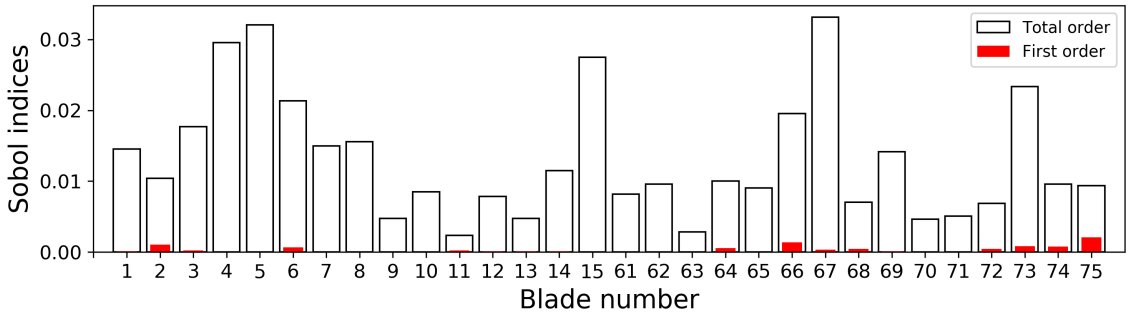

(b)

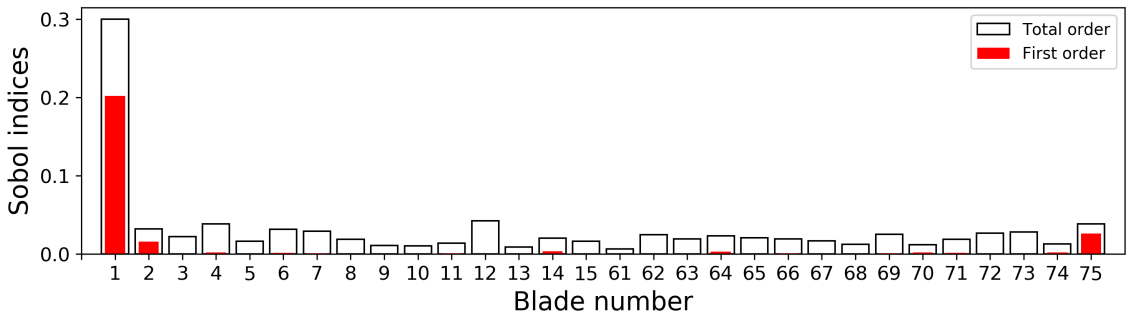

(c)

Figure 4.14: Sobol index for axial displacement w.r.t angle (a) α (b) β and ζ.

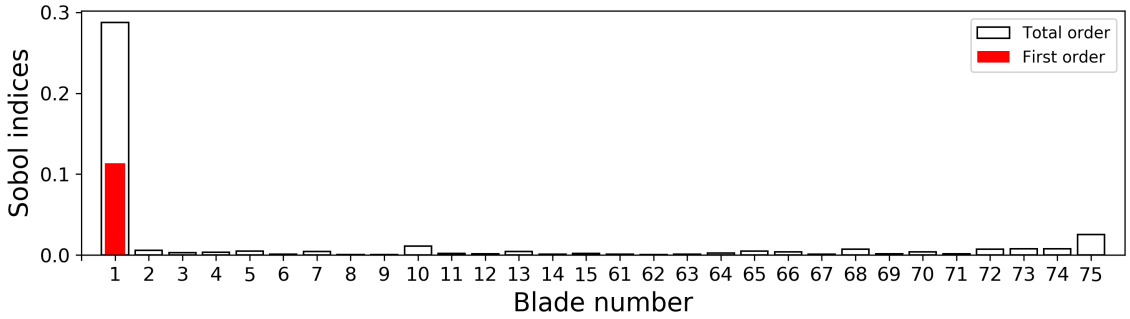

(a)

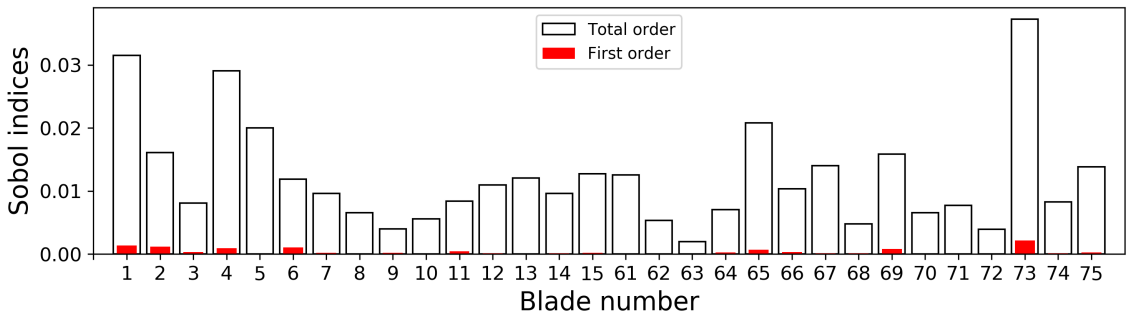

(b)

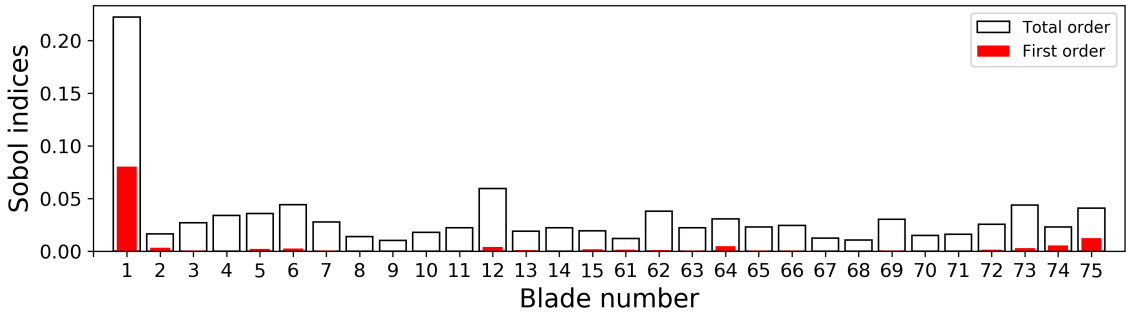

(c)

Figure 4.15: Sobol index for tangential displacement w.r.t angle (a) α (b) β and ζ.

of blade 1 to variance in tip displacements of that blade is slightly more than 50% of the total variance. From Fig. 4.16(a), (b) and (c), the value of Sobol index for radial displacement corresponding to angle α_1 is approximately 0.55, to angle β is 0.037, and to angle ζ_1 is 0.18. The values suggest that the most significant contribution to variance in radial displacement is due to uncertainty in anisotropy angle α of blade 1, followed by, that of angle ζ. This is again in contradiction to what was inferred from the local sensitivity analysis results shown in Fig. 4.9. The Sobol indices corresponding to all the three displacement component shows that the contribution of anisotropy angle β to the variance of displacement is an order of magnitude smaller compared to that of α and ζ. For the manufacturing of single

crystal blades, the results obtained from local and global sensitivity analysis suggest that a strict tolerance value for anisotropy angle α is beneficial on two accounts. Primarily, a reduction in the range of scattering of angle α will result in subsequent reduction in uncertainty in the static displacement of the bladed disk. Further, the effect of angle ζ on displacement is significantly higher when the value of angle α is higher. Therefore, by reducing the mean value of scattering in angle α with tighter tolerance value, the uncertainty in static displacements resulting from scattering in angle ζ can be reduced.

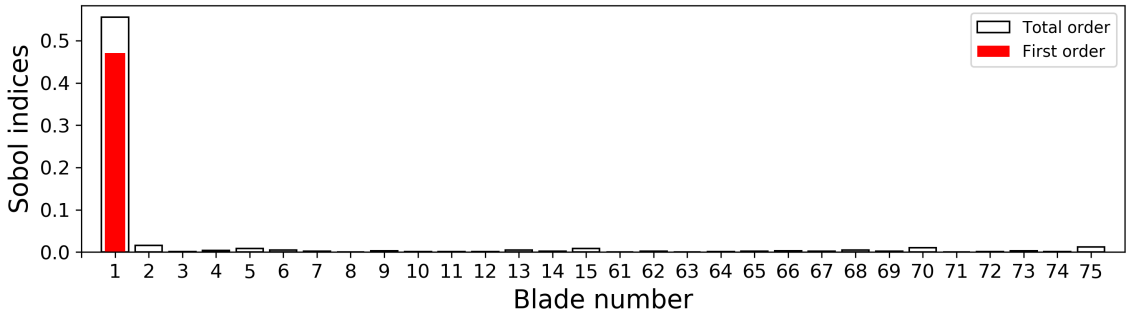

(a)

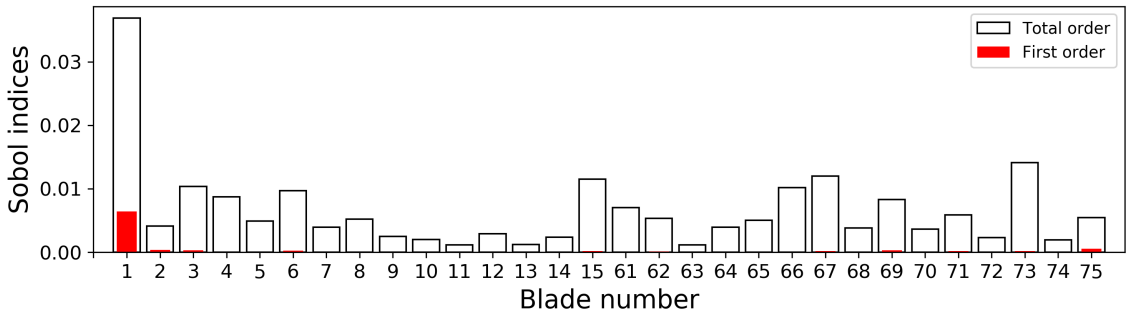

(b)

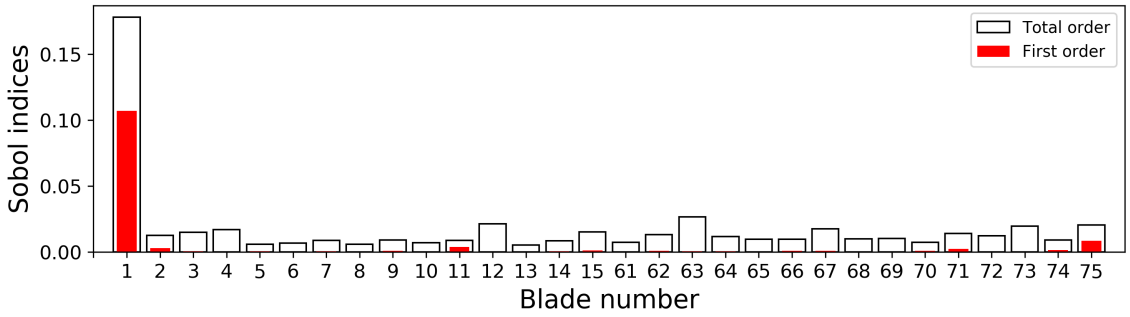

(c)

Figure 4.16: Sobol index for radial displacement w.r.t angle (a) α (b) β and ζ.

Chapter 5

Analysis of static deformation considering variations in root geometry and anisotropy orientation

The blades of a gas turbine engine are secured to the disk using fir–tree joints and are connected through shrouds. Due to tolerances in manufacturing, the geometry of the fir–tree joint and the shroud joint will differ from the design geometry. Due to such small variations in the contact geometry, the area of contact will also differ from that of the design geometry. For a given centrifugal loading, depending on the contact area at fir–tree root and at shroud, contact pressure and contact stresses at joints will be higher or lower than that experienced by the design geometry. In this chapter, the effects of variation in bladed disk fir–tree root and shroud geometry on non–linear static deformation of a tuned blade disk are investigated. Moreover, for different root and shroud geometry variants of the tuned bladed disk, the effects of crystal orientation of blades are also investigated. To minimise the high computational cost associated with the analysis of the non-linear model, bladed disk sector models are used for this analysis with cyclic symmetric constraints applied. Friction contacts at fir–tree and shroud joints are modelled based on the surface–to–surface penalty contact method.

To study the effects of variations in the fir-tree root and shroud joints on static deformation, the following nine different geometry variants are analysed:

i *Nominal* : The design geometry with contact area on all surfaces, two each at upper and lower fir-tree (see Fig. 5.1(a)), and four contact areas at shrouds.

ii *Max–1* : A variant of the design geometry having maximum material on both disk slot and blade fir-tree root as shown in Fig. 5.1(b). This variant also has a maximum contact area at all four shroud contact regions.

iii *Max–2* : This is a geometry variant similar to *Max–1* at fir–tree root joints but with shrouds having minimum contact area at all four shroud contact regions.

iv *Min–1* : A variant of the design geometry with minimum material on both disk slot and blade fir-tree root as shown in Fig. 5.1(c). This variant has minimum contact at shrouds.

v *Min–2* : This is a geometry variant similar to *Min–1* at fir–tree root joints but with a maximum area of contact at the shrouds.

vi *Upper* : This variant of the design geometry has fir-tree root contacts at the two upper fir–tree surfaces as shown in Fig.5.1 (d). For this variant, and the three variants described below, the shrouds contact regions are the same as that of the *Nominal* geometry.

vii *Lower* : A variant of the design geometry with fir–tree root contacts at lower fir-tree surfaces alone as shown in Fig. 5.1(e).

viii *Asym–A and Asym–B* : These are two different variants of the design geometry with asymmetric root geometry contacts as shown in Fig. 5.1(f) and 5.1(g) respectively.

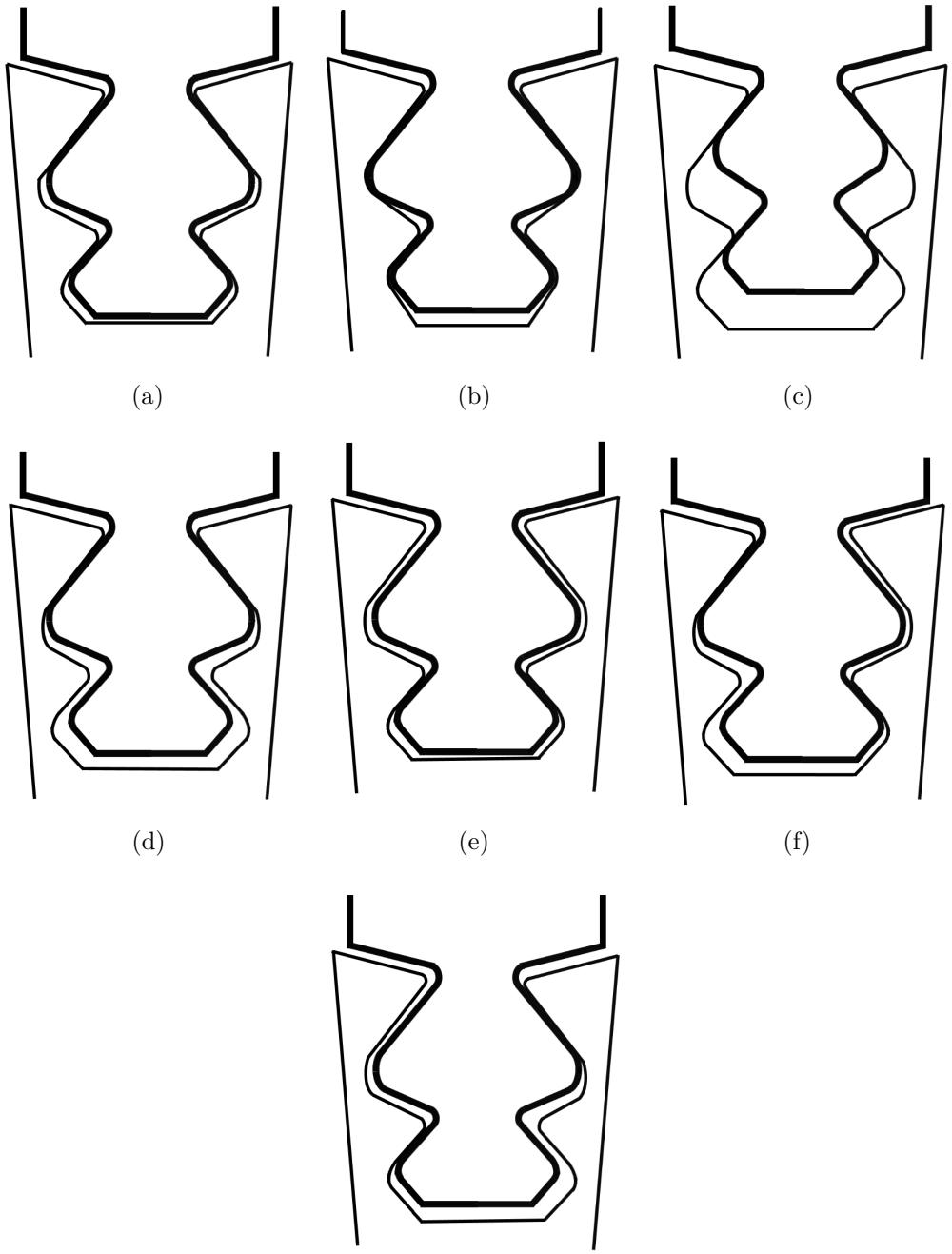

Figure 5.1: Schematic diagram of fir–tree root joint for (a) *Nominal*, (b) *Max-1* and *Max-2*, (c) *Min-1* and *Min-2*, (d) *Upper*, (e) *Lower*, (f) *Asym-A* and (g) *Asym-B* root geometry variants.

5.1 Effects of root geometry variations.

To study the effects of manufacturing tolerance of root geometry on non-linear deformation of the tuned bladed disks, blade sector models with similar FE meshes

but different root and shroud geometries were investigated. Figure 5.2 shows an example of the radial displacement of blades for the *Nominal* and *Asym-A* geometry. The figure shows that there is a noticeable difference in displacements, especially near the blade tip region. For the nine different geometry variants studied, Table 5.1 shows the values of maximum blade displacements under static centrifugal load. The centrifugal load is calculated based on a realistic rotational speed for a gas turbine bladed disk obtained from the industry. The displacements of all variants are normalised by the maximum radial displacement value of the *Nominal* geometry. From the Table, it is clear that a maximum deviation of 14.0%, from *Nominal* geometry, is possible for the maximum resultant displacement. The magnitude of the displacement is the highest in the radial direction, followed by that along the axial direction. Under same centrifugal loading, the Lower geometry variant has the largest radial deformation which can be attributed to a reduction in stiffness due to an increase in the effective length of the blade as the contact is restricted to lower fir–tree surfaces for this variant. The magnitude of the tangential component of displacement is the smallest for all geometry variants analysed except for the *Asym-B* variant.

Table 5.1: Variation in normalised maximum blade displacements

Root geometry variants	Normalised maximum blade displacements				
	Radial	Tangential	Axial	Resultant	% change
Nominal	1.000	0.398	0.623	1.205	0.000
Max–1	1.006	0.406	0.675	1.198	-0.581
Max–2	1.016	0.455	0.627	1.227	1.826
Min–1	1.021	0.483	0.685	1.239	2.822
Min–2	1.021	0.477	0.638	1.251	3.817
Upper	1.023	0.431	0.598	1.202	-0.249
Lower	1.045	0.546	0.648	1.288	6.888
Asym-A	1.004	0.157	0.686	1.174	-2.573
Asym-B	1.094	0.656	0.648	1.374	14.024

The variation in fir–tree root and shroud geometry will influence the contact pressure

and therefore friction contact stresses at the blade–disk root joint and at shroud joints. The deviations from the *Nominal* geometry can result in higher or lower contact pressure at fir–tree root surfaces compared to that of the design geometry depending on the actual area of contact. Fig. 5.3(a) and (b) shows the variation in normalised contact pressure at lower fir–tree surfaces for *Nominal* geometry. The contact pressure values are normalised by the value of average contact pressure at upper–left surface of fir–tree root for *Nominal* geometry. The value of contact pressure, and therefore contact stresses, are significantly higher towards the edges of the contact region due to high stress concentration at the edges of the fir–tree root geometry. Since the contact area is smaller at lower surfaces of the fir–tree root (see Fig. 5.1), the maximum contact pressure at lower surfaces are significantly higher compared to that of upper.

For the case of *Max–1* geometry variant, Fig. 5.4(a) to (d) shows the distribution of contact pressure at lower and upper surfaces of the fir–tree. For both upper and lower fir–tree surfaces, the contact pressure at the edges are significantly higher

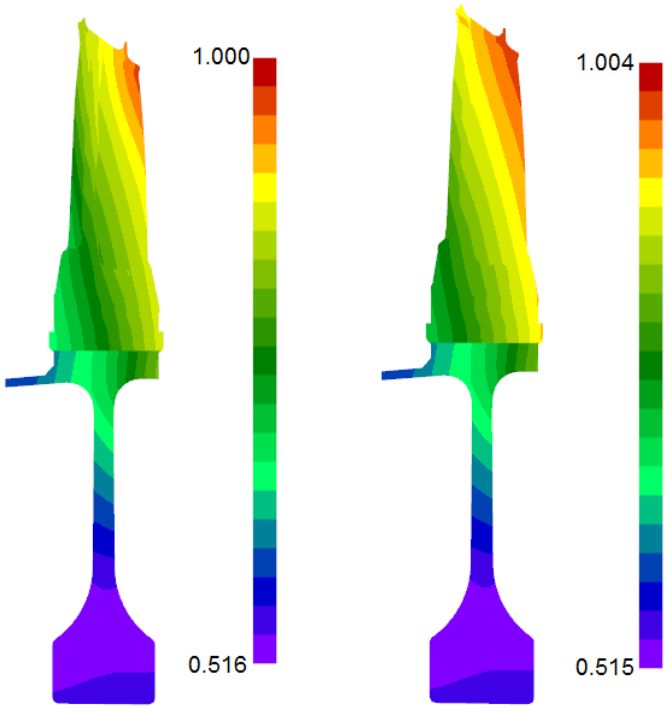

(a) (b)

Figure 5.2: Radial displacement of blade sector for (a) *Nominal* and (b) *Asym-A* geometry variant.

compared to that over the interior of the surface. The resulting stress concentration is detrimental for the life of the blade as it could result in fretting wear under different operational loads experienced by the bladed disk. When the geometry variations within manufacturing tolerance of blade root and disk geometries result in restriction of contacts to the lower fir–tree surfaces alone, as in the *Lower* geometry variant, the maximum contact pressure increases significantly as shown in Fig. 5.5(a) and (b). For the two asymmetric geometry variants analysed, the contacts between fir–tree root and disk slot are restricted to two surfaces, one each on the left and right side of the fir–tree. Fig. 5.6(a) and (b) shows the distribution of contact pressure at lower fir–tree contact surfaces for *Asym–A* and *Asym–B* variant respectively. For *Asym–A*, even though contact exists on the upper–left surface of fir–tree, since the contact is restricted to the lower surface on the right side of fir–tree, the peak contact pressure is comparable to that for the *Lower* geometry variant.

From the above analysis of variations in static displacements of the bladed disk and contact pressure at fir–tree root joints, it is evident that the small variations in the geometry of contact regions, even though within the tolerance limits, could result in often undesirable variations in contact pressure at fir–tree joints of the structure. Therefore, in order to ensure that the life of the bladed disk is not limited by the

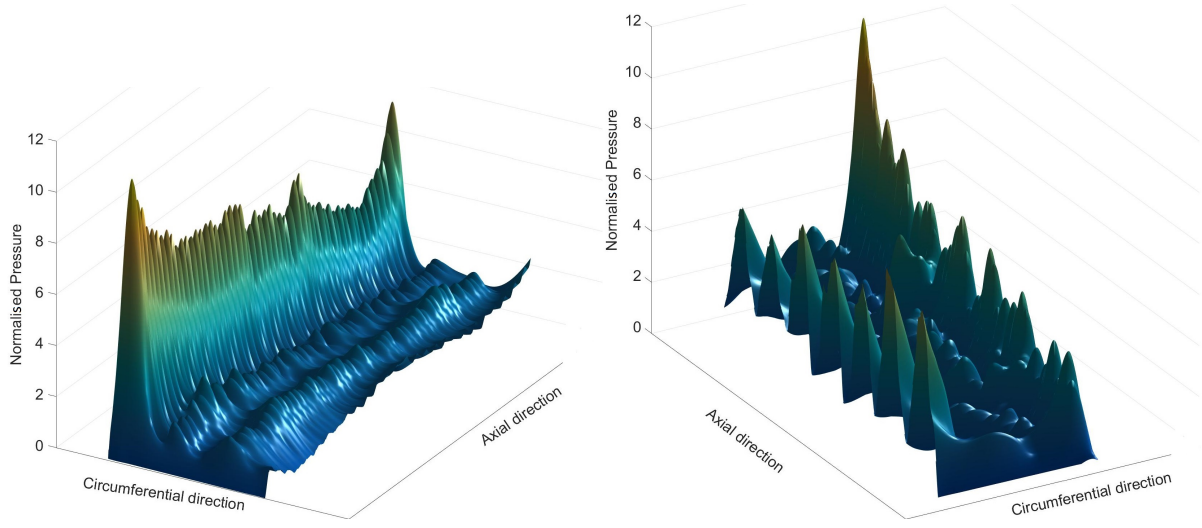

(a) (b)

Figure 5.3: Contact pressure for geometry *Nominal* on (a) lower-left and (b) lower-right fir-tree surfaces normalized w.r.t average contact pressure on upper-left surface.

life of the fir–tree joint, it is essential to account for the effect of variations in the geometry on static deformation of the bladed disk.

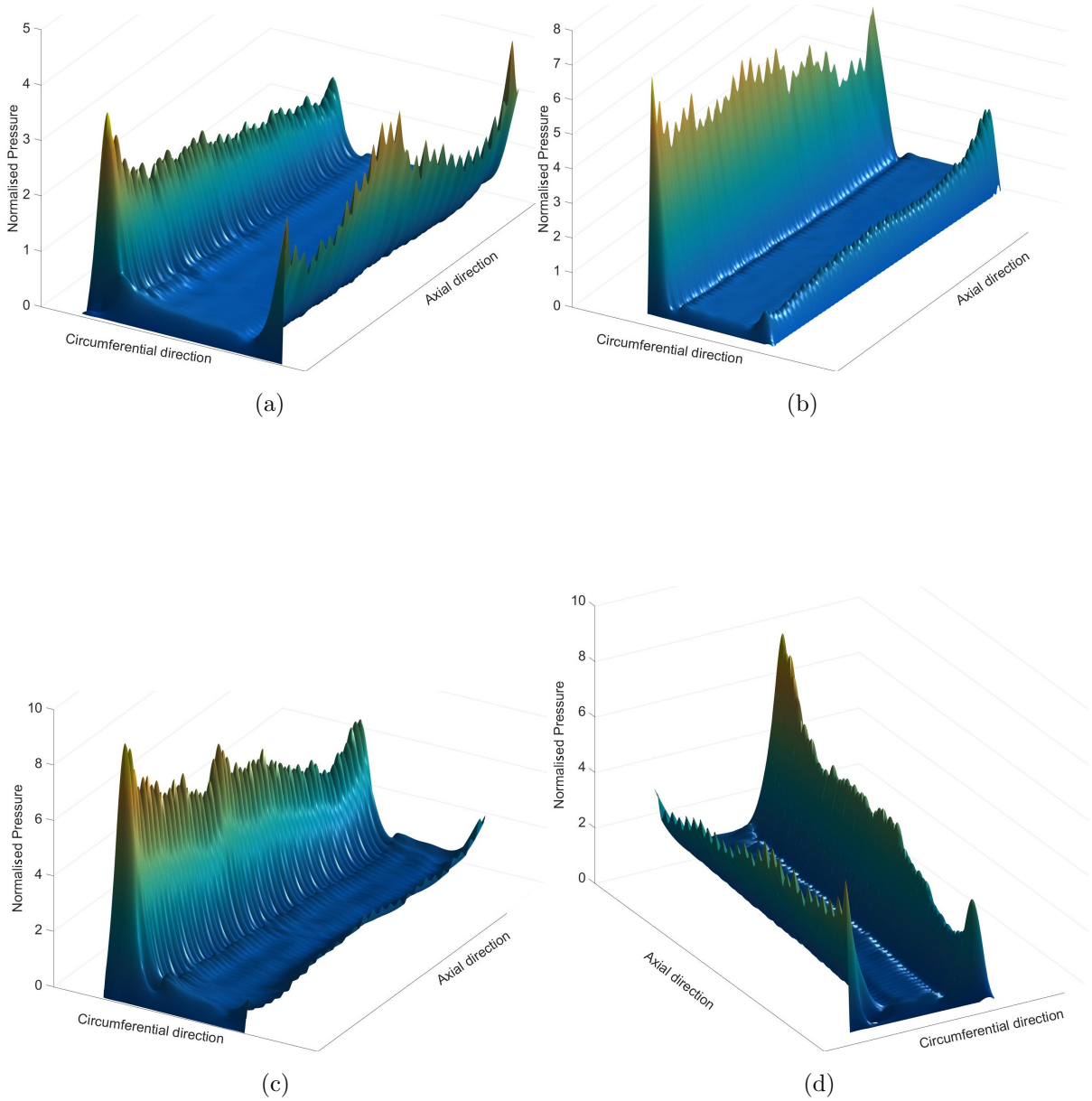

Figure 5.4: Contact pressure for geometry *Max–1* on (a) upper-left, (b) upper-right, (c) lower-left, and (d) lower-right fir-tree surfaces normalized w.r.t average contact pressure on upper-left surface of *Nominal* geometry.

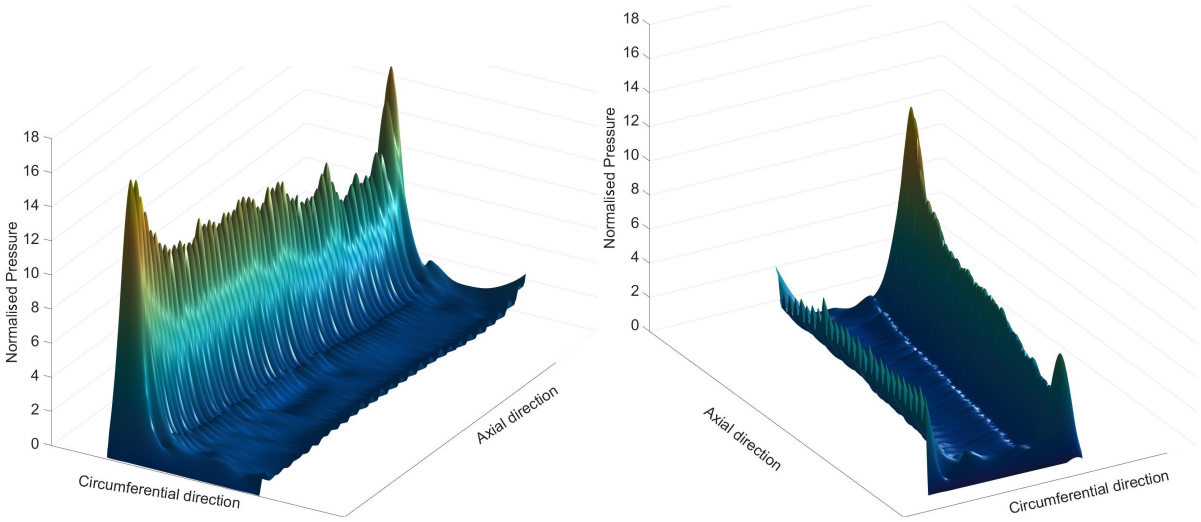

(a) (b)

Figure 5.5: Contact pressure for geometry *Lower* on (a) lower-left and (b) lower-right fir-tree surfaces normalized w.r.t average contact pressure on upper-left surface of *Nominal* geometry.

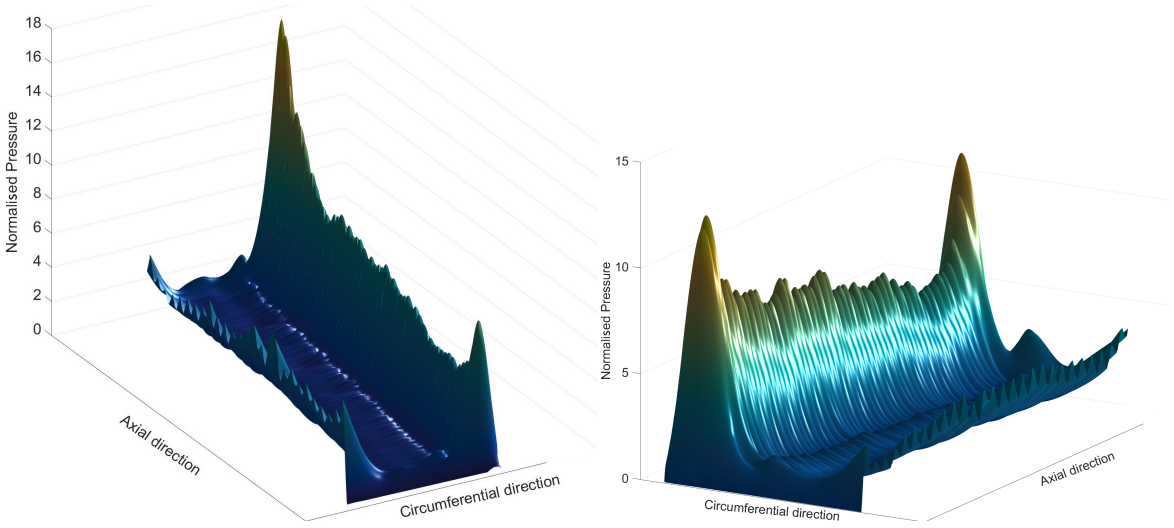

(a) (b)

Figure 5.6: Contact pressure on the lower fir–tree surface for (a) *Asym–A* and (b) *Asym–B* geometry variant normalized w.r.t average contact pressure on upper-left surface of *Nominal* geometry.

5.2 Effects of variation in material anisotropy orientation.

The investigation on local and global sensitivity of static deformation of the non-linear bladed disk to blade material anisotropy orientation was presented in Chapter 4. It was concluded that the variation in the crystal orientation of the blades will affect the static response of the bladed disk. It is expected that effects of blade anisotropy orientation will be different for different fir–tree root and shroud geometry variants. This study aims to quantify the effects of blade material anisotropy angles on static displacements and contact pressure at fir–tree roots of single crystal blades for different variants of the contact geometry. Moreover an investigation on the variation of local sensitivity of displacements to anisotropy angles with respect to different orientation of the crystal axis is also undertaken. In this study non-linear models of the bladed disk with friction joints at blade–disk interface and at shrouds are investigated.

From results obtained for local and global sensitivity analysis, it was concluded that the blade displacements along radial direction are significantly influenced by the primary anisotropy angle α, followed by ζ and β. To study local sensitivity at different crystal orientations, the orientation of the blade anisotropy axis is varied by varying the primary anisotropy angle α keeping the two other angles constant at the mean value obtained from their respective probability distribution. First we consider the variation in blade tip displacements along axial, tangential and radial directions with respect to the orientation of crystal axis as plotted in Fig. 5.7(a), (b) and (c) respectively. In Figure 5.7 to 5.10, the X-axis represents the angle α normalised w.r.t the maximum permissible value of that angle. In this section, the blade displacements and its sensitivity values presented are normalised with respect to the maximum radial displacement for nominal geometry with friction joints and crystal axis aligned with geometry axis. The effect of blade material anisotropy orientation on axial displacement is higher compared to that for tangential and radial displacement. Note that while axial and radial displacements at blade tip for all geometry variants decreases as the blade material anisotropy axis moves away

from the blade geometry axis, the tangential displacement shows only small variation for most geometry variants.

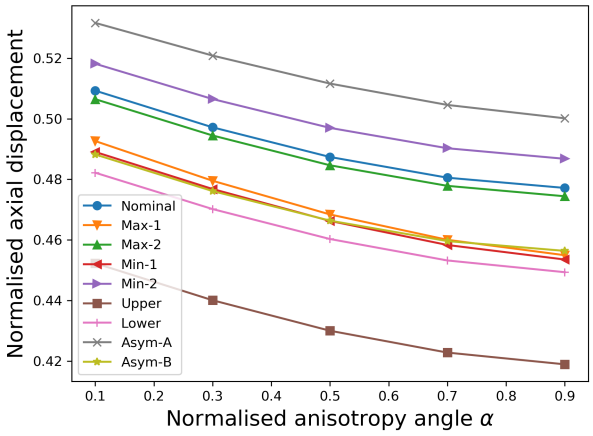

(a)

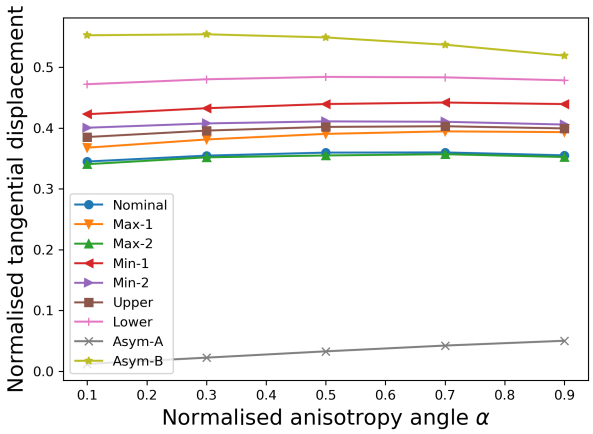

(b)

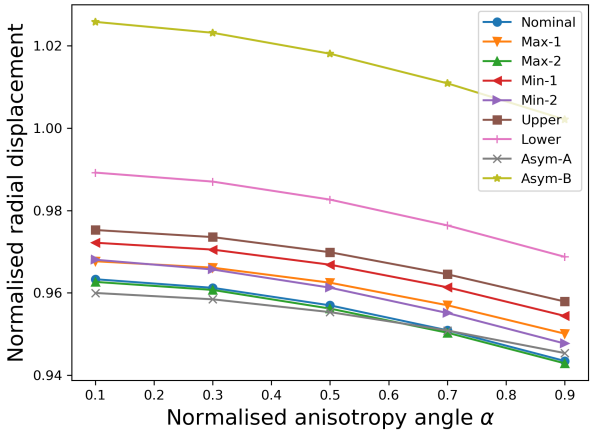

(c)

Figure 5.7: Variation in normalised blade tip displacement along (a) axial (b) tangential and (c) radial direction w.r.t orientation of the crystal defined by anisotropy angle α.

Considering local sensitivity, we know that the sensitivity of displacements to blade anisotropy angles vary for different orientations of the crystal. To study the variation

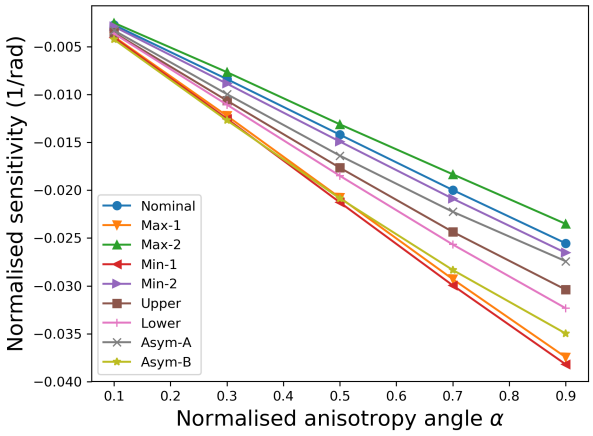

(a)

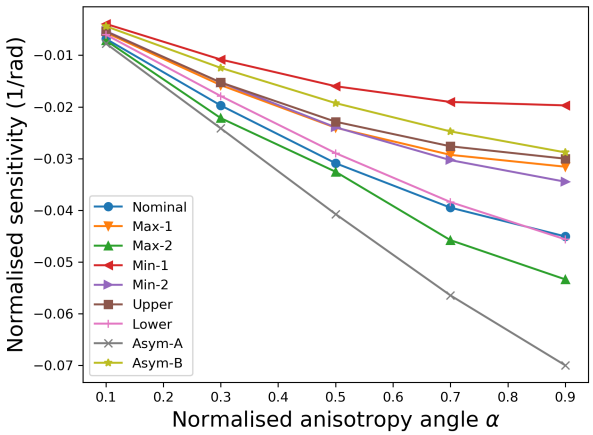

(b)

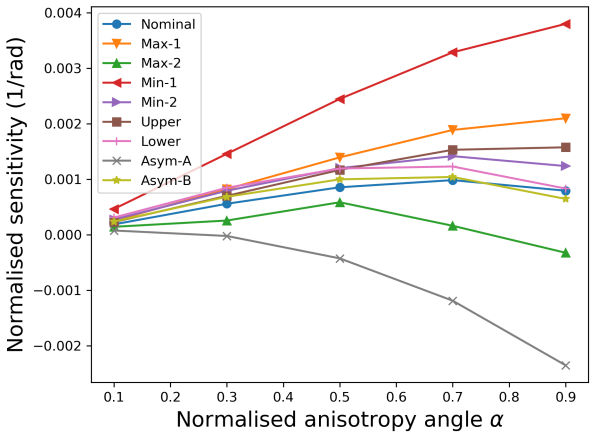

(c)

Figure 5.8: Variation in sensitivity to angle ζ for (a) axial, (b) tangential and (c) radial displacement w.r.t orientation of the crystal defined by anisotropy angle α.

in sensitivity of the blade displacements, local sensitivity values are calculated at different crystal orientations obtained by varying the primary anisotropy angle α. Fig. 5.8(a), (b) and (c) shows the variation in local sensitivity of blade tip displacements along the axial, tangential and radial direction to angle ζ for different orientations of the anisotropy axis. The sensitivity values are normalised with respect to the maximum radial displacement of the *Nominal* geometry for the case when crystal axis is aligned with the blade geometry axis. While a positive value of the displacement sensitivity indicates that a small change in the value of the anisotropy angle increases the displacement, the negative value for sensitivity means a decrease in the displacement. From Fig. 5.8(a) to (c), it is clear that the local sensitivity of blade tip displacements to angle ζ increases as the anisotropy axis inclines away from the blade geometry axis. This is intuitive from the definition of anisotropy angles (see Fig. 1.2). As the value of α increases, the blade material anisotropy axis inclines away from the blade geometry axis, and therefore, any variation in angle ζ changes the orientation of the anisotropy axis significantly. Finally, note that for any given orientation, the sensitivity of radial displacement with respect to angle ζ is an order of magnitude smaller compared to that of axial and tangential displacement.

The variation in axial, tangential and radial displacement sensitivity to anisotropy angle β for different orientations of the anisotropy axis is shown in Fig. 5.9 (a), (b) and (c) respectively. Note that for most of the geometry variants analysed, the change in displacement sensitivity with respect to angle β is small compared to that of angle ζ. For any given orientation of the blade anisotropy axis, the magnitude of tangential displacement sensitivity with respect to angles β and ζ is an order of magnitude higher than that of axial and radial displacement sensitivity. The magnitude of tangential displacement for most of the variants are smaller compared to the values for axial and radial displacements (see Table. 5.1). Therefore, even though the sensitivity of tangential displacement with respect to β is comparatively higher, the effect of scattering in that angle on the resultant displacement of the bladed disk will not be significant. For *Nominal* geometry, this proposition is validated by the value of Sobol indices for anisotropy angle β presented in Chapter 4.

The variation in local sensitivity of displacement to primary angle α with respect to variation in crystal orientation is plotted in Fig. 5.10(a), (b) and (c), for axial,

tangential, and radial displacement respectively. Based on a comparison of the values of local sensitivity of displacements to α for different crystal orientations with corresponding values for angle ζ and β (see Fig. 5.8 and 5.9), it can be inferred that the blade displacements are significantly more sensitive to primary anisotropy angle α compared to angle β and ζ. For all the root and shroud geometry variants analysed, the sensitivity of axial displacement with respect to α decreases monotonically as anisotropy axis inclines away from the blade geometry axis. On the contrary, the sensitivity of radial displacement increases consistently. The negative value of sensitivity suggests that the axial and radial displacement decreases with a small change in anisotropy angle alpha whereas tangential displacement for the considered node can increase or decrease depending on the orientation of the crystal.

The change in blade anisotropy orientation affects the deformation of the bladed disk, and therefore, can change the contact conditions at blade–disk interface, i.e. from gap to contact and vice-versa. A comparison of Fig. 5.11(a) and (b) for *Asym–A* shows a small increase in the contact area as indicated by an increase in the contact area with a positive value of contact pressure.

Considering the variation in contact pressure on fir–tree root surfaces with respect to crystal orientation, Tables 5.2 and 5.3 gives the normalised maximum contact pressure and average contact pressure for different root and shroud geometry variants analysed. The normalisation factor is the average contact pressure at upper–left fir–tree surface for *Nominal* geometry when blade anisotropy orientation is aligned with blade geometry axis. Maximum and average value of contact pressure at right and left side of fir–tree are obtained for different crystal orientations obtained by varying α. The inclination of anisotropy axis to blade geometry axis is increased by increasing the anisotropy angle, α, keeping the angles β and ζ constant. The average contact pressure for a given side of the fir–tree geometry is calculated as the mean of contact pressures obtained for all finite element nodes, with non-zero contact pressure, on upper and lower contact surfaces of that side. Among the different geometry variants studied, the variation in maximum and average contact pressure with the orientation of blade anisotropy axis is relatively high for the two variants with asymmetric fir-tree geometry.

For example, for *Asym–B* geometry the average contact pressure on the right side of the fir–tree root increases by 1.4%. Since the crystal orientation of the blade influences the deformation of the bladed disk, the contact area at joints can also

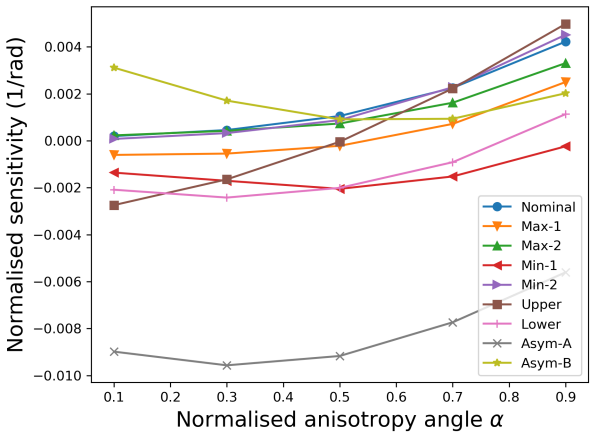

(a)

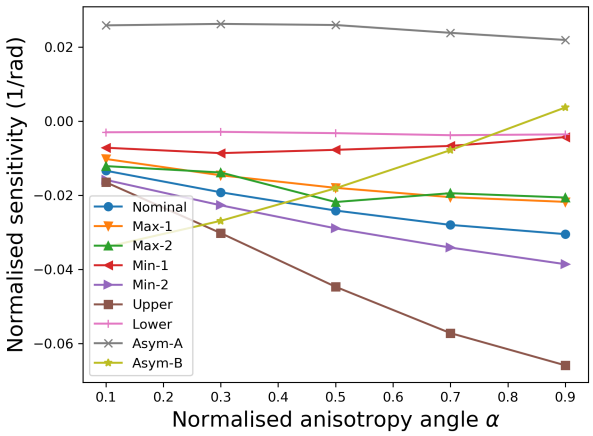

(b)

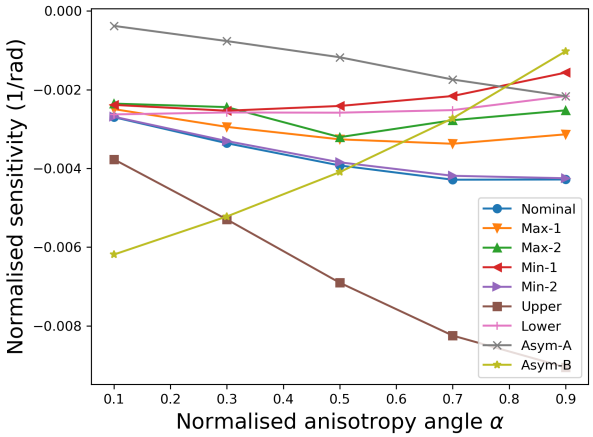

(c)

Figure 5.9: Variation in sensitivity to angle β for (a) axial, (b) tangential and (c) radial displacement w.r.t orientation of the crystal defined by anisotropy angle α.

vary with crystal orientation. A comparison of Fig. 5.11(a) and (b), showing contact pressure on right side of upper fir–tree of *Asym–A* geometry variant shows a small

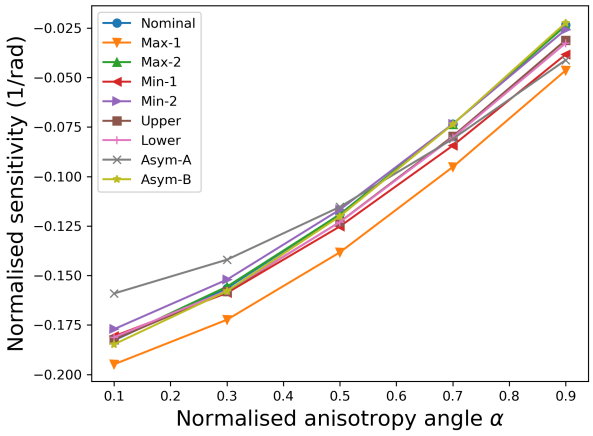

(a)

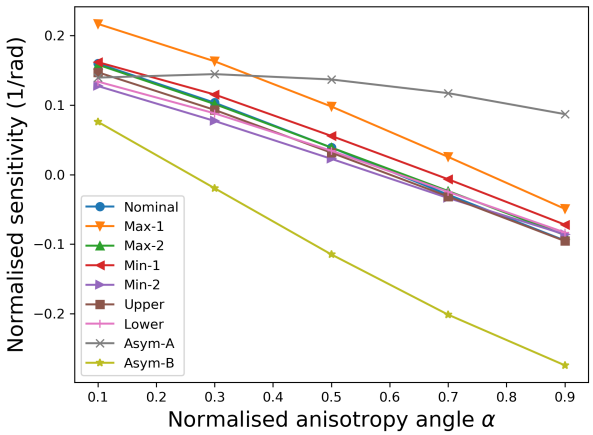

(b)

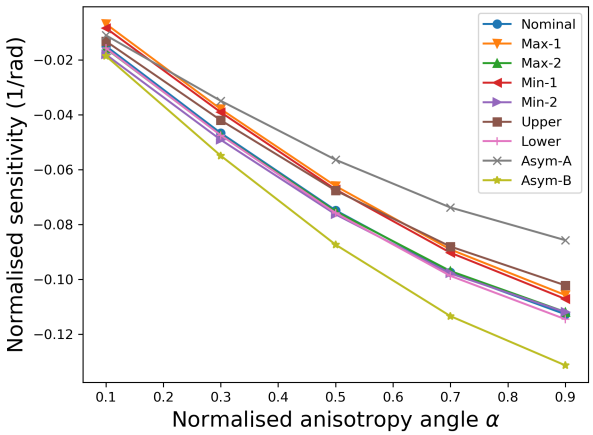

(c)

Figure 5.10: Variation in sensitivity to angle α (a) axial, (b) tangential and (c) radial displacement w.r.t orientation of the crystal defined by anisotropy angle α.

increase in the contact area as anisotropy angle increases from $\alpha = X$ to $\alpha = 9 \times X$. The increase in contact area has resulted in a decrease in maximum contact pressure on the surface by 4.3%.

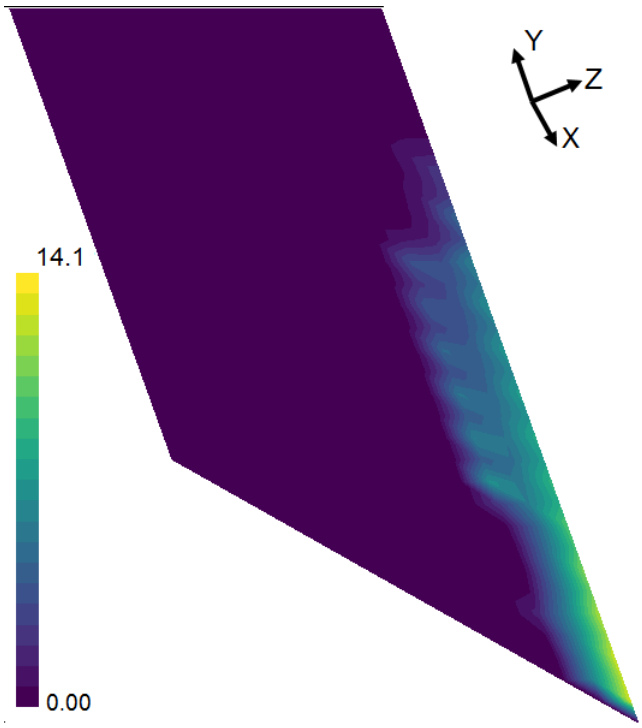

(a)

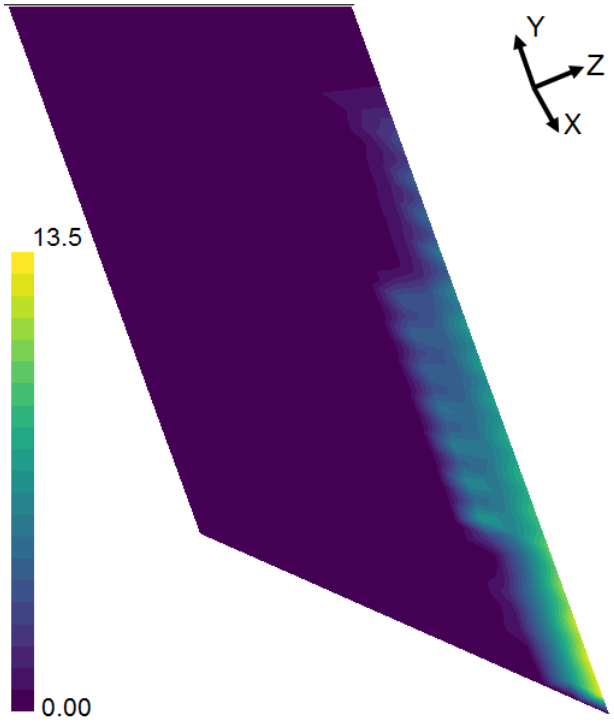

(b)

Figure 5.11: Normalised contact pressure on fir–tree upper right surface of *Asym–A* geometry variant for (a) $\alpha = X$, (b) $\alpha = 9 \times X$, where X is the reference value of α. In the coordinate system for bladed disk, X is the axial, Y is the tangential, and Z is the radial direction.

Table 5.2: Variation in maximum contact pressure w.r.t anisotropy angle α

Root geometry variants	Normalised maximum contact pressure for different values of α									
	Left side of fir-tree					Right side of fir-tree				
	X	$3 \times X$	$5 \times X$	$7 \times X$	$9 \times X$	X	$3 \times X$	$5 \times X$	$7 \times X$	$9 \times X$
Asym-A	15.273	14.554	14.443	14.315	14.165	14.991	14.721	14.271	13.759	13.499
Asym-B	13.066	12.497	12.770	13.013	13.198	13.847	13.781	13.750	13.666	13.578
Lower	17.493	17.604	17.771	17.657	17.432	11.905	11.428	11.000	10.607	10.276
Nominal	11.751	11.728	12.104	11.945	12.095	10.391	10.131	10.550	10.267	9.998
Upper	9.349	9.084	8.970	8.820	8.643	8.625	8.630	8.550	8.449	8.338
Max–1	10.003	10.166	10.179	10.108	9.976	7.588	7.363	7.138	6.930	6.763
Max–2	9.972	10.126	9.897	9.950	9.835	7.416	7.336	7.027	6.935	6.754
Min–1	6.710	6.754	6.763	6.798	6.754	4.374	4.323	4.391	4.441	4.472
Min–2	7.049	7.032	7.085	6.877	6.608	4.604	4.445	4.422	4.423	4.423

Table 5.3: Variation in average contact pressure w.r.t anisotropy angle α

Root geometry variants	Normalised average contact pressure for different values of α									
	Left side of fir-tree					Right side of fir-tree				
	X	$3 \times X$	$5 \times X$	$7 \times X$	$9 \times X$	X	$3 \times X$	$5 \times X$	$7 \times X$	$9 \times X$
Asym-A	2.077	2.031	2.010	1.969	1.974	2.629	2.620	2.624	2.653	2.640
Asym-B	2.521	2.521	2.513	2.527	2.507	1.825	1.834	1.837	1.843	1.850
Lower	2.150	2.150	2.151	2.149	2.151	2.056	2.055	2.058	2.057	2.047
Nominal	1.517	1.520	1.533	1.541	1.545	1.477	1.480	1.484	1.484	1.486
Upper	1.124	1.123	1.124	1.126	1.132	1.293	1.297	1.299	1.300	1.301
Max–1	0.845	0.844	0.843	0.842	0.841	0.952	0.954	0.955	0.954	0.950
Max–2	0.886	0.857	0.879	0.857	0.859	0.928	0.938	0.930	0.937	0.935
Min–1	0.793	0.786	0.787	0.792	0.786	0.773	0.775	0.776	0.776	0.777
Min–2	0.745	0.737	0.736	0.737	0.731	0.797	0.796	0.794	0.793	0.791

5.3 Statistical analysis using Random Forest based surrogate model

It is evident from the analysis presented in Section 5.2 that the effect of blade crystal orientation can influence the static deformation of a bladed disk with non–linear friction joints between blade and disk and at shrouds. From the analysis of different fir–tree root geometry variants, it can be inferred that the crystal orientation of the blade influences the contact pressure at fir–tree root in varying degree for different geometries analysed. Random forest (RF) based surrogate model is used to quantify the uncertainty in contact pressure at fir–tree root joints disk while accounting for the uncertainty in crystal orientation and possible variations in contact geometry. A categorical variable is used to determine whether the blade root surfaces are in contact or out of contact with the corresponding disk surfaces, the continuous variables are the three anisotropy angles. The input parameters for this model will include four categorical variables and three continuous variables. The probability distribution function for the anisotropy angles used for this analysis are normal distribution for primary anisotropy angle α, uniform distribution for angle β, and Weibull distribution for angle ζ.

In order to build the RF-based surrogate model, FE model evaluations are obtained corresponding to random samples of the three anisotropy angles from the realistic probability distribution for these angles provided by the manufacturer. Sobol sampling sequence is used to obtain the samples of anisotropy angle α, β and ζ. The contact pressure values obtained from model evaluations are divided into training set and test set in the proportion 9:1. For the present study the non-linear FE model evaluations are computationally expensive and therefore a relatively high ratio of the training set to test set is used to build the RF model. The ratio of 9:1 for the training set to test set allows the majority of the model evaluations to be used for constructing the surrogate model. The total number FE model evaluations obtained is 180 which include 20 number of FE model evaluations of Nominal, Upper and Lower geometry variants each and 60 number of FE model evaluations of Asym-A and Asym-B models. From the results of our previous analysis for varia-

tion in contact pressure with respect to the crystal orientation of blades, presented in Table (5.2) and (5.3), it is evident that the variation in average and maximum contact pressure is comparatively high for the two models with asymmetric fir–tree geometry. Therefore to capture the higher variation in contact pressure for those two geometry variants, a higher number of FE model evaluations for those variants are obtained compared to that for the other three variants.

The residual error in predicted values for normalised average contact pressure on the left side and right side of the fir–tree root surface is shown in Fig. 5.12(a) and (b). The residual error is calculated as the difference between the RF model predicted value and the actual value obtained using the FE model evaluation. The values of predicted average contact pressure and the corresponding residual are normalised with respect to the value of average contact pressure for *Nominal* geometry for the case when the material anisotropy axis is aligned with the blade geometry axis. The maximum error in prediction for average contact pressure on left and right side of fir–tree contact surfaces is less than 6.5% of the predicted value for all root geometry variants analysed. The figure shows that the predicted values for the contact pressure forms cluster where each of the clusters corresponds to different root geometry variant. Similarly, Fig. 5.13(a) and (b) shows the residual error in the prediction of maximum contact pressure on the left and right side contact surfaces of fir–tree root geometry respectively. The RF-based surrogate model predicts the maximum contact pressure at fir–tree root surfaces with a maximum percentage error of 7.0%.

The accuracy of the surrogate model can also be estimated using the normalised mean squared error which is defined as the ratio of the difference in the variance of predicted value from mean squared error to variance of predicted value:

$$R^2 = (Var(y) - MSE(y))/Var(y) \tag{5.1}$$

where, $Var(y) = \sum_{i=1}^{n}(y^{(i)} - \bar{y})^2/n$; $\bar{y}$ being the mean of the predicted value, $y^{(i)}$ is the i^{th} predicted value, and $MSE(y)$ is the mean square error of RF model. For the case when $R^2 = 1$, the model captures the variation in response variable perfectly. For the present RF model, the value of error estimates for the training set and test set are shown in Table 5.4. The error estimate indicates that the RF model

can sufficiently capture the variation in average and maximum contact pressure at fir–tree root joints w.r.t variation in root geometry and blade material anisotropy angles.

Table 5.4: Error estimates for RF model

	Contact	Error estimate (1-R^2)	
	surface	Training set	Test set
Maximum	Left side	0.003	0.017
contact pressure	Right side	0.005	0.013
Average	Left side	0.001	0.009
contact pressure	Right side	0.001	0.008

For Monte Carlo simulations using FE model and RF based surrogate model, the convergence of mean and STD of normalised average contact pressure on left side contact of the fir-tree root joint for *Asym-B* variant is shown in Fig.5.14(a). The mean value of average contact pressure obtained using the surrogate model converges faster compared to that obtained using the FE model based Monte Carlo simulation. Fig.5.14(b) shows the convergence of mean and STD of normalised maximum contact pressure for both RF surrogate model and for MCS using FE analysis. For both maximum and average contact pressure, the accuracy of mean values obtained using the surrogate model is good whereas the accuracy of STD can only be considered as acceptable for the case shown.

The normalised mean and STD for average contact pressure w.r.t variation in anisotropy angles are calculated for different root geometry variants using the RF model. Table 5.5 gives the value of mean and STD for average contact pressure on left and right side of fir–tree for different root geometry variants. The values for average contact pressure is normalised with respect to the average contact pressure at the left fir–tree root for nominal geometry variant with blade anisotropy axis aligned with blade geometry axis. As indicated by the value of STD, the variation in average contact pressure is significant for the two geometries with asymmetric contacts. For a given geometry variant, the effective reduction in simulation time is calculated as the difference between simulation time required for as many Monte

Carlo evaluations required to obtain a unit place convergence for the mean value and the total simulation time, required for the number of model evaluation of that geometry variant, to build the RF model. The convergence of statistical mean obtained from MCS is slow for the two variants with asymmetric contact geometry (see Fig.5.14 for the case of Asym-B), and therefore, the savings in computational time obtained by using surrogate models is significant for those two variants.

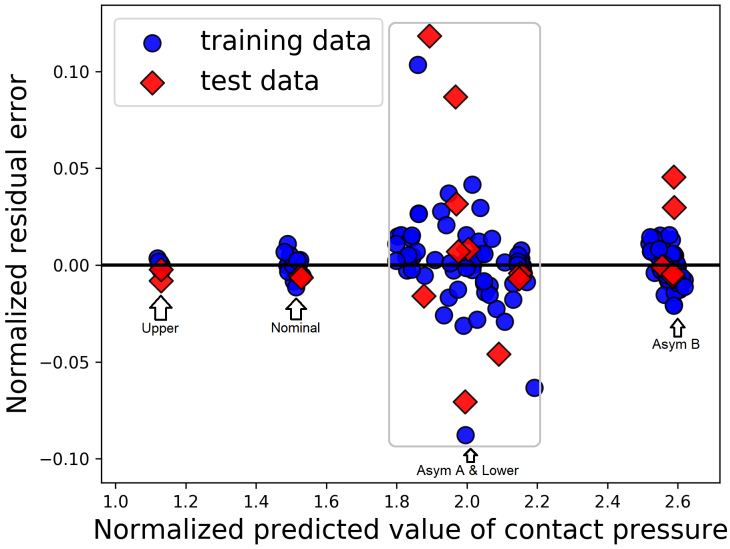

(a)

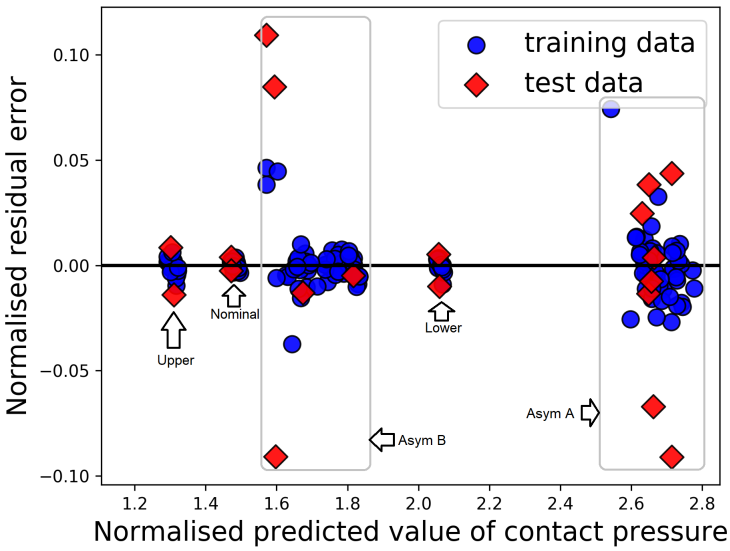

(b)

Figure 5.12: Residual error in RF model prediction of normalised average contact pressure on (a) left side and (b) right side of the fir–tree.

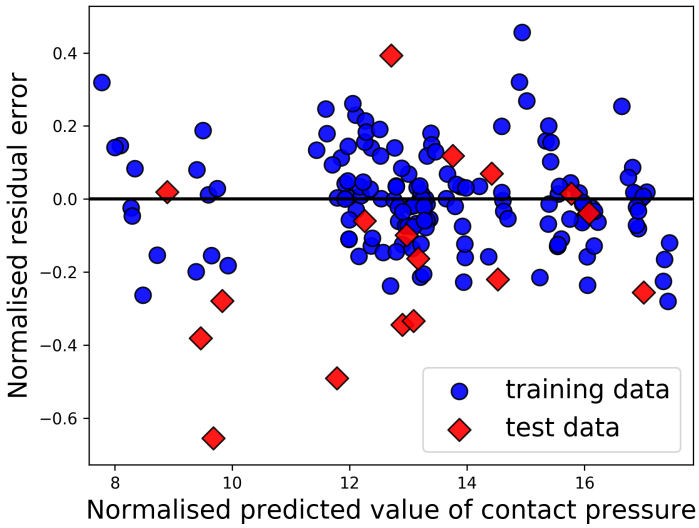

(a)

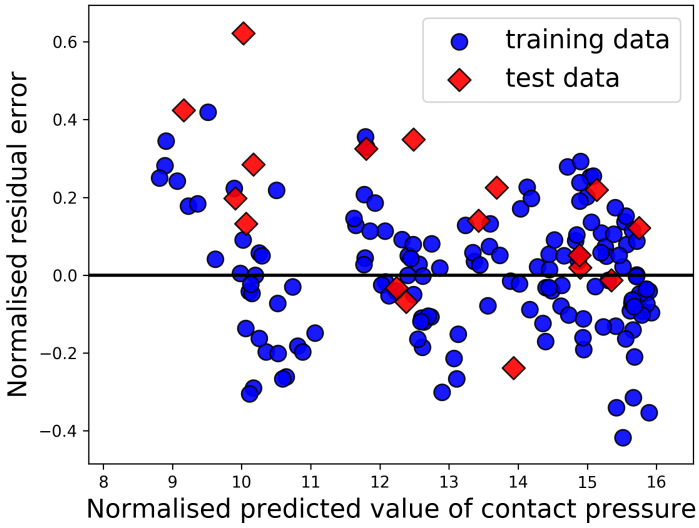

(b)

Figure 5.13: Residual error in prediction of normalised maximum contact pressure for (a) on left side and (b) on right side of the fir–tree.

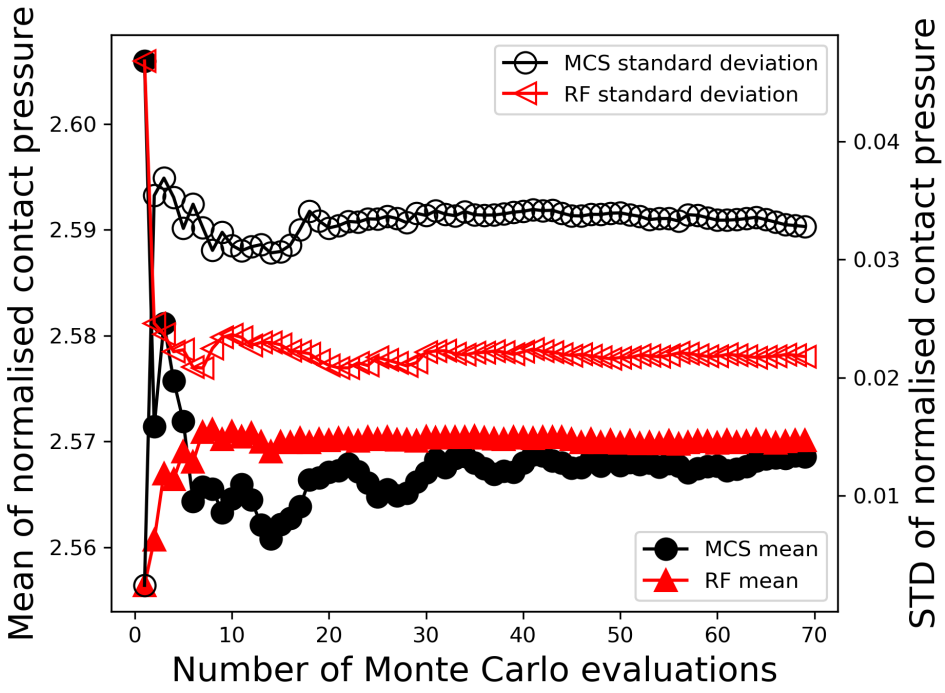

(a)

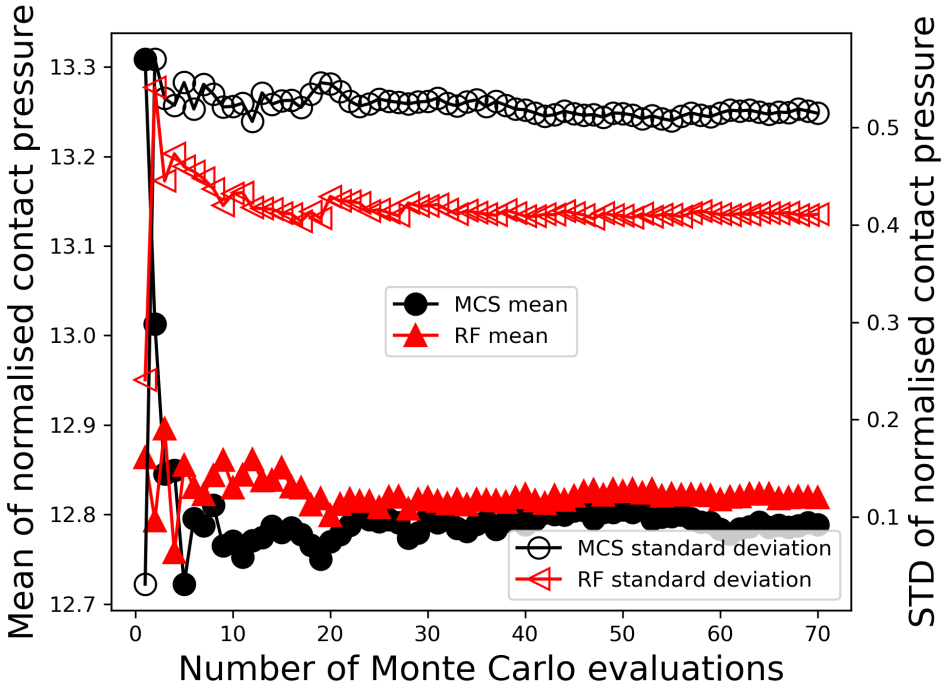

(b)

Figure 5.14: Convergence of normalised mean and STD of (a) average contact pressure and (b) maximum contact pressure on left side of fir–tree joint for *Asym-B* variant.

Table 5.5: Statistics of normalised average contact pressure on fir–tree contact surfaces

Root geometry variant	Statistical characteristics							
	Left Side				Right Side			
	Mean		STD		Mean		STD	
	RF	MCS	RF	MCS	RF	MCS	RF	MCS
Asym-A	1.960	1.964	0.086	0.095	2.689	2.685	0.061	0.064
Asym-B	2.571	2.568	0.022	0.0325	1.740	1.732	0.062	0.079
Nominal	1.509	1.513	0.012	0.016	1.480	1.479	0.006	0.008
Upper	1.125	1.127	0.004	0.005	1.307	1.306	0.010	0.013
Lower	2.072	2.061	0.006	0.008	2.150	2.149	0.006	0.008

Chapter 6

Uncertainty analysis for static deformation of mistuned bladed disks

From the sensitivity analysis for static deformation of the mistuned bladed disk with respect to crystal orientation presented in Chapter 4, it is evident that displacements and stresses are sensitive to the orientation of the blade crystal. Uncertainty analysis presented in this chapter aims is to quantify the scattering in static deformation of mistuned bladed disk considering the scattering in blade crystal orientation. The statistics for blade displacements and stresses for the mistuned bladed disk is presented. The statistical mean and standard deviation are obtained from Eqn. 2.50 and 2.51 presented in Chapter 2, based on gradient-based polynomial chaos expansion. The values obtained from polynomial chaos expansion for statistical mean and standard deviation are compared with values obtained from conventional Monte Carlo simulation.

6.1 Scatter in deformation due to randomness in the crystal orientation of blades

In order to obtain an estimate for the range of scattering in blade displacements and stresses, a sample of 250 different mistuning patterns was obtained from the known

probability distribution of the blade anisotropy angles. Based on the analysis of the mistuning patterns, for linear and non-linear bladed disk, the range of variation in blade tip displacement, considering all the 75 blades is shown in Table 6.1. The value of static displacements are normalised with respect to the maximum value of radial displacement for a non-linear tuned bladed disk with blade anisotropy axis aligned with blade geometry axis. Comparing the range of variation in displacements for linear and non-linear bladed disk, it is evident that the effect of material anisotropy mistuning creates significantly high scatter in the absence of friction joints. In Chapter 4, based on local sensitivity analysis we concluded that friction interfaces at fir–tree root and shrouds tend to localize the influence of blade crystal orientation of a blade in the bladed disk to its immediately adjacent blades. The smaller range of variation in displacements for non-linear bladed disk further substantiates this argument. The percentage variation in displacement components along the axial and circumferential direction is higher compared to that along the radial direction.

The scattering also influences similar to displacements, the stresses generated in the structure in blade anisotropy angles. The stresses at fir–tree root of a bladed disk is of particular interest as the life of the joint usually becomes critical in determining the life of the bladed disk. As an example case, for a non-linear model of the bladed disk, the range of variation in von Mises stresses at a selected node position on blade root of all the 75 blades due to scattering in blade anisotropy orientations was calculated. Based on 250 different mistuning patterns analysed it was found that the maximum variation in von Mises stresses considering all blades is 28%.

It can be inferred from the analysis of several mistuning patterns that there are noticeable variations in the static deformation of a bladed disk under centrifugal loading when the scattering of the crystal orientation of blades are considered. In order to account for this variation in the design of a gas turbine, it is required to quantify the uncertainty in static deformation of the bladed disk.

Table 6.1: Variation in normalised blade tip displacement in mistuned bladed disk

Displacement		FE model type		Percentage variation	
		linear	non-linear	linear	non-linear
Axial	Maximum	0.5002	0.5220	59.4	16.7
	Minimum	0.2713	0.4412		
Circumferential	Maximum	0.2285	0.4172	71.3	18.6
	Minimum	0.1084	0.3460		
Radial	Maximum	0.8325	0.9907	7.0	3.1
	Minimum	0.7762	0.9609		

6.2 Uncertainty analysis using polynomial chaos expansion

While analysing high–fidelity FE models of the bladed disk with non-linear friction contacts, conventional Monte Carlo simulation approach for uncertainty analysis is prohibitive due to high computational cost. The possibility of using polynomial chaos expansion to perform uncertainty analysis of mistuned bladed disk is explored in this section. The computational cost associated with constructing the polynomial chaos approximation is depended on the number of FE model evaluations required for calculation of coefficients in the expansion. The higher the number of random variables, the higher the number of model evaluations required and, therefore higher the associated computational cost. The number of terms in the expansion increases factorially with an increase in the dimension of the design parameter space. For a mistuned bladed disk with 75 blades and each blade having three anisotropy angles, the number of terms in the polynomial chaos expansion of order two is 25651. Therefore, a three-fold strategy is used to reduce the computational cost associated with the building of the surrogate model which are listed below.

1. Use gradient values of functions with respect to design parameters, along with function evaluations to calculate the unknown coefficients in the expansion.

2. Use a truncation scheme that excludes the interaction terms between design variables in the polynomial chaos expansion.

3. Reduce the dimension of the design parameter space based on insights gained from sensitivity analysis.

For uncertainty analysis of static deformation of a bladed disk presented in this section, the statistical characteristics for deformation of blade number one are calculated as a representative case. The gradient-based polynomial chaos expansion method used for uncertainty analysis can be used to obtain the statistical characteristics for deformation at any chosen location in the bladed disk. For a mistuned bladed disk, in order to quantify the scattering in displacements and stresses of blade number 1, the variation in the crystal orientation of nine blades shown in Fig. 6.1, are considered which constitutes a total of 27 anisotropy angles as random variables. While studying the variation in blade tip displacements of blade number 1, the choice of these nine blades is justified based on the local sensitivity analysis results presented in Chapter 4 which suggests that only a few blades in the immediate neighbourhood of the considered blade have a significant influence on the displacements and stresses.

The PCE obtained for deformation of the bladed disk is compared for the two cases, when coefficients of expansion are obtained from (i) function evaluation alone and, (ii) function evaluations together with gradient values. The author uses the term "gradPCE" to refer to polynomial chaos expansions when the expansion coefficients are evaluated from gradient values as well as function values at sample points whereas PCE will refer to polynomial chaos expansion when the coefficients are evaluated based on function values alone. The sampling of input parameter space is based on Sobol sequence which was found to be useful in the exploration of multidimensional space [114]. The anisotropy angles α, β and ζ of all blades in the bladed disk are assumed to have a Normal, Uniform and Uniform probability distribution respectively. The range of variation of the three anisotropy angles are the same as that provided by the manufacturer of the blades and are not revealed to comply with the confidentiality agreement.

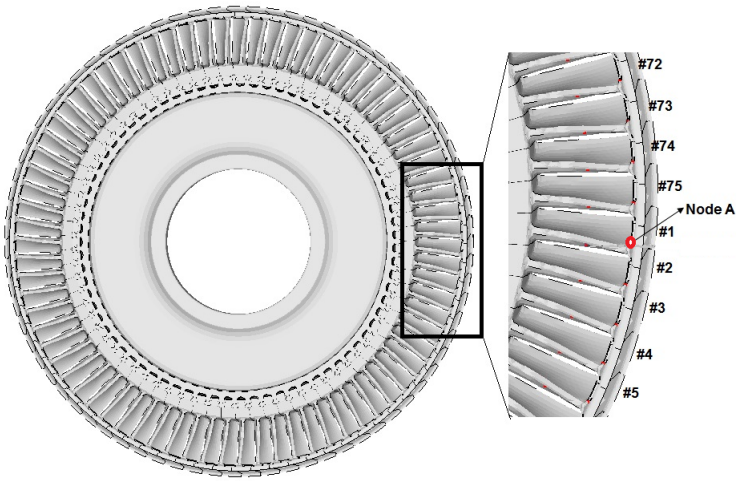

Figure 6.1: Geometry of bladed disk showing the considered 9 blades with random anisotropy angles.

6.2.1 Analysis of the linear bladed disk.

As a first step, for a linear bladed disk, considering only the first two anisotropy angles of blade number as random variables the accuracy of 2^{nd} order polynomial chaos expansion in approximating blade displacements is investigated. The original variation in displacements is obtained from FE analysis of bladed disks by varying the anisotropy angles α and β of blade number 1 keeping ζ constant. For a mistuned bladed disk, polynomial chaos approximation for variation in axial, tangential and radial component of displacements at node A (see Fig.6.1) with respect to the anisotropy angle α and β of blade number one is shown in Fig. 6.2(a), (b), and (c) respectively. The expansion coefficients in PCE and gradPCE are calculated from ten and six FE model evaluations respectively. It is clear that the gradient-based PC expansion provides a reasonable approximation over the realistic domain of variation of anisotropy angle α and β considered here. The variations obtained for axial and radial displacement shows that displacements are more sensitive to anisotropy angle α over the entire domain. Note that while the radial displacement is maximum for α equal to zero, i.e. when the blade anisotropy axis is aligned with the geometric axis.

To further investigate the usefulness of PC-based surrogate model, considering a more realistic case when the anisotropy angles of 9 blades, shown in Fig. 6.1, are considered as random variables, the statistical characteristics of bladed tip displace-

ments at blade one are obtained based on truncated PCE and gradPCE. In order to obtain the expansion coefficients in PCE and gradPCE a least squares regression method (see Eqn. 2.45) is used with values of weight coefficients $w_1 = w_2 = 1$. Table 6.2 compares the values for mean and STD of blade tip displacements for blade

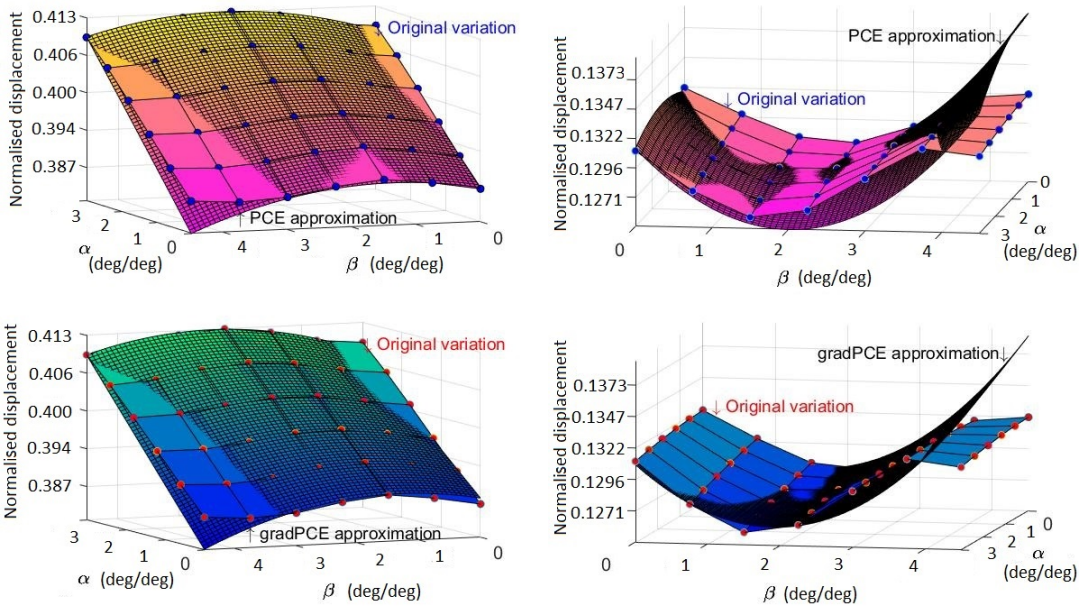

(a) (b)

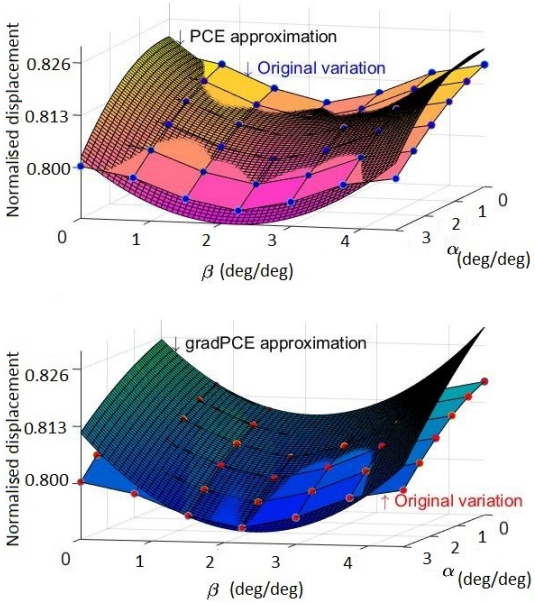

(c)

Figure 6.2: PCE and gradPCE approximations for (a) axial, (b) tangential and (c) radial displacement at blade tip of blade number one.

number 1 obtained using PCE and gradPCE to the corresponding Monte Carlo estimates based on 2850 evaluations of the linear bladed disk model. For the linear bladed disk analysed, increasing the degree of PC expansion from 2 to 3 provides no improvement in the statistics obtained using gradPCE. For the case of PCE, increasing the degree of PC expansion deteriorate the accuracy of statistics obtained. This behaviour could be explained by considering the ratio of a number of function evaluations to the number of expansion coefficients, referred to as oversampling ratio (OSR) by Hosder et al.[115]. Compared to an oversampling ratio of approximately two used for PCE of degree 2, OSR of nearly one is used for PCE of degree 3. The more accurate statistics from the former case, confirms the observation made by Hosder et al. regarding better statistical characteristics obtained from PCE using an OSR of value two.

For any given order of PC expansion, the expansion can be further truncated by ignoring the interaction terms between random variables. Even though such a truncation of the PC expansion can considerably reduce the computational cost involved in constructing the surrogate model it is possible that the accuracy of the approximation is compromised. For PC expansion of order two, the effect of truncation on the accuracy of the approximation is investigated by comparing the statistics for displacements obtained from full and truncated PC expansion with Monte Carlo estimates. Table 6.3 compares the statistics of displacements obtained using PCE of degree two with full basis set and the truncated basis set to results obtained using MCS. For the problem studied, accurate statistics can be obtained by using a truncated basis set at a computational time as low as one-third of that required when using a full basis set.

For building the gradPCE based surrogate models, additional computational effort is spent in calculating the gradient values of displacements. When the computational time for FE analysis is smaller than that required for calculating gradient values, as is the case for linear bladed disks, the advantage of using a fewer numbers of model evaluations for the gradPCE method is offset by the additional time required for calculating gradient values. Therefore, for linear bladed disk models, gradPCE offers no reduction in computational cost compared to PCE.

Table 6.2: Statistics for blade tip displacements obtained from polynomial chaos expansion and MCS

Degree of PC expansion	Number of coefficients in PC expansion	Number of evaluations		Displacement component	Normalised mean			Normalised standard deviation		
		grad-PCE	PCE		gradPCE	PCE	MCS	gradPCE	PCE	MCS
2	55	40	120	Axial	0.3800	0.3842	0.3835	0.0272	0.0355	0.0264
				Tangential	0.1785	0.1817	0.1832	0.0116	0.0120	0.0133
				Radial	0.8130	0.8130	0.8127	0.0138	0.0086	0.0124
3	433	90	460	Axial	0.3812	0.3846	0.3835	0.0238	0.0458	0.0264
				Tangential	0.1793	0.1824	0.1832	0.0142	0.0269	0.0133
				Radial	0.8137	0.8132	0.8127	0.0118	0.0175	0.0124

Table 6.3: Statistics for blade displacements of a linear mistuned bladed disk

Type of PC basis	Number of coefficients	Number of evaluations of bladed disk	Model evaluation time (hrs)	Displacement component	Mean		Standard deviation	
					PCE	MCS	PCE	MCS
Full	406	410	34	Axial	0.3827	0.3835	0.1232	0.0264
				Tangential	0.1838	0.1832	0.0409	0.0133
				Radial	0.8131	0.8127	0.0418	0.0124
Truncated	55	120	10	Axial	0.3842	0.3835	0.0355	0.0264
				Tangential	0.1817	0.1832	0.0120	0.0133
				Radial	0.8130	0.8127	0.0086	0.0124

6.2.2 Analysis of the non-linear bladed disk.

Non-linear bladed disk models with friction contacts at blade–disk and shroud interfaces are solved iteratively using Newton–Raphson iteration procedure, and hence, the computational cost required for analysis of non-linear models are significantly higher than those required for linear models. Therefore the use of surrogate models that can replace high–fidelity computational models is particularly advantageous.

As a representative case, the statistical mean and standard deviation for displacements at blade tip node of blade number one is calculated for a mistuned bladed disk considering anisotropy angles of the nine blades, shown in Fig. 6.1, as random parameters. In Table 6.4, a comparison of the mean and standard deviation of displacements obtained from 2^{nd} order truncated PCE and gradPCE with values obtained from Monte Carlo simulation using 250 FE evaluations is presented. While the mean and standard deviation obtained using PCE and gradPCE from 105 FE realisations shows close correspondence with Monte Carlo estimates, the corresponding values obtain using 60 realisations differ, especially when using PCE. The smaller number of model evaluations required using gradPCE compared to PCE results in a reduction in the computational cost involved in calculating statistics. Fig. 6.3 shows the convergence of standard deviation for displacements at node A (see Fig.6.1), obtained from PCE and gradPCE, with respect to the number of non-linear bladed disk models evaluated to obtain the coefficients in the expansion. The proposed gradPCE method is shown to achieve fast convergence for STD of displacements with respect to model evaluations for non-linear bladed disks analysed. Therefore, it reduces the computational cost for calculating displacement statistics for non-linear bladed disks from 271 hrs (105 model evaluations required for PCE) to 185 hrs (60 model evaluations).

Considering von Mises stress at fir–tree root nodes of all blades in a mistuned bladed disk blade, based on analysis of 250 different mistuning patterns, a maximum variation of 28% was obtained compared to the maximum variation of 18.6% obtained for blade tip displacement along circumferential direction. For non-linear bladed disk, considering the higher percentage variation in von Mises stress compared to that obtained for displacements, the anisotropy angles of 30 blades are considered

as random variables to obtain the statistical characteristics using full polynomial chaos expansion of order 2. The 2^{nd} order polynomial chaos expansion including anisotropy angles of 30 blades as random variables has 4186 terms. The convergence of mean and standard deviation of von Mises stress at fir–root node of blade number 1 obtained from Monte Carlo simulation and 2^{nd} order gradPCE is shown in Figures 6.4(a) and (b) respectively. While the statistical mean of von Mises stress obtained using gradPCE converges for 100 evaluations of the FE model, the convergence for standard deviation is comparatively slow and requires more than 150 evaluations in order to converge to the value obtained using Monte Carlo simulation. The coefficient of variation of von Mises stress, calculated as ratio of standard deviation to mean value, expressed in percentage is 4.86% compared to 3.3% for axial, 3.15% for tangential, and 0.5% for radial displacement at blade tip.

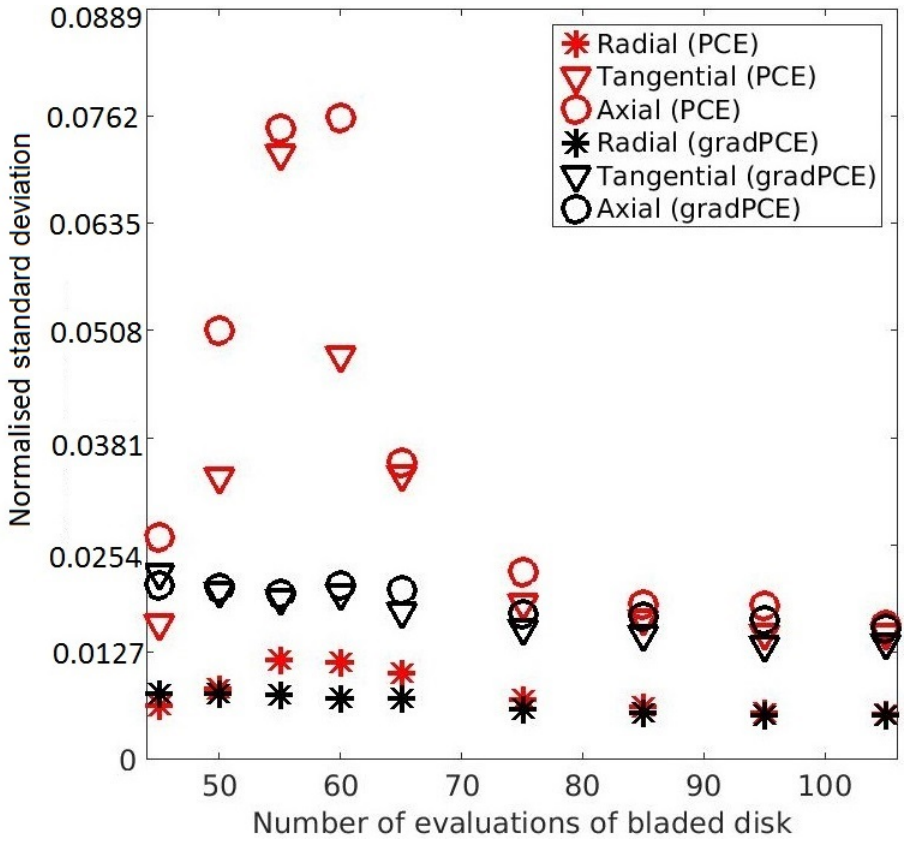

Figure 6.3: Normalised standard deviation of blade tip displacements for non-linear bladed disk.

Table 6.4: Statistics for displacements of a mistuned non-linear bladed disk

Model evaluations	Model evaluation time		Displacement	Normalised Mean			Normalised STD		
	PCE (hrs)	grad-PCE (hrs)		PCE	grad-PCE	MCS	PCE	grad-PCE	MCS
60	155	185	Axial	0.4771	0.4762	0.4751	0.0760	0.020	0.0157
			Tangential	0.3744	0.3747	0.3743	0.0477	0.0197	0.0118
			Radial	0.9871	0.9869	0.9866	0.0115	0.0073	0.0052
105	271	323	Axial	0.4775	0.4774	0.4751	0.0160	0.0155	0.0157
			Tangential	0.3743	0.3740	0.3743	0.0150	0.0138	0.0118
			Radial	0.9867	0.9867	0.9866	0.0053	0.0053	0.0052

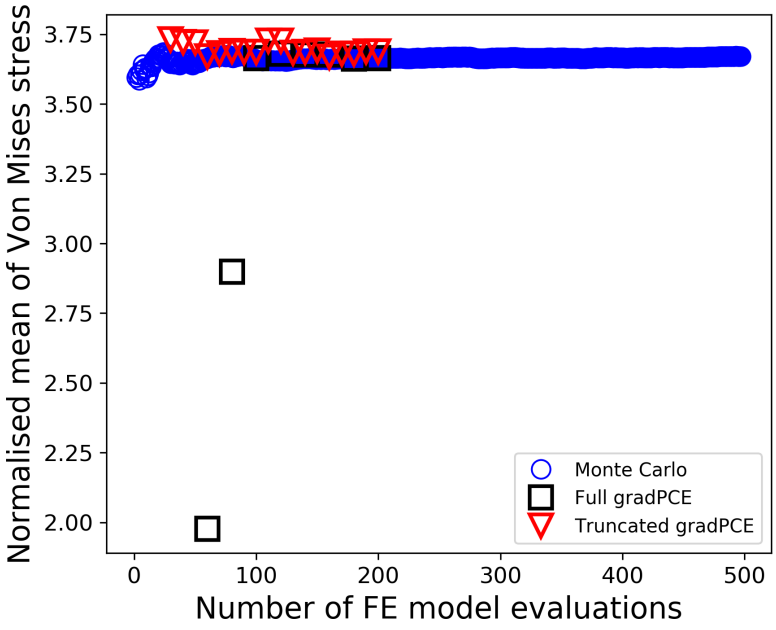

(a)

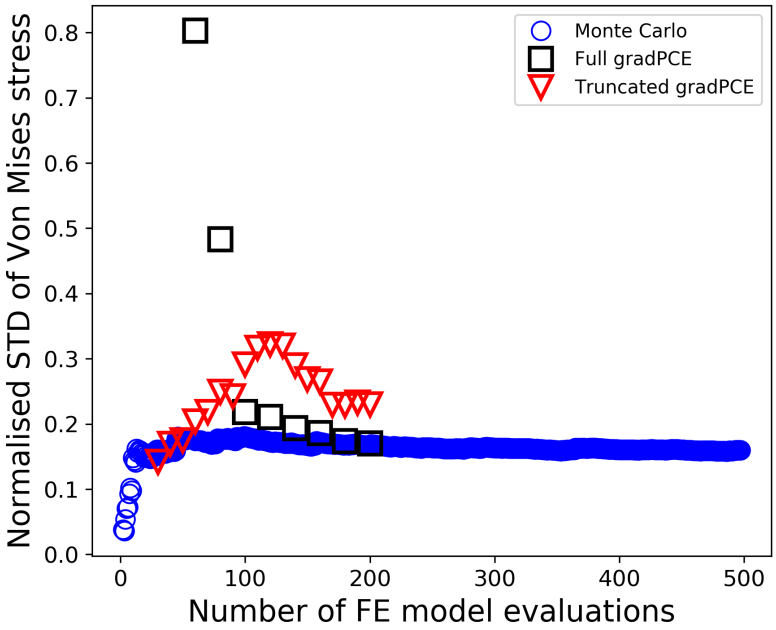

(b)

Figure 6.4: Convergence of (a) mean and (b) standard deviation of von Mises stress.

6.3 Analytically derived PDF using sensitivity-based linear approximation

In Chapter 2, the methodology for an analytical derivation of probability density function (PDF) of blade response using sensitivity based linear approximation was presented. In this section, for a tuned bladed disk, PDF for static displacements considering the uncertainty in the crystal orientation is obtained from Eqn. 2.68 and 2.69 presented in Chapter 2.

In a tuned bladed disk, the crystal orientation of all blades are identical and therefore, under centrifugal loading, all blades in the bladed disk will experience the same deformation. Even for the theoretical case of a tuned bladed disk, different bladed disks will deform differently when the uncertainty in crystal orientation is considered. The study aims to obtain the PDF of blade displacements with respect to the assumed probability distribution of the three anisotropy angles of a blade. For this analysis sector model of the bladed disk is used with linear bonded contacts at fir–tree roots and shrouds. The PDF of displacement components are obtained for two different sets of distribution of blade anisotropy angles shown in Table 6.5. The limits of variation of anisotropy angles are obtained, from a sensitivity-based linear approximation of the variation of blade displacements, such that a pre-defined value of the displacement is not exceeded. In order to construct the linear approximation, the displacements and its sensitivity to anisotropy angles are calculated at a chosen point in the domain of variation of the anisotropy angles.

Table 6.5: Probability distribution of anisotropy angles.

Case	Probability distribution			Solution type	
	α	β	ζ	Analytical	Semi-analytical
1	Normal	Uniform	Uniform	✓	
2	Normal	Uniform	Weibull		✓

In order to test the implementation of the analytical formulation for PDF in Maple, for a test case, the analytical PDF for radial displacement was compared to PDFs obtained from numerous function evaluations. The function evaluations are obtained

from sensitivity-based linear approximation corresponding to 1000, 10000, 100000, and 500000 samples of the anisotropy angles for the two different cases of the probability distribution for those angles. Fig. 6.5(b) and (a) shows a comparison of the PDFs obtained from function evaluations to that obtained analytically for the two different sets of distributions of anisotropy angles specified as in case – 1 and case – 2 respectively. For the case when the PDF is determined fully analytically (Fig. 6.5b), a good comparison of the PDFs was obtained when the number of function evaluations is of the order of 10^5. For the case when the PDF is determined using a semi-analytical expression, the comparison with PDFs obtained through function evaluations shows a small difference.

Analytical PDFs for blade displacements are obtained based on a linear approximation of the blade displacements, used to obtain the limits for anisotropy angles over which their known PDFs are integrated, are constructed using one evaluation of the FE model at a chosen point in the domain of variation. The quality of the PDF obtained analytically will depend on the accuracy of the linear approximation of blade displacements. Therefore the choice of the design point used to construct the linear approximation is critical. For axial, radial, and tangential displacements, the PDFs obtained semi-analytically using a linear approximation of displacements for the different choices of value for anisotropy angles is shown in Fig. 6.6(a), (b) and (c) respectively for case – 2. In order to validate the PDFs obtained from the analytical expression, a comparison is made with the PDF of blade displacements obtained numerically based on 5000 sample evaluations of the FE model. Among the PDFs obtained using the analytical expression, the PDF obtained based on linear approximation at the mean value of the anisotropy angles, represented as α_0, β_0 and ζ_0, gives a comparatively good approximation for axial displacement. In general, the PDF obtained using analytical expression does not provide a good comparison to that obtained numerically. This is true also for the case – 1, where the distribution of anisotropy angles allows a fully analytical derivation of the PDF for blade displacements, as shown in Fig. 6.7(a), (b) and (c) for axial, radial, and tangential displacement respectively. This suggests that a linear approximation is not sufficient to model the variation in displacements of the bladed disk with respect to the variation in anisotropy angles.

The quality of the linear approximation could be improved by approximating the displacements over a smaller domain of variation of the anisotropy angles. In order to investigate this possibility, the original probability distribution of anisotropy angles

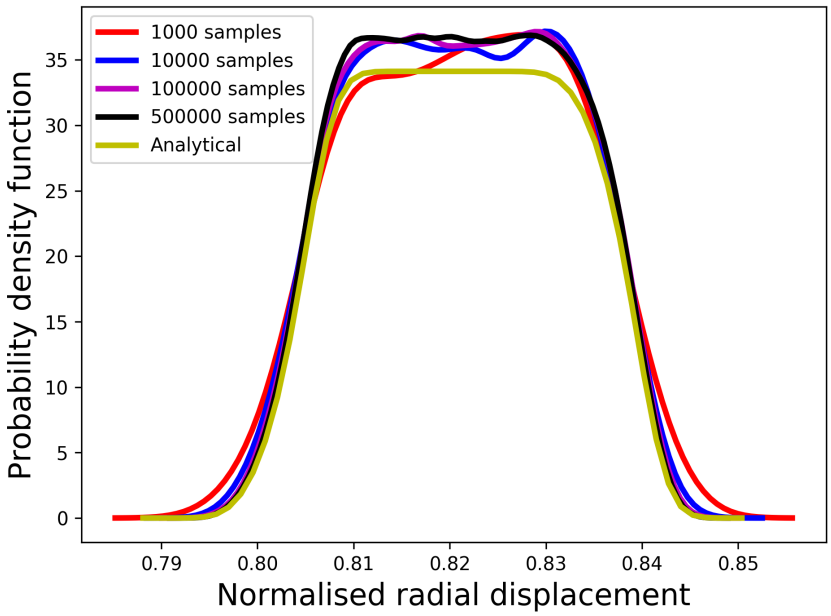

(a)

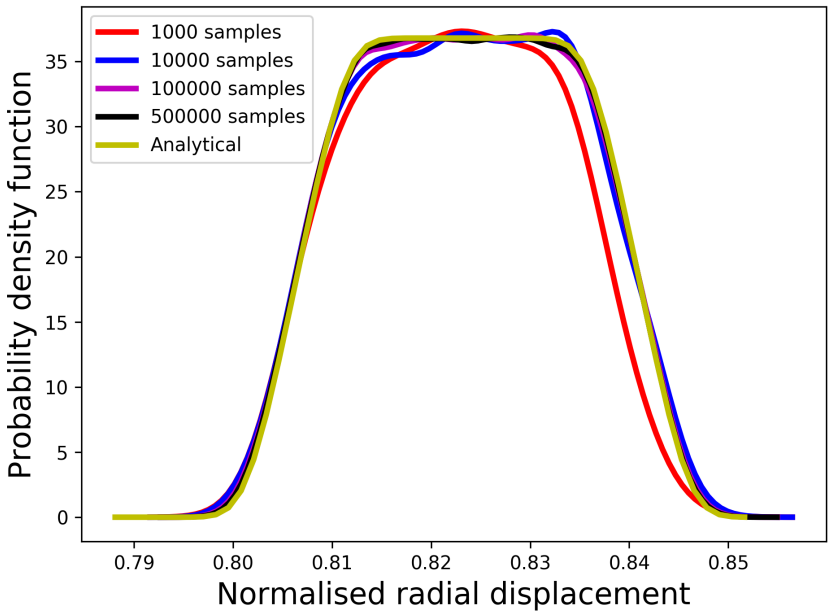

(b)

Figure 6.5: Comparison of PDF obtained analytically to those obtained from a linear approximation when the anisotropy angles are distributed as defined for (a) case-2 and (b) case-1.

α was modified by reducing the mean (α_0) and standard deviation of the normal distribution by a factor of 2. The uniform distribution defining anisotropy angle β was modified by increasing the lower limit and decreasing the lower limit such that the modified standard deviation of the distribution is one-third of the original distribution. The probability distribution of the third anisotropy angle ζ was left unmodified. For the modified distribution of anisotropy angles, the PDF of blade displacement along the axial, tangential and radial direction is shown in Fig. 6.8(a), (b) and (c) respectively. For the reduced range of variation of the anisotropy angles α and β, the comparison of PDF obtained from the analytical expression with that obtained from 5000 evaluations of FE model shows some improvement, especially for the radial displacement. Further improvement could be achieved by using a quadratic approximation of the displacements which will increase the complexity in the derivation of the analytical expression.

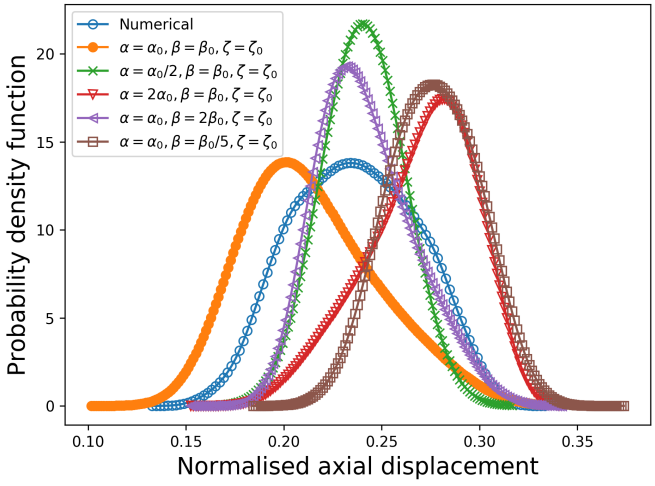

(a)

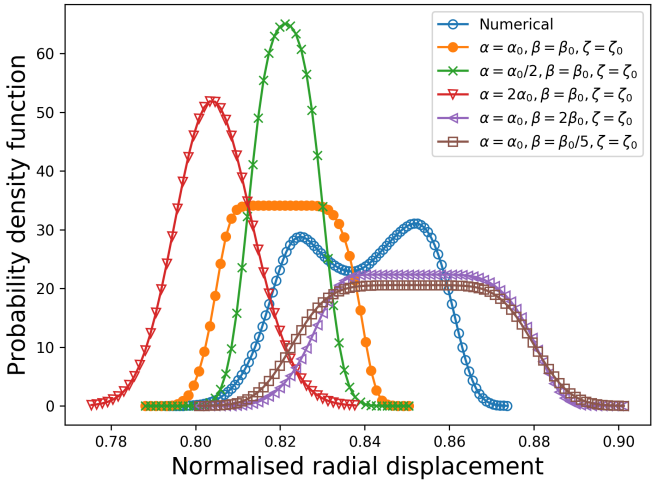

(b)

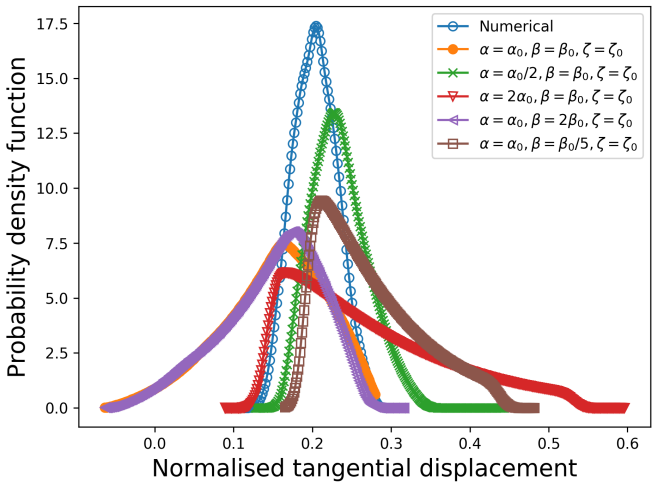

(c)

Figure 6.6: Comparison of PDFs obtained analytically to that obtained numerically based on FE model evaluations for (a) axial, (b) radial, and (c) tangential displacement when the anisotropy angles have distribution as defined for case–2.

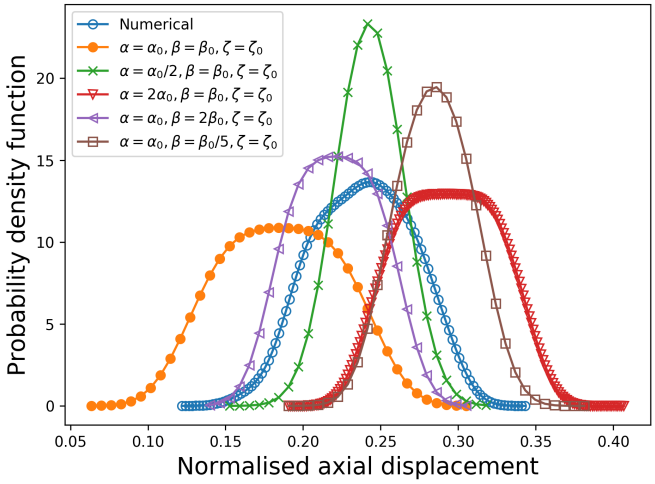

(a)

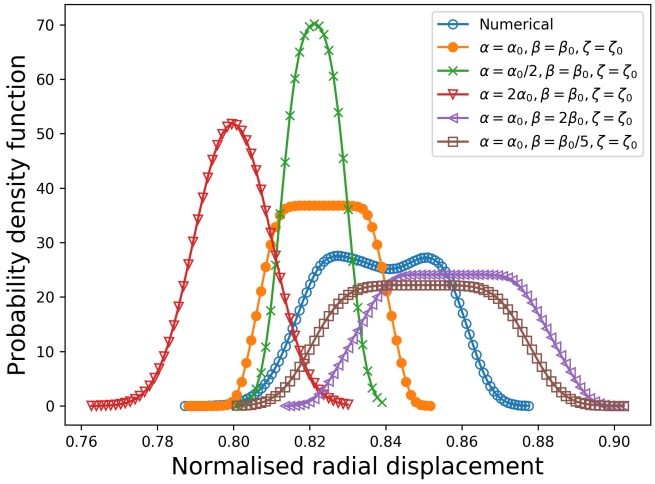

(b)

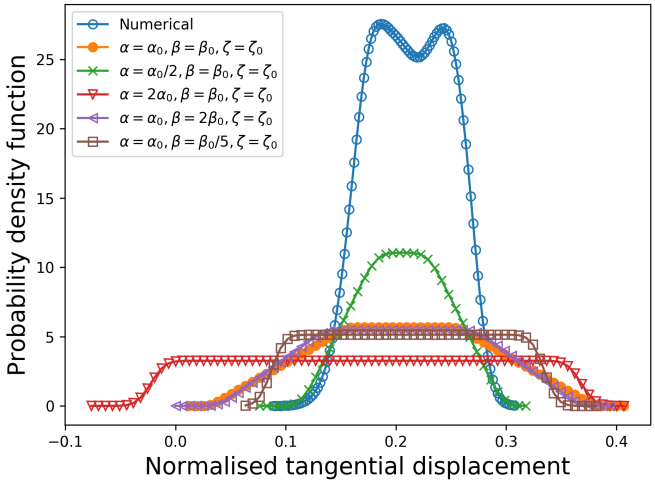

(c)

Figure 6.7: Comparison of PDFs obtained analytically to that obtained numerically based on FE model evaluations for (a) axial, (b) radial, and (c) tangential displacement when the anisotropy angles have distribution as defined for case–1.

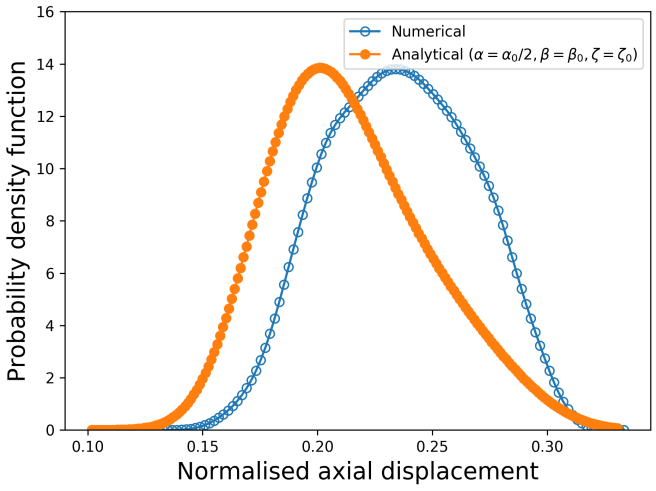

(a)

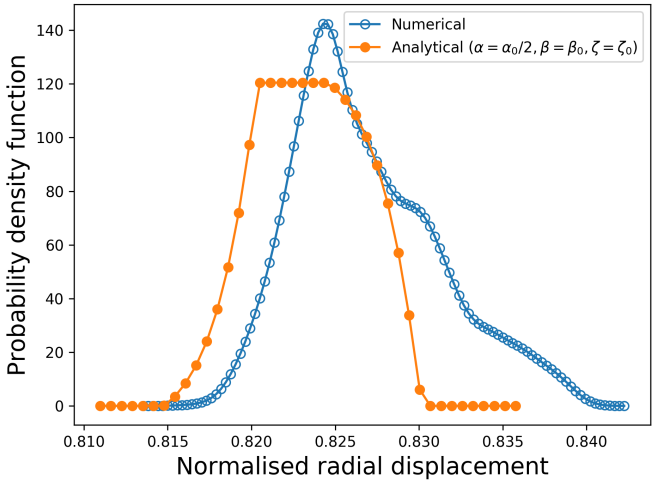

(b)

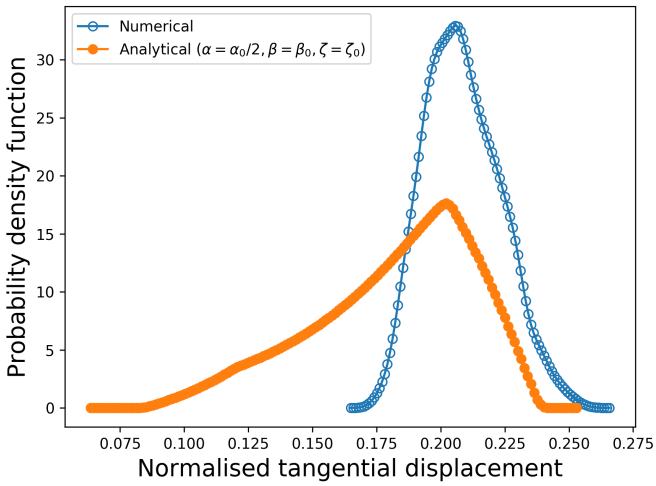

(c)

Figure 6.8: Comparison of analytically and numerically obtained PDFs for (a) axial, (b) radial, and (c) tangential displacement when the PDF of anisotropy angles are distributed as in case–2 but with reduced mean and standard deviation for angles α and β compared to the original distribution.

Chapter 7

Forced response analysis of mistuned bladed disks

A gas turbine bladed disk is not only subjected to centrifugal load but also experience gas pressure loads. It is well known that the response of a mistuned bladed disk to dynamic loading is significantly different from that of a corresponding tuned bladed disk. The amplitude of the response of a mistuned bladed disk is usually higher than that of a tuned bladed disk which is referred to as mistuning amplification. In this chapter, the effect of blade anisotropy mistuning on the forced response of a bladed disk is investigated in detail. Moreover, due to random variations in the crystal orientation of the blades, the mistuning amplification could be significantly different for different blade anisotropy mistuning patterns. Therefore, in order to ensure safe operation of the gas turbine engine, it is essential to quantify the uncertainty in forced response of the bladed disk.

The methodology developed for uncertainty analysis has been applied to the forced response of a realistic bladed disk model. The FE model of the bladed disk is shown in Fig.7.1. The blades are attached to disk using fir-tree root joints, and the adjacent blades are also connected through shrouds. The contacts at root and shroud are modelled as linear bonded contact. Following are the two types of bladed disk models used in this study:

- Sector model of the bladed disk with cyclic symmetric constraints applied is

used for modal analysis.

- Full model of the bladed disk for forced response analysis of mistuned bladed disk.

In order to investigate the effects of scattering in blade anisotropy orientations on modal characteristics, tuned bladed disk sector models are used. For analysis of tuned bladed disk, the use of sector model reduces the computational cost significantly. Excitation loads of unit magnitude are applied, in the X, Y and Z, direction on the leading edge at midspan and at blade tip nodes, represented by circles in Fig. 7.1. The damping of the structure is modelled as viscous damping. Due to additional stiffness provided by the shrouds, the forced response of the bladed disk usually peaks at a location between the mid-span of the blade and the blade tip. Therefore, for this study, the forced response of a node, represented by squares in Fig.7.1, located close to mid-span and towards trailing edge of the blade is chosen.

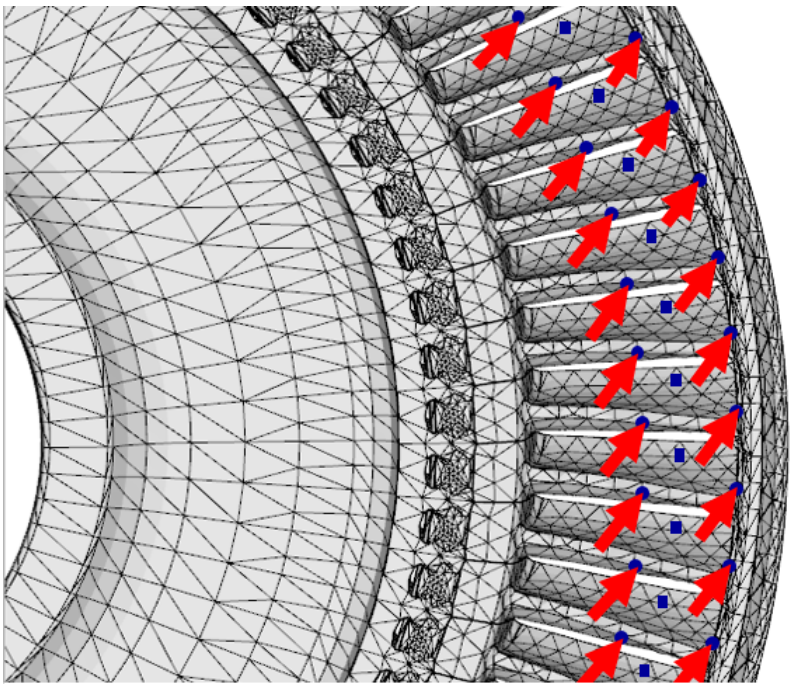

Figure 7.1: Finite element mesh of a section of the bladed disk model showing the location of the excitation load applied and the node for which blade response is obtained.

7.1 Effects of scattering in anisotropy orientation on modal properties and forced response

7.1.1 Effect of blade anisotropy orientation on modal properties.

The natural frequency and mode shapes of a single crystal blade will vary depending on the orientation of the crystal. In order to avoid extreme vibration due to resonance, it is important to quantify the variation in natural frequency of the blade with respect to blade anisotropy orientation. In this study, the effect of crystal orientation on natural frequency of a bladed disk with bonded contacts at fir–tree root joints and shrouds are investigated. Bonded contacts at blade roots and shrouds are used for modal analysis as it simplifies the modelling process, and moreover, the the mode shapes and natural frequencies of the bladed disk are relatively insensitive to the presence of interfaces under normal operating conditions. and are In order to quantify the uncertainty in natural frequency resulting from variations in crystal orientation, modal analysis is performed using sector model of bladed disk with cyclic symmetric constraints. For tuned bladed disk, with all blades having the same crystal orientation, the sector model is used to reduce the computational cost involved in uncertainty analysis using Monte Carlo simulation. The value of natural frequencies presented in this study are normalised with respect to the natural frequency of the first mode family, corresponding to zero nodal diameter, for a bladed disk with no shroud contact and the crystal orientation aligned with blade geometry axis.

In a gas-turbine, flow distortions occur due to the presence of stator and rotor blades present upstream or downstream of the flow. Such flow distortions result in excitation of a bladed disk in the order of its rotational speed. For example, for a bladed disk rotating at N r.p.m, M number of flow distortions will result in an excitation of the frequency $N \times M/60$ Hz, which is also referred to as M engine order (EO) excitation. In the case of a tuned bladed disk, M engine order excitation can only excite a mode shape that has the same spatial frequency. A mode shape

of spatial frequency M will result in M lines of zero modal deflections across the diameter of the disk, and hence M nodal diameters. Therefore, for a tuned bladed disk, M engine order excitation will excite a mode shape with M nodal diameters.

Based on 150 different mistuning patterns analysed, the mean and standard deviation for natural frequencies are obtained. Different orientations are obtained by sampling, from the realistic probability distribution of the anisotropy angles provided by the manufacturer, using Sobol sampling scheme. Anisotropy angle α is assumed to have normal distribution whereas β and ζ are assumed to be uniformly distributed. For the first 12 mode families, the variation in mean and STD of frequencies as a function of nodal diameter is shown in Fig. 7.2. In the figure, the STD of a particular frequency is indicated by the length of the error bar for that frequency. For smaller nodal diameters, the coupling of disk mode and blade mode is significant which results in an increase in the natural frequency with increase in nodal diameter. As the number of nodal diameter increases, the disk becomes progressively stiffer resulting in the disk modes becoming fully decoupled from blade modes. For any mode family, the blade–dominant modes are indicated by the horizontal lines in the frequency against nodal diameter plot.

In general, the influence of anisotropy orientation on the frequency of vibration of the bladed disk is significant for higher modes. For the modes studied, the variation in anisotropy angles can result in a coefficient of variation, defined as the ratio of standard deviation to mean value, of the natural frequency of up to 2.1%.

7.1.2 Effect of blade anisotropy orientation on the forced response.

The random variation in blade anisotropy angles will induce mistuning in the bladed disk. The forced response of a mistuned bladed disk is usually very different from that of the corresponding tuned bladed disk. There can be a significant increase in the maximum forced response amplitude of a bladed disk due to mistuning. In a mistuned bladed disk, the forced response amplitude of a certain blade can be higher or lower than its response for corresponding tuned. Usually the forced response amplitude of most blades in a mistuned bladed disk is lower than the corresponding

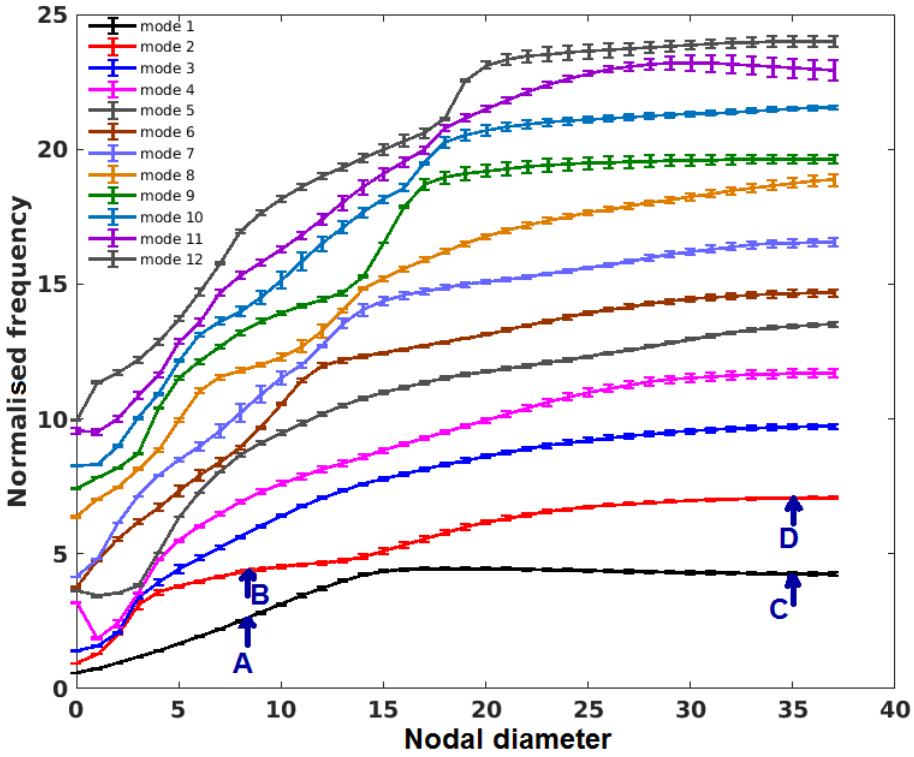

Figure 7.2: Variation in mean value and standard deviation of the frequency of tuned bladed disk with respect to the nodal diameter.

amplitude for the tuned bladed disk, a few blades will experience significant increase in the forced response amplitude. In order to study the effect of blade anisotropy mistuning on the forced response, several mistuning patterns were investigated. The effect of blade anisotropy mistuning on the forced response of the bladed disk is illustrated using plots of the envelope of normalised blade amplitudes for five different mistuning patterns of anisotropy angles. The mistuning patterns are obtained by random sampling of the anisotropy angles from the probability distribution provided by the manufacturer. Within a frequency range, the envelope of blade response is obtained as the maximum forced response amplitude across all blades in the bladed disk for the considered frequency. For the plots shown in Fig. 7.3, the value of forced response amplitude is normalised w.r.t the maximum forced response amplitude of the tuned blade disk in the considered frequency range.

Fig.7.3(a) shows the envelope of normalised blade response, for five different mistuning patterns, corresponding to 8EO excitation of frequencies in the range of first mode family, which is a disk-dominated mode (marked as 'A' in Fig. 7.2), along

with the envelope of forced response for tuned bladed disk where all blade anisotropy angles are aligned with blade geometry axis. Notice that for this particular case of forced response, when the disk-dominant mode is excited, even though additional resonance peaks appear, the forced response of mistuned bladed disk resemble that of the tuned case. Moreover, the magnitude of the maximum forced response amplitude for the mistuned case is only marginally higher than that of the tuned case.

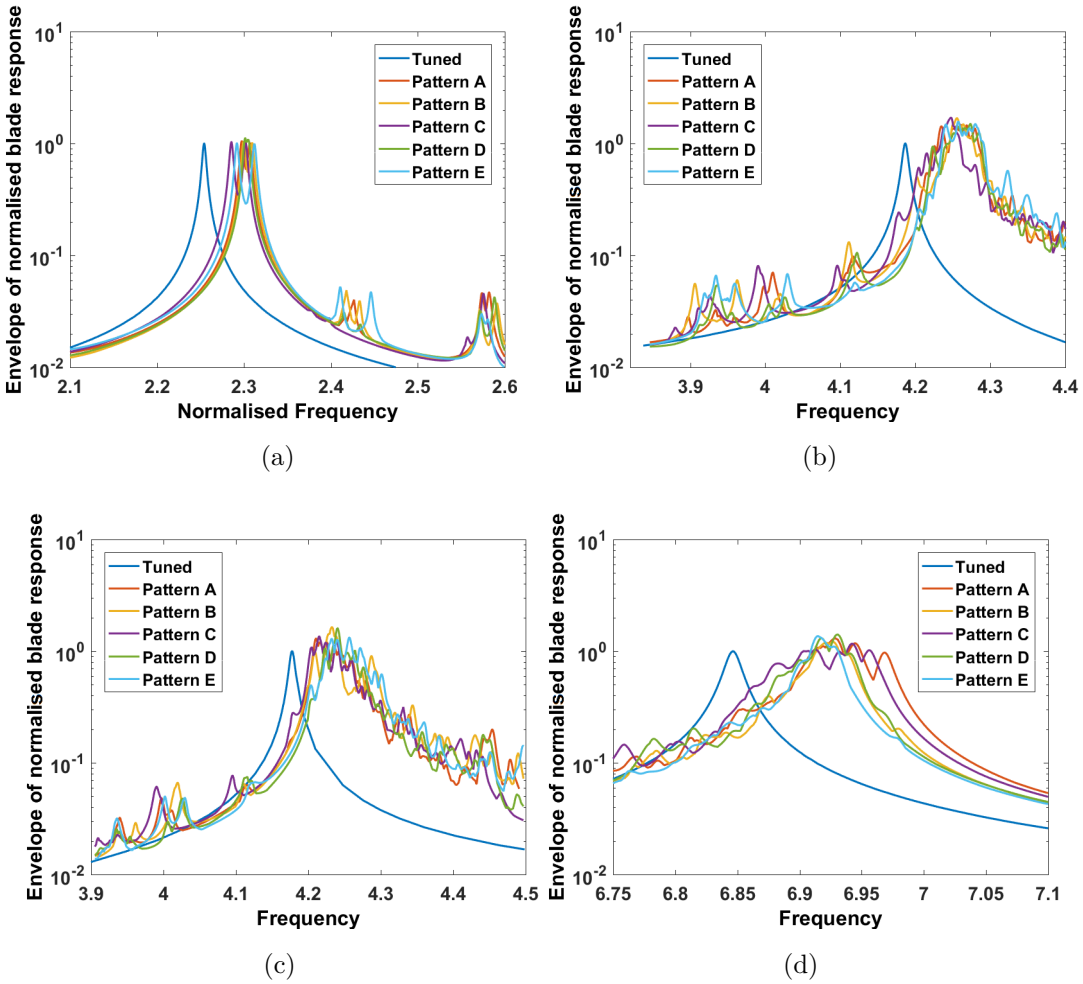

Figure 7.3: Envelope of forced response of bladed disk for 8EO excitation of frequencies in the range of (a) 1^{rst} mode family and (b) 2^{nd} mode family; 35EO excitation of frequencies in the range of (c) 1^{rst} mode family and (d) 2^{nd} mode family.

The effect of blade anisotropy mistuning on forced response due to excitation of blade dominated modes are more pronounced. For 8EO excitation of frequencies in the range of second mode family (marked as 'B' in Fig. 7.2), Fig. 7.3(b) shows the envelope of forced response for different mistuning patterns and for the tuned

case. The forced response for mistuned bladed disk has multiple resonances and the magnitude of maximum response is noticeably higher than that for the tuned case. The forced response of mistuned and tuned bladed disk for 35EO excitation of frequencies in the range of first (marked as 'C' in Fig. 7.2) and second mode family (marked as 'D' in Fig. 7.2) are shown in Fig. 7.3(c) and (d) respectively. Note that, for 35EO excitation, the forced response amplification due to mistuning is significantly higher for the excitation of frequencies in the range of first mode family compared to that for the second mode family.

In order to investigate the effects of scattering in anisotropy angles on the forced response of a mistuned bladed disk, several mistuning patterns are obtained using pseudo-random sampling approach from the known probability distributions for the three blade material anisotropy angles. For a mistuned bladed disk, three different schemes for the set of blades with random anisotropy angles are studied: (i) anisotropy angles of 30 blades, as shown in Fig. 7.4(a), are considered as a random variable, (ii) anisotropy angles of every other blade, as shown in Fig. 7.4(b), are considered as a random variable and (iii) anisotropy angles of all 75 blades, as shown in Fig.7.4(c), are considered as a random variable.

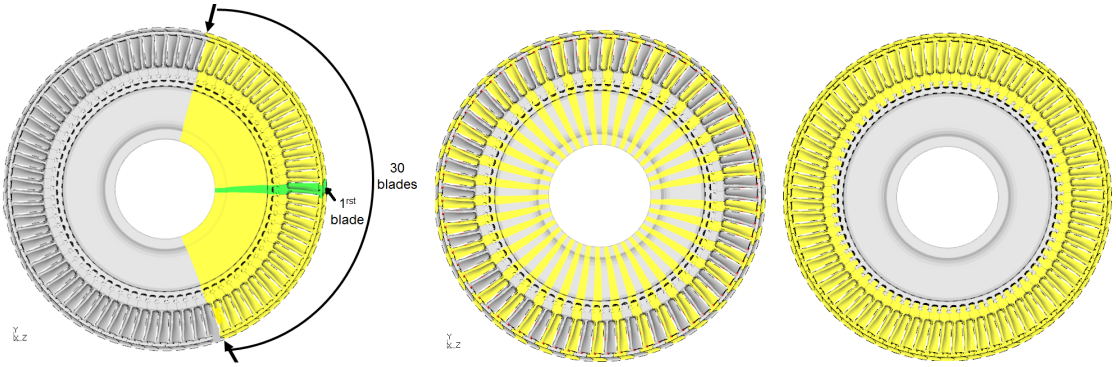

(a) (b) (c)

Figure 7.4: A mistuned bladed disk showing (a) 30 blades having random anisotropy angles, (b) 37 blades having random anisotropy angles, and (c) all 75 blades having random anisotropy angles.

For 140 different mistuning patterns obtained by random sampling of anisotropy angles of 30 blades in the bladed disk, the scatter in normalised maximum blade amplitude due to 8EO and 35EO excitation of frequencies in the range of first mode

family is plotted in Fig. 7.5(a) and (b) respectively. The values for maximum blade displacements are normalised using corresponding value for a tuned bladed disk with blade anisotropy axis aligned with the blade geometry axis. For frequencies in the range of first mode family, 8EO and 35EO excite a disk-dominant mode and a blade-dominant mode respectively (see Fig. 7.2). Therefore, the scattering in blade anisotropy angles can be expected to have a larger influence on forced response due to 35EO excitation compared to that due to 8EO. This is evident from the comparison of the range of scattering in maximum blade amplitudes shown in Fig. 7.5(a) and (b).

From a comparison of Fig. 7.5(a) and (b) for 8EO and 35EO excitation, it is evident that when a blade-dominant mode is excited, the variation in anisotropy angles of the selected 30 blades result in a different range of scattering in the maximum response of the blades in the considered frequency range. This suggests that the variation in anisotropy orientations of a blade significantly influence the forced response of blades located adjacent to that blade and marginally influence the response of blades located farther from that blade in the bladed disk. Similarly, the scatter in normalised maximum blade displacements due to 8EO and 35EO excitation of frequencies in the range of second mode family is shown in Figs. 7.5(c) and (d). For frequencies in the range of second mode, 8EO and 35EO excite blade dominated modes, and therefore, there is an appreciable difference in the range of scattering of maximum forced response of blades due to scatter in blade anisotropy angles. For the 30 blades, for which the anisotropy angles were obtained randomly, the scatter in maximum blade displacement in the considered frequency range is higher compared to that for the rest of the blades in the bladed disk.

For the three schemes used for obtaining different mistuning patterns, based on 140 different patterns analysed, mean and standard deviation of maximum blade response are calculated. Statistics of maximum blade response for frequencies in the range of first and second mode family due to 8EO and 35EO are shown in Fig. 7.6 and 7.7 respectively. Fig. 7.6(a), (b) and (c) show the mean and standard deviation of maximum forced response, in the considered frequency range of first and second mode family, for the three different choices of the set of blades with random anisotropy angles. Similarly, Fig. 7.6(a), (b) and (c) show the mean and

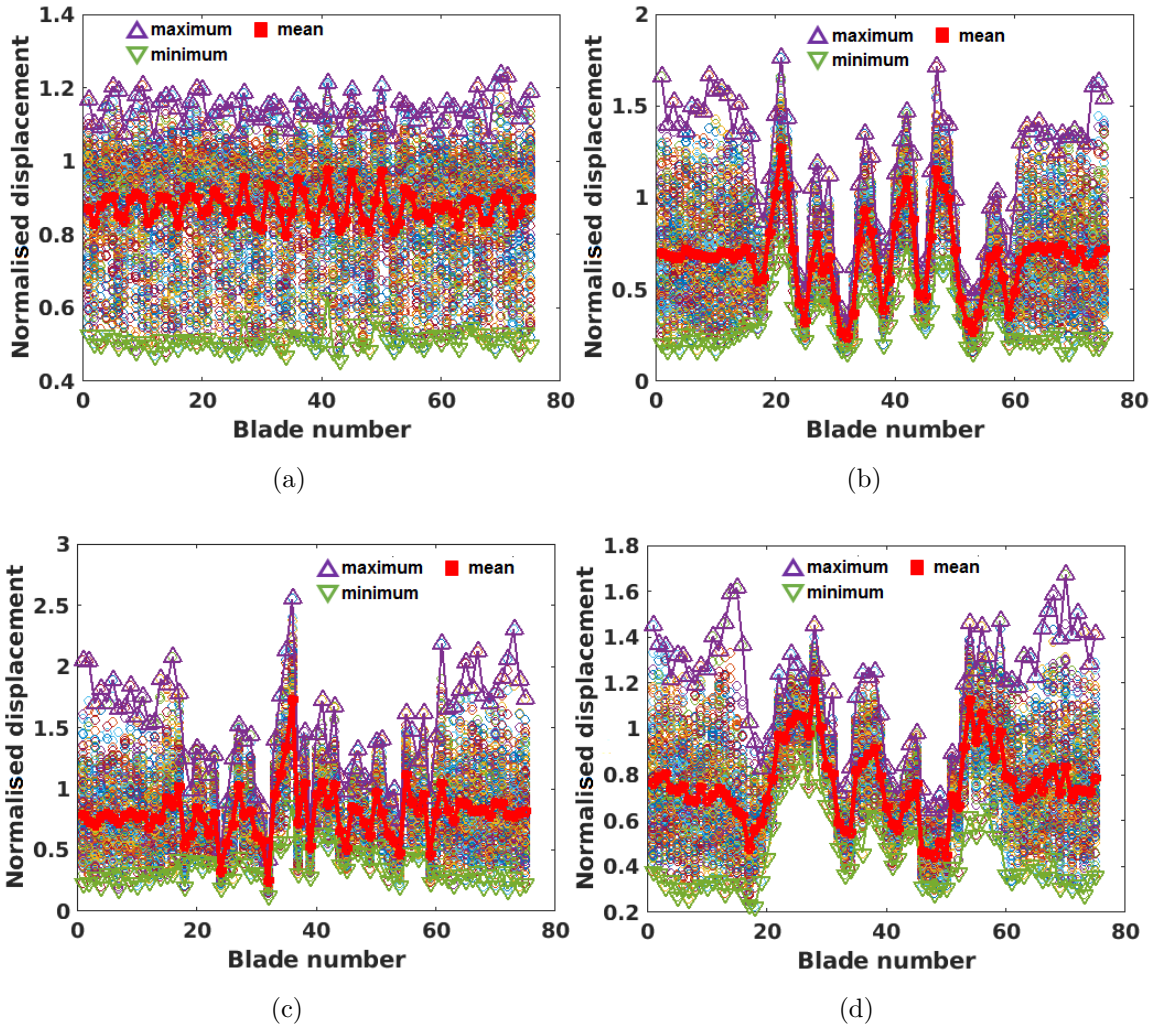

Figure 7.5: Scatter in maximum amplitude of blades in mistuned bladed disks for excitation frequencies in the range of 1^{rst} mode family due to (a) 8EO and (b) 35EO, 2^{nd} mode family due to (c) 8EO and (d) 35EO considering 30 blade anisotropy angles as random variables.

standard deviation of maximum forced response for frequencies in the range of first and second mode family for 35EO excitation.

As explained before, for frequencies in the range of first mode family, 8EO excites disk-dominant mode whereas for frequencies in the range of second mode family blade-dominant modes are excited. For 35EO, excitation of frequencies in the range of both first and second mode family results in the excitation of a blade-dominant mode. In Figs. 7.6(a), (b) and (c), by comparing the standard deviation of maximum blade response for blade dominated and disk dominated modes it is evident that

when blade dominated modes are excited the standard deviation of the maximum response of those blades, for which anisotropy angles are varied, is higher compared to that for disk dominated mode. This further confirms the observation, made from the envelope of blade response for different mistuning patterns, that the influence of variation in blade anisotropy angles on the forced response of disk-dominant modes is comparatively small.

As shown in Fig. 7.6(a) for most blades, among the 30 blades with random anisotropy angles, the standard deviation for maximum blade response in the considered frequency range is high compared to that of blades for which the anisotropy angles are fixed. Again, this suggests that the variation in anisotropy angle of a blade has a significant influence on the forced response of immediately adjacent blades and only marginal influence on the forced response of blades positioned farther in the bladed disk. Note from Figs. 7.7(c) that the standard deviation of maximum blade response to 35EO is high, for most of the blades, when frequencies in the range of first mode family are excited compared to that for those in the range of second mode family. This is in contrast to what was observed for the case of 8EO excitation.

For the case when anisotropy angles of all 75 blades are considered as random parameters, based on the analysis of 900 different anisotropy mistuning patterns, the histogram for normalised maximum forced response of bladed disk, known as amplification factor (AF), for forced response excitation frequencies in the range of first and second mode family due 8EO and 35EO excitation was obtained. The normalization is based on the maximum response of a tuned bladed disk, in the considered frequency range, when the blade anisotropy angles are aligned with the blade stacking axis. Fig. 7.8 shows the histogram for AF due to excitation of frequencies in the range of first and second mode respectively for 8EO and 35EO. Comparing Fig. 7.8(a) and (b), it is clear that for most of the mistuning patterns analysed the maximum response corresponding to 8EO excitation is only marginally higher than that of the tuned bladed disk when disk-dominant modes are excited. For frequencies in the range of the second mode, both 8EO and 35EO excites blade-dominant modes. For this case, the mean AF is considerably higher for 8EO excitation compared to that for 35EO excitation as seen in Fig. 7.8(c) and (d). This suggests that when a disk-dominant mode in a similar frequency range is excited, the effect of mistuning

is critical for lower engine order excitations compared to that for higher engine order excitations.

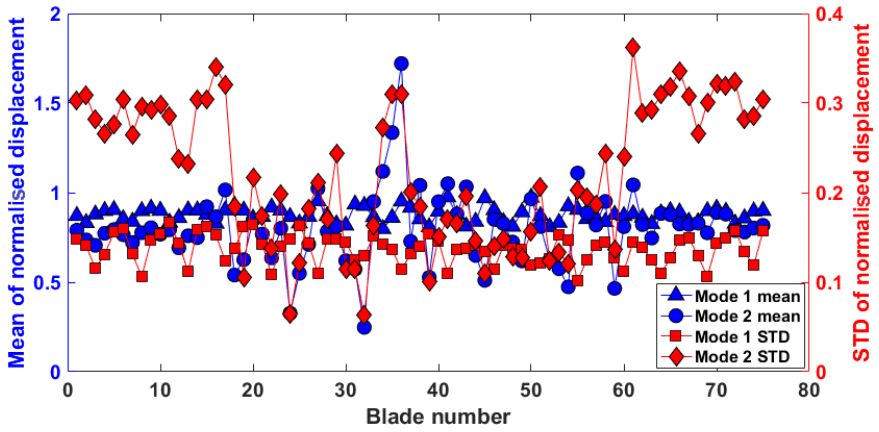

(a)

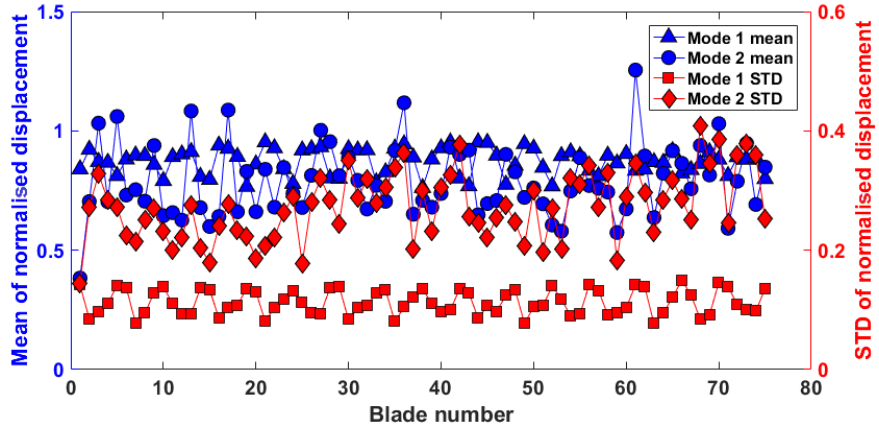

(b)

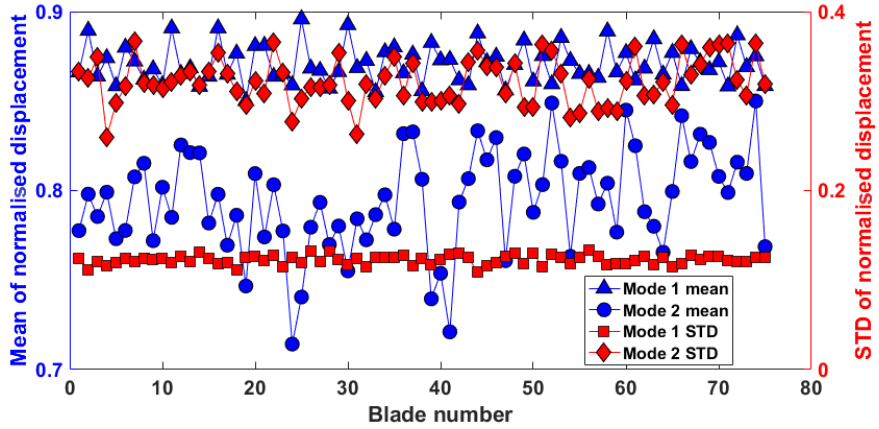

(c)

Figure 7.6: Mean and STD of normalised maximum amplitude of blade for 8EO excitation of (a) 30 blades, (b) 37 blades and (b) all 75 blades having random anisotropy angles.

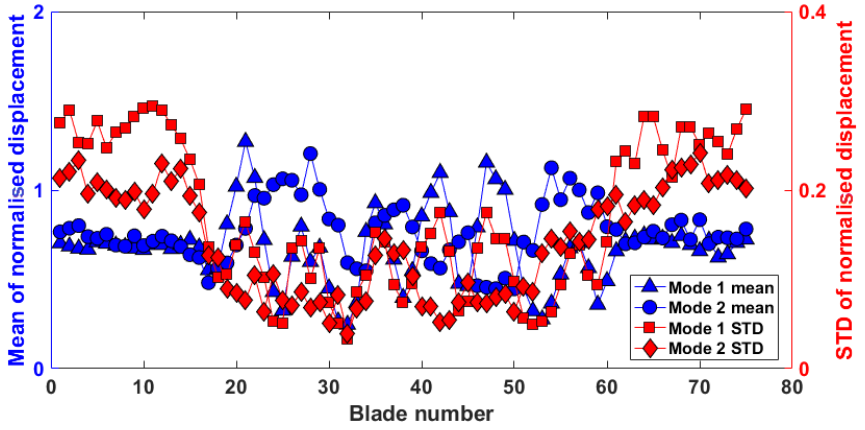

(a)

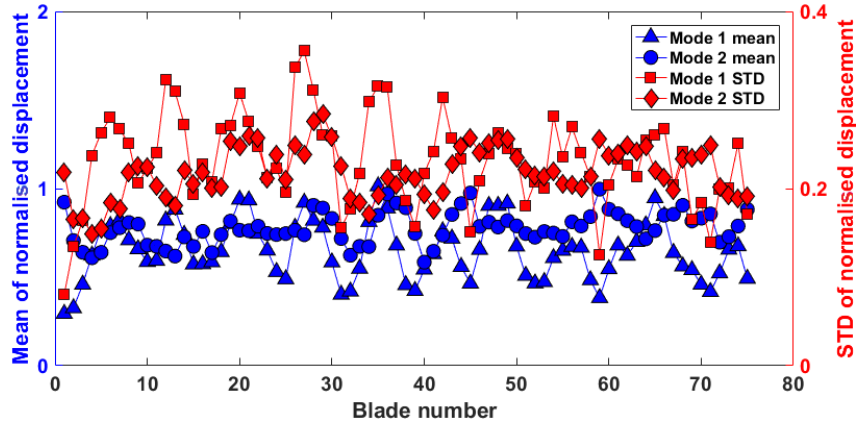

(b)

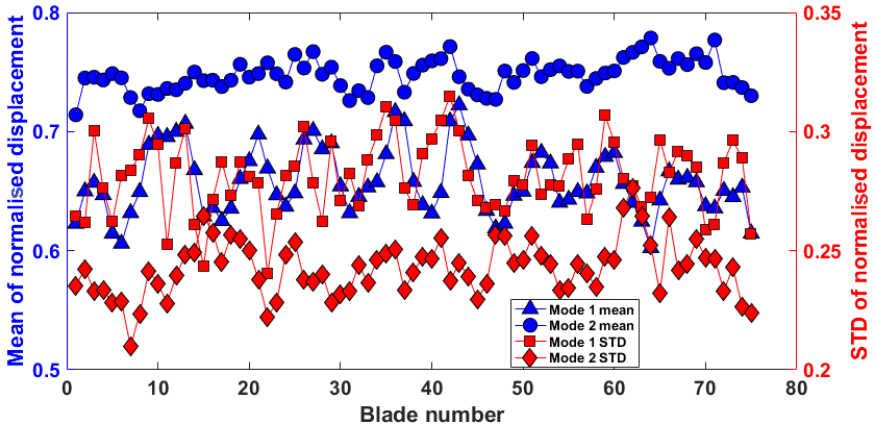

(c)

Figure 7.7: Mean and STD of normalised maximum amplitude of blade for 35EO excitation for the case (a) 30 blades (b) 37 blades chosen alternatively and (c) all 75 blades having random anisotropy angles.

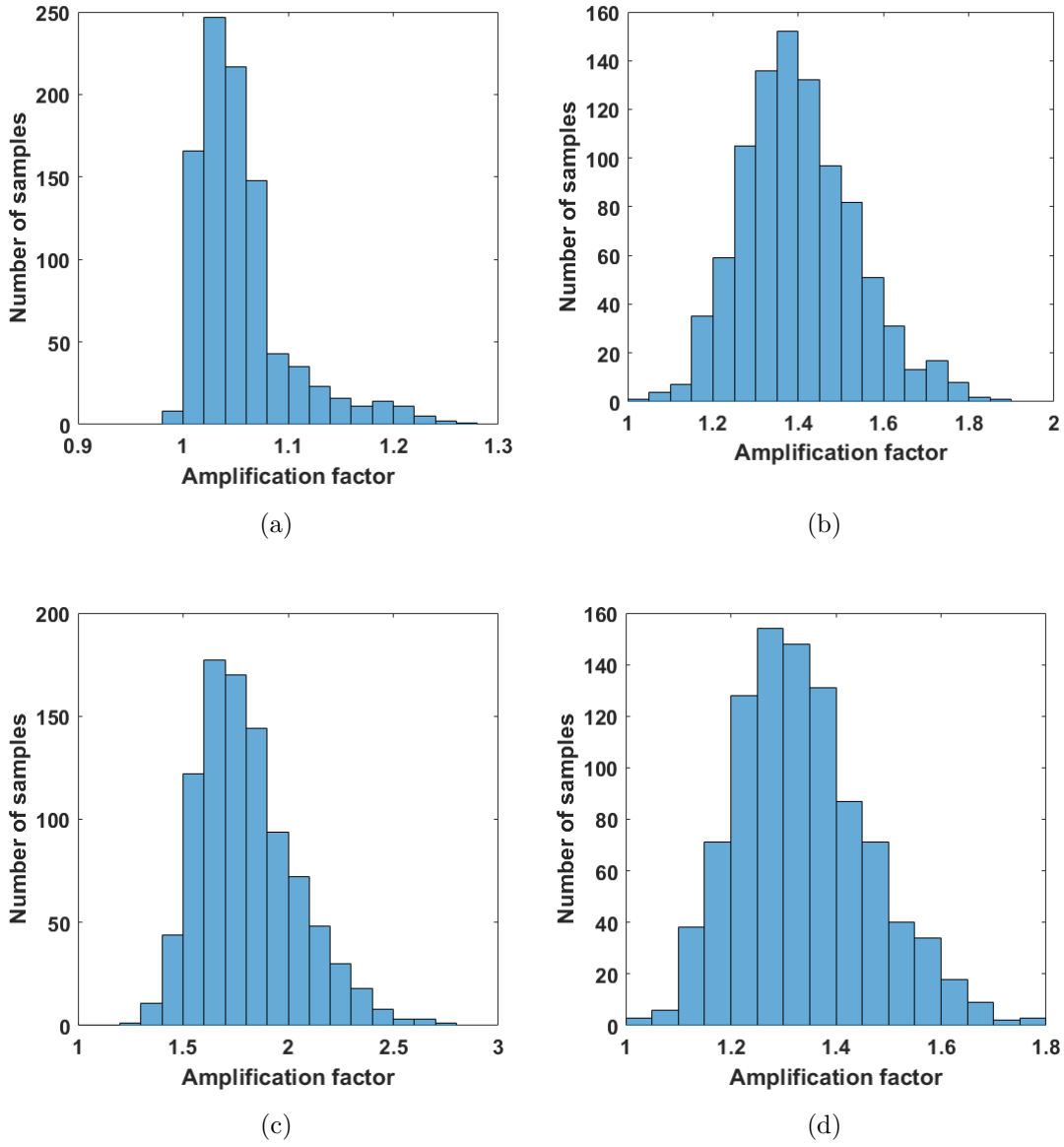

Figure 7.8: Histogram for normalised maximum amplitude of bladed disk for 1^{rst} mode family due to (a) 8EO and (b) 35EO excitation, 2^{nd} mode family due to (c) 8EO and (d) 35EO excitation.

7.2 Uncertainty analysis using polynomial chaos expansion

From the results presented in Section 7.1 for anisotropy mistuned bladed disk, it is evident that the forced response of a bladed disk varies due to inevitable scattering in blade anisotropy angles. Therefore, considering the safe operation of the gas turbine engine, it is essential to quantify the uncertainty in forced response of the mistuned bladed disk. In this section, a thorough investigation of the usefulness of polynomial chaos expansion (PCE) based surrogate model for uncertainty analysis is presented. In particular, the statistical characteristics for the maximum forced response amplitude of a mistuned bladed disk are obtained considering the anisotropy angles of all blades, or a set of blades, as random variables. The bladed disk model analysed for this study has linear bonded contacts at fir–tree root and shrouds.

For a bladed disk with 75 blades, the total number of anisotropy angles is 225. A PCE of order 2 with 225 random variables will have 25651 terms, and therefore,the same number of unknown coefficients. The computational cost associated with the calculation of unknown coefficients, using FE model evaluations, for such a surrogate model is prohibitive even if gradient values are used for the evaluation of those coefficients in addition to using function evaluations. In order to reduce the computational cost associated with constructing the surrogate model, we begin by considering a scheme of the mistuned bladed disk where the anisotropy angles of only 30 blades are considered as random variables (see Fig.7.4b). For the considered scheme of the mistuned bladed disk, the statistical characteristics are obtained using full and truncated polynomial chaos of order 2. While full PCE of order 2 contain basis terms of all anisotropy angles and their combinations of up to order to 2, the truncated PCE is obtained by excluding all basis terms in the expansion which are a combination of two anisotropy angles. Therefore in PCE of order 2, if α_i, β_i and ζ_i are anisotropy angles of the i^{th} blade, then truncated PCE is obtained by excluding basis terms of the form $\alpha_i\beta_j$, $\alpha_i\zeta_j$ and $\beta_i\zeta_j$ for both the cases of $i = j$ and $i \neq j$. For the present scheme of the mistuned bladed disk with anisotropy angles of 30 blade considered as random variables, the full PCE and truncated PCE has 4186 and 181

terms respectively.

In the mistuned bladed disk analysed, the crystal orientation of all the 75 blades is different from one another. In order to obtain different mistuning patterns, the blade anisotropy angles of the considered 30 blades were randomly sampled from the assumed probability distribution of these angles which is normal distribution for angle α and uniform distribution for the angles β and ζ. The convergence of standard deviation of normalised maximum forced response amplitude is compared to that obtained using Monte Carlo Simulation (MCS). The convergence of mean and standard deviation of normalised maximum forced response amplitude obtained from gradient-based PCE is investigated for different choice of weight coefficients used to set additional weight for value of gradient evaluations over function evaluations or vice-versa depending on the choice of the two weight coefficients w_1 and w_2 in Eqn. (2.45). The following two cases are considered: (i) when the weight coefficient w_1 and w_2 are of different value, and (ii) when the value of the two weight coefficient are chosen to be equal.

For 8EO excitation of frequencies in the range of first and second mode family, the convergence of standard deviation for normalised maximum forced response is shown in Fig. 7.9(a) and (b) respectively. As described in section 7.1, 8EO excitation of the first mode family results in excitation of a disk-dominant mode. The variation in maximum forced response amplitude is comparatively smaller when a disk-dominant mode is excited. This is evident from the comparison of the converged value of standard deviation for the maximum forced response due to 8EO excitation of first and second mode family, where the latter value is around four times higher than the former. As the EO increases, the disk becomes stiffer, and therefore the modes excited by higher engine orders are predominantly blade dominated. Therefore 35EO excitation of first mode family results in excitation of a blade-dominant mode. Fig. 7.9(c) shows the convergence of standard deviation for the maximum forced response for this case.

It is evident from Fig. 7.9(a), (b) and (c) that the convergence of standard deviation obtained from PCE can be hastened by using a carefully chosen value for weight coefficients. For the considered scheme of mistuning pattern with 90 anisotropy

angles considered as random variables, the choice of a weight coefficient value of 5 considerably improves the rate of convergence compared to the case when no weight coefficients are used, i.e. when $w_1 = w_2 = 1.0$. Similarly for the case when the value of the two weight coefficients are equal, thus leaving the system of linear algebraic equations unmodified. Fig. 7.10(a), (b) and (c) shows the convergence of standard deviation of maximum forced response for the three different forced response excitations cases studied. It is evident that the convergence of statistical characteristics are faster when truncated PCE is used compared to the full PCE. As the value of weight coefficient is increased, an optimum value of weight coefficient could be found for which the accuracy of standard deviation obtained from PCE is in good comparison to that obtained from Monte Carlo simulation. Any further increase in the value of weight coefficient will result in a deterioration of the accuracy of statistical characteristics. For example, for the present case of 90 random anisotropy angles, the two combinations of weight coefficient values that provide good convergence of standard deviation are $w_1 = 5.0$, $w_2 = 1.0$ and $w_1 = 5.0$, $w_2 = 5.0$.

For the case when different values are chosen for w_1 and w_2, the convergence of mean value of normalised maximum forced response of bladed disk for 8EO excitation of frequencies in the range first and second mode family, and 35EO excitation of those in the range of first mode family are shown in Fig. 7.11(a), (b) and (c) respectively. Note that the variation in mean value with increasing FE model evaluations is smaller compared to that for standard deviation. The accuracy of mean value obtained from PCE approximation is good for most cases of truncated, and full PCE studied for different values of weight coefficients studied. In general, this is true for the case when the value of the two weight coefficients are equal as is indicated by Fig. 7.12(a), (b) and (c) showing convergence of the mean value of maximum forced response for three cases of forced response excitation studied.

For a more realistic case, when the anisotropy angles of all blades in the bladed disk are considered as random variables, the number of terms in the full polynomial chaos approximation of order 2 is 25651. In order to reduce the computational cost associated with the evaluation of unknown coefficients in the expansion, truncated polynomial chaos of order 2 is used to obtain the statistical characteristics. The truncated polynomial chaos expansion, obtained by ignoring the interaction terms

between random variables, contain 451 terms. Based on a trial and error approach, a weight coefficient value of $w_1 = 10$ and $w_2 = 1$ was found to give a good convergence for statistical characteristics for this case. For 8EO and 35EO excitation of frequencies in the range of 1^{rst} and 2^{nd} mode family, a comparison of the mean and standard deviation of the normalised maximum response of the bladed disk obtained from PCE and MCS is provided in Table 7.1. The Monte Carlo estimates are obtained using 500 evaluations of the FE model for random mistuning patterns of the blade anisotropy angles. For the two different cases of EO excitation and frequency ranges analysed, the value of mean and standard deviation obtained using PCE is in good comparison with that obtained using the Monte Carlo method.

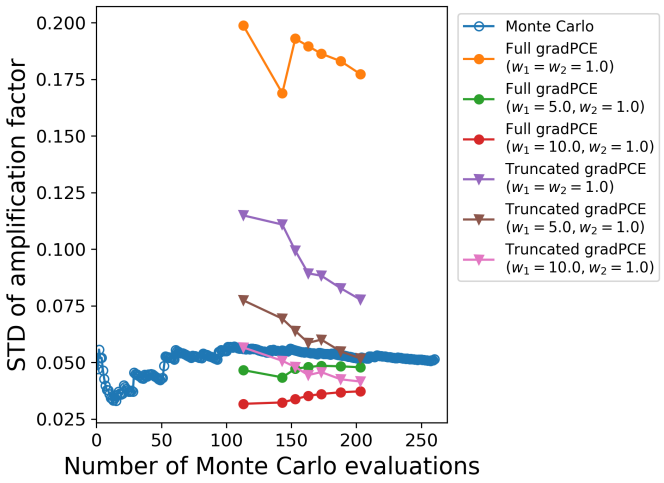

(a)

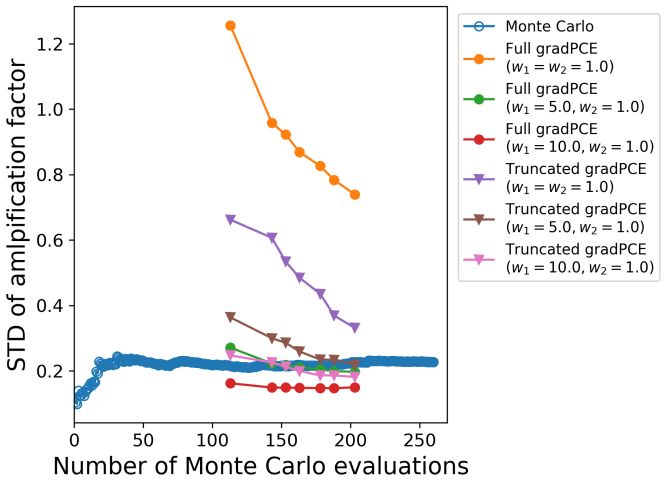

(b)

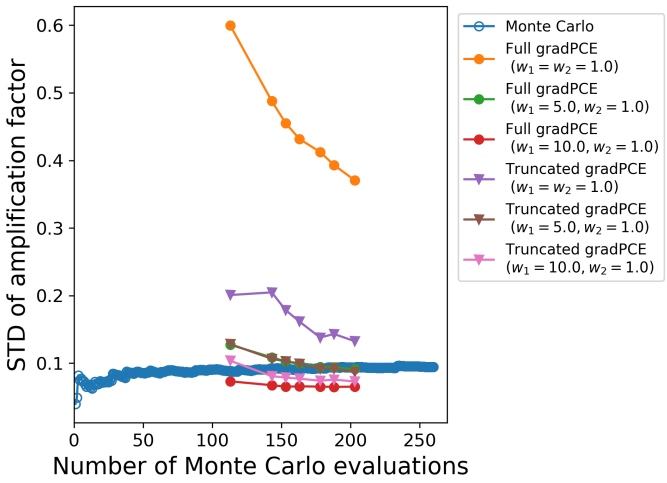

(c)

Figure 7.9: Convergence of STD of maximum forced response with number of FE model evaluations for 8EO excitation of frequencies in the range of (a) 1^{rst} mode family, (b) 2^{nd} mode family; and (c) 35EO excitation of 1^{rst} mode family for the case when weight coefficients w_1 and w_2 are different.

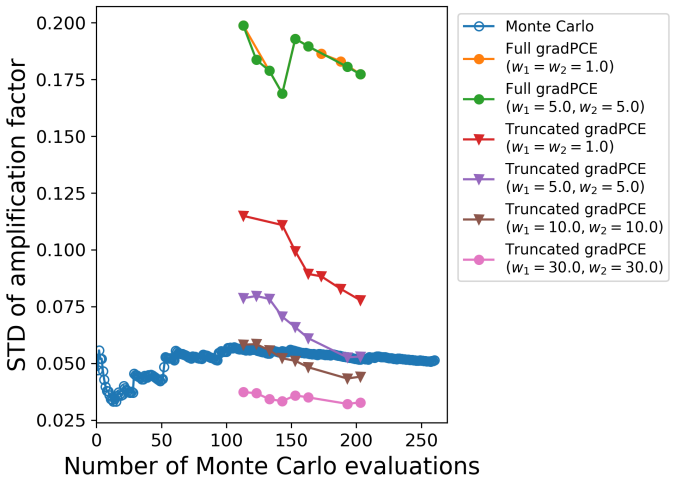

(a)

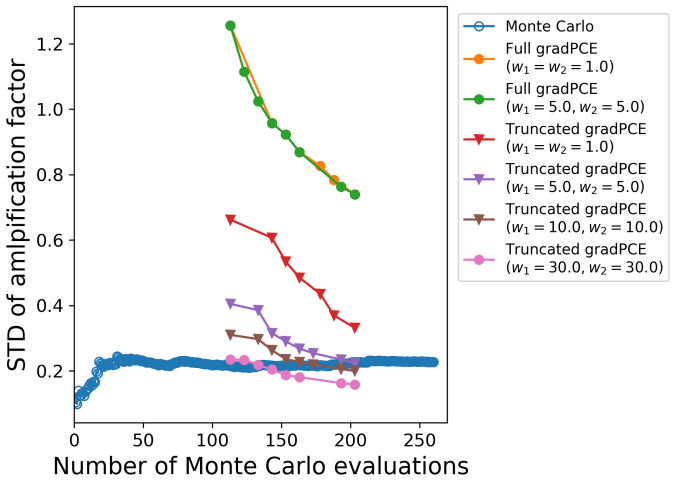

(b)

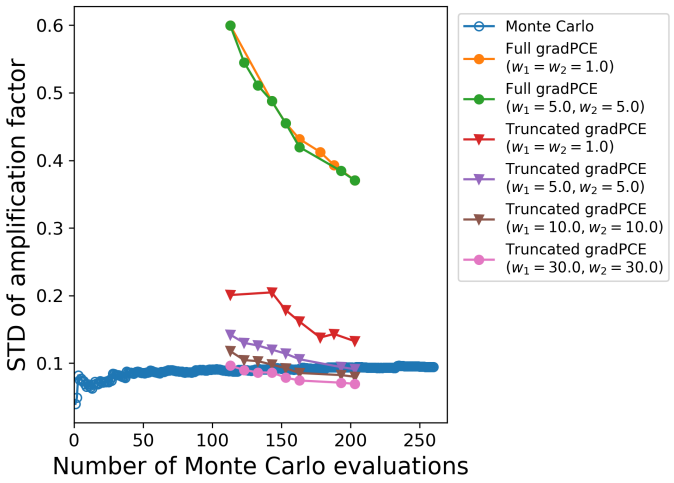

(c)

Figure 7.10: Convergence of STD of maximum forced response with number of FE model evaluations for 8EO excitation of frequencies in the range of (a) 1^{rst} mode family, (b) 2^{nd} mode family; and (c) 35EO excitation of 1^{rst} mode family for the case when weight coefficients w_1 and w_2 are equal.

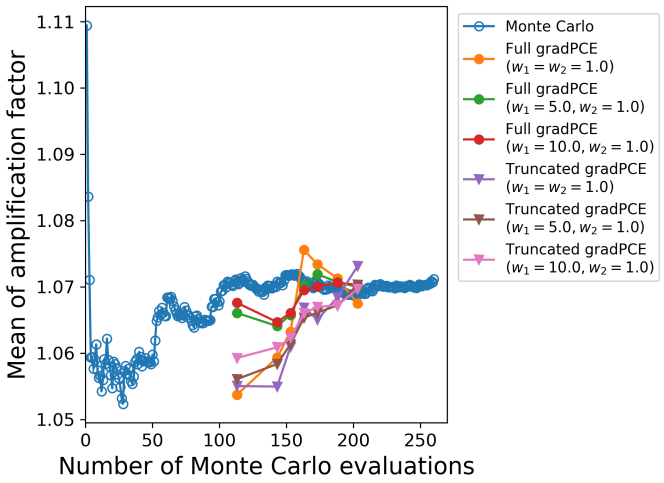

(a)

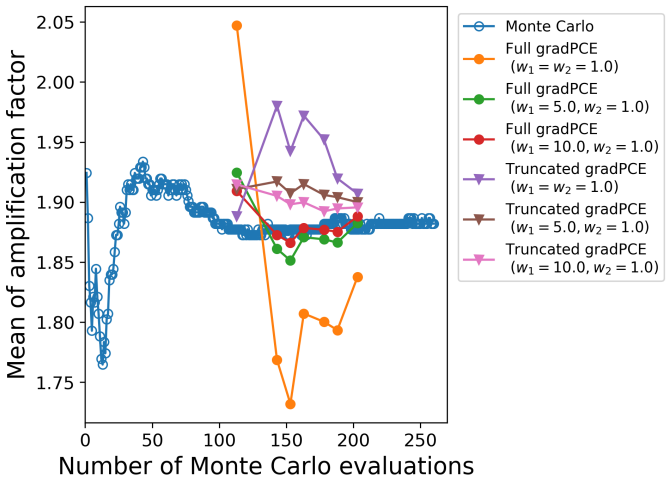

(b)

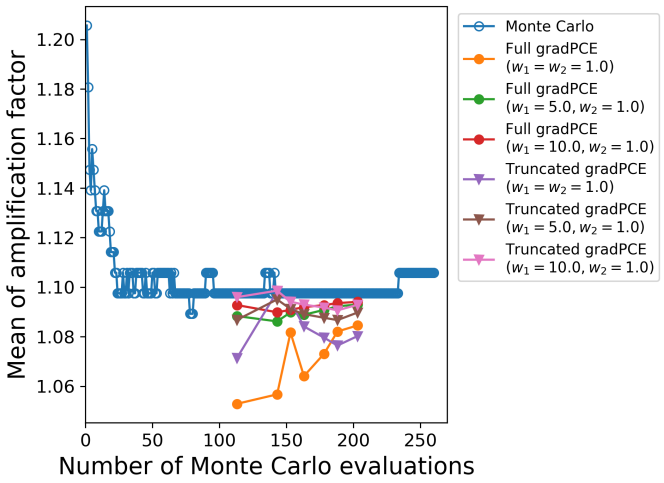

(c)

Figure 7.11: Convergence of mean of maximum forced response with number of FE model evaluations for 8EO excitation of frequencies in the range of (a) 1^{rst} mode family, (b) 2^{nd} mode family; and (c) 35EO excitation of 1^{rst} mode family for the case when weight coefficients w_1 and w_2 are different.

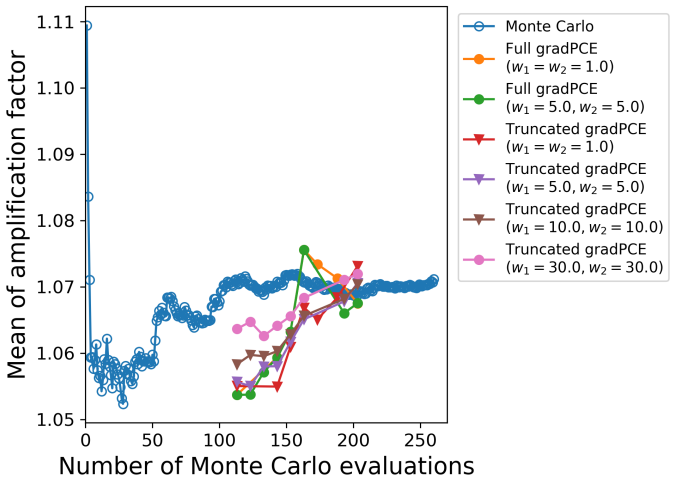

(a)

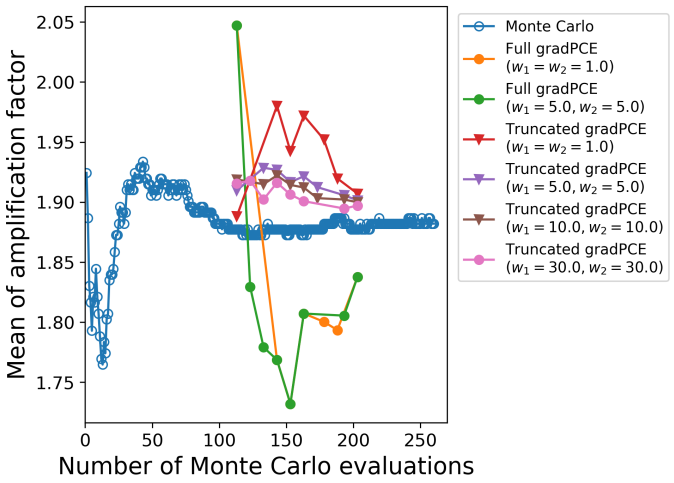

(b)

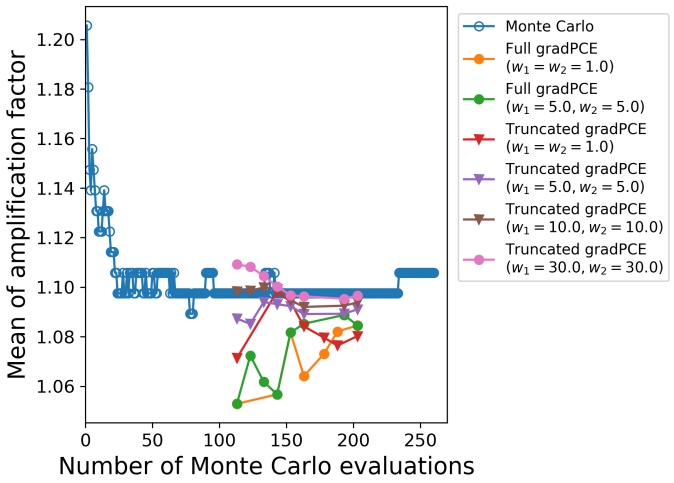

(c)

Figure 7.12: Convergence of mean of maximum forced response with number of FE model evaluations for 8EO excitation of frequencies in the range of (a) 1^{rst} mode family, (b) 2^{nd} mode family; and (c) 35EO excitation of 1^{rst} mode family for the case when weight coefficients w_1 and w_2 are equal.

Table 7.1: Statistics for amplification factor for response of a linear mistuned bladed disk.

Mode family	FE realisations	8EO				35 EO			
		Mean		Standard deviation		Mean		Standard deviation	
		gradPCE	MCS	gradPCE	MCS	gradPCE	MCS	gradPCE	MCS
1	119	1.0450	1.0483	0.0483	0.0428	1.3741	1.3665	0.1372	0.1242
	159	1.0421	1.0483	0.0459	0.0428	1.3528	1.3665	0.1352	0.1242
	199	1.0434	1.0483	0.0454	0.0428	1.3406	1.3665	0.1341	0.1242
2	119	1.7903	1.8186	0.2435	0.2312	1.3711	1.3435	0.1548	0.1339
	159	1.8104	1.8186	0.2407	0.2312	1.3713	1.3435	0.1596	0.1339
	199	1.7997	1.8186	0.2268	0.2312	1.3529	1.3435	0.1595	0.1339

7.3 Sensitivity of forced response to anisotropy angles

From a manufacturing point of view, it is essential to know the rank order of importance of anisotropy angles in terms of its contribution to uncertainty in forced response of the bladed disk. This knowledge can be used to relax the manufacturing tolerance values for those anisotropy angles that are less influential and to prescribe tighter tolerance for anisotropic angles that contribute significantly to uncertainty in forced response. In order to quantify the effects of variation in individual blade anisotropy angles on the maximum forced response amplitude of mistuned bladed disk with linear bonded contacts at fir–tree root and shrouds, sensitivity analysis is performed. In addition to first order derivative based sensitivity, Sobol indices for anisotropy angles relating to the maximum forced response of bladed disk are also presented in this section.

In order to investigate the effects of scattering of the three different anisotropy angles on uncertainty in the forced response, several mistuning patterns were generated by obtaining the values of anisotropic angles of each blade in the bladed disk based on the three schemes listed below.

- Scheme–1 :- $\alpha \sim Normal(\mu_0, \sigma_0)$; $\beta = \beta_0$; $\zeta = \zeta_0$
- Scheme–2 :- $\alpha = \alpha_0$; $\beta \sim Uniform(a, b)$; $\zeta = \zeta_0$
- Scheme–3 :- $\alpha = \alpha_0$; $\beta = \beta_0$; $\zeta \sim Uniform(c, d)$

where, α_0, β_0, and ζ_0 are the mean values of the three anisotropy angles. While the first scheme considers variation in anisotropy angle α while keeping β and ζ as a constant, the second and third schemes are based on varying anisotropy angles β and ζ respectively. From 150 different mistuning patterns obtained for each of the above schemes, the standard deviation of maximum forced response amplitude of bladed disk was calculated using Monte Carlo method. Fig. 7.13(a) and (b) shows the convergence in normalised standard deviation of maximum forced response due to eight engine order (8EO) excitation of frequencies in the range of first and second mode family. The values of standard deviation for the maximum forced response of

the mistuned system due to a particular engine order excitation in the considered frequency range is normalised with respect to the corresponding value of maximum forced response for a tuned system. The 8EO excitation of frequencies in the range of first mode family results in excitation of disk-dominant modes. For the excitation of disk-dominant modes, the value of standard deviation is smaller for all the three schemes analysed when compared to the corresponding values for blade-dominant modes, i.e. when frequencies in the range of second mode family are excited by 8EO. For the excitation of the disk-dominant mode, contribution of anisotropy angle ζ to uncertainty in maximum forced response is higher compared to that of α and ζ as indicated by the higher value of standard deviation for Scheme–3. Fig. 7.13(c) shows the convergence in the standard deviation of maximum forced response due to 35EO of first mode family which is a case of blade-dominant mode. For the maximum forced response of the two cases of blade-dominant modes analysed (Fig. 7.13(b) and (c)) the value of standard deviation are only marginally different between the three different schemes. Therefore the relative importance of the three anisotropy angles in terms of their contribution to uncertainty in forced response is not conclusive from this analysis.

For an example case of blade anisotropy mistuning pattern, Fig. 7.14(a) shows the normalised value of local sensitivity of maximum forced response to 35EO excitation of frequencies in the range of first mode family. The 35EO excitation was chosen because, while considering the first mode family, higher engine order excitations result in excitation of blade-dominant modes for which the effect of blade anisotropy mistuning is significant compared to that for disk-dominant modes. For the considered case, blade number 53 has the maximum forced response in the considered frequency range. From the figure, it is evident that the sensitivity of anisotropy angles for many blades close to blade number 53 is significant, in particular, the primary anisotropy angle α of those blades. The local sensitivity of forced response to blade anisotropy angles considering 35EO excitation of frequencies in the range of second mode family is shown in Fig.7.14(b). Similar to that observed for the case of excitation of frequencies in the range of first mode family, anisotropy angles of many blades located close to the blade experiencing maximum response, blade number six, has high sensitivity values. From local sensitivity analysis, it could be

inferred that the anisotropy angle α is significantly more influential on the maximum forced response of bladed disk compared to angle β, and ζ.

The rank order of importance of anisotropy angles obtained from local sensitivity analysis is not conclusive because it is based on gradient values evaluated at a particular sample point in the domain of variation of the anisotropy angles. Therefore, global sensitivity analysis for forced response based on Sobol indices is performed. The Sobol indices are obtained analytically from PCE coefficients which are calculated based on hundreds of evaluations of the FE model for different mistuning patterns of blade anisotropy angles. In Fig. 7.15(a), Sobol indices of blade anisotropy angles for maximum forced response corresponding to 35EO excitation of frequencies in the range of first mode family is shown. Sobol indices for anisotropy angles show that the contribution of anisotropy angle ζ to uncertainty in maximum forced response is significantly higher compared to that of anisotropy angles β and ζ. Note that the domain of variation of anisotropy angle ζ is largest, followed by β, and α. Therefore, even though the gradient of the maximum forced response with respect to α is higher than that for β and ζ, as indicated by local sensitivity values, since Sobol indices account for variation of the anisotropy angles over its entire domain of variation, the rank order of importance is different from that obtained using local sensitivity analysis. Fig. 7.15(b) shows Sobol indices for anisotropy angles for maximum forced response corresponding to 35EO excitation of frequencies in the range of second mode family. Similar to that for the forced response excitation of frequencies in the range of first mode family, the rank order of anisotropy angles in terms of contribution to uncertainty in forced response is ζ, followed by β, and α.

The rank order of importance of the anisotropy angles is also dependent on the parameters defining the probability distribution of those angles. To illustrate this point, Sobol indices were calculated by samples of anisotropy angles from a modified probability distribution of anisotropy angle α. The mean and standard deviation of the original normal distribution was reduced by a factor of 2 and 3.5 respectively. For the modified distribution of angle α, the Sobol indices of anisotropy angles for the maximum forced response corresponding to 35EO excitation of frequencies in the range of first and second mode family are shown in Fig.7.16(a) and (b) respectively. For the considered cases, the Sobol indices of anisotropy angle α indicate that the

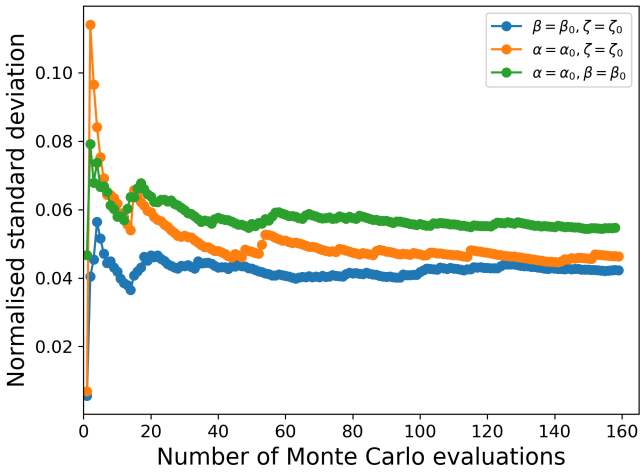

(a)

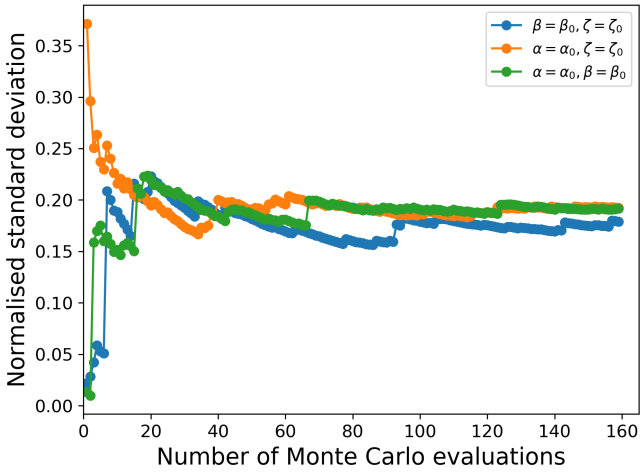

(b)

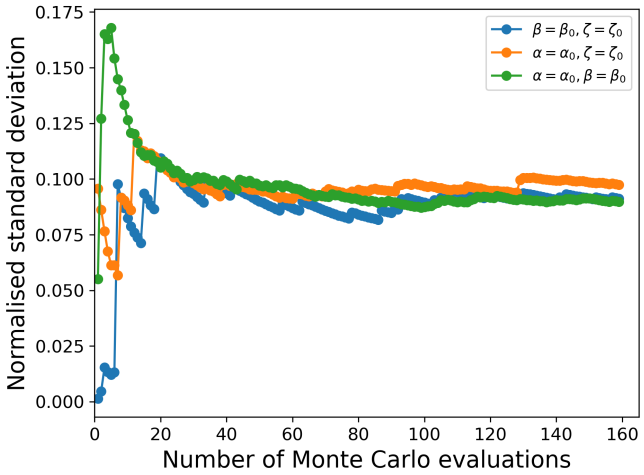

(c)

Figure 7.13: Convergence of STD of maximum forced response for 8EO excitation of frequencies in the range of (a) 1^{rst}, (b) 2^{nd} mode family, and (c) 35EO excitation of frequencies in the range of 1^{rst} mode family.

contribution of that angle to uncertainty in maximum forced response is higher compared to that due to angles β and ζ. This is in contrast to what was observed while considering the original normal distribution of angle α. This contradiction could be explained by considering the physical definition of the three anisotropy angles. The contribution of anisotropy angle ζ, defining the rotation of the crystal axis about the blade geometry axis, to uncertainty in forced response amplification is smaller when the crystal axis is aligned closer to the blade geometry axis, indicated

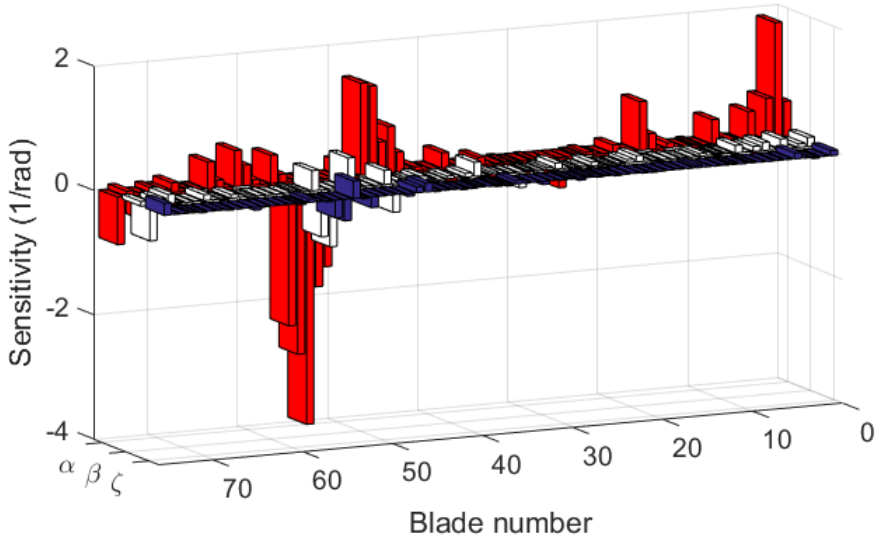

(a)

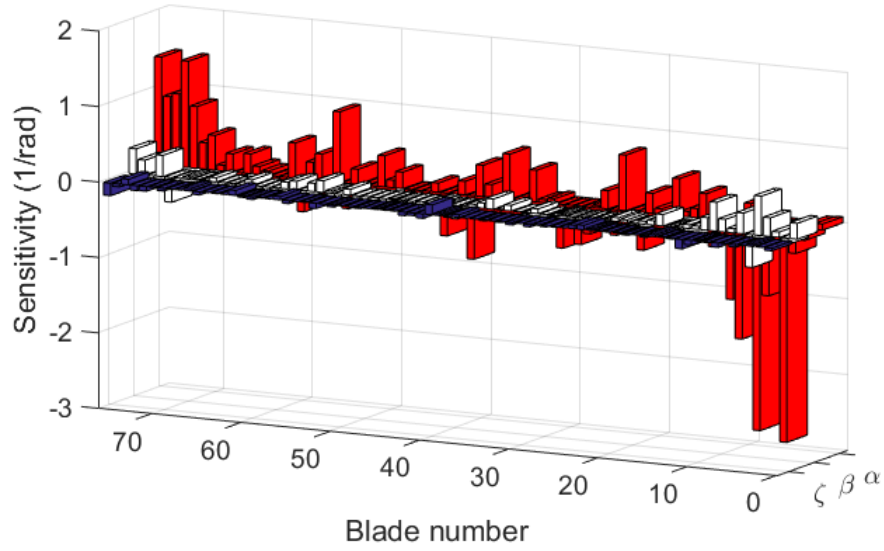

(b)

Figure 7.14: (a) Normalised local sensitivity of maximum forced response amplitude of the bladed disk corresponding to 35EO excitation of frequencies in the range of (a) 1^{rst} mode family and (b) 2^{nd} mode family.

by small values of angle α, compared to the case when it is aligned away from the geometry axis as is the case for large values of angle α.

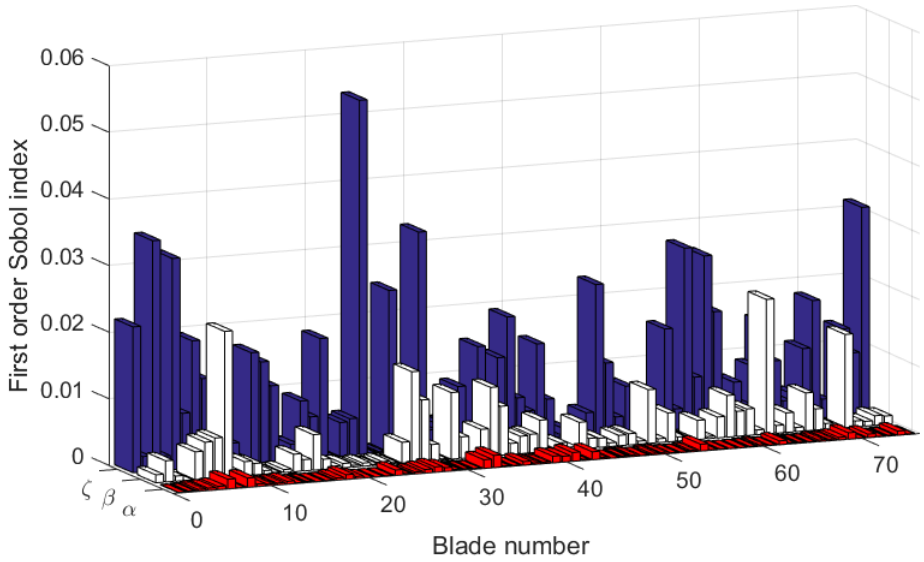

(a)

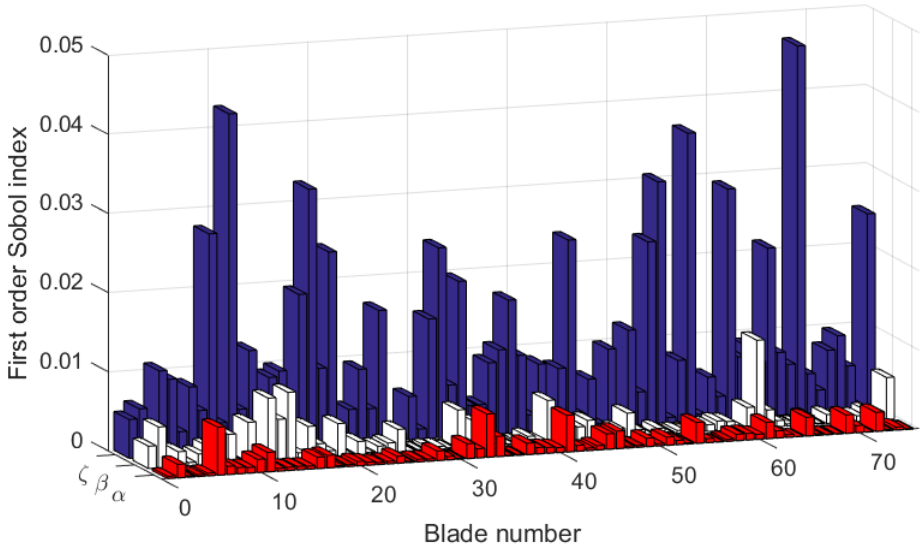

(b)

Figure 7.15: Sobol indices for maximum forced response amplitude of bladed disk corresponding to 35EO excitation of frequencies in the range of (a) 1^{rst} mode family and (b) 2^{nd} mode family.

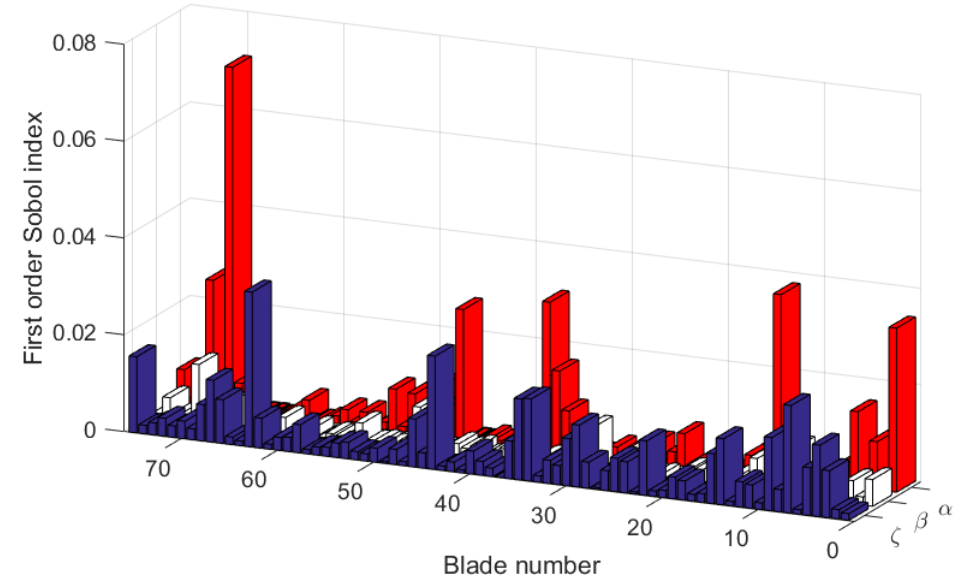

(a)

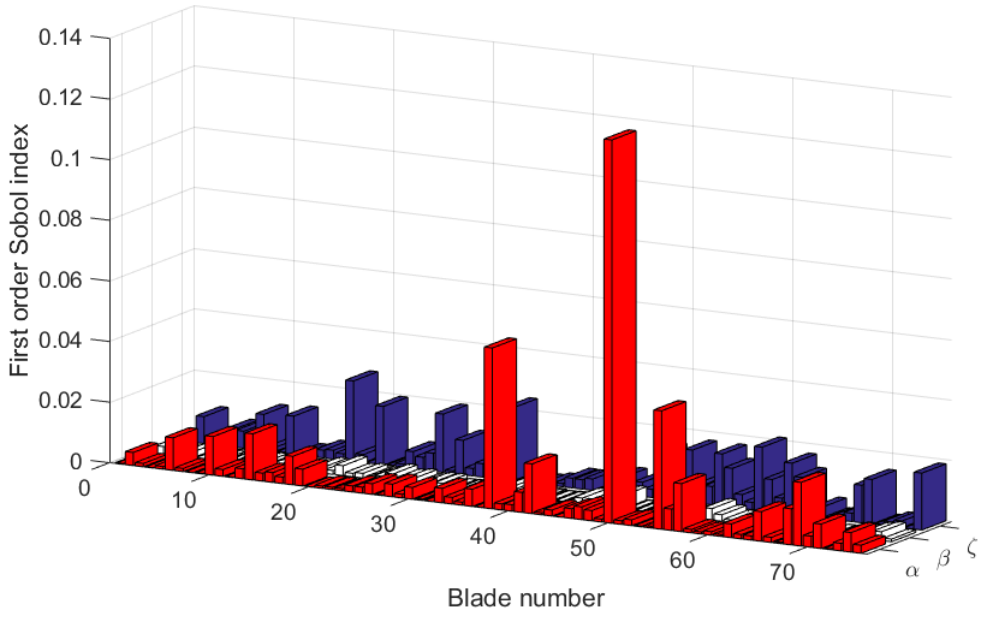

(b)

Figure 7.16: Sobol indices for normalised maximum amplitude of bladed disk corresponding to 35EO excitation of frequencies in the range of (a) 1^{rst} mode and (b) 2^{nd} mode family.

7.4 Optimisation of blade anisotropy angles

For blade anisotropy mistuned bladed disk, to minimise the force response amplification due to random mistuning of the bladed disk, the possibility of using intentional mistuning is investigated. The problem of intentional mistuning of bladed disk is formulated as an optimisation problem where the optimum value of the anisotropy angles that minimise the forced response amplification is sought. The FE model of the bladed disk with linear bonded contacts at fir–tree root and shrouds is used to obtain an optimum value of the anisotropy angles of blades such that the maximum forced response amplification of the bladed disk is minimised.

The performance of two different optimisation algorithms, namely NELDER-MEAD simplex and Constrained Optimisation By Linear Approximation (COBYLA) is compared. For the present study, the chosen objective function for the optimisation problem is the amplification factor (AF) for frequencies in the range of second mode family due to 8EO excitation which is a blade-dominant mode, and therefore, significantly influenced by the variation in blade anisotropy angles. From analysis of the effects of crystal orientation on forced response of mistuned bladed disks presented in the Section 7.1.2, it is evident that for excitation of blade-dominant modes in the similar frequency range, lower engine order excitation results in significantly high amplification of the forced response of bladed disk compared to that for higher engine order excitations. Therefore, the forced response corresponding to 8EO excitation was chosen as objective function for the optimisation of anisotropy angles.

From the manufacturing point of view, it is desirable to optimize the anisotropy angles of only a few blades even though this makes the choice of the set of blades to be optimized critical in achieving a significant reduction in amplification of the forced response. For an example case of mistuning pattern, the anisotropy angles of five blades are chosen as design parameters for optimisation. The choice of the position of the five blades in the bladed disk is based on a trial and error approach. The idea is to select at least one blade close to the location of the maximum response of the bladed disk. As the results presented from local sensitivity analysis in Section 7.3 indicate, the anisotropy angles of the blade experiencing maximum forced response

amplification and that of the adjacent blades has most significant influence on the maximum forced response of the mistuned bladed disk. Figure 7.17(a) and (b) shows the reduction in amplification of blade response, in the considered frequency range, obtained using two different optimisation algorithms, namely Nelder-Mead simplex and COBYLA. The chosen blades for which anisotropy angles are optimised are, for this case, blade number 1, 15, 30, 45, and 60. For the case of mistuning pattern analysed, it is evident that the optimisation using COBYLA is faster, in terms of optimisation step, even though the optimised AF achieved using this method is slightly higher than that obtained using NELDER-MEAD simplex method.

For two different initial blade anisotropy mistuning patterns, the variation in amplification factor (AF) and the location of maximum response of the bladed disk against the optimisation step are shown in Fig. 7.18(a). For mistuning pattern A, the maximum response in the considered frequency range occurs at blade number 46. For this case, the five blades whose anisotropy angles are chosen to be optimized are blade number 1, 15, 30, 45 and 60. Similarly for pattern B, considering that maximum response occurs at blade number 62, the five blades chosen are blade number 6, 21, 36, 51 and 63. The percentage reduction in AF obtained is 21% and 7% for mistuning pattern A and B respectively. Note that for pattern A, the blade experiencing the maximum response is the same for the first 26 optimisation steps when a significant reduction in AF is achieved. For mistuning pattern A, the variation in blade anisotropy angle α and β, of each of the five blades is shown in Fig. 7.19(a) and (b) respectively. The variation in the third blade anisotropy angle ζ is small compared to that of the two angles shown here. For three different random mistuning patterns, Fig. 7.18(b) shows reduction AF when anisotropy angles of every other blade from blade number 1 to 75 are optimized. For the three mistuning patterns studied, reduction in AF of 16.8%, 13.9% and 14.2 % were obtained. The number of optimisation steps required has increased significantly as the dimension of the parameter space has increased from 15 for five blades to 114 when anisotropy angles of every other blade are optimized.

From a practical design perspective, the possibility of reducing the maximum forced response by optimising the anisotropy angles of a single blade in the bladed disk is the most interesting. Fig. 7.20 shows the reduction in AF with subsequent opti-

misation steps when anisotropy angles of blade number 46, which also experience the maximum forced response amplification for the initial mistuning pattern, is optimised using NELDER-MEAD algorithm. For the mistuning pattern analysed the

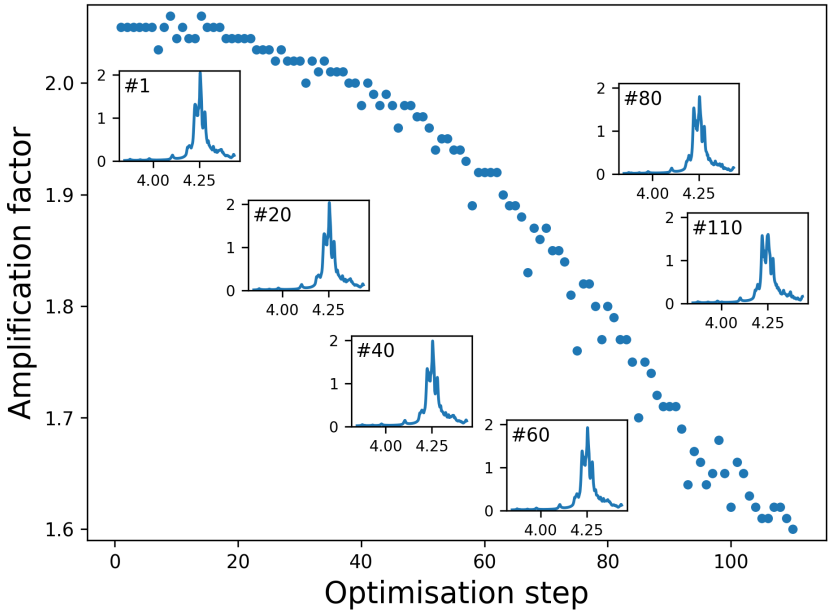

(a)

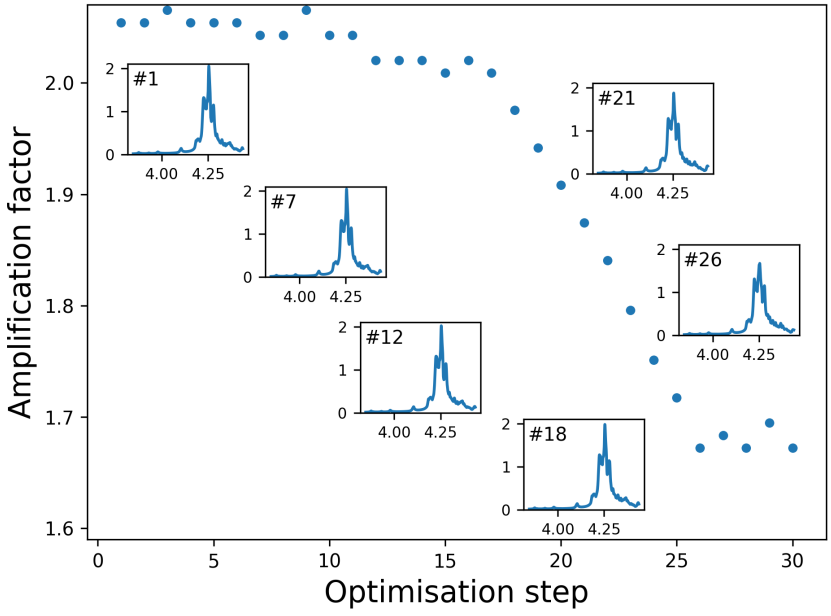

(b)

Figure 7.17: Variation in maximum forced response amplitude of bladed disk with optimisation of blade anisotropy angles of the chosen 5 blades using (a) NELDER-MEAD and (b) COBYLA.

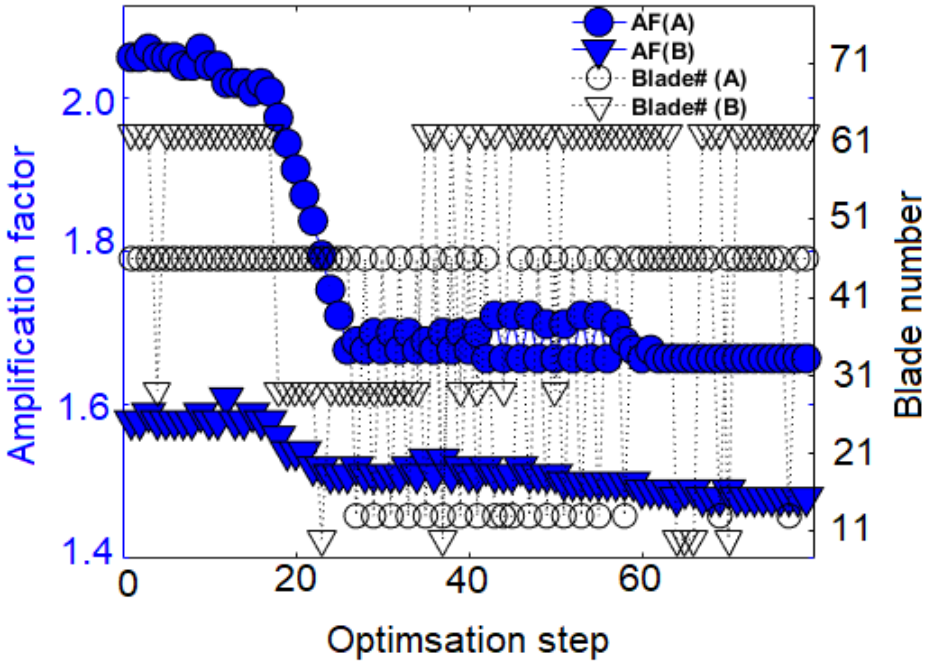

(a)

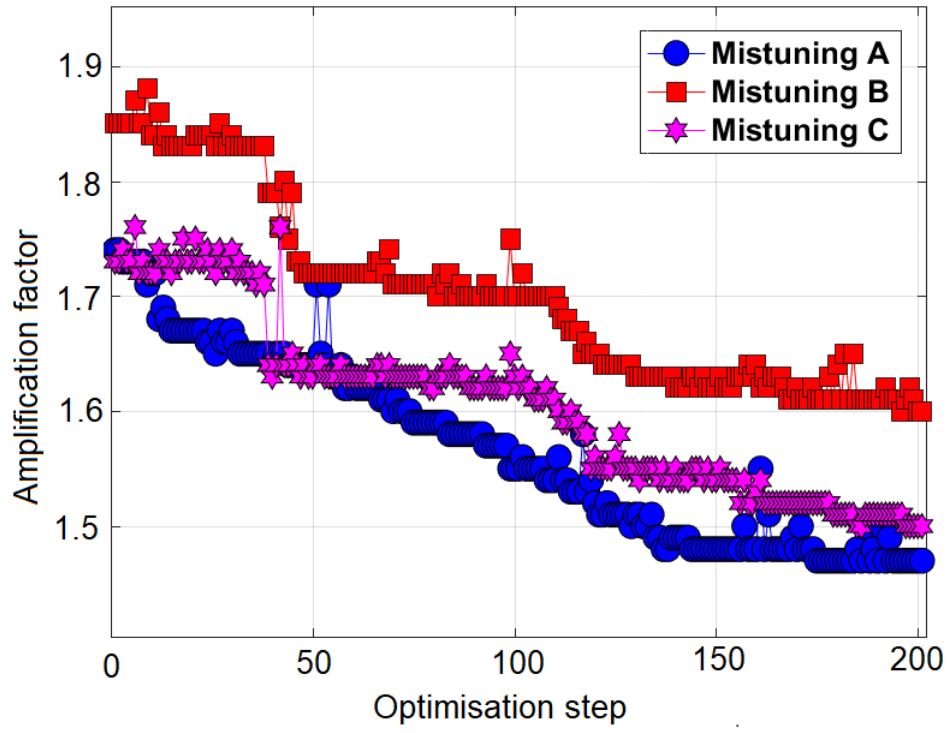

(b)

Figure 7.18: Variation in normalised maximum forced response amplitude of bladed disk with respect to optimisation of the blade anisotropy angles of the chosen (a) 5 blades and (b) 38 blades in the bladed disk.

location of the blade with maximum amplitude does not changed until optimisation step thirteen. This is clear from Fig. 7.21(a)–(d) which shows the forced response amplitude of all blades in the bladed disk in the considered frequency range. In the figure, the forced response of the blade experiencing maximum forced response amplification is represented using a thicker line. For the considered initial mistuning pattern, the reduction in the forced response amplification due to mistuning

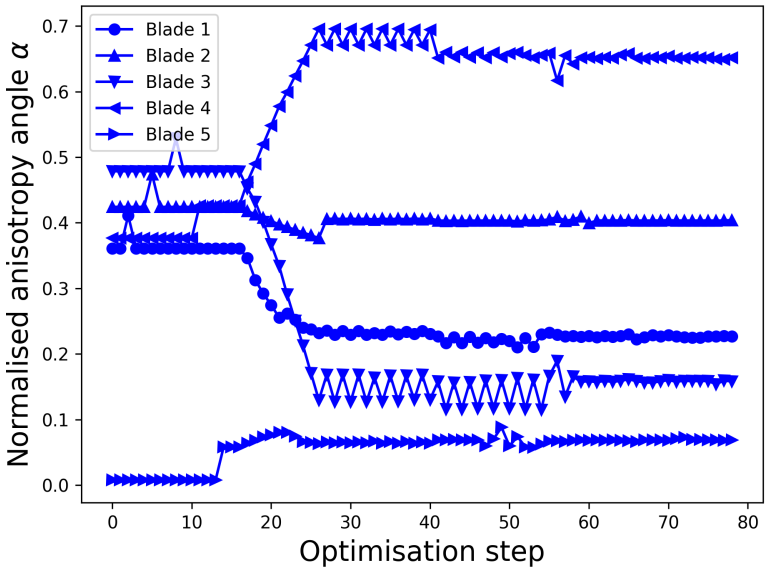

(a)

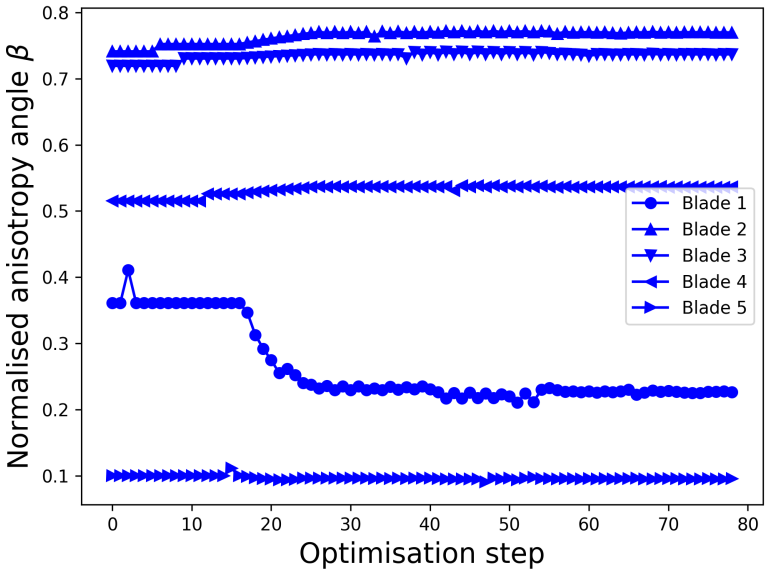

(b)

Figure 7.19: Variation in normalised anisotropy angles (a) α, and (b) β of the chosen five blades with respect to optimisation step.

achieved by optimising the three anisotropy angles of a single blade is 38%.

The analysis presented in this section demonstrates the potential to reduce the forced response amplification of mistuned bladed disk by optimising the blade anisotropy angles of a few selected blades in the bladed disk. It is important to realise that the optimum anisotropy angles obtained for forced response excitation of frequencies in the range of a specific mode family, due to a particular engine order excitation, does not guarantee an optimum forced response response for excitation of frequencies in the range of other mode families or even for that of the same mode family but for a different engine order excitation. While this does not limit the the potential gain of optimising the blade anisotropy angles for forced response excitation for a chosen frequency range and engine order, it requires a knowledge of the most critical modes of the structure to make a good choice of the frequency range and engine order.

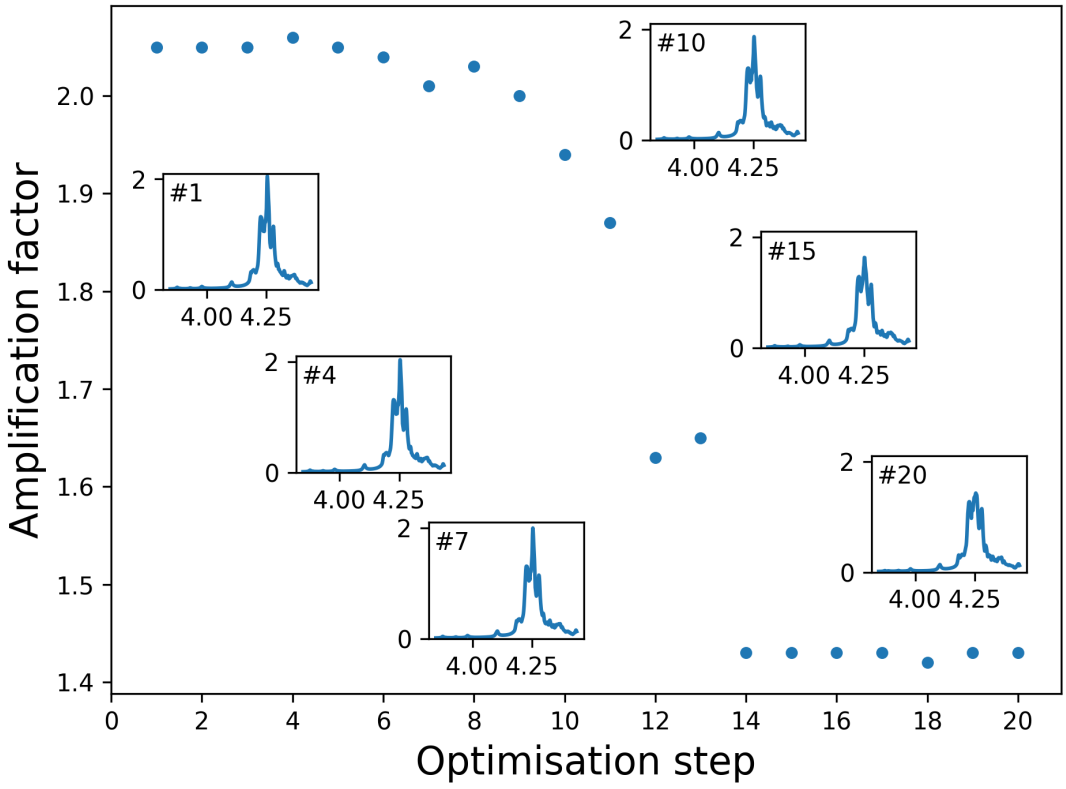

Figure 7.20: Variation in normalised maximum forced response amplitude of bladed disk with respect to the optimisation of blade anisotropy angles of the chosen one blade in the bladed disk.

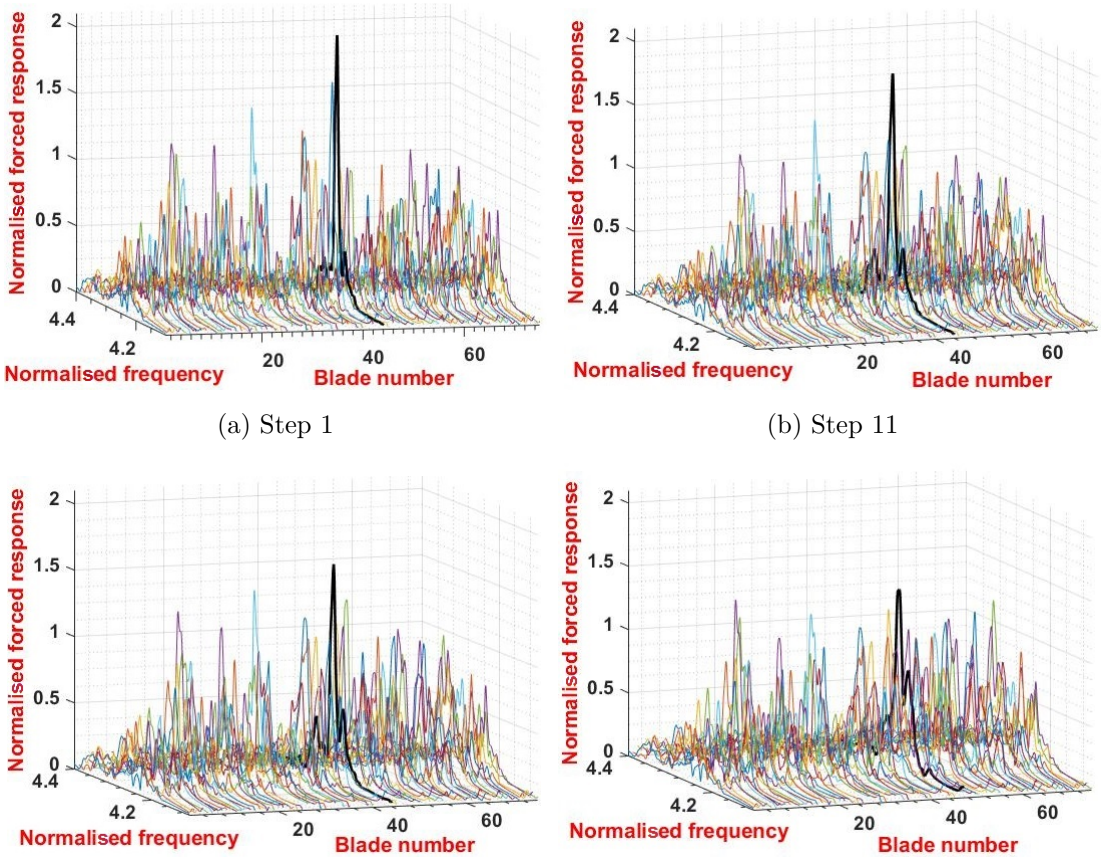

(a) Step 1

(b) Step 11

(c) Step 13

(d) Step 15

Figure 7.21: Variation in normalised forced response amplitude of blades with respect to optimisation step number (a) one, (b) eleven, (c) thirteen, and (d) fifteen.

Chapter 8

Concluding remarks

In the present study, considering the scatter in crystal orientation of single crystal blades used in gas turbine engines, uncertainty and sensitivity analysis has been performed for static displacements and stresses, and maximum forced response amplitude of bladed disk using realistic, high–fidelity finite element models.

8.1 Summary of methodology development

The main contributions of the present study are summarized in the following points:

- For a bladed disk with friction contacts at root and shroud interfaces, uncertainty analysis using conventional Monte Carlo simulations could be prohibitively expensive. Therefore surrogate modelling based on polynomial chaos expansion, that can closely approximate the FE model has been used in this study. For mistuned bladed disks, with numerous design parameters that are random variables, the use of polynomial chaos results in the so-called "curse of dimensionality" problem. To address this issue, the use of gradients of function values, in addition to function values itself, is proposed. It has been demonstrated through the study of static deformation of the non-linear bladed disk that a faster convergence in statistical characteristics can be obtained by using gradient enhanced polynomial chaos expansion compared to conventional PCE.

- A methodology for global sensitivity analysis, hitherto unused in the analysis

of mistuned bladed disk, has been introduced to investigate the contribution of scattering in individual blade anisotropy angles on variance in the static and dynamic response of bladed disk. The Sobol indices for blade anisotropy angles are obtained analytically from deterministic coefficients in gradient enhanced polynomial chaos expansion.

- For uncertainty analysis of non-linear static deformation of the bladed disk, considering the manufacturing variations in root geometry and blade anisotropy angles, a surrogate model based on random forest, is proposed for uncertainty analysis. It has been demonstrated that the RF-based surrogate models can predict the variations in average contact pressure at blade–disk interface accurately, and therefore, can reduce the computational time required for uncertainty analysis.

- Considering the blade anisotropy angles as random variables, with a known probability distribution, analytical expressions for probability density function of the stochastic response of bladed disk, using sensitivity based linear approximation, have been derived.

- The possibility of optimising the blade anisotropy angles to minimise the forced response amplification due to anisotropy mistuning has been investigated for the first time. It has been demonstrated that by optimising anisotropy angles of only a few blades in the bladed disk, considerable reduction in the forced response amplification can be achieved.

8.2 Summary of results from numerical studies

The conclusions drawn from the present study can be summarised into three groups as follows:

(a) **Effects of blade anisotropy mistuning on static deformation of the mistuned bladed disk.**

- Based on local and global sensitivity analysis, it can be concluded that the crystal orientation of a blade influences the static deformation of that blade and of immediately adjacent blades in the mistuned bladed disk. The effect

of crystal orientation of a blade on deformation of the blades positioned farther from the considered blades is negligible, especially for bladed disk with friction joints on roots and shrouds.

- Based on the analysis of numerous mistuning patterns, it has been concluded that the scatter in blade anisotropy angles could result in significant scatter in blade displacements under centrifugal loading. Among the three components of displacements studied, scatter in axial and tangential displacement has been found to be significant while that for radial displacement is marginal. Based on studying the variation in von Mises stress at fir–tree root of a blade in the bladed disk, for 250 different mistuning patterns, a maximum variation of 28% has been obtained.

- Among the three anisotropy angles, defining the orientation of the crystal axis with respect to blade geometry axis, local sensitivity analysis shows that sensitivity of displacements and stresses to primary anisotropy angle that define the semi-cone angle between crystal axis and blade geometry axis is the highest. The results obtained from local and global sensitivity analysis contradict, especially regarding the importance of the third anisotropy angle defining the rotation of the crystal axis about the blade geometry axis. Global sensitivity analysis suggests that the contribution of the third anisotropy angle to uncertainty of axial and radial displacement of blades is significant.

- A comparison of the analytically derived PDF obtained using linear approximation of static displacements of a tuned bladed disk with PDF obtained numerically from FE model evaluations of numerous samples of crystal orientations suggest that a linear approximation is inadequate to model the variation of blade displacements in the original domain of variation of anisotropy angles.

(b) **Effects of blade anisotropy orientation and root geometry variation on the static deformation of bladed disk.**

- To understand the effects of root geometry variation on non-linear static deformation of bladed disk, different root geometry variants were analysed.

It was concluded that significant variation in contact pressure can result from variation in root geometry within the manufacturing tolerance limits.

- The local sensitivity of blade displacements with respect to anisotropy angles is different for different orientation of the anisotropy axis. It was found that the sensitivity of displacements to the third anisotropy angle increases monotonically for most root and shroud geometry variants when the primary anisotropy angle or the semi-cone angle between anisotropy axis and geometry axis increases.

- The effects of blade anisotropy orientation on average and maximum contact pressure at fir–tree root have been investigated for different root geometry variants. Based on the uncertainty and sensitivity analysis, it has been concluded that the contact pressure on fir–tree root surfaces are more sensitive to blade anisotropy orientation for some root geometry variants compared to that for other variants analysed.

(c) **Effects of blade anisotropy mistuning on forced response amplification of bladed disk.**

- For a mistuned bladed disk with bonded contacts at root and shroud interfaces, the effect of blade anisotropy mistuning on forced response has been investigated. Based on the analysis of numerous anisotropy mistuning patterns it was concluded that the effects of blade anisotropy mistuning is significant for forced response excitation of blade-dominant modes compared to that for the excitation of disk-dominant modes.

- Sensitivity analysis using local and global sensitivity methods suggest that while the maximum forced response of mistuned bladed disk shows high sensitivity to primary anisotropy angle, the anisotropy angle defining the rotation of the crystal axis about blade geometry axis contribute significantly to the uncertainty in forced response.

- Based on a comparison of statistics obtained from gradient based polynomial chaos expansion and Monte Carlo simulations, it can be concluded that polynomial chaos expansion can provide accurate statistical charac-

teristics for variation in maximum forced response of anisotropy mistuned bladed disk. In the present study, the case of bladed disk with linear bonded contacts was considered. Since the computational time required for modal analysis and forced response analysis of linear models of bladed disk are comparable to the time required to obtain gradient values for maximum forced, the use of polynomial chaos does not provide any computational gain. It is expected that the use of gradient based polynomial chaos expansion will result in significant gain in computational cost while analysing bladed disk with non-linear friction contacts at interfaces.

- The possibility of optimising the blade anisotropy angles of few blades in the mistuned bladed disk to minimise the forced response amplification factor has been demonstrated. For a sample mistuning pattern analysed, reduction in amplification factor of 38% has been achieved by optimising the crystal orientation of a single blade in the mistuned bladed disk.

8.3 Further scope of research

The objectives set forward in Chapter 1, section 1.4 have been achieved by various analyses undertaken and the results have been presented. Nonetheless, there is ample scope for further research on topics related to anisotropy mistuned bladed disk such as:

(a) The investigation of the effects of variation in blade crystal orientation and root geometry on forced response remains to be investigated.

(b) The investigation of the effects of uncertainty in crystal orientation on forced response of bladed disk considering non-linear friction contacts at fir–tree root and shroud interfaces.

(c) A generalized approach for considering the effect of root geometry variation on static and dynamic response of the bladed disk, such as using parametrization of critical fir–tree geometry features, would be of great practical interest.

(d) For the tuned bladed disk, the analytical expressions obtained for calculating the probability of blade response exceeding a critical value based on linear approxi-

mation of the blade displacements are not sufficiently accurate. The derivation of analytical expression gets more mathematically challenging when using higher order approximation for blade displacements. Further research is necessary to find simple mathematical models which can predict the variation in response of bladed disk with respect to variation in blade anisotropy angles.

Bibliography

[1] Rolls-Royce, 2005. *The Jet Engine*. John Wiley & Sons Ltd on behalf of Rolls Royce Plc, London, England, pp. 76–87.

[2] Langston, L., 2015. "Each blade a single crystal". *American Scientist,* ***103***(1), pp. 30–33.

[3] Bounazef, M., Guessasma, S., and Bedia, E. A. A., 2007. "Blade protection and efficiency preservation of a turbine by a sacrificial material coating". *Advanced Powder Technology,* ***18***(2), pp. 123 – 133.

[4] Ibrahim, R. A., 1987. "Structural dynamics with parameter uncertainties". *Applied Mechanics Reviews,* ***40***(3), pp. 309–328.

[5] Smith, R. C., 2014. *Uncertainty Quantification: Theory, Implementation, and Applications*. SIAM, pp. 7–8.

[6] Breiman, L., 2001. "Random forests". *Machine Learning,* ***45***(1), pp. 5–32.

[7] Ling, J., Ruiz, A., Lacaze, G., and Oefelein, J., 2017. "Uncertainty analysis and data-driven model advances for a jet-in-crossflow". *Journal of Turbomachinery,* ***139***(2), pp. 021008(1)–021008(9).

[8] Yu, D., Li, F., Yang, J., Cheng, K., Shu, W., Lv, K., and Li, M., 2016. "Structural optimization of fir-tree root and groove for turbine blade with splines and genetic algorithm". In *Proceedings of the ASME Turbo Expo*. GT2016-56518. Seoul, South Korea, June 13-17, 2016.

[9] O'Hagan, A., 2013. "Polynomial chaos: A tutorial and critique from a statistician's perspective". *SIAM/ASA J. Uncertainty Quantification,* ***20***, pp. 1–20.

[10] Wiener, N., 1938. "The homogeneous chaos". *American Journal of Mathematics,* ***60***(4), pp. 897–936.

[11] Cameron, R. H., and Martin, W. T., 1947. "The orthogonal development of non-linear functionals in series of fourier-hermite functionals". *Annals of Mathematics,* ***48***(2), pp. 385–392.

[12] Xiu, D., and Karniadakis, G. E., 2003. "Modeling uncertainty in flow simulations via generalized polynomial chaos". *Journal of Computational Physics,* ***187***(1), pp. 137–167.

[13] Roderick, O., Anitescu, M., and Fischer, P., 2010. "Polynomial regression approaches using derivative information for uncertainty quantification". *Nuclear Science and Engineering,* ***164***(2), pp. 122–139.

[14] Ganapathysubramanian, B., and Zabaras, N., 2007. "Sparse grid collocation schemes for stochastic natural convection problems". *Journal of Computational Physics,* ***225***(1), pp. 652–685.

[15] Reagan, M. T., Najm, H. N., Ghanem, R. G., and Knio, O. M., 2003. "Uncertainty quantification in reacting-flow simulations through non-intrusive spectral projection". *Combustion and Flame,* ***132***(3), pp. 545–555.

[16] Winokur, J., Kim, D., Bisetti, F., Le Maitre, O. P., and Knio, O. M., 2016. "Sparse pseudo spectral projection methods with directional adaptation for uncertainty quantification". *Journal of Scientific Computing,* ***68***(2), pp. 596–623.

[17] Saltelli, A., and Annoni, P., 2010. "How to avoid a perfunctory sensitivity analysis". *Environmental Modelling & Software,* ***25***(12), pp. 1508–1517.

[18] Tortorelli, D. A., and Michaleris, P., 1994. "Design sensitivity analysis: Overview and review". *Inverse Problems in Engineering,* ***1***(1), pp. 71–105.

[19] Hesse, S. H., Lukaszewicz, D. H. J. A., and Duddeck, F., 2015. "A method to reduce design complexity of automotive composite structures with respect to crashworthiness". *Composite Structures,* ***129***, pp. 236–249.

[20] Saltelli, A., and Annoni, P., 2010. "How to avoid a perfunctory sensitivity analysis". *Environmental Modelling & Software,* ***25***(12), pp. 1508–1517.

[21] Cukier, R. I., Levine, H. B., and Shuler, K. E., 1978. "Nonlinear sensitivity analysis of multiparameter model systems". *Journal of Computational Physics,* ***26***(1), pp. 1–42.

[22] Sobol, I. M., 2001. "Global sensitivity indices for nonlinear mathematical models and their monte carlo estimates". *Mathematics and Computers in Simulation,* ***55***(1-3), pp. 271–280.

[23] Saltelli, A., and Scott, M., 1997. "Guest editorial: The role of sensitivity analysis in the corroboration of models and itslink to model structural and parametric uncertainty". *Reliability Engineering & System Safety,* ***57***(1), pp. 1 – 4.

[24] Meguid, S. A., Kanth, P. S., and Czekanski, A., 2000. "Finite element analysis of fir-tree region in turbine discs". *Finite Elements in Analysis and Design,* ***35***(4), pp. 305 – 317.

[25] Meguid, S., Refaat, M., and Papanikos, P., 1996. "Theoretical and experimental studies of structural integrity of dovetail joints in aeroengine discs". *Journal of Materials Processing Technology,* ***56***(1-4), pp. 668–677.

[26] Sinclair, G. B., Cormier, N. G., Griffin, J. H., and Meda, G., 1999. "Contact stresses in dovetail attachments: Finite element modeling". *Journal of Engineering for Gas Turbines and Power,* ***124***(1), pp. 182–189.

[27] Witek, L., 2006. "Failure analysis of turbine disc of an aero engine". *Engineering Failure Analysis,* ***13***(1), pp. 9–17.

[28] Sun, C., Zhou, Y., Chen, J., and Miao, H., 2015. "Measurement of deformation close to contact interface using digital image correlation and image segmentation". *Experimental Mechanics,* ***55***(8), pp. 1525–1536.

[29] Gean, M., and Farris, T., 2005. "Finite element analysis of the mechanics of blade/disk contacts". In 46th AIAA/ASME/ASCE/AHS/ASC Structures, Structural Dynamics and Materials Conference, Structures, Structural

Dynamics, and Materials and Co-located Conferences, American Institute of Aeronautics and Astronautics. AIAA 2005-1907.

[30] Beisheim, J. R., and Sinclair, G. B., 2003. "On the three-dimensional finite element analysis of dovetail attachments". *Journal of Turbomachinery,* ***125***(2), pp. 372–379.

[31] Beisheim, J. R., and Sinclair, G. B., 2008. "Three-dimensional finite element analysis of dovetail attachments with and without crowning". *Journal of Turbomachinery,* ***130***(2), pp. 021012(1)–021012(8).

[32] Wagner, F., Kuhhorn, A., Weiss, T., and Otto, D., 2016. "Influence of different parametrizations on the optimum design of a high pressure turbine blade firtree". In *Proceedings of the ASME Turbo Expo*. GT2016-56749. Seoul, South Korea, June 13-17, 2016.

[33] Song, W., Keane, A., Rees, J., Bhaskar, A., and Bagnall, S., 2002. "Turbine blade fir-tree root design optimisation using intelligent cad and finite element analysis". *Computers & Structures,* ***80***(24), pp. 1853–1867.

[34] Song, W., Keane, A., Rees, J., Bhaskar, A., and Bagnall, S., 2002. "Local shape optimisation of turbine disc firtrees using nurbs". In *9th AIAA/ISSMO Symposium on Multidisciplinary Analysis and Optimization*, Multidisciplinary Analysis Optimization Conferences, American Institute of Aeronautics and Astronautics. AIAA 2002-5486.

[35] Ou, H., Lu, B., Cui, Z. S., and Lin, C., 2013. "A direct shape optimization approach for contact problems with boundary stress concentration". *Journal of Mechanical Science and Technology,* ***27***(9), pp. 2751–2759.

[36] Zboinski, G., 1995. "Physical and geometrical non-linearities in contact problems of elastic turbine blade attachments". *Proceedings of the Institution of Mechanical Engineers, Part C: Journal of Mechanical Engineering Science,* ***209***(4), pp. 273–286.

[37] Deshpande, A. S., Keane, J. A., Sobester, A., and Toal, J. J. D., 2012. "Geometric parameterisation of firtree joints in gas turbine discs considering man-

ufacturing variability". In *Proceedings of 3rd Aircraft Structural Design Conference*, Delft, Netherlands, 9-11 October 2012, pp. 470–478.

[38] Qin, F., Chen, L., Li, Y., and Zhang, X., 2006. "Fundamental frequencies of turbine blades with geometry mismatch in fir-tree attachments". *Journal of Turbomachinery,* ***128***(3), pp. 512–516.

[39] Arakere, N. K., and Swanson, G., 2002. "Effect of crystal orientation on fatigue failure of single crystal nickel base turbine blade superalloys". *Journal of Engineering for Gas Turbines and Power,* ***124***(1), pp. 161–176.

[40] Pollock, T. M., and Tin, S., 2006. "Nickel-based superalloys for advanced turbine engines: Chemistry, microstructure and properties". *Journal of Propulsion and Power,* ***22***(2), pp. 361–374.

[41] Wang, L. N., Liu, Y., Yu, J. J., Xu, Y., Sun, X. F., Guan, H. R., and Hu, Z. Q., 2009. "Orientation and temperature dependence of yielding and deformation behavior of a nickel-base single crystal superalloy". *Materials Science and Engineering: A,* ***505***(1), pp. 144–150.

[42] MacKay, R. A., and Maier, R. D. "The influence of orientation on the stress rupture properties of nickel-base superalloy single crystals". *Metallurgical Transactions A,* ***13***(10), pp. 1747–1754.

[43] Yue, Z. F., and Lu, Z. Z., 1998. "The influence of crystallographic orientation and strain rate on the high-temperature low-cyclic fatigue property of a nickel-base single-crystal superalloy". *Metallurgical and Materials Transactions A,* ***29***(3), pp. 1093–1099.

[44] Hou, N. X., Gou, W. X., Wen, Z. X., and Yue, Z. F., 2008. "The influence of crystal orientations on fatigue life of single crystal cooled turbine blade". *Materials Science and Engineering: A,* ***492***(1), pp. 413–418.

[45] Segersall, M., Leidermark, D., and Moverare, J. J., 2015. "Influence of crystal orientation on the thermomechanical fatigue behaviour in a single-crystal superalloy". *Materials Science and Engineering: A,* ***623***, pp. 68 – 77.

[46] Adair, B. S., Johnson, W. S., Antolovich, S. D., and Staroselsky, A., 2015. "Crystallographic orientation and temperature effects on the fatigue crack growth rate and resulting fracture surface morphology in pwa1484 single crystal superalloy". *Fatigue and Fracture of Engineering Materials and Structures,* ***38***(1), pp. 56–68.

[47] Amaro, R. L., Antolovich, S. D., and Neu, R. W., 2012. "Mechanism-based life model for out-of-phase thermomechanical fatigue in single crystal ni-base superalloys". *Fatigue and Fracture of Engineering Materials and Structures,* ***35***(7), pp. 658–671.

[48] He, Z., Qiu, W., Fan, Y. N., Han, Q. N., Shi, H. J., and Ma, X., 2017. "Effects of secondary orientation on fatigue crack initiation in a single crystal superalloy". *Fatigue and Fracture of Engineering Materials and Structures,* ***41***(4), pp. 935–948.

[49] Latief, F. H., Kakehi, K., Murakami, H., and Kasai, K., 2012. "Influence of crystallographic orientation on creep behavior of aluminized ni-base single crystal superalloys". In *Proceedings of the Superalloys 2012: International Symposium on Superalloys*, pp. 311–320.

[50] Wen, Z., Zhang, D., Li, S., Yue, Z., and Gao, J., 2017. "Anisotropic creep damage and fracture mechanism of nickel-base single crystal superalloy under multiaxial stress". *Journal of Alloys and Compounds,* ***692***, pp. 301–312.

[51] Weiss, T., Voigt, M., Schlums, H., Mucke, R., Becker, K.-H., and Vogeler, K., 2009. "Probabilistic finite-element analyses on turbine blades". In *Proceedings of the ASME Turbo Expo.* GT2009-59877. Orlando, Florida, USA, June 8-12, 2009.

[52] Kaneko, Y., 2011. "Study on vibration characteristics of single crystal blade and directionally solidified blade". In *Proceedings of the ASME Turbo Expo.* GT2011-45032. Vancouver, Canada, June 6-10, 2011.

[53] Manetti, M., Giovannetti, I., Pieroni, N., Horculescu, H., Peano, G., Zonfrillo, G., and Giannozzi, M., 2009. "The dynamic influence of crystal orientation on

a second generation single crystal material for turbine buckets". In *Proceedings of the ASME Turbo Expo*. GT2009-59091. Orlando, Florida, USA, June 8-12, 2009.

[54] Wen, Z., Mao, H., Yue, Z., and Wang, B., 2014. "The influence of crystal orientation on vibration characteristics of dd6 nickel-base single crystal superalloy turbine blade". *Journal of Materials Engineering and Performance,* ***23***(2), pp. 372–377.

[55] Kaneko, Y., 2012. "Study on vibration characteristics on directionally solidified blade". *Nihon Kikai Gakkai Ronbunshu, C Hen/Transactions of the Japan Society of Mechanical Engineers, Part C,* ***78***(789), pp. 1388–1397.

[56] Kaneko, Y., Mori, K., and Ooyama, H. "Resonant response and random response analysis of mistuned bladed disk consisting of directionally solidified blade". In *Proceedings of the ASME Turbo Expo*. GT2015-4287. Montreal, Canada, June 15-19, 2015.

[57] Savage, M., 2012. "The influence of crystal orientation on the elastic stresses of a single crystal nickel-based turbine blade". *Journal of Engineering for Gas Turbines and Power,* ***134***(1).

[58] Fang, Y., and Li, Y., 2013. "Dynamic responses of nickel-based single crystal superalloy dd6 blade". *Journal of Materials Engineering and Performance,* ***22***(6), pp. 1565–1573.

[59] Zhang, X. H., Gao, H. S., Yu, K. H., Wen, Z. X., Zhao, Y. C., and Yue, Z. F., 2018. "Crystal orientation effect and multi-fidelity optimization of a solid single crystal superalloy turbine blade". *Computational Materials Science,* ***149***, pp. 84–90.

[60] Ling, J., and Templeton, J., 2015. "Evaluation of machine learning algorithms for prediction of regions of high reynolds averaged navier stokes uncertainty". *Physics of Fluids,* ***27***(8), pp. 085103(1)–(20).

[61] Burges, C. J. C., 1998. "A tutorial on support vector machines for pattern recognition". *Data Mining and Knowledge Discovery,* ***2***(2), pp. 121–167.

[62] Trehan, S., Carlberg, K. T., and Durlofsky, L. J., 2017. "Error modeling for surrogates of dynamical systems using machine learning". *International Journal for Numerical Methods in Engineering,* ***112***(12), pp. 1801–1827.

[63] Mezic, I., and Runolfsson, T., 2008. "Uncertainty propagation in dynamical systems". *Automatica,* ***44***(12), pp. 3003–3013.

[64] West, T., and Gumbert, C., 2017. "Multifidelity, multidisciplinary design under uncertainty with non-intrusive polynomial chaos". In 58th AIAA/ASCE/AHS/ASC Structures, Structural Dynamics, and Materials Conference. AIAA 2017-1936. Grapevine, Texas.

[65] Panunzio, A. M., Salles, L., Schwingshackl, C., and Gola, M., 2015. "Asymptotic numerical method and polynomial chaos expansion for the study of stochastic non-linear normal modes". In *Proceedings of the ASME Turbo Expo.* GT2015-43560. Montreal, Cananda, June 15-19, 2015.

[66] Sinha, A., 2006. "Computation of the statistics of forced response of a mistuned bladed disk assembly via polynomial chaos". *Journal of Vibration and Acoustics, Transactions of the ASME,* ***128***(4), pp. 449–457.

[67] Kala, Z., and Vales, J., 2017. "Global sensitivity analysis of lateral-torsional buckling resistance based on finite element simulations". *Engineering Structures,* ***134***, pp. 37–47.

[68] Sudret, B., 2008. "Global sensitivity analysis using polynomial chaos expansions". *Reliability Engineering & System Safety,* ***93***(7), pp. 964–979.

[69] Antinori, G., Duddeck, F., and Fischersworring-Bunk, A. "Sensitivity analysis and uncertainty quantification for a coupled secondary air system thermomechanical model of a jet engine low pressure turbine rotor". In Vulnerability, Uncertainty, and Risk: Quantification, Mitigation, and Management - Proceedings of the 2nd International Conference on Vulnerability and Risk Analysis and Management, ICVRAM 2014 and the 6th International Symposium on Uncertainty Modeling and Analysis, ISUMA 2014, pp. 1543–1553.

[70] Griffin, J. H., and Hoosac, T. M., 1984. "Model development and statistical investigation of turbine blade mistuning". *Journal of Vibration, Acoustics, Stress, and Reliability in Design,* ***106***(2), pp. 204–210.

[71] Wei, S.-T., and Pierre, C., 1990. "Statistical analysis of the forced response of mistuned cyclic assemblies". *AIAA Journal,* ***28***(5), pp. 861–868.

[72] Avalos, J., Mignolet, M. P., and Soize, C. "Response of bladed disks with mistuned blade-disk interfaces". In *Proceedings of the ASME Turbo Expo.* GT2009-59580, June 8-12, 2009, Orlando, Florida, USA.

[73] Beck, J. A., Brown, J. M., Slater, J. C., and Cross, C. J., 2013. "Probabilistic mistuning assessment using nominal and geometry based mistuning methods". *Journal of Turbomachinery,* ***135***(3), pp. 051004(1)–(9).

[74] Myhre, M., Moyroud, F., and Fransson, T. H., 2003. "Numerical investigation of the sensitivity of forced response characteristics of bladed disks to mistuning". In *Proceedings of the ASME Turbo Expo.* GT2003-38007. Atlanta, Georgia, USA, June 16-19, 2003, pp. 171–182.

[75] Joshi, A. G. S., and Epureanu, B. I. "Reduced order models for blade-to-blade damping variability in mistuned blisks". In *Proceedings of the ASME Turbo Expo.* GT2011-45661. Voncouver, British Columbia, Canada, 6-10 June 2011, Vol. 6, pp. 1033–1045.

[76] D'Souza, K. X., and Epureanu, B. I. "A statistical characterization of the effects of mistuning in multi-stage bladed disks". In *Proceedings of the ASME Turbo Expo* GT2011-46698. Voncouver, British Columbia, Canada, 6-10 June 2011, Vol. 6, pp. 1137–1147.

[77] Laxalde, D., and Pierre, C., 2011. "Modelling and analysis of multi-stage systems of mistuned bladed disks". *Computers & Structures,* ***89***(3-4), pp. 316–324.

[78] Vishwakarma, V., and Sinha, A., 2015. "Forced response statistics of a bladed rotor with geometric mistuning". *AIAA Journal,* ***53***(9), pp. 2776–2781.

[79] Wang, P., and Li, L., 2014. "Parametric dynamics of mistuned bladed disk". In *Proceedings of the ASME Turbo Expo.* GT2014-26678, Dusseldorf, Germany, 16-20 June 2014., Vol. 7B.

[80] Tan, Y., Zang, C., Zhou, B., Duan, Y., and Petrov, E. P., 2016. "Sensitivity analysis of high-frequency forced response for mistuned bladed discs based on high-fidelity models". In *Proceedings of the ASME Turbo Expo.* GT2016-57690. Seoul, South Korea, 13-17 June 2016.

[81] Hohl, A., Kriegesmann, B., Wallaschek, J., and Panning, L. "The influence of blade properties on the forced response of mistuned bladed disks". In *Proceedings of the ASME Turbo Expo* GT2011-46826. Voncouver, British Columbia, Canada, 6-10 June 2011, Vol. 6, pp. 1159–1170.

[82] Bah, M. T., Nair, P. B., Bhaskar, A., and Keane, A. J. "Forced response statistics of mistuned bladed disks: a stochastic reduced basis approach". *Journal of Sound and Vibration,* ***263***(2), pp. 377–397.

[83] Liao, H., Wang, J., Yao, J., and Li, Q., 2010. "Mistuning forced response characteristics analysis of mistuned bladed disks". *Journal of Engineering for Gas Turbines and Power,* ***132***(12), pp. 122501(1)–11.

[84] Raeisi, E., and Ziaei-Rad, S., 2013. "The worst response of mistuned bladed disk system using neural network and genetic algorithm". *Meccanica,* ***48***(2), pp. 367–379.

[85] Bhartiya, Y., and Sinha, A., 2013. "Reduced order modeling of a bladed rotor with geometric mistuning via estimated deviations in mass and stiffness matrices". *Journal of Engineering for Gas Turbines and Power,* ***135***(5), pp. 052501(1)–(8).

[86] Rahimi, M., and Ziaei-Rad, S., 2010. "Uncertainty treatment in forced response calculation of mistuned bladed disk". *Mathematics and Computers in Simulation,* ***80***(8), pp. 1746–1757.

[87] Yuan, J., Allegri, G., Scarpa, F., Rajasekaran, R., and Patsias, S., 2015.

"Probabilistic dynamics of mistuned bladed disc systems using subset simulation". *Journal of Sound and Vibration,* ***350***, pp. 185–198.

[88] Bhartiya, Y., and Sinha, A., 2012. "Reduced order model of a multistage bladed rotor with geometric mistuning via modal analyses of finite element sectors". *Journal of Turbomachinery,* ***134***(4), pp. 04001(1)–(8).

[89] Yuan, J., Allegri, G., Scarpa, F., Patsias, S., and Rajasekaran, R., 2016. "A novel hybrid neumann expansion method for stochastic analysis of mistuned bladed discs". *Mechanical Systems and Signal Processing,* ***72-73***, pp. 241–253.

[90] Nikolic, M., Petrov, E. P., and Ewins, D. J., 2008. "Robust strategies for forced response reduction of bladed disks based on large mistuning concept". *Journal of Engineering for Gas Turbines and Power,* ***130***(2), pp. 022501(1)–(11).

[91] Chan, Y. J., and Ewins, D. J., 2010. "Management of the variability of vibration response levels in mistuned bladed discs using robust design concepts. part 2: Tolerance design". *Mechanical Systems and Signal Processing,* ***24***(8), pp. 2792–2806.

[92] De Cazenove, J., Cogan, S., Baye, M. M., and Berthillier, M. "Forced response prediction of a mistuned bladed disk in the presence of aeroelastic coupling and model uncertainties". In *Institution of Mechanical Engineers - 10th International Conference on Vibrations in Rotating Machinery*, 11-13 September 2012, IMechE London, UK, pp. 281–291.

[93] Cha, D., and Sinha, A., 2006. "Statistics of responses of a mistuned and frictionally damped bladed disk assembly subjected to white noise and narrow band excitations". *Probabilistic Engineering Mechanics,* ***21***(4), pp. 384–396.

[94] Capiez-Lernout, E., Soize, C., and Mbaye, M., 2015. "Mistuning analysis and uncertainty quantification of an industrial bladed disk with geometrical nonlinearity". *Journal of Sound and Vibration,* ***356***, pp. 124–143.

[95] Petrov, E. P., 2009. "Analysis of sensitivity and robustness of forced response

for nonlinear dynamic structures". *Mechanical Systems and Signal Processing,* ***23***(1), pp. 68–86.

[96] Petrov, E. P., 2014. "Sensitivity analysis of multiharmonic self-excited limit-cycle vibrations in gas-turbine engine structures with nonlinear contact interfaces". In *Proceedings of the ASME Turbo Expo.* GT2014-26673, Dusseldorf, Germany, 16-20 June 2014., Vol. 7A.

[97] Petrov, E. P., 2008. "A sensitivity-based method for direct stochastic analysis of nonlinear forced response for bladed disks wirh friction interfaces". *Journal of Engineering for Gas Turbines and Power,* ***130***(2), pp. 022503(1)–(9).

[98] Martel, C., Sanchez-Alvarez, and J., J., 2018. "Intentional mistuning effect in the forced response of rotors with aerodynamic damping". *Journal of Sound and Vibration,* ***433***, pp. 212–229.

[99] Castanier, M., and Pierre, C., 1998. "Investigation of the combined effects of intentional and random mistuning on the forced response of bladed disks". In *34th AIAA/ASME/SAE/ASEE Joint Propulsion Conference and Exhibit.*, Joint Propulsion Conferences, American Institute of Aeronautics and Astronautics. AIAA-98-3720.

[100] Petrov, E., Vitali, R., and Haftka, R., 2000. "Optimization of mistuned bladed discs using gradient-based response surface approximations". *41st Structures, Structural Dynamics, and Materials Conference. AIAA2000-1522.*

[101] Beirow, B., Figaschewsky, F., Kuhhorn, A., and Bornhorn, A., 2017. "Modal analyses of an axial turbine blisk with intentional mistuning". *Journal of Engineering for Gas Turbines and Power,* ***140***(1), pp. 012503(1)–(11).

[102] Dhondt, G., 2018. "CalculiX CrunchiX user's manual version 2.14". In URL *http:www.dhondt.de/ccx_2.14.pdf*, accessed on 6 January 2019.

[103] Feinberg, J., and Langtangen, H. P., 2015. "Chaospy: An open source tool for designing methods of uncertainty quantification". *Journal of Computational Science,* ***11***(Supplement C), pp. 46 – 57.

[104] Adelman, H. M., and Haftka, R. T., 1986. "Sensitivity analysis of discrete structural systems". *AIAA Journal,* ***24***(5), pp. 823–832.

[105] Koscso, A., Dhondt, G., and Petrov, E. P., 2018. "High-fidelity sensitivity analysis of modal properties of mistuned bladed disks regarding material anisotropy". *Journal of Engineering for Gas Turbines and Power,* ***141***(2), pp. 021036(1)–(11).

[106] Torgo, L., 2000. "Inductive learning of tree-based regression models". *Ai Communications,* ***13***(2), pp. 137–138.

[107] Hastie, T., Friedman, J., and Tibshirani, R., 2001. *Additive Models, Trees, and Related Methods.* Springer New York, New York, NY, pp. 257–298.

[108] Pedregosa, F., Varoquaux, G., Gramfort, A., Michel, V., Thirion, B., Grisel, O., Blondel, M., Prettenhofer, P., Weiss, R., Dubourg, V., Vanderplas, J., Passos, A., Cournapeau, D., Brucher, M., Perrot, M., and Duchesnay, E., 2011. "Scikit-learn: Machine learning in Python". *Journal of Machine Learning Research,* ***12***, pp. 2825–2830.

[109] Gautschi, W., 2004. *Orthogonal polynomials: computation and approximation.* Oxford University Press, New York, USA, pp. 10–12.

[110] Koscso, A., and Petrov, E. "Sensitivity and forced response analysis of anisotropy-mistuned bladed disks with nonlinear contact interfaces". In *Proceedings of the ASME Turbo Expo.* GT2019-90629, June 17-21, 2019, Pheonix, Arizona, USA.

[111] Petrov, E. P., and Ewins, D. J., 2005. "Method for analysis of nonlinear multiharmonic vibrations of mistuned bladed disks with scatter of contact interface characteristics". *Journal of Turbomachinery,* ***127***(1), pp. 128–136.

[112] Jones, E., Oliphant, T., Peterson, P., et al., 2001–. SciPy: Open source scientific tools for Python. accessed on 6 January 2019.

[113] Gray, J. S., Moore, K. T., and Naylor, B. A., 2010. "Openmdao: An open-source framework for multidisciplinary analysis and optimization". In 13th

AIAA/ISSMO Multidisciplinary Analysis and Optimization Conference, Fort Worth, TX, AIAA, AIAA-2010-9101, AIAA.

[114] Saltelli, A., Annoni, P., Azzini, I., Campolongo, F., Ratto, M., and Tarantola, S., 2010. "Variance based sensitivity analysis of model output. design and estimator for the total sensitivity index". *Computer Physics Communications,* ***181***(2), pp. 259 – 270.

[115] Hosder, S., Walters, R., and Balch, M., 2007. "Efficient sampling for non-intrusive polynomial chaos applications with multiple uncertain input variables". In *48th AIAA/ASME/ASCE/AHS/ASC Structures, Structural Dynamics and Materials Conference*. AIAA 2007-1939. Hawaii, Honolulu, 23-26 April, 2007.